Sapienza
Università di Roma

FCC-ee collimation system design

Dottorato di Ricerca in Fisica degli Acceleratori (XXXVIII cycle)

Giacomo Broggi
ID number 2100600

Advisors
Dr. Manuela Boscolo
Dr. Roderik Bruce

Co-Advisor
Dr. Andrey Abramov

Academic Year 2025/2026

Thesis defended on 3 February 2026
in front of a Board of Examiners composed by:

Prof. Philip Burrows
Dr. Sara Casalbuoni
Prof. Antonio Morandi

FCC-ee collimation system design
PhD thesis. Sapienza Università di Roma

This thesis has been typeset by LaTeX and the Sapthesis class.

Author's email: giacomo.broggi@cern.ch

Abstract

The Future Circular electron–positron Collider (FCC-ee) is a proposed highest-energy, luminosity-frontier lepton collider designed to enable precision measurements in the electroweak and Higgs sectors. The machine is being designed to operate in four distinct running modes, with beam energies of 45.6 GeV, 80 GeV, 120 GeV, and 182.5 GeV, optimized for the production of different particles (Z, W, H, and $t\bar{t}$). Owing to beam intensities far exceeding those of any previous lepton collider, required to achieve unprecedented luminosities, the FCC-ee beams will feature stored beam energies up to 17.7 MJ—about two orders of magnitude higher than the current state-of-the-art lepton collider, SuperKEKB, and comparable to the stored beam energy of the heavy-ion beams in the Large Hadron Collider (LHC).

The FCC-ee thus represents a new operational regime for lepton colliders, where the combination of high stored beam energy and ultra-low emittances makes the beams highly destructive. This regime is extremely challenging from a beam-collimation standpoint. At the FCC-ee, a beam collimation system is indispensable—not only to reduce beam-induced backgrounds in the experimental detectors, as in previous lepton colliders, but also to protect the machine itself from unavoidable beam losses. A robust and efficient beam collimation system is therefore essential both to minimize detector backgrounds and to ensure machine protection, operational safety, and sustained availability as the FCC-ee progresses toward its integrated luminosity goals.

This thesis presents a comprehensive design study of a beam collimation system for the FCC-ee, combining analytical studies and advanced simulations to evaluate performance under a wide range of beam-loss scenarios expected during regular operation as well as abnormal conditions. In this work, dedicated simulation routines have been developed to model beam losses from beam–residual gas scattering and Touschek scattering. The simulation tools and developed routines have been benchmarked against measured data from the SuperKEKB collider, as well as with beam loss data from the LHC, reproducing observed beam-induced background trends or beam loss patterns with excellent accuracy. This validation demonstrates their reliability for predicting collimation performance not only at the FCC-ee but also at other existing or future colliders.

The outcome of this thesis is a proposed multi-stage beam collimation system for the FCC-ee, included in the machine's baseline design. More importantly, this work provides a comprehensive documentation of the principles and methods for developing a robust and efficient collimation system for any future electron–positron collider. The methodologies, tools, and design strategies developed here provide a solid foundation for future optimization of the FCC-ee collimation system and will play a key role in the forthcoming technical design phase of the machine. Finally, complementary studies on a crystal collimation system are presented, demonstrating its promising potential and identifying it as an interesting alternative to a traditional collimation system.

Contents

Chapter 1

Introduction

1.1 Lepton colliders

Particle colliders, a class of particle accelerators that collide particle beams, are powerful instruments in particle physics, enabling the exploration of the fundamental constituents of matter and the forces that govern their interactions.

Colliders can be broadly classified into two families: lepton colliders, which collide beams of leptons such as electrons or positrons, and hadron colliders, which collide beams of hadrons such as protons or heavy ions.

Hadron colliders, such as proton-proton (p-p) colliders, collide non-elementary particles having an internal structure composed of quarks and gluons. This implies that the initial state of the collisions is not well-defined on an event-by-event basis, thereby limiting the achievable precision in the measurements. Additionally, p-p collisions generate high rates of QCD backgrounds, thus requiring complex triggering schemes and detection systems operating under high levels of radiation. On the other hand, hadron colliders typically achieve the highest center-of-mass energies and are well-suited for discovery physics, thanks to the broad energy spectrum of the parton-parton collisions within the hadrons.

In contrast, lepton colliders, such as electron-positron (e^+e^-) colliders, collide elementary point-like particles with a well-defined initial state in terms of energy, momentum, and polarization, thus enabling high-precision measurements. They offer a cleaner experimental environment with trigger-less readout and low radiation levels. Circular e^+e^- colliders can achieve very large luminosities at lower energies ($\lesssim 350$ GeV), while higher energy e^+e^- collisions require linear collider designs due to limitations imposed by energy loss from synchrotron radiation emission, which scales as γ^4, with $\gamma = E/E_0$ being the relativistic gamma factor, E the particle energy and E_0 the particle rest energy.

Such limitations due to synchrotron radiation energy loss typically do not apply to circular hadron colliders, as the much larger rest energy of protons compared to electrons and positrons significantly reduces synchrotron radiation

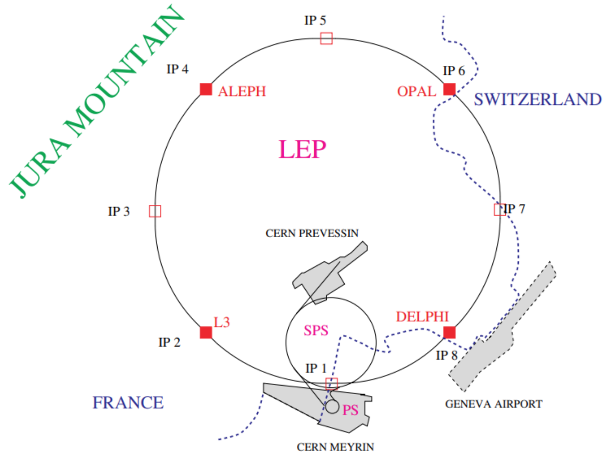

Figure 1.1. Layout of the LEP ring [5]. The eight access points are denoted IP1–8. The four LEP experiments L3, ALEPH, OPAL and DELPHI are installed at the even-numbered access points. Positrons travel clockwise, electrons anticlockwise from points 1 to 8. The location of two LEP injectors, the SPS (Super Proton Synchrotron) and the PS (Proton Synchrotron), is also indicated.

energy losses. This makes it possible to build and operate high-energy hadron colliders, such as the CERN Large Hadron Collider (LHC) [1], which collide proton beams with energies up to 6.8 TeV.

In summary, lepton colliders are best suited for high-precision measurements, allowing detailed studies of fundamental particles and interactions in cleaner experimental environments, while hadron colliders with their much higher achievable beam energies offer direct discovery potential, making them the primary tool for searching for new physics beyond the Standard Model. In the following, the focus will primarily be on lepton colliders, as they form the core subject of this work.

One of the most notable lepton colliders ever built is the Large Electron-Positron Collider (LEP) [2, 3], a 27 km circumference e^+e^- collider that operated at CERN from 1989 to 2000 [4]. LEP was housed in the same underground tunnel that now hosts the LHC, as shown in Fig. 1.1.

LEP was instrumental in testing the Standard Model of particle physics, particularly in measuring the properties of the Z and W bosons [4]. The results obtained from LEP experiments helped solidify the understanding of electroweak interactions and provided constraints on the search for the Higgs boson [6], which was later discovered at the LHC in 2012 [7].

At the time of writing this thesis, five e^+e^- colliders, all of circular type, are in operation [8], as listed in Table 1.1.

Future lepton colliders, such as the Future Circular Electron-Positron Collider (FCC-ee) [9], on which this thesis work is focused, are being designed

Table 1.1. Operating e^+e^- colliders as of 2025 [8]. All listed machines are of the circular type. The parameter E denotes the beam energy in GeV.

Parameter	VEPP-4M	DAΦNE	VEPP-2000	BEPC II	SuperKEKB
Laboratory	INP	INFN-LNF	INP	IHEP	KEK
Location	Novosibirsk, Russia	Frascati, Italy	Novosibirsk, Russia	Beijing, China	Tsukuba, Japan
First operation	1994	1999	2006	2008	2018
E [GeV]	6	0.510	1.0	2.45	7 (e^-), 4 (e^+)
Circumference [m]	366	98	24	240	3016
Luminosity [10^{30} cm^{-2} s^{-1}]	20	453	100	1000	24000

to advance our understanding of particle physics [10]. These colliders aim to explore higher energy regimes and achieve unprecedented luminosities by leveraging the latest developments in accelerator physics and technology.

The FCC-ee will be described in detail in the following section. The SuperKEKB collider will be discussed further in Section 1.3. This operating collider plays an important role in this work, as it has been used to benchmark the simulation tools employed in the design studies for the FCC-ee, utilizing measured data from this machine.

1.2 FCC-ee: the Future Circular electron–positron Collider

The Future Circular Electron-Positron Collider (FCC-ee) [9, 11] is a proposed high-energy, high-luminosity e^+e^- collider that is being designed to explore physics beyond the current energy and luminosity frontiers for leptons [10]. With a circumference of 90.7 km, the FCC-ee will operate in four distinct modes, each with a center-of-mass energy optimized for the production of different particles: Z bosons, W bosons, Higgs bosons (H), and top quark-antiquark pairs ($t\bar{t}$). These modes will require beam energies of 45.6 GeV, 80 GeV, 120 GeV, and 182.5 GeV. The collider is foreseen to operate in the Z mode for the first four years, collecting a total of 5×10^{12} Z bosons, which corresponds to 10^5 times the statistics collected by LEP [12]. This will be followed by two years in W mode, producing more than 10^8 W boson pairs, a 10^4-fold increase over LEP [12]. The FCC-ee is then expected to operate in the H (ZH) mode for three years, accumulating 2×10^6 Higgs bosons, before transitioning to the $t\bar{t}$ mode for five years, where it will collect 2×10^6 top quark-antiquark pairs [12].

The baseline layout for the FCC-ee [11], see Fig. 1.2, includes four interaction points (IPA, IPD, IPG, and IPJ), each equipped with an experimental detector, and four long straight sections (PB, PF, PH, and PL) to host various technical systems, such as injection/extraction, collimation, and RF.

The FCC-ee project is planned to progress through multiple phases, starting with the pre-TDR phase (2025–2027) and environmental evaluation (2026–2030). A key milestone will be the project approval by the CERN Council, scheduled for 2028. If the project is approved, this will be followed by civil engineering design and tendering, expected to continue until 2032. Civil engineering construction

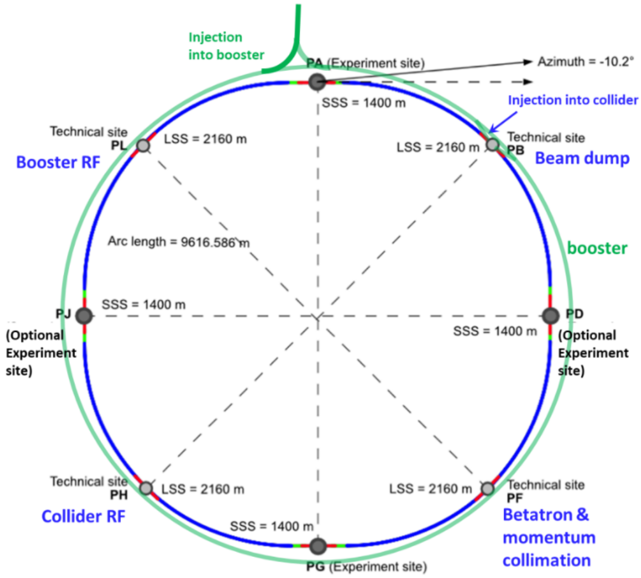

Figure 1.2. FCC-ee layout [12], featuring four interaction points (IPA, IPD, IPG, IPJ). The experimental insertions at IPA, IPD, IPG, and IPJ alternate with long straight sections (LSS) serving different technical purposes: injection and extraction (beam dump) at PB, collimation at PF, and RF at PH. The collider ring is shown in blue, while the top-up injection booster is shown in green.

is planned to take place between 2033 and 2041, with technical infrastructure installation foreseen from 2039 to 2043. The accelerator installation is expected to occur between 2041 and 2045, followed by hardware commissioning in 2046. Beam commissioning is planned to begin in mid-2046, with nominal operation targeted for 2048. In parallel, the FCC-ee injector project is expected to follow a similar timeline, with civil construction foreseen from 2031 to 2034, component installation planned for 2035 to 2040, and beam commissioning for 2042. The overall timeline of the project, according to Ref. [12], is illustrated in Fig. 1.3.

The FCC-ee is designed as a double-ring collider [11], thus allowing a large number of particle bunches per beam to maximize luminosity while satisfying strict operational constraints. A key limitation is the synchrotron radiation power emission, which by design is bound to 50 MW per beam at all energies by limiting the beam current [11].

To optimize performance across all operational scenarios, the FCC-ee includes several advanced design features. The two beam lines intersect at the interaction points with a horizontal crossing angle of 30 mrad [11], while the critical energy of synchrotron radiation near the collision points is kept below 100 keV to minimize detector backgrounds [11]. A common lattice configuration is employed for all energy modes, with only minor modifications in the RF section required for the $t\bar{t}$ mode [11]. Machine parameters, including the

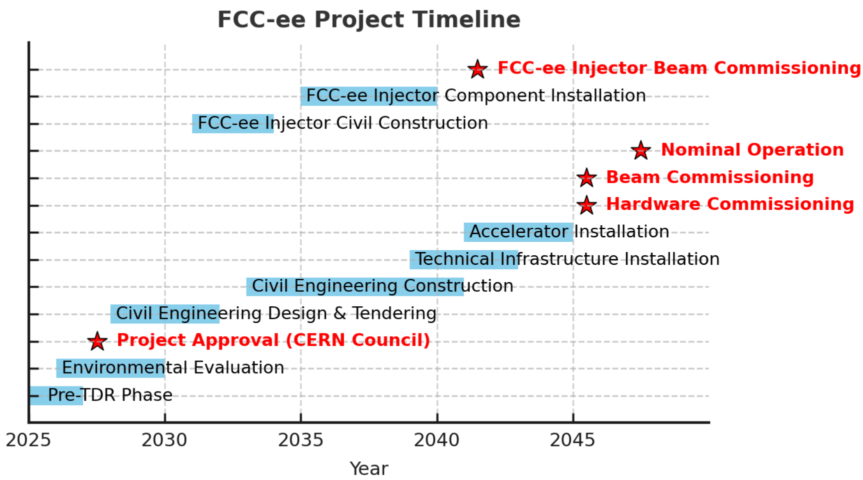

Figure 1.3. Timeline of the FCC-ee project [12].

betatron tune, phase advance in the arc cell, final focus optics, and sextupole configuration, are adjusted at each energy by varying the strengths of the magnets [11]. At the highest beam energy of 182.5 GeV, synchrotron radiation leads to an energy loss of approximately 5% per turn [11]. To compensate for this effect, a tapering scheme is implemented [11], in which the strength of all magnets (except for the solenoids) is scaled according to the local beam energy.

A crucial aspect for the success of the FCC-ee is the top-up injection scheme [13], which ensures continuous replenishment of electron and positron beams at their collision energy. By maintaining a nearly constant beam current, this approach sustains luminosity at peak levels throughout the physics run, increasing the integrated luminosity by an order of magnitude [9]. Implementing this scheme requires the installation of a booster synchrotron within the collider tunnel.

The machine parameters of the FCC-ee Global Hybrid Correction (GHC) lattice [14] version V25.2 [15] are summarized in Table 1.2. At the time of writing, the FCC-ee GHC lattice constitutes the baseline lattice design for the FCC-ee and is the configuration on which the studies presented in this work have been developed (specifically using version V25.2). In parallel, an alternative optics design is under development, namely the Local Chromatic Correction (LCC) lattice [16].

A distinctive feature of the FCC-ee is that, unlike in any lepton collider to date, where the equilibrium beam parameters are primarily determined by synchrotron radiation (SR) emitted as the beams traverse the dipole magnets in the collider arcs, in the FCC-ee, they are also significantly influenced by beamstrahlung (BS) emission, see Table 1.2. Beamstrahlung is the electromagnetic radiation emitted by a particle during a collision due to the intense electromagnetic field of the opposing bunch [17].

The technological foundation required to construct such a high-energy, high-luminosity circular lepton collider is already in place. The current focus is, therefore, on refining the design, cost, and performance optimization to ensure the feasibility and success of the FCC-ee.

Table 1.2. FCC-ee collider parameters for the GHC lattice V25.2 [15].

Beam energy [GeV]	45.6	80	120	182.5
# of IPs		4		
Circumference [km]		90.658499		
Bend. radius of arc dipole [km]		10.021		
Energy loss / turn [GeV]	0.0390	0.369	1.86	9.99
SR power / beam [MW]		50		
Beam current [mA]	1281	135	26.8	5.0
Colliding bunches / beam	12000	1852	300	60
Colliding bunch population [10^{11}]	2.02	1.38	1.69	1.57
Horizontal emittance at collision ε_x [nm]	0.74	2.16	0.66	1.69
Vertical emittance at collision ε_y [pm]	1.9	2.0	1.0	1.39
Lattice v. emittance $\varepsilon_{y,\mathrm{lattice}}$ [pm]	0.65	1.20	0.57	0.81
Arc cell	Long	90/90	90/90	90/90
Momentum compaction α_p [10^{-6}]	28.55	28.67	7.52	7.47
Arc sext families	73	73	144	144
β_x^*/β_y^* [mm]	90 / 0.7	220 / 1	240 / 1	900 / 1.4
Transverse tunes Q_x/Q_y	214.168 / 214.200	218.185 / 222.220	398.150 / 394.220	390.148 / 390.218
Chromaticities Q'_x/Q'_y	+5 / +5	0 / +5	0 / 0	0 / 0
Energy spread (SR/BS) σ_δ [%]	0.0395 / 0.1133	0.069 / 0.105	0.102 / 0.176	0.158 / 0.192
Bunch length (SR/BS) σ_z [mm]	5.22 / 15.0	3.46 / 5.28	3.26 / 5.59	1.86 / 2.26
RF voltage 400/800 MHz [GV]	0.0885 / 0	1.00 / 0	2.09 / 0	2.10 / 9.17
Harm. number for 400 MHz		121200		
RF frequency (400 MHz) [MHz]	400.788083	400.788026		400.787964
Synchrotron tune Q_s	0.0354	0.0809	0.0334	0.0873
Long. damping time [turns]	1169	218	65.4	19.2
RF acceptance [%]	1.20	3.32	2.06	2.94
Energy acceptance (DA) [%]	±1.0	±1.0	±1.9	-2.8 / +2.5
Beam crossing angle at IP θ_x [mrad]		±15		
Crab waist ratio [%]	60	55	50	40
Beam-beam ξ_x/ξ_y [a]	0.0018 / 0.0955	0.013 / 0.129	0.0108 / 0.130	0.067 / 0.140
Piwinski angle $\theta_c\sigma_z/\sigma_x^*$	27.6	3.6	6.6	0.87
Lifetime (q + BS + lattice) [s]	5000	4500	6000	940
Lifetime (lum) [b] [s]	1324	960	600	650
Luminosity / IP [10^{34} cm^{-2}s^{-1}]	143	20	7.5	1.41

[a] Including hourglass effect.
[b] Only the energy acceptance is taken into account for the cross-section, no beam size effect.

1.2.1 Collimation for the FCC-ee

The FCC-ee presents unique challenges for beam collimation due to its unprecedented stored beam energy for a lepton collider, as shown in Fig. 1.4.

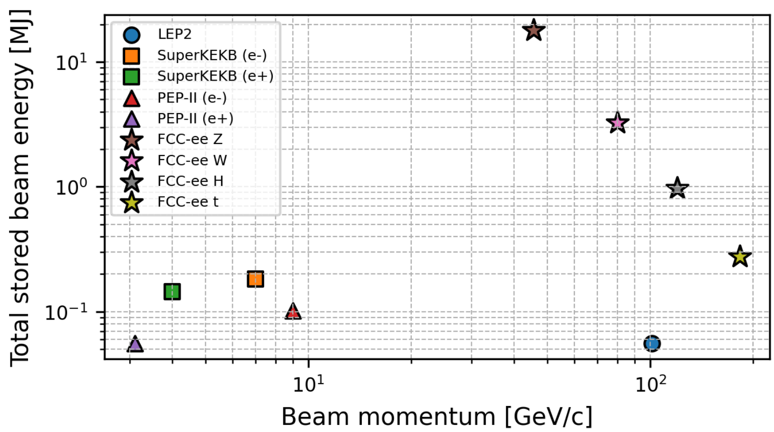

Figure 1.4. Total stored beam energy in various lepton colliders.

In the FCC-ee Z operation mode at 45.6 GeV beam energy, the stored beam energy reaches up to 17.7 MJ, a value two orders of magnitude higher than that of SuperKEKB [18], the current state-of-the-art e^+e^- collider in terms of stored beam energy, and comparable to the stored beam energy during the heavy-ion operation of the LHC [19]. It is worth noting that, at SuperKEKB, collimators were damaged on several occasions due to uncontrolled beam losses [20], as shown in Fig. 1.5.

The high FCC-ee stored beam energy, combined with the extremely small target emittances, makes, therefore, a collimation system indispensable not only to control backgrounds in the experiments, as in any lepton collider to date, but also to protect the machine from unavoidable beam losses and ensure machine availability.

To address these challenges, the FCC-ee collimation strategy foresaw two types of collimation: a *beam halo collimation* (or *global collimation*), to remove stray particles from the beam halo before they can impact sensitive machine components, and a *SR collimation* upstream of each interaction point, to control SR-induced backgrounds and reduce the power loads in the vacuum pipe due to SR photon hits.

A detailed description of the FCC-ee collimation system, including its design choices, implementation, and optimization, will be presented in Chapter 5.

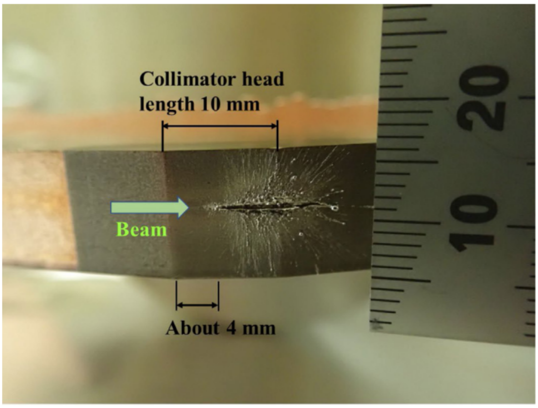

Figure 1.5. Damage to a SuperKEKB collimator jaw caused by accidental beam losses [21].

1.3 The SuperKEKB collider

SuperKEKB [18] is a high-luminosity e^+e^- collider located at KEK (High Energy Accelerator Research Organization) in Tsukuba, Ibaraki, Japan. It is the successor to the KEKB collider [22], and it is designed to achieve unprecedented luminosities to explore rare phenomena in flavor physics. SuperKEKB operates at a center-of-mass energy of 10.58 GeV, corresponding to the mass of the $\Upsilon(4S)$ resonance, enabling the production of B-meson pairs for the Belle II experiment [23]. For this reason, it is also commonly referred to as a B-factory.

SuperKEKB is a double-ring circular collider with a circumference of 3016.315 m. It collides beams with asymmetric energies: 4 GeV for the positron beam and 7 GeV for the electron beam. For this reason, the positron ring is commonly referred to as the Low Energy Ring (LER), while the electron ring is known as the High Energy Ring (HER). The asymmetry in the beam energies helps to boost the center-of-mass system, improving the kinematic reconstruction of B-meson decays. The overall layout of SuperKEKB, including the interaction region, electron and positron rings, and damping rings, is illustrated in Fig. 1.6.

One of the most significant upgrades from KEKB to SuperKEKB is the adoption of the "Nano-Beam" scheme. Inspired by the concept developed for SuperB [25] and originally proposed by P. Raimondi, this technique reduces the beam sizes at the interaction point to the nanoscale level by strongly squeezing the beta functions, leading to a substantial increase in collision rates. A critical element enabling this reduction of the beta functions is the large crossing angle at the interaction point (83 mrad, compared to 22 mrad at KEKB). Specifically, at SuperKEKB, this approach decreases the vertical beta function at the interaction point (β_y^*) to 0.3 mm (compared to 6 mm at KEKB). To further enhance luminosity and mitigate beam-beam instabilities, the crab-waist (CW) collision scheme [26, 27] is implemented. This scheme introduces

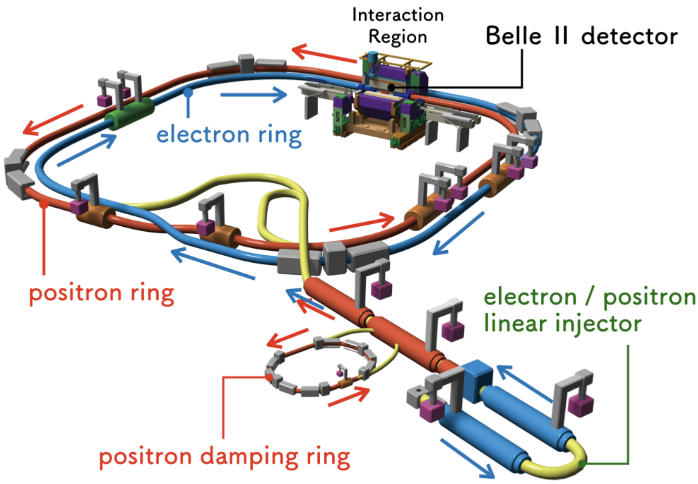

Figure 1.6. Schematic layout of the SuperKEKB collider [24]. The figure illustrates the electron (HER) and positron (LER) rings, the interaction region housing the Belle-II detector, the injector LINAC, and the positron damping ring. Arrows indicate the beam directions in each ring.

a nonlinear focusing transformation using sextupole magnets placed near the interaction point, which rotates the beta function waist of one beam along the trajectory of the other beam. This transformation suppresses synchro-betatron resonances, allowing higher tune shifts and reducing the probability of beam blow-up. As a result, luminosity is increased without necessitating a reduction in bunch length, mitigating problems such as higher-order mode heating and synchrotron radiation.

The design luminosity of SuperKEKB is 8×10^{35} cm^{-2}s^{-1}, 40 times higher than that achieved at KEKB [18]. As of 2024, the collider reached a peak luminosity of 5.1×10^{34} cm^{-2}s^{-1} [28], demonstrating progresses toward its ultimate goal. The SuperKEKB machine parameters as of December 2024 are summarized in Table 1.3.

Achieving and sustaining high luminosity at SuperKEKB poses several challenges, particularly in terms of beam-induced backgrounds and collimation. The machine operates with high-intensity beams, leading to significant beam-beam interactions and Touschek scattering. These effects contribute to beam losses, which, if uncontrolled, can increase background levels in the Belle II detector and cause damage to accelerator components. To mitigate these risks, SuperKEKB is equipped with a distributed collimation system [29] designed to absorb stray particles and reduce beam backgrounds. However, several events leading to collimator damage have been reported due to unexpected beam losses, highlighting the challenges associated with operating such an intense

Table 1.3. SuperKEKB machine parameters as of December 27, 2024 [28].

Parameter	**LER**	**HER**
Beam energy [GeV]	4.0	7.0
Emittance [nm]	4.0	4.6
Beam current [mA]	1632	1259
Number of bunches	2346	
Bunch current [mA]	0.696	0.537
Horizontal beam size at collision point σ_x^* [μm]	15.5	16.6
Vertical beam size at collision point σ_y^* [μm]	0.265	
Betatron tunes ν_x/ν_y	44.525 / 46.589	45.531 / 43.599
β_x^*/β_y^* [mm]	60 / 1.0	60 / 1.0
σ_z [mm]	4.6 (6.0[a])	5.1 (6.1[a])
Piwinski angle	12.3	12.7
Crab waist ratio [%]	80	60
Beam–beam parameter ξ_y	0.036	0.027
Specific luminosity [10^{31} cm^{-2}s^{-1}mA^{-2}]	5.8	
Luminosity [10^{34} cm^{-2}s^{-1}]	**5.1**	

[a] Bunch lengthening is considered by using streak camera measurements.

lepton collider [21].

SuperKEKB provides valuable insights for the FCC-ee design, particularly, but not only, in beam dynamics, collimation, and high-luminosity operation. The experience gained from mitigating beam losses and optimizing collimation at SuperKEKB serves as a benchmark for developing simulation tools and experimental strategies for the FCC-ee collimation system. In this work, measured data from SuperKEKB has been used to validate and improve the simulation models employed in the FCC-ee design studies. Further details on this benchmarking process will be discussed in Chapter 4.

Chapter 2

Theoretical background

This chapter reviews the theoretical background underlying the studies presented in this thesis. It begins with the fundamentals of charged–particle motion and the linear theory of transverse and longitudinal dynamics in Section 2.1, followed by an introduction to synchrotron radiation and its implications for beam dynamics and accelerator design. General aspects of beam losses and collimation are then outlined in Section 2.2, followed by a discussion of the specific beam-loss processes most relevant to this work—generic halo losses in Section 2.2.1, beam losses due to beam–residual gas interactions in Section 2.2.2, Touschek-scattering losses in Section 2.2.3, and losses due to beam–beam interactions in Section 2.2.4. Finally, crystal collimation is introduced, which provides the basis for the FCC-ee studies discussed in Chapter 7.

Because of its direct relevance to this work, the discussion in this chapter focuses primarily on circular accelerators, although most of the concepts presented are general and can also be extended to linear accelerators.

2.1 Accelerator physics

This section provides an overview of key concepts in accelerator physics that are essential for understanding the beam dynamics and beam loss mechanisms discussed throughout this thesis. It begins with the fundamentals of transverse and longitudinal dynamics and concludes with a discussion of synchrotron radiation, which plays a central role in determining the performance limits of circular electron–positron colliders such as the FCC-ee. For a more comprehensive treatment, the reader is referred to standard references such as [30, 31, 32, 33, 34], from which the core results presented in Sections 2.1.1, 2.1.2, and 2.1.3 are derived. Additional details on beam losses and collimation can be found in specialized resources such as [35], which also form the basis for Section 2.2.

Throughout this discussion, the curvilinear coordinate system commonly used in accelerator beam dynamics is adopted, as illustrated in Fig. 2.1. In this moving reference frame, the longitudinal coordinate s denotes the path length along the design trajectory (also referred to as the *reference orbit*), with its unit vector always parallel to the tangent of the reference orbit, while the transverse coordinates x and y represent perpendicular horizontal and vertical displacements from it.

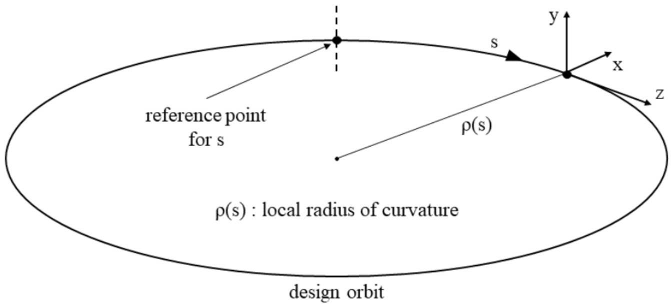

Figure 2.1. Curvilinear reference frame commonly used in accelerator physics. The s-axis follows the design orbit, while x and y denote the horizontal and vertical transverse directions, respectively. Figure adapted from [31].

In circular accelerators, charged particles are guided and confined along the reference orbit by magnetic fields. Dipole magnets provide the bending forces that steer the beam along a closed path, while quadrupole magnets exert linear focusing forces that keep particles near the design trajectory. This configuration, based on the lowest-order multipole fields, forms the foundation of what is known as *linear beam dynamics*. Owing to its analogy with ray optics, the arrangement of magnetic elements in an accelerator is often referred to as the *beam optics*.

In practice, particles within a beam do not exactly follow the reference orbit. Instead, each particle undergoes small oscillations around this ideal path due to variations in initial conditions and collective effects. These oscillations are typically decomposed into two independent components:

- **Transverse motion**, describing oscillations in the x–y plane, is governed by the focusing forces of the lattice and is discussed in Section 2.1.1;

- **Longitudinal motion**, describing oscillations in energy and arrival time along the s-axis, is governed by the RF system and is discussed in Section 2.1.2.

In the simplest case, an ideal charged particle with elementary charge e moving in a perfectly uniform dipole magnetic field follows a circular orbit whose curvature is determined by the balance between the Lorentz and centrifugal forces,

$$F_{\text{Lorentz}} = evB = F_{\text{centrifugal}} = \frac{\gamma m_0 v^2}{\rho},$$

where v is the particle velocity, γ the Lorentz factor, m_0 the particle rest mass, and ρ the bending radius. This relation leads to the well-known beam rigidity condition,

$$p_0 = \gamma m_0 v = B\rho,$$

which links the nominal particle momentum p_0 to the magnetic field strength and the bending radius. The beam rigidity determines the maximum momentum that can be maintained in a ring for a given magnetic field and thus sets the overall scale of the machine. For ions with charge q, the expression generalizes naturally by replacing e with q.

2.1.1 Linear theory of transverse beam dynamics

The transverse beam dynamics of charged particles in a circular accelerator describes the motion of individual particles under the influence of external bending and focusing fields. These forces arise from the arrangement of magnets along the accelerator, whose positions and strengths determine both the trajectories of individual particles and the collective behavior of the beam as an ensemble.

The treatment presented in this section is restricted to the *linear approximation*. In this regime, particles are assumed to undergo small oscillations around the reference trajectory, and the transverse components of the external magnetic fields are assumed to depend at most linearly on the transverse displacement from it. This implies that only dipole magnets (for bending) and quadrupole magnets (for focusing) are considered. Under these assumptions, the equations of motion can be solved analytically, providing valuable insight into the fundamental properties of transverse motion. Nonlinear effects—such as higher-order multipole fields or large-amplitude oscillations—are typically treated as perturbations to the linear motion.

Within this framework, the equation of motion for a charged particle in a magnetic field can be expressed in the curvilinear reference frame of the accelerator, using the longitudinal coordinate s as the independent variable instead of time t. Under these conditions, the linear, uncoupled equations of motion for an on-momentum particle in the horizontal and vertical planes take the form [32]

$$x''(s) + \left(\frac{1}{\rho(s)^2} - k(s)\right) x(s) = 0, \tag{2.1a}$$

$$y''(s) + k(s)\, y(s) = 0, \tag{2.1b}$$

where x and y are the transverse displacements from the design orbit, s is the longitudinal coordinate along the reference trajectory, $\rho(s)$ the local bending radius, and

$$k(s) = \frac{e\, g(s)}{p_0}$$

is the normalized gradient of the quadrupole field, with e the elementary charge, $g(s)$ the local magnetic field gradient, and p_0 the nominal particle momentum.

It is worth noting that in Eq. (2.1), there is an additional focusing term $1/\rho^2$ in the horizontal plane even in the absence of quadrupole fields. This so-called *weak focusing* arises from the bending strength of the dipole magnets and contributes only in the plane of bending.

General solution. The general solution to Eq. (2.1) can be written as [32]

$$u(s) = \sqrt{\epsilon_u \, \beta_u(s)} \cos[\phi_u(s) + \phi_{u,0}], \quad u \in \{x, y\}, \tag{2.2}$$

where ϵ_u is a constant related to the oscillation amplitude, called the single-particle emittance; $\beta_u(s)$ is the betatron function; and $\phi_{u,0}$ is an integration constant representing the initial phase. The phase advance is defined as

$$\phi_u(s) = \int_0^s \frac{ds'}{\beta_u(s')}. \tag{2.3}$$

Equation (2.1) therefore describes the *betatron oscillations*, which are the natural transverse oscillations of particles about the design orbit. The betatron function $\beta_u(s)$ reflects the focusing properties of the lattice and governs the evolution of the beam envelope. The *betatron tune*, defined as the number of betatron oscillations per revolution,

$$Q_u = \frac{1}{2\pi} \int_0^C \frac{ds}{\beta_u(s)},$$

must be chosen carefully during machine design to avoid resonances that could lead to large, unstable oscillations [30].

The amplitude of motion is related to the single-particle emittance ϵ_u. Introducing the *Twiss parameters* (or *Courant-Snyder parameters*),

$$\alpha_u(s) = -\frac{1}{2}\beta_u'(s), \quad \gamma_u(s) = \frac{1 + \alpha_u^2(s)}{\beta_u(s)},$$

and using Eq. (2.2) and its derivative, it can be shown that ϵ_u is a constant of motion, as it satisfies the ellipse equation

$$\gamma_u u^2 + 2\alpha_u u u' + \beta_u u'^2 = \epsilon_u.$$

The area enclosed by this ellipse in the transverse phase space (u, u'), illustrated in Fig. 2.2, is proportional to the emittance:

$$\int du \, du' = \pi \epsilon_u.$$

According to Liouville's theorem, ϵ_u remains constant as long as only conservative forces are considered. The quantity $A_u = \pi\epsilon_u$ thus represents the area occupied by the particle in the transverse phase space.

For an ensemble of particles, the beam emittance is defined statistically as

$$\epsilon_{\mathrm{rms},u} = \sqrt{\langle u^2 \rangle \langle u'^2 \rangle - \langle u u' \rangle^2}.$$

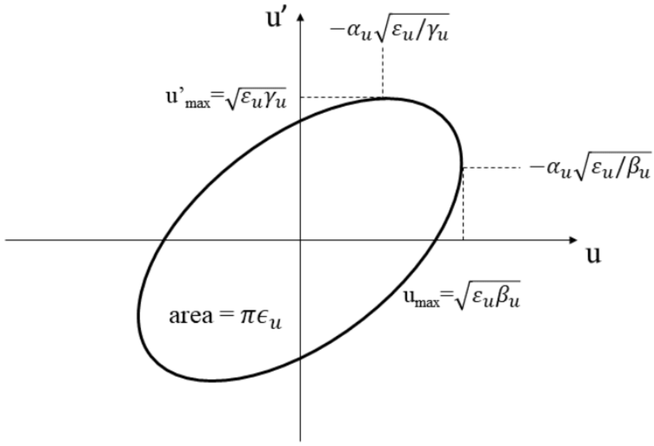

Figure 2.2. Phase-space ellipse describing the transverse motion of a particle in the u–u' plane.

Assuming a Gaussian beam, the transverse beam size for on-energy beam is given by

$$\sigma_u(s) = \sqrt{\epsilon_{\mathrm{rms},u}\,\beta_u(s)}, \quad \sigma'_u = \sqrt{\gamma_u\,\epsilon_{\mathrm{rms},u}}.$$

It is this dependence of the transverse beam size σ_u on the focusing properties of the lattice through the betatron function $\beta_u(s)$ that enables the design of beam transport systems with tailored characteristics such as small or large beam sizes at specific locations.

Normalized coordinates. The differential equations (2.1) have the same mathematical form as that of a harmonic oscillator, which is expected since in both planes the restoring force increases linearly with the displacement from equilibrium. In beam dynamics, however, the oscillatory solution (Eq. (2.2)) exhibits an amplitude and phase that vary along the lattice. By introducing a suitable transformation of coordinates, the particle motion can be expressed in a form that is mathematically equivalent to that of a simple harmonic oscillator. This formulation is particularly convenient for analyzing perturbations to particle trajectories, as it allows the direct application of analytical tools developed for harmonic oscillators to particle beam dynamics.

The transformation that achieves this correspondence converts the real-space coordinates (u, u') into the *normalized coordinates* (U, U'), defined by

$$\begin{pmatrix} U \\ U' \end{pmatrix} = \frac{1}{\sqrt{\beta_u(s)}} \begin{pmatrix} 1 & 0 \\ \alpha_u(s) & \beta_u(s) \end{pmatrix} \begin{pmatrix} u \\ u' \end{pmatrix}. \tag{2.4}$$

Equivalently,

$$\begin{aligned} U(s) &= \frac{u(s)}{\sqrt{\beta_u(s)}}, \\ U'(s) &= \frac{\alpha_u(s)}{\sqrt{\beta_u(s)}}\, u(s) \;+\; \sqrt{\beta_u(s)}\, u'(s). \end{aligned} \tag{2.5}$$

In these normalized coordinates, the dependence on the optical functions $\alpha_u(s)$ and $\beta_u(s)$ is absorbed into the transformation, and the equations of motion reduce to

$$\frac{d^2U}{d\phi_u^2} + U = 0, \tag{2.6}$$

where ϕ_u is the phase advance. Thus, the motion in normalized phase space corresponds to a uniform circular trajectory of radius $\sqrt{\epsilon_u}$, where ϵ_u is the Courant–Snyder invariant (i.e., the single-particle emittance introduced above).

This representation is particularly advantageous because it maps the position-dependent motion in real space into a simple rotation in normalized phase space, providing an intuitive visualization of transverse dynamics and a convenient framework for studying trajectory perturbations.

Dispersion and momentum spread. In realistic particle beams, a finite momentum spread is always present. It originates from the acceleration process itself, since cyclic (i.e., non-electrostatic) accelerators rely on the time-varying longitudinal electric field component of electromagnetic waves in devices such as RF cavities to accelerate particles. The relative momentum deviation of an individual particle with respect to the reference momentum p_0 is defined as

$$\delta = \frac{\Delta p}{p_0} = \frac{p - p_0}{p_0}. \tag{2.7}$$

The ensemble of particles in a beam exhibits a distribution of such momentum deviations, whose r.m.s. value typically lies in the range

$$\sigma_\delta \sim 10^{-4}\text{–}10^{-3}. \tag{2.8}$$

This intrinsic spread affects the transverse motion, as the bending of dipoles depend on the particle momentum.

In addition to this intrinsic contribution from the acceleration process, other mechanisms in a real machine—such as beam–residual gas interactions, collective effects such as Touschek scattering, and beam–beam interactions—further contribute to a nonzero momentum spread within the beam.

As a consequence, the transverse equation of motion in the bending (horizontal) plane, which for the on-momentum case is homogeneous, acquires an additional term on its right-hand side. It then takes the form [32]

$$x''(s) + \left(\frac{1}{\rho^2(s)} - k(s)\right) x(s) = \frac{1}{\rho(s)}\,\delta. \tag{2.9}$$

The term on the right-hand side represents the horizontal displacement of off-momentum particles due to their different magnetic rigidity. The general solution of this inhomogeneous differential equation can be written as

$$x(s) = x_\beta(s) + x_\delta(s), \tag{2.10}$$

where $x_\beta(s)$ is the solution of the homogeneous equation, corresponding to the betatron oscillations derived earlier (Eq. (2.2) with $u = x$), and $x_\delta(s)$ is a particular solution that accounts for the momentum deviation.

In the linear approximation, the effect scales linearly with the relative momentum deviation. It is therefore convenient to define the *dispersion function* $D_x(s)$ as

$$D_x(s) = \frac{x_\delta(s)}{\delta}. \tag{2.11}$$

Substituting Eq. (2.10) into Eq. (2.9) gives the corresponding inhomogeneous differential equation for x_δ:

$$x_\delta''(s) + \left(\frac{1}{\rho^2(s)} - k(s)\right) x_\delta(s) = \frac{1}{\rho(s)}\,\delta. \tag{2.12}$$

This equation shows that x_δ is subject to the same focusing that governs the betatron motion, but with a driving term on the right-hand side. The dispersion function $D_x(s)$ therefore represents the trajectory of a particle with a unit momentum offset ($\delta = \Delta p/p_0 = 1$) in the absence of betatron oscillations ($x_\beta = x_\beta' = 0$).

Physically, dispersion describes how particles with different momenta follow different closed orbits in the bending plane. An off-momentum particle with $\delta > 0$ (higher rigidity) will follow a trajectory with a larger bending radius, while a particle with $\delta < 0$ (lower rigidity) will follow one with a smaller radius. The betatron oscillations of each particle then take place around its individual off-momentum closed orbit, defined by the local value of $D_x(s)$. In this sense, dispersion and momentum spread together define a new reference trajectory about which the betatron oscillations occur.

The underlying physical effect is analogous to the spectrometer (or prism) effect, in which particles (or rays) of different momenta (or wavelengths) are deflected by different amounts—by magnetic fields in the former case and by refraction in the latter. The dispersion function thus provides a quantitative description of this phenomenon within the framework of accelerator beam dynamics.

Dispersion and beam size. It should be noted that, although Eq. (2.10) expresses the single-particle motion as a simple sum of the betatron and dispersive components, in a Gaussian-distributed particle beam (i.e., an ensemble of many particles), the betatron and off-momentum contributions to the beam size must be added in quadrature rather than linearly. The r.m.s. horizontal beam size therefore reads

$$\sigma_x(s) = \sqrt{\epsilon_{\mathrm{rms},x}\,\beta_x(s) + D_x^2(s)\,\sigma_\delta^2}, \tag{2.13}$$

where $\epsilon_{\text{rms},x}$ is the r.m.s. emittance, $\beta_x(s)$ the betatron function, and σ_δ the r.m.s. momentum spread within the beam.

Momentum spread and chromaticity While dispersion describes how off-momentum particles experience different bending in dipole magnets, a similar effect occurs in the focusing strength of quadrupoles. This phenomenon is known as *chromaticity.* It arises because, for a given magnetic field gradient g, the focusing strength $k = eg/p$ depends inversely on the particle momentum p. Particles with lower momentum experience stronger focusing, while higher-momentum particles experience weaker focusing. As a result, the betatron tune of each particle shifts with its momentum deviation.

In the linear approximation, this dependence is expressed as

$$\Delta Q = Q'\,\delta, \tag{2.14}$$

where ΔQ is the tune shift, Q' the *chromaticity*, and $\delta = \Delta p/p_0$ the relative momentum deviation.

A first-order expansion of the focusing strength gives

$$k(p) \approx k_0\,(1-\delta)\,, \tag{2.15}$$

leading to a focusing error

$$\Delta k = -k_0\,\delta. \tag{2.16}$$

The negative sign indicates that a positive momentum deviation (i.e., higher rigidity) reduces the focusing strength and therefore decreases the tune.

The so-called *natural chromaticity* of a lattice, which represents the uncorrected chromatic behavior, is obtained by integrating the focusing strength weighted by the betatron function [32]:

$$Q'_{\text{nat}} = -\frac{1}{4\pi}\int k(s)\,\beta(s)\,ds. \tag{2.17}$$

A negative natural chromaticity implies that particles with higher momentum have smaller betatron tunes. Although this effect is inherent to any focusing lattice, it can have severe consequences: the tune spread within the beam may drive particles with certain momentum deviations into resonance conditions, leading to beam degradation or losses.

To mitigate this, sextupole magnets are used to introduce a position-dependent correction to the focusing strength. When placed in regions of nonzero dispersion, where particles are spatially separated according to their momentum, sextupoles provide an additional gradient proportional to the horizontal displacement, effectively restoring the focusing balance for off-momentum particles. By properly adjusting the strengths of dedicated sextupole families, the chromaticity can be compensated in both transverse planes, yielding an overall chromaticity close to zero and thereby preserving beam stability.

Dynamic aperture. The introduction of sextupole magnets, necessary to compensate for the chromaticity of the lattice, inevitably introduces nonlinear components into the transverse magnetic fields. In an ideal linear lattice composed of dipoles and quadrupoles, the transverse motion of a particle follows a quasi-harmonic oscillation that can be described analytically, and all particles remain confined to invariant ellipses in phase space. The situation changes once sextupole fields are included: the magnetic field now depends quadratically on the transverse displacement, and particles with large oscillation amplitudes experience stronger nonlinear effects.

As a result, the motion of particles with small amplitudes—near the beam core—remains approximately linear and stable, while particles at larger amplitudes are gradually driven away from their ideal trajectories. Beyond a certain threshold amplitude, the nonlinear perturbations lead to unstable motion and eventual particle loss. The boundary between stable and unstable trajectories defines the so-called *dynamic aperture*.

The dynamic aperture thus represents the maximum transverse amplitude for which particle motion remains stable over many revolutions. It is determined by the nonlinearities in the magnetic lattice, primarily those introduced by sextupoles used for chromaticity correction, but also by higher-order multipole errors, field imperfections, and intentionally introduced higher-order fields such as octupole and decapole correctors. Because the dynamic aperture sets the effective acceptance of the storage ring, it constitutes a fundamental performance limit of circular accelerators, particularly for high-intensity colliders, where maintaining large transverse stability regions is essential for achieving long beam lifetimes and high luminosity.

The evaluation of the dynamic aperture is typically carried out through particle tracking simulations, in which a grid of test particles is generated in normalized transverse phase space over a range of initial amplitudes. Different betatron phases can also be explored. The particle grid is then tracked for a large number of turns through the nonlinear magnetic lattice. By recording which particles remain stable (survive) or are lost during tracking, the region of long-term stability can be mapped, and the dynamic aperture determined as the boundary between stable and unstable motion. When multiple betatron phases are scanned, the dynamic aperture contour can be obtained by averaging the results over the different phases. An example of a dynamic aperture contour obtained with this method is shown in Fig. 6.38.

2.1.2 Longitudinal beam dynamics

Longitudinal beam dynamics in particle accelerators concerns the acceleration and longitudinal focusing (or bunching) of charged particles along the reference trajectory of the machine. It describes how the energy and phase of individual particles evolve with respect to an ideal reference particle—called the *synchronous particle*—which defines the nominal energy and timing of the beam.

In a circular accelerator, charged particles are accelerated by exploiting the time-varying longitudinal electric field component of electromagnetic fields produced by radiofrequency (RF) cavities. The use of an electric field aligned with the particle trajectory is essential, as only the longitudinal component of the Lorentz force $\mathbf{F} = q(\mathbf{E} + \mathbf{v} \times \mathbf{B})$ can change the particle's energy. Magnetic fields, being always orthogonal to the velocity, can only deflect the trajectory without performing work on the particles. For this reason, the acceleration process relies exclusively on electric fields oriented along the beam path.

RF cavities generate oscillating longitudinal electric fields that not only provide the energy required to accelerate particles to their target momenta but also confine them into discrete bunches. Within each bunch, individual particles perform small oscillations in energy and longitudinal position relative to the synchronous particle. These oscillations, known as *synchrotron oscillations*, constitute the essence of longitudinal beam dynamics.

The longitudinal motion arises from two coupled effects: differences in particle velocity and variations in the effective path length per revolution. A particle arriving early or late in the RF phase experiences a different accelerating field and therefore a different energy gain, which in turn modifies its revolution time and path length. This feedback mechanism produces stable oscillatory motion in the longitudinal phase space (z, δ), where z represents the longitudinal displacement with respect to the synchronous particle and $\delta = \Delta E / E_0$[1] is the relative energy deviation, where E_0 is the nominal energy of the reference particle.

In electron and positron storage rings, where synchrotron radiation losses are significant, RF cavities also serve to continuously replenish the energy lost to radiation. This compensation is essential for maintaining a stable beam energy and thus stable operation.

The accelerating field generated by an RF cavity can be described as a sinusoidally varying voltage V_{RF} oscillating at an angular frequency ω_{RF}. The energy gain of a particle traversing the cavity depends on its arrival time relative to the oscillation phase and is given by

$$\Delta E = eV_{\mathrm{RF}}(t) = eV_{\mathrm{RF}} \sin(\omega_{\mathrm{RF}} t + \phi),$$

where e is the elementary charge. For particles to remain properly phased with the accelerating field, the RF frequency must be synchronized with the beam's revolution frequency ω_{rev} through the condition [33]

$$\omega_{\mathrm{RF}} = h\,\omega_{\mathrm{rev}},$$

where h is an integer called the *harmonic number* [33].

An important concept arising from this synchronous motion is the *RF bucket*, which represents the region in longitudinal phase space within which

[1] In the relativistic regime—typical of high-energy particle accelerators—energy and momentum are effectively interchangeable. Throughout this thesis, the symbol δ is therefore used to denote either the relative energy deviation $\Delta E/E_0$ or, equivalently, the relative momentum deviation $\Delta p/p_0$, depending on context.

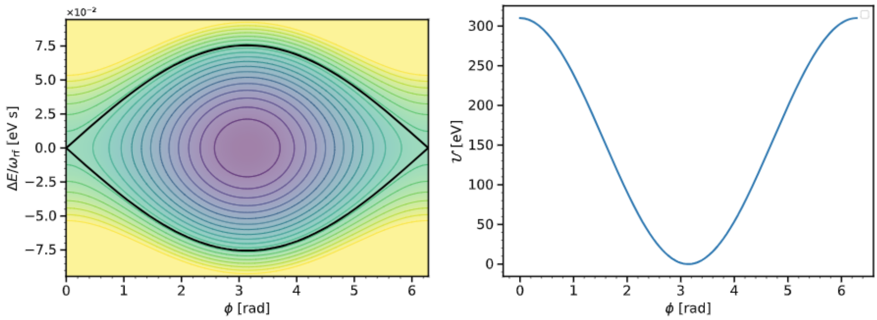

Figure 2.3. Trajectories in the longitudinal phase space (left), together with the corresponding RF potential well (right). The black line represents the *separatrix*, which delimits the boundary of the RF bucket. Particles inside the separatrix perform stable synchrotron oscillations around the synchronous particle, whereas those outside do not execute closed trajectories and eventually become debunched or lost. The separatrix corresponds to the limit defined by the maxima of the RF potential well. Figure from Ref. [33].

particles undergo stable synchrotron oscillations. Particles with energy and phase deviations that place them inside this bucket remain captured and synchronized, while those outside become unstable and are eventually lost or debunched.

The RF bucket can be understood as the closed region in the longitudinal phase space (z, δ) bounded by the *separatrix* of the longitudinal equations of motion. Inside this region, particles execute bounded synchrotron oscillations, i.e., oscillations in energy and time, around the position of the reference synchronous particle (typically taken as zero); outside it, the motion becomes unstable and particles slip in phase until they are debunched or lost. The bucket thus acts as a potential well that confines the beam longitudinally. An illustration of the separatrix and the corresponding RF potential well is shown in Fig. 2.3. The synchrotron oscillations are described by equations of motion in the longitudinal plane, which can be solved to obtain the dynamic behaviour of individual particles. As this is not a central concept in this thesis, we refer the interested reader to standard textbooks for more details—see, for example, Refs. [30, 33].

The size of the RF bucket is characterized by two important quantities: the *bucket height*, corresponding to the maximum energy deviation $(\Delta E)_{\text{max}}$ for which particles remain captured, and the *bucket area*, which represents the total phase-space area enclosed by the separatrix. The latter provides a measure of the longitudinal acceptance of the RF system and determines the maximum longitudinal emittance that can be stably confined.

The maximum relative energy deviation

$$\delta_{\text{max}} = \frac{(\Delta E)_{\text{max}}}{E_0} \tag{2.18}$$

for which a particle remains confined in the RF bucket defines the so-called *RF acceptance*, or *RF energy acceptance*. This parameter is critical for determining the longitudinal beam stability and for setting thresholds for beam losses caused by large energy deviations.

When an ensemble of particles is confined within an RF bucket, forming a particle bunch, one can characterize its longitudinal properties statistically. The *rms relative energy spread*, denoted by σ_δ, and the *rms bunch length*, σ_z, are defined as the root-mean-square values of the particle distribution in the (z, δ) longitudinal phase space. The *longitudinal rms emittance* of the bunch can then be approximated as

$$\varepsilon_z = \sigma_z \, \sigma_\delta .$$

Momentum acceptance. A concept similar to the transverse dynamic aperture discussed in the previous section is the *momentum acceptance*, which represents a longitudinal analogue of it.

The momentum acceptance defines the maximum relative momentum deviation δ for which particles remain long-term stable, taking into account the coupling of δ into the transverse plane. As discussed in Section 2.1.1, this coupling arises from the lattice dispersion, which links momentum deviations to transverse displacements and is therefore most significant in the horizontal (bending) plane. As such, the momentum acceptance lies at the interface between longitudinal and transverse beam dynamics: while it quantifies stability against momentum deviations (a longitudinal property), these deviations can lead to transverse instability due to the momentum dependence of the closed orbit and optical functions. It is important to note that the momentum acceptance is distinct from the RF acceptance, as it includes nonlinear transverse effects in addition to the RF bucket constraints—effectively making it a *longitudinal dynamic aperture*. It also differs from the so-called *linear momentum acceptance*, defined as $\delta_a = A_x / D_x$, where A_x is the physical aperture limit and D_x the linear dispersion function in the horizontal plane. Unlike this simplified linear estimate, the momentum acceptance includes nonlinear effects that cannot be captured through linear optics alone.

In practice, the momentum acceptance is evaluated through particle tracking, using a method analogous to that employed for evaluating the transverse dynamic aperture described in Section 2.1.1. The difference is that the particle grid that is tracked is prepared in the (X, δ) plane instead of the (X, Y) plane, where X and Y represent the normalized amplitudes in the horizontal and vertical planes, respectively. An example of momentum acceptances obtained with this method is shown in Fig. 5.3.

The *momentum acceptance* discussed here is a different concept from the *local momentum acceptance* (LMA) introduced later in Sections 6.4 and 3.5.2 in the context of Touschek scattering. Unlike the LMA, which characterizes the effect of sudden momentum deviations, the momentum acceptance described in this section assumes particles to be matched to their corresponding off-momentum closed orbits for a given value of δ. This condition is satisfied when a particle slowly reaches a given δ starting from $\delta \approx 0$, rather than undergoing an instantaneous δ-jump as considered in the LMA evaluation. In particle-tracking simulations of the momentum acceptance, this condition can be most easily fulfilled by generating and tracking the (X, δ) particle grid starting from a dispersion-free region, where the off-momentum closed orbit coincides with the on-momentum one. Notably, as also pointed out in Section 6.4, in dispersion-free regions the LMA coincides with the (non-local) momentum acceptance defined here.

2.1.3 Synchrotron radiation

The emission of synchrotron radiation originates from a well-known physical mechanism: any charged particle subjected to acceleration emits electromagnetic radiation. In circular accelerators, a transverse acceleration is always present due to the guiding magnetic field of the dipole magnets, which continuously bend the particle trajectory and therefore cause the emission of synchrotron radiation.

The power radiated by a single particle undergoing transverse acceleration can be expressed as [34]:

$$P_\gamma = \frac{q^2}{6\pi\epsilon_0}\frac{\beta^4 c}{\rho^2}\left(\frac{E}{E_0}\right)^4 = \frac{q^2}{6\pi\epsilon_0}\frac{\beta^4 c}{\rho^2}\gamma^4, \tag{2.19}$$

where q is the electric charge, ϵ_0 the vacuum permittivity, $\beta = v/c$ the ratio between the particle velocity v and the speed of light c, ρ the bending radius, E the total energy, E_0 the rest energy, and $\gamma = E/E_0$ the Lorentz factor.

From Eq. (2.19), the contrast between light and heavy charged particles becomes evident. The large difference in rest energy—approximately a factor of 2000 between electrons and protons—implies that synchrotron radiation constitutes a dominant energy-loss mechanism for electrons (and positrons), whereas it remains comparatively negligible for protons and heavier ions.

This phenomenon has several important implications for the design and operation of circular accelerators. The energy lost by charged particles through synchrotron radiation must be continuously replenished by the accelerating system to maintain a constant beam energy. Additionally, the emitted radiation may interact with accelerator components, resulting in heating, vacuum degradation, and possible material deterioration. Finally, the substantial energy losses associated with synchrotron radiation impose a practical lower limit on the bending radius of electron and positron storage rings, thereby constraining the achievable beam energy in circular machines.

In addition to the energy loss, synchrotron radiation also affects the beam dynamics. As synchrotron radiation emission reduces the particle energy, the transverse and longitudinal oscillation amplitudes decrease—a process known as *radiation damping*, which over many revolutions tends to shrink the beam's phase-space volume. The characteristic time over which this damping occurs is known as the *damping time*.

However, because the radiation is emitted in discrete photons with random energies and emission angles, a competing *quantum excitation* effect arises. These stochastic fluctuations continuously perturb the particle trajectories, preventing complete damping. The balance between radiation damping and quantum excitation establishes an equilibrium state characterized by finite values of the energy spread and the transverse beam emittances—referred to as the *equilibrium emittances* of the storage ring.

These equilibrium emittances depend strongly on the lattice design and define the practically achievable beam sizes and, in a collider, the luminosity.

In the context of the FCC-ee, synchrotron radiation plays a central role in determining the overall design and performance of the machine. The 90 km circumference of the FCC-ee is primarily dictated by the need to minimize synchrotron radiation losses, since a larger bending radius reduces the emitted power according to Eq. (2.19). The corresponding energy loss per turn for a particle in an arbitrary accelerator lattice can be calculated by the following ring integral [34]:

$$U_0 = \frac{C_\gamma}{2\pi} E^4 \oint_C \frac{1}{\rho^2}\, ds, \tag{2.20}$$

where E is the beam energy and

$$C_\gamma = \frac{e^2}{3\epsilon_0 (mc^2)^4}. \tag{2.21}$$

At the FCC-ee, this energy loss per turn is far from negligible, as summarized in Table 1.2. In particular, during the $t\bar{t}$ operation mode at a beam energy of 182.5 GeV, the synchrotron radiation losses amount to approximately 5% of the total beam energy per revolution. To compensate for this effect, a *tapering* scheme is implemented [11], in which the strength of all magnets—except for the solenoids—is scaled according to the local beam energy.

Moreover, the total synchrotron radiation power per beam is limited to 50 MW in all operational modes, imposing a fundamental constraint on the maximum achievable beam current as the beam energy increases.

2.2 Beam losses and collimation

This section first discusses beam losses and collimation at a general level. Additional collimation concepts not covered here—such as single- and multi-stage collimation, the positioning of secondary collimators, and the required settings in a multi-stage system—are introduced and developed in Chapter 5 in the context of the FCC-ee collimation system design. The focus then shifts to two mechanisms central to this thesis: beam–residual gas interactions and Touschek scattering, for which dedicated simulation routines were developed (see Chapter 3). For completeness, beam–beam losses are also briefly discussed.

Regular and abnormal beam loss mechanisms

In an ideal accelerator, beam particles would circulate indefinitely in the vacuum chamber without losses, and no collimation system would be required. In reality, however, a wide range of mechanisms can lead to particle losses, making collimation systems essential. These mechanisms include, for example, space-charge effects, interactions with residual gas in the vacuum chamber, intra-beam and Touschek scattering, beam–beam interactions in colliders, feedback noise, and the crossing of transverse or longitudinal resonances. In addition, magnet misalignments and field errors can populate the beam tails and eventually cause losses.

Beam loss mechanisms can be grouped into two categories: *regular loss mechanisms*, which are unavoidable during nominal operation, and *abnormal loss mechanisms*, which are caused by component failures or incorrect beam manipulations.

This thesis primarily focuses on regular beam loss mechanisms. The FCC-ee collimation system design developed in this work mainly targets these losses, but also incorporates safety margins to ensure robustness against abnormal loss scenarios. A quantitative assessment of its effectiveness in such cases requires dedicated studies. Work in this direction has already begun in parallel to this thesis, as reported for example in Ref. [36], and will continue as the FCC-ee design evolves.

In general, regular beam loss mechanisms lead to the gradual population of the beam halo, with characteristic timescales that depend on the specific process and the machine under consideration.

Betatron and off-momentum collimation

The beam halo is typically composed of two types of particles: *betatron halo particles* and *off-momentum halo particles*. Betatron halo particles reach large transverse amplitudes due to larger-than-nominal single-particle transverse emittance, while off-momentum halo particles acquire large transverse amplitudes as a result of a momentum offset δ with respect to the reference beam momentum p_0.

Beam halo collimation can be defined as the controlled and safe disposal of halo particles to minimize beam losses in sensitive regions of the machine. This is achieved by reducing the effective transverse aperture at dedicated devices called collimators, which act as the limiting aperture bottleneck of the ring and hence intercept losses before they reach other locations.

As will be discussed in detail for the FCC-ee in Chapter 5, the strategic placement of collimators at locations with suitable linear optics functions enables selective cleaning of the different halo components. Collimators placed in regions with large beta functions and small dispersion provide efficient removal of betatron halo particles (*betatron collimation*), whereas those located in regions with large dispersion and relatively small beta functions are effective against off-momentum halo particles (*off-momentum collimation*). This can be understood by considering the transverse amplitude u of a particle in terms of the local optics functions:

$$u(s) \;=\; u_\beta(s) + u_\delta(s) \;=\; \sqrt{\epsilon_u\,\beta_u(s)}\,\cos\!\big[\phi_u(s) + \phi_{u,0}\big] \;+\; D_u(s)\,\delta, \quad (2.22)$$

where $u \in \{x, y\}$, u_β is the betatron contribution, u_δ the dispersive contribution, ϵ_u the single-particle emittance in plane u, $\beta_u(s)$ the betatron function, $\phi_u(s)$ the betatron phase, $\phi_{u,0}$ an initial phase, $D_u(s)$ the dispersion function, and $\delta = \Delta p/p_0$ the relative momentum deviation.

Equation 2.22 shows that a transverse displacement can originate either from betatron oscillations or from momentum deviations, which couple into the transverse plane through dispersion.

2.2.1 Generic beam halo losses

As introduced above, several regular beam loss mechanisms can populate the beam halo and ultimately cause particle losses. These processes are diverse in nature, but in first approximation, for collimation purposes it is often not necessary to model each mechanism in detail. A common approach is instead to condense their overall effect into a finite beam lifetime, since their ultimate consequence is the progressive population of the beam halo. The finite beam lifetime thus provides a measure of the overall losses that a machine—and in particular its collimation system—must cope with during regular operation.

In first approximation, the beam intensity, or equivalently the beam current, can be described as an exponentially decaying function of time, with the characteristic time constant defining the beam lifetime:

$$I(t) = I_0 \exp\left(-\frac{t}{\tau}\right),$$

where $I(t)$ is the beam intensity at time t, I_0 the initial intensity, and τ the beam lifetime.

Figure 2.4 illustrates the relative beam intensity as a function of time for three example lifetimes.

An adequate collimation system must be capable of handling the maximum expected loss rate, corresponding to the minimum beam lifetime during the operational cycle, particularly when the stored beam energy is highest.

It is worth noting that when the underlying processes populate the halo slowly—meaning the increase in transverse amplitude per turn is small—these *generic beam halo losses* are also the easiest to simulate. In this regime, the details of the initial halo formation mechanism can be neglected, and it can be assumed that halo particles are always intercepted by the smallest aperture in the machine, known as the *aperture bottleneck*. In the design of a collimation system, collimators are deliberately positioned to act as such bottlenecks, ensuring that halo particles are removed before reaching sensitive components.

Consequently, the collimation performance can be evaluated by assuming that halo particles directly impact the collimator imposing the smallest trans-

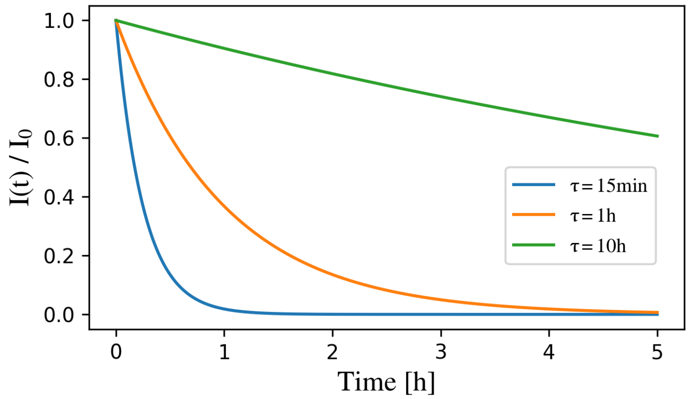

Figure 2.4. Relative reduction of beam intensity versus time, $I(t)/I_0$, for beam lifetime values of 15 min, 1 h and 10 h.

verse cut[2]. The corresponding impact rate is linked to the beam lifetime: in practice, the beam losses associated with a given lifetime are assumed to occur at the impacted collimator. Since the beam lifetime varies over the operational cycle, appropriate safety margins must be included to ensure that the system remains effective even during temporary lifetime drops.

This simplified, yet robust, approach has been successfully applied in the design and operation of the LHC collimation system [37] and remains a standard methodology for collimation performance studies. As presented in Chapter 6, it has also been adopted to study the performance of the FCC-ee collimation system designed in this thesis.

2.2.2 Beam–gas losses

Beam–gas losses occur when beam particles interact with residual gas molecules in the vacuum chamber. Since no accelerator vacuum is perfectly empty, these interactions are unavoidable. They must therefore be carefully quantified and, where necessary, mitigated or intercepted by dedicated devices such as collimators.

These interactions can reduce the beam lifetime and contribute to emittance growth, thereby degrading the beam quality and ultimately the collider luminosity. They also generate secondary particle showers that can produce experimental backgrounds or lead to localized beam losses, particularly in the event of pressure bursts. As a result, beam–gas interactions can give rise to distinct and sometimes localized loss patterns around the machine.

In the FCC-ee, the overall beam lifetime will be dominated by radiative Bhabha scattering at the interaction points. Nevertheless, a good understanding

[2]These collimators are typically referred to as *primary collimators*.

of beam–gas interactions, and of their contribution to the total beam lifetime, remains essential. They provide key input for evaluating local loss distributions, estimating background levels, and guiding the design of both the vacuum system and the collimation system.

Beam–gas effects are particularly relevant in circular machines, where the beam executes many revolutions through the vacuum chamber and the cumulative probability of interaction increases accordingly. To ensure reliable operation, the vacuum system must therefore maintain sufficiently low pressures so that these interactions remain within tolerable limits.

In electron and positron machines, beam–gas interactions are primarily electromagnetic in nature. The dominant processes are elastic Coulomb scattering and inelastic bremsstrahlung of beam particles on residual gas nuclei. These two mechanisms determine the beam–gas losses in the machines considered in this thesis—SuperKEKB and the FCC-ee—and are discussed in the following subsections.

Bremsstrahlung

Bremsstrahlung refers to the electromagnetic radiation emitted when a charged particle, such as an electron or positron, is accelerated in the Coulomb field of another particle. In the context of particle–matter interactions, bremsstrahlung most commonly arises from the deflection of energetic electrons or positrons by the Coulomb field of atomic nuclei. Because the nucleus is much heavier than the incident lepton, it absorbs negligible recoil energy, and nearly all of the lepton's lost kinetic energy is carried away by the emitted photon. The bremsstrahlung spectrum is continuous, extending from zero up to the full kinetic energy of the incoming particle, with the emission probability increasing strongly at low photon energies and small emission angles relative to the particle's trajectory. The process is particularly important for high-energy electrons and positrons, where it dominates over collisional energy loss, and it forms the basis of electromagnetic shower development in matter.

For ultra-relativistic electrons and positrons ($E \gtrsim 1$ GeV), the differential cross-section (DCS) for the emission of a bremsstrahlung photon of energy k in the field of an atom with atomic number Z takes, in the *complete-screening approximation*, the form [38, 39, 40]:

$$\boxed{\begin{aligned}\frac{\mathrm{d}\sigma}{\mathrm{d}k} = \frac{4\,\alpha\, r_e^2}{3k}\Bigg[&\left\{y^2 + 2\left[1 + (1-y)^2\right]\right\}\left[Z^2\left(F_{\mathrm{el}} - f_c\right) + Z\,F_{\mathrm{inel}}\right] \\ &+ (1-y)\,\frac{Z^2+Z}{3}\Bigg]\end{aligned}} \tag{2.23}$$

where $y \equiv k/E$, E is the total energy of the incident lepton, α is the fine-structure constant, and r_e is the classical electron radius. The quantities $F_{\mathrm{el}}(Z)$ and $F_{\mathrm{inel}}(Z)$ are the *elastic* and *inelastic* radiation logarithms, which describe scattering on the nucleus and on the shell electrons, respectively [38, 40].

For $Z > 4$, these logarithms can be evaluated using the Thomas–Fermi model of the atom [38, 39, 40]:

$$F_{\mathrm{el}}(Z) = \ln\left(\frac{184.15}{Z^{1/3}}\right), \qquad F_{\mathrm{inel}}(Z) = \ln\left(\frac{1194}{Z^{2/3}}\right). \tag{2.24}$$

For light elements ($Z \leq 4$), the Thomas–Fermi model becomes inaccurate, and a more precise description is provided by the Dirac–Fock atomic model [41]. Accordingly, for $Z \leq 4$ we use tabulated Dirac–Fock values, $F_{\mathrm{el}}^{(\mathrm{DF})}(Z)$ and $F_{\mathrm{inel}}^{(\mathrm{DF})}(Z)$, taken from Geant4 (see Section 3.2 and references therein) [41]. These replace F_{el} and F_{inel} in Eq. (2.23).

The term $f_c(Z)$ is the *Coulomb correction factor*, accounting for multi-photon exchange between the lepton and the nuclear Coulomb field [38, 42, 43]:

$$\begin{aligned} f_c(Z) &= \alpha^2 Z^2 \sum_{n=1}^{\infty} \frac{1}{n(n^2 + \alpha^2 Z^2)} \\ &\approx \left(K_1 a^4 + K_2 + \tfrac{1}{1+a^2}\right) a^2 - \left(K_3 a^4 + K_4\right) a^4, \end{aligned} \tag{2.25}$$

with $a = \alpha Z$ and constants $K_1 = 0.0083$, $K_2 = 0.20206$, $K_3 = 0.0020$, and $K_4 = 0.0369$.

In this thesis, and in particular in the beam–gas simulation routine developed as part of this work and described in detail in Section 3.5.1, the DCS of Eq. (2.23) is used for $Z \leq 4$, with tabulated Dirac–Fock values for the elastic and inelastic radiation logarithms. For $Z > 4$, a more general form of the DCS is employed, in which the complete-screening approximation is relaxed and Tsai's analytical screening functions are used instead, consistently with the Geant4 relativistic bremsstrahlung model.

This reads [40, 41]:

$$\boxed{\begin{aligned} \frac{\mathrm{d}\sigma}{\mathrm{d}k} = \frac{16\,\alpha\, r_e^2\, Z^2}{3k} \Bigg\{ & \\ & \left(1 - y + \tfrac{3}{4}y^2\right)\Bigg[\left(\tfrac{1}{4}\phi_1(\gamma) - \tfrac{\ln Z}{3} - f_c(Z)\right) \\ & \qquad + \frac{1}{Z}\left(\tfrac{1}{4}\psi_1(\varepsilon) - \tfrac{2\ln Z}{3}\right)\Bigg] \\ & + \frac{1-y}{8}\Bigg[\phi_1(\gamma) - \phi_2(\gamma) \\ & \qquad + \frac{1}{Z}\left(\psi_1(\varepsilon) - \psi_2(\varepsilon)\right)\Bigg]\Bigg\} \end{aligned}} \tag{2.26}$$

The dimensionless variables γ and ε are defined, following Tsai [40, 41], as

$$\gamma = \frac{y}{E-k}\,\Gamma_Z, \qquad \varepsilon = \frac{y}{E-k}\,\mathcal{E}_Z, \\ \Gamma_Z = \frac{100\,mc^2}{Z^{1/3}}, \qquad \mathcal{E}_Z = \frac{100\,mc^2}{Z^{2/3}}, \tag{2.27}$$

where m is the electron mass.

The functions $\phi_{1,2}(\gamma)$ and $\psi_{1,2}(\varepsilon)$ represent the *coherent* (nuclear) and *incoherent* (atomic-electron) screening functions, respectively [40, 41]. The combinations of these functions appearing in Eq. (2.26) can be expressed analytically as proposed by Tsai [40, 41]:

$$\phi_1(\gamma) = 16.863 - 2\ln\left(1 + 0.311877\,\gamma^2\right) \tag{2.28}$$
$$+ 2.4\,e^{-0.9\gamma} + 1.6\,e^{-1.5\gamma}, \tag{2.29}$$

$$\phi_1(\gamma) - \phi_2(\gamma) = \frac{2}{3 + 19.5\gamma + 18\gamma^2},$$

$$\psi_1(\varepsilon) = 24.34 - 2\ln\left(1 + 13.111641\,\varepsilon^2\right) \tag{2.30}$$
$$+ 2.8\,e^{-8\varepsilon} + 1.2\,e^{-29.2\varepsilon}, \tag{2.31}$$

$$\psi_1(\varepsilon) - \psi_2(\varepsilon) = \frac{2}{3 + 120\varepsilon + 1200\varepsilon^2},$$

For $\gamma, \varepsilon \to 0$, Eq. (2.26) reduces to the DCS in the complete-screening approximation, Eq. (2.23), with F_{el} and F_{inel} given by Eq. (2.24).

Although the total cross-section $\int (\mathrm{d}\sigma/\mathrm{d}k)\,\mathrm{d}k$ is divergent, in practical computations a lower cutoff k_{min} is applied. In the beam–gas routine, k_{min} is determined by the maximum energy deviation δ_{max}, below which bremsstrahlung-induced energy losses are not expected to cause particle losses. For the studies presented in this thesis, a value of $k_{\mathrm{min}} = 20$ MeV is typically assumed.

It is worth noting that the Geant4 relativistic bremsstrahlung model [41] can also include the Landau–Pomeranchuk–Migdal (LPM) and Ter–Mikaelian effects, which describe density-dependent suppression of bremsstrahlung at very high energies or in dense media [44, 45, 46]. However, these effects are negligible in the regime relevant to this work—namely, electron and positron interactions in low-density (UHV[3]-level) gases—and are therefore not included here.

Coulomb scattering

Coulomb scattering refers to the elastic deflection of charged particles by the electrostatic field of atomic nuclei. For electrons and positrons, single scattering on nuclei arises from the long-range Coulomb potential, producing predominantly small-angle deflections with a probability that scales approximately as Z^2. Since the nucleus is much heavier than the incident lepton, the process

[3] Ultra-high vacuum, corresponding to pressures in the range of roughly 10^{-12}–10^{-7} mbar

is effectively elastic, and the energy transferred to the nucleus is typically negligible. At high energies, most scattering angles are very small ($\theta \sim 1/\gamma$), although rare large-angle events can still drive particles beyond the physical or dynamic aperture.

The classical description of this process was first developed by Rutherford (1911) to explain the large-angle deflections of α particles, leading to the well-known *Rutherford scattering formula*. For an electron of charge e, rest mass m, and velocity $v = \beta c$, scattering elastically off a nucleus of charge Ze and rest mass M through an angle θ, the differential cross-section (DCS)—that is, the scattering probability per unit solid angle $d\Omega = 2\pi \sin\theta \, d\theta$—is given by [47]

$$\frac{d\sigma}{d\Omega} = \frac{Z^2 r_e^2}{4\beta^4} \frac{1}{\sin^4\left(\frac{\theta}{2}\right)},$$

where r_e is the classical electron radius. A detailed derivation can be found in standard texts such as [48].

The Rutherford formula is valid in the non-relativistic limit. For relativistic projectiles, the Lorentz factor γ modifies the cross-section, yielding [47]

$$\frac{d\sigma}{d\Omega} = \frac{Z^2 r_e^2}{4\,\beta^4 \gamma^2} \frac{1}{\sin^4\left(\frac{\theta}{2}\right)}. \tag{2.32}$$

which reduces to the non-relativistic DCS for $\gamma \to 1$.

Screening. For an unscreened $1/r$ potential, the Rutherford DCS diverges as $\theta \to 0$. However, in an atom, the nuclear field is screened by the surrounding atomic electrons, which removes the divergence [47]. A convenient way to include this effect is to introduce a screening factor $\mathfrak{F}(\theta)$ and write the *screened* Rutherford DCS as [47]

$$\frac{d\sigma}{d\Omega} = \left(\frac{d\sigma}{d\Omega}\right)_{\text{Rutherford}} \mathfrak{F}^2(\theta). \tag{2.33}$$

A widely used choice is the Wentzel–Molière screening factor [38, 47, 49]

$$\mathfrak{F}(\theta) = \frac{\sin^2\left(\frac{\theta}{2}\right)}{A_{s,M} + \sin^2\left(\frac{\theta}{2}\right)}, \tag{2.34}$$

where the Molière screening parameter is [38, 50, 51, 52]

$$A_{s,M} = \left(\frac{\hbar c}{2p\, a_{\text{TF}}}\right)^2 \left[1.13 \; + \; 3.76\left(\frac{Z\alpha}{\beta}\right)^2\right], \tag{2.35}$$

with p the projectile momentum, $\beta = v/c$, α the fine-structure constant, and $a_{\text{TF}} \simeq 0.8853\, a_0\, Z^{-1/3}$ the Thomas–Fermi radius (a_0 the Bohr radius). With this choice, Eqs. (2.33)–(2.34) are often referred to as the *Wentzel differential cross-section*.

Spin (Mott) correction. For electrons and positrons, the interaction of the lepton magnetic moment with the nuclear field introduces an additional correction to the Rutherford result. It is customary to factor this through a ratio $\mathcal{R}_{\text{Mott}}(\theta)$ between the (spin-aware) Mott and Rutherford cross-sections. A compact analytic expression proposed by McKinley and Feshbach for $\mathcal{R}_{\text{Mott}}(\theta)$ is [47, 53]

$$\mathcal{R}_{\text{McF}}(\theta) = 1 \;-\; \beta^2 \sin^2\!\left(\tfrac{\theta}{2}\right) \;-\; q_0\, Z\, \alpha\, \beta\, \pi\, \sin\!\left(\tfrac{\theta}{2}\right)\left[1 - \sin\!\left(\tfrac{\theta}{2}\right)\right], \tag{2.36}$$

where q_0 is the projectile charge number including its sign ($q_0 = -1$ for electrons, $q_0 = +1$ for positrons).

Finite nuclear size. At sufficiently high momentum transfer, the finite nuclear size suppresses large-angle scattering. This can be included via a nuclear form factor $\mathcal{F}(q)$. A commonly used choice is the exponential form factor, which can be written as [47, 54]

$$\mathcal{F}_{\text{exp}}(q) = \left[1 + \frac{1}{12}\left(\frac{q r_N}{\hbar}\right)^2\right]^{-2}, \tag{2.37}$$

where r_N is the nuclear radius, which can be estimated as $r_N = 1.27 A^{0.27}$ fm, with A being the mass number, and q the momentum transfer.

Factorized working formula. Collecting the above ingredients, an operational expression for the elastic Coulomb scattering DCS of $e^{\pm}$ on nuclei, including relativistic kinematics, screening, spin (Mott) correction, and finite nuclear size, is

$$\frac{d\sigma}{d\Omega} = \left(\frac{d\sigma}{d\Omega}\right)_{\text{Rutherford, rel}} \mathfrak{F}^2(\theta)\; \mathcal{R}_{\text{Mott}}(\theta)\; |\mathcal{F}(q)|^2, \tag{2.38}$$

With the factors given by Eqs. (2.32), (2.34), (2.36), and (2.37), this reads:

$$\boxed{\begin{aligned} \frac{d\sigma}{d\Omega} = {} & \frac{Z^2 r_e^2}{4\,\beta^4\,\gamma^2}\,\frac{1}{\sin^4\!\left(\frac{\theta}{2}\right)} \times \left[\frac{\sin^2\!\left(\frac{\theta}{2}\right)}{A_{s,M} + \sin^2\!\left(\frac{\theta}{2}\right)}\right]^2 \\ & \times \left[1 - \beta^2 \sin^2\!\left(\tfrac{\theta}{2}\right) - q_0\, Z\, \alpha\, \beta\, \pi\, \sin\!\left(\tfrac{\theta}{2}\right)\left(1 - \sin\!\left(\tfrac{\theta}{2}\right)\right)\right] \\ & \times \left[1 + \frac{1}{12}\left(\frac{q r_N}{\hbar}\right)^2\right]^{-4}, \end{aligned}} \tag{2.39}$$

The beam–gas simulation routine developed in this thesis (see Section 3.5.1) employs the differential cross-section of Eq. (2.39) to model Coulomb scattering interactions between beam particles and residual gas nuclei, in consistency with the `G4eCoulombScatteringModel` implementation of single Coulomb scattering in Geant4 [55].

Disclaimer. Geant4 also provides a single-Coulomb-scattering model, `G4eSingleCoulombScatteringModel` [56, 49], which treats the interaction in the center-of-mass frame and then applies the corresponding Lorentz transformations to the laboratory frame, thereby accounting for the finite rest mass (recoil) of the target nucleus. This approach implements a complete two-body kinematic treatment, including the recoil energy transfer, making it more general than the `G4eCoulombScatteringModel`, which uses Eq. (2.38). However, for the purposes of this work—specifically, evaluating beam losses due to Coulomb scattering interactions with residual gas nuclei—the primary interest is in the distribution of scattering angles for given electron/positron energies incident on residual gas nuclei. This distribution is unaffected by whether or not the finite rest mass of the target nucleus (and thus its recoil) is taken into account. Comparative simulations performed with both Geant4 models, along with the routine developed in this thesis, yielded indistinguishable scattering-angle distributions. Consequently, the inclusion of this additional correction is not relevant to the scope of this work [4].

2.2.3 Touschek scattering losses

Touschek scattering, also known as the Touschek effect, originates from single Coulomb scattering events between two relativistic electrons (or positrons) within the same bunch. During such a collision, transverse momentum can be converted into longitudinal momentum. If the resulting momentum (or energy) deviation exceeds the RF or momentum acceptance of the machine, or if the resulting closed-orbit or betatron oscillations exceed the physical or dynamic aperture, particles are consequently lost from the beam.

This effect was first observed in the early 1960s in the first electron storage ring ever built [57], AdA (*Anello di Accumulazione* [58], Italian for "storage ring"), built at the INFN Frascati National Laboratories under the leadership of Bruno Touschek, from whom the effect takes its name. Its theoretical description was subsequently developed in a series of works [59, 60]. Today, the Touschek effect represents the primary limitation to the beam lifetime in modern low-emittance $e^{\pm}$ storage rings.

The Touschek effect is a relativistic effect. In the laboratory frame, electrons (or positrons) move at relativistic velocities along the longitudinal direction, with a large Lorentz factor γ, and their momentum is mainly longitudinal, $p_z \gg p_x, p_y$, where p_z is the longitudinal momentum component, p_x and p_y are the transverse components, and p is the total particle momentum. In

[4] It is important to highlight—as emphasized in Refs. [47, 49, 38]—that the recoil of the target nucleus should not be neglected in studies involving quantities such as stopping power or non-ionizing energy loss (NIEL), as ignoring this effect results in an underestimation of both stopping power and NIEL.

the center-of-mass (c.m.) frame of two hypothetically colliding particles,[5] the situation is reversed. In this frame, the transverse oscillation energy due to betatron motion is larger than the longitudinal one due to synchrotron motion, and $p_z^* \ll p_x^*, p_y^*$. Additionally, in this frame the two particles move slowly, with non-relativistic velocities and small momenta $\mathbf{p}^*$. If the two particles undergo a Coulomb collision, their momentum components are redistributed. Using primed quantities for the values after scattering, and labeling the two hypothetically scattering particles as 1 and 2, one has

$$\mathbf{p_1^*} = (p_{x,1}^*, p_{y,1}^*, p_{z,1}^*) \xrightarrow{\text{scattering}} \mathbf{p_1^*}' = (p_{x,1}^{*'}, p_{y,1}^{*'}, p_{z,1}^{*'}),$$

$$\mathbf{p_2^*} = (p_{x,2}^*, p_{y,2}^*, p_{z,2}^*) \xrightarrow{\text{scattering}} \mathbf{p_2^*}' = (p_{x,2}^{*'}, p_{y,2}^{*'}, p_{z,2}^{*'}),$$

with

$$p_{x,1}^{*'} = p_{x,1}^* + \Delta p_{x,1}^*, \qquad p_{y,1}^{*'} = p_{y,1}^* + \Delta p_{y,1}^*, \qquad p_{z,1}^{*'} = p_{z,1}^* + \Delta p_{z,1}^*,$$

$$p_{x,2}^{*'} = p_{x,2}^* + \Delta p_{x,2}^*, \qquad p_{y,2}^{*'} = p_{y,2}^* + \Delta p_{y,2}^*, \qquad p_{z,2}^{*'} = p_{z,2}^* + \Delta p_{z,2}^*,$$

and, by momentum conservation in the c.m. frame,

$$\Delta p_{x,1}^* = -\Delta p_{x,2}^*, \qquad \Delta p_{y,1}^* = -\Delta p_{y,2}^*, \qquad \Delta p_{z,1}^* = -\Delta p_{z,2}^*.$$

Applying the Lorentz transformation back to the laboratory frame, one can write

$$E_1' = \gamma\left(E_1^{*'} + c\beta\, p_{z,1}^{*'}\right),$$

$$p_{x,1}' = p_{x,1}^{*'}, \qquad p_{y,1}' = p_{y,1}^{*'}, \qquad p_{z,1}' = \gamma\left(p_{z,1}^{*'} + \beta\,\frac{E_1^{*'}}{c}\right),$$

$$E_2' = \gamma\left(E_2^{*'} + c\beta\, p_{z,2}^{*'}\right),$$

$$p_{x,2}' = p_{x,2}^{*'}, \qquad p_{y,2}' = p_{y,2}^{*'}, \qquad p_{z,2}' = \gamma\left(p_{z,2}^{*'} + \beta\,\frac{E_2^{*'}}{c}\right).$$

Expressing the variation of the momentum components due to the scattering for the two particles in the laboratory frame, one obtains

$$\Delta p_{x,1} = \Delta p_{x,1}^*, \qquad \Delta p_{x,2} = \Delta p_{x,2}^*, \qquad \Delta p_{z,1} = \gamma\,\Delta p_{z,1}^*,$$

$$\Delta p_{y,1} = \Delta p_{y,1}^*, \qquad \Delta p_{y,2} = \Delta p_{y,2}^*, \qquad \Delta p_{z,2} = \gamma\,\Delta p_{z,2}^*.$$

From these equations, one can clearly see that even a small redistribution of the momentum components from transverse to longitudinal directions in the c.m. frame, Δp_x^*, Δp_y^*, Δp_z^*, are amplified by the Lorentz factor γ in the laboratory frame.

[5] Quantities in the c.m. frame will be distinguished, from here on, by an asterisk "*".

In the following, the theoretical framework of Touschek scattering is developed in more detail, introducing the concepts and quantities required for a quantitative description of the effect. These provide the basis for the Touschek scattering simulation routine implemented as part of this work and presented in Section 3.5.2.

In the c.m. frame, the probability that one of the two interacting particles is scattered into the element of solid angle $d\Omega^*$ is given by the Møller differential cross-section [61]

$$\frac{d\sigma^*}{d\Omega^*}(\Theta^*, \Psi^*) = \frac{r_e^2}{4\gamma^{*2}} \left[\left(1 + \frac{1}{\beta^{*2}}\right)^2 \frac{4 - 3\sin^2\Theta^*}{\sin^4\Theta^*} + \frac{4}{\sin^2\Theta^*} + 1 \right], \tag{2.40}$$

where r_e is the classical electron radius, γ^* and β^* are the relativistic factors in the c.m. frame, Θ^* is the c.m. scattering polar angle, Ψ^* the azimuthal angle, and $d\Omega^* = \sin\Theta^*\, d\Theta^*\, d\Psi^*$.

The total Touschek scattering rate is obtained by integrating over all scattering angles and over all particles in the bunch [61]. In the c.m. frame,

$$R^* = 2 \int |v^*|\, \sigma^*\, \rho(\vec{x}_1^*)\, \rho(\vec{x}_2^*)\, dV^*, \tag{2.41}$$

where $|v^*|$ is the particles' velocity, $\rho(\vec{x}_i^*)$ the single-particle phase-space density, and

$$dV^* = dx^*\, dy^*\, dz^*\, dp^*_{x1}\, dp^*_{y1}\, dp^*_{z1}\, dp^*_{x2}\, dp^*_{y2}\, dp^*_{z2}.$$

The quantity σ^* is the total Møller cross-section in the c.m. frame [61]

$$\sigma^* = \int_0^{2\pi} \int_0^{\pi/2} \frac{d\sigma^*}{d\Omega^*}\, \sin\Theta^*\, d\Theta^* d\Psi^*. \tag{2.42}$$

Transforming to the laboratory frame gives [61],

$$|v|\, \sigma = \frac{|v^*|}{\gamma}\, \frac{\sigma^*}{\gamma}, \tag{2.43}$$

and [61]

$$R = 2 \int |v|\, \sigma\, \rho(\vec{x}_1)\, \rho(\vec{x}_2)\, dV, \tag{2.44}$$

with

$$dV = dx_\beta\, dy_\beta\, dz\, dx'_{\beta 1}\, dx'_{\beta 2}\, dy'_{\beta 1}\, dy'_{\beta 2}\, d\Delta p_1\, d\Delta p_2,$$

where (x_β, x'_β) and (y_β, y'_β) denote betatron coordinates (i.e., dispersive contributions removed) and Δp_i the momentum deviation.

Inserting Eq. (2.42) into Eq. (2.43) and substituting the result into Eq. (2.44), one can expand the expression for the Touschek scattering rate in the laboratory frame as

$$R = 2 \int\!\!\int_0^{2\pi} \int_0^{\pi/2} \frac{|v^*|}{\gamma^2}\, \frac{d\sigma^*}{d\Omega^*}\, \sin\Theta^*\, \rho(\vec{x}_1)\, \rho(\vec{x}_2)\, d\Theta^*\, d\Psi^*\, dV. \tag{2.45}$$

For a Gaussian-distributed bunch, Piwinski [60] performed a detailed evaluation of Eq. (2.45) and obtained a widely used closed-form expression for the Touschek scattering loss rate. This result, commonly referred to as the Piwinski formula, expresses the Touschek loss rate in terms of the linear optics functions and beam parameters of the storage ring. The formula reads [60]

$$\begin{aligned} R_P = & \frac{r_e^2 c N^2}{8\pi\gamma^2\sigma_z\sqrt{\sigma_x^2\sigma_y^2 - \sigma_\delta^4 D_x^2 D_y^2}} \sqrt{\pi(B_1^2 - B_2^2)} \\ & \times \int_{\tau_m}^{\infty} \left[\left(\left(2 + \frac{1}{\tau}\right)^2 \left(\frac{\tau/\tau_m}{1+\tau} - 1\right) + 1 - \frac{\sqrt{1+\tau}}{\sqrt{\tau/\tau_m}} \right) \right. \\ & \left. - \frac{1}{2\tau}\left(4 + \frac{1}{\tau}\right) \ln\frac{\tau/\tau_m}{1+\tau} \right] e^{-B_1\tau} I_0(B_2\tau) \frac{\sqrt{\tau}\,d\tau}{\sqrt{1+\tau}}. \end{aligned} \tag{2.46}$$

In Eq. (2.46), r_e is the classical electron radius, c the speed of light in vacuum, N the number of particles per bunch, and γ the relativistic Lorentz factor. The quantities σ_x and σ_y denote the rms transverse beam sizes, defined as

$$\sigma_x = \sqrt{\varepsilon_x\beta_x + D_x^2\sigma_\delta^2}, \qquad \sigma_y = \sqrt{\varepsilon_y\beta_y + D_y^2\sigma_\delta^2},$$

where ε_x and ε_y are the horizontal and vertical rms emittances, respectively, $D_{x,y}$ are the dispersion functions, and σ_δ is the rms relative momentum (or energy) spread. The bunch length is denoted by σ_z.

The parameter τ_m is related to the (local) momentum acceptance δ_a (see the last paragraph of this section) through

$$\tau_m = \beta^2\delta_a^2,$$

where β is the relativistic velocity factor ($\beta = v/c$).

The auxiliary functions B_1 and B_2 appearing in Eq. (2.46) are defined as

$$B_1 = \frac{\beta_x^2}{2\beta^2\gamma^2\sigma_{x\beta}^2}\left(1 - \frac{\sigma_h^2\widetilde{D}_x^2}{\sigma_{x\beta}^2}\right) + \frac{\beta_y^2}{2\beta^2\gamma^2\sigma_{y\beta}^2}\left(1 - \frac{\sigma_h^2\widetilde{D}_y^2}{\sigma_{y\beta}^2}\right),$$

$$B_2^2 = B_1^2 - \frac{\beta_x^2\beta_y^2\sigma_h^2}{\beta^4\gamma^4\sigma_{x\beta}^4\sigma_{y\beta}^4\sigma_\delta^2}\left(\sigma_x^2\sigma_y^2 - \sigma_\delta^4 D_x^2 D_y^2\right),$$

where $\beta_{x,y}$ are the betatron functions, and $\sigma_{x\beta}$ and $\sigma_{y\beta}$ are the rms betatron beam sizes (excluding dispersive contributions).

The functions $\widetilde{D}_x$ and $\widetilde{D}_y$ are given by

$$\widetilde{D}_x = \alpha_x D_x + \beta_x D_x', \qquad \widetilde{D}_y = \alpha_y D_y + \beta_y D_y',$$

with $\alpha_{x,y}$ being the Twiss–α functions and $D_{x,y}'$ the derivatives of the dispersion functions.

The parameter σ_h is defined through

$$\frac{1}{\sigma_h^2} = \frac{1}{\sigma_\delta^2} + \frac{D_x^2 + \widetilde{D}_x^2}{\sigma_{x\beta}^2} + \frac{D_y^2 + \widetilde{D}_y^2}{\sigma_{y\beta}^2}.$$

Finally, I_0 in Eq. (2.46) denotes the modified Bessel function of the first kind of order zero.

It is worth noting that, as indicated by Eq. (2.46), the Touschek scattering loss rate decreases rapidly with increasing beam energy (γ).

Piwinski formula is a standard tool for estimating Touschek lifetimes in low-emittance storage rings and colliders. The Touschek lifetime τ_T can be estimated as [60]

$$\frac{1}{\tau_T} = \left\langle \frac{R_P}{N} \right\rangle = \frac{1}{C} \oint_C \frac{R_P(s)}{N}\, ds, \tag{2.47}$$

with R_P given by Eq. (2.46) and N being the number of particles per bunch (at time $t = 0$). Since the optics functions, beam sizes, and momentum acceptance vary along the ring, the Piwinski Touschek loss rate must be averaged over the circumference C of the machine.

Local Momentum Acceptance. The local momentum acceptance (LMA) is the maximum momentum deviation that a particle can sustain at a specific longitudinal position in the accelerator without being lost. It thus represents the largest instantaneous momentum deviation for which the particle motion remains stable. The LMA is *local* because it depends on the local optical properties. For example, if a particle experiences a sudden momentum deviation in a dispersion-free region, it remains transversely matched to its off-momentum closed orbit (which in that case coincides with the on-momentum closed orbit), whereas in a region with nonzero dispersion, the same momentum deviation would cause an immediate mismatch with respect to the off-momentum closed orbit. Consequently, the LMA is smaller in regions with nonzero dispersion than in dispersion-free regions. It is worth noting that, in dispersion-free regions, the LMA coincides with the (non-local) momentum acceptance (or longitdudinal dynamic aperture) introduced earlier in Section 2.1.2. The LMA can be evaluated through particle tracking, using the method described in Section 3.5.2.

2.2.4 Beam–beam losses

In high-intensity colliders, the mutual electromagnetic interactions between counter-rotating colliding beams—known as the *beam–beam interactions*—a fundamental limitation to the collider performance. Each bunch generates an electromagnetic field that acts as a non-linear lens on the particles of the opposite beam. These non-linear forces perturb the transverse and longitudinal particle motion, leading to tune shifts, emittance growth, and potentially unstable or chaotic dynamics. As a consequence, the beam–beam interactions play a crucial role in defining both the achievable luminosity and the overall beam stability.

For small amplitudes, the beam–beam force can be approximated by a linear focusing term, analogous to that of a thin quadrupole lens, except that it provides focusing in both transverse planes simultaneously. The strength of this linear interaction is characterized by the *beam–beam parameter*, ξ:

$$\xi_{x,y} = \frac{N r_e \, \beta^*_{x,y}}{2\pi\gamma \, \sigma^*_{x,y}(\sigma^*_x + \sigma^*_y)} \,, \tag{2.48}$$

where N is the number of particles per bunch, r_e the classical electron radius, $\beta^*_{x,y}$ the betatron functions at the interaction point (IP), γ the relativistic Lorentz factor, and $\sigma^*_{x,y}$ the horizontal and vertical r.m.s. beam sizes at the IP. The beam–beam parameter provides a useful measure of the strength of the coupling and of the tune shift experienced by small-amplitude particles.

However, the beam–beam force is intrinsically non-linear. Particles at larger amplitudes experience a weaker average focusing, leading to an amplitude-dependent tune shift and a corresponding tune spread within the bunch. As a result, particles may cross resonances or undergo diffusive motion in phase space. Over time, these effects can drive particles away from the beam core and populate the beam halo; once their transverse amplitudes exceed the dynamic or physical aperture, such particles are lost. *Beam–beam losses* therefore refer to those beam losses that arise as a consequence of beam–beam interactions in a particle collider.

The most direct consequences of beam–beam losses are a reduction of the beam lifetime and a possible increase in background rates observed by the experimental detectors. In extreme cases, localized beam–beam losses, if not properly mitigated, can also lead to increased heat loads on sensitive components or even cause damage.

While beam–beam interactions are present in all types of colliders, they play a particularly important role in high-luminosity electron–positron machines such as SuperKEKB and the FCC-ee. This is because achieving high luminosity requires extremely small beam sizes at the IP, which, according to Eq. (2.48), increase the beam–beam parameter ξ and therefore strengthen the beam–beam force. Two beam–beam effects of particular relevance for electron–positron colliders, and thus for this thesis, are *beamstrahlung* and *radiative Bhabha scattering*. In the FCC-ee, these processes contribute to the determination of the equilibrium beam parameters (beamstrahlung) and sizable particle losses, thereby affecting the overall collider performance. The two processes are discussed in more detail in the next subsections.

Beamstrahlung

Beamstrahlung is the synchrotron radiation emitted by ultra-relativistic particles as they traverse the electromagnetic field of the opposite bunch during collisions. In high-energy circular e^+e^- colliders such as FCC-ee, this effect becomes a major source of quantum excitation in addition to the standard synchrotron radiation produced in the bending magnets. Its main consequences are (i) an increase in the equilibrium energy spread and bunch length, (ii) a possible blow-up of the transverse emittances if the dispersion at the interaction point (IP) is nonzero, and (iii) a limitation of the beam lifetime through rare emission of high-energy photons [62].

The intensity of the effect is characterized by the *beamstrahlung parameter* [62, 63, 64]

$$\Upsilon = \frac{B}{B_c} = \frac{2\hbar\omega_c}{3E}, \tag{2.49}$$

where E is the electron (or positron) beam energy, $B_c \simeq 4.4$ GT is the Schwinger critical field, and $\hbar\omega_c$ is the critical photon energy corresponding to the local curvature of the particle trajectory. For the FCC-ee, $\Upsilon \ll 1$, which implies that the radiation can be described within the classical regime [62]. Under these conditions, the average parameter $\langle\Upsilon\rangle$ for two colliding Gaussian bunches with transverse beam sizes (σ_x^*, σ_y^*), longitudinal size σ_z, and bunch population N_b, can be approximated as [62, 64]

$$\langle\Upsilon\rangle \approx \frac{5}{6}\,\frac{r_e^2\,\gamma\,N_b}{\alpha\,\sigma_z(\sigma_x^* + \sigma_y^*)}, \tag{2.50}$$

where r_e is the classical electron radius, α the fine-structure constant, and γ the Lorentz factor.

The equilibrium beam parameters result from the balance between radiation damping and the quantum excitation produced by both arc synchrotron radiation and beamstrahlung. For zero IP dispersion, beamstrahlung increases only the longitudinal emittance. The total relative energy spread in collision can be written as [62]

$$\sigma_{\delta,\mathrm{tot}}^2 = \sigma_{\delta,\mathrm{SR}}^2 + \frac{n_{\mathrm{IP}}\,\tau_{E,\mathrm{SR}}}{4\,T_{\mathrm{rev}}}\,\{n_\gamma\langle u^2\rangle\}_{\mathrm{BS}}, \tag{2.51}$$

where $\sigma_{\delta,\mathrm{SR}}$ is the natural energy spread due to synchrotron radiation, $\tau_{E,\mathrm{SR}}$ the longitudinal damping time, T_{rev} the revolution period, n_{IP} the number of collision points, and $\{n_\gamma\langle u^2\rangle\}_{\mathrm{BS}}$ represents the mean square photon energy emitted per collision (see Eq. (18) in Ref. [62]).

The equilibrium bunch length is related to the total energy spread through the longitudinal dynamics relation [62, 31]

$$\sigma_{z,\mathrm{tot}} = \frac{\alpha_C\,C}{2\pi Q_s}\,\sigma_{\delta,\mathrm{tot}}, \tag{2.52}$$

where α_C is the momentum compaction factor, C the ring circumference, and Q_s the synchrotron tune. Analytical estimates indicate that, for the FCC-ee, beamstrahlung increases the equilibrium bunch length and relative energy spread by factors of about two to three compared with their synchrotron-radiation-only values (see Table 1.2), in good agreement with detailed beam–beam tracking simulations [62].

Radiative Bhabha scattering

Radiative Bhabha scattering (RBS) refers to the inelastic scattering process

$$e^+e^- \longrightarrow e^+e^-\gamma,$$

in which one of the colliding leptons emits a hard photon during the Coulomb interaction with a particle from the opposite bunch. The emission of such a photon leads to an energy reduction of the radiating lepton and can result in particle loss if the energy deviation exceeds the machine's momentum acceptance, or if the resulting orbit or betatron oscillations fall outside the physical or dynamic aperture. In high-luminosity circular e^+e^- colliders such as the FCC-ee, RBS is among the dominant mechanisms limiting the beam lifetime (see Table 1.2) [65].

Following Ref. [65], at small scattering angles the radiative Bhabha process can be modeled using the *Equivalent Photon Approximation* (EPA). In this framework, the electromagnetic field of a relativistic charged particle is treated as a spectrum of quasi-real (or "equivalent") photons with a continuous energy distribution. The interaction between two ultrarelativistic leptons can thus be approximated as the scattering of one lepton from the equivalent-photon flux generated by the other. Under this assumption, the differential cross-section for radiative Bhabha scattering in the forward region can be expressed as the product of the equivalent-photon density and the classical Compton-scattering cross-section [65],

$$\mathrm{d}\sigma_{\mathrm{Bhabha}} \approx \mathrm{d}n \times \mathrm{d}\sigma_{\mathrm{C}}, \tag{2.53}$$

where $\mathrm{d}n$ represents the number density of equivalent photons and $\mathrm{d}\sigma_{\mathrm{C}}$ is the differential Compton cross-section. This approximation replaces the full QED calculation with a simplified but accurate[6] description of radiative Bhabha scattering in the small-angle, low-momentum-transfer regime relevant for high-energy circular colliders [65].

The differential cross-section for RBS is strongly peaked at small angles and low photon energies, but its high-energy tail is responsible for particle losses. The expected number of RBS events per bunch crossing with an energy loss greater than the momentum-acceptance threshold δ_m can be written as

$$R_k \;=\; L_{\mathrm{int}}\,\sigma_{\mathrm{RBS}}(\delta > \delta_m), \tag{2.54}$$

where L_{int} is the integrated luminosity per bunch crossing, and $\sigma_{\mathrm{RBS}}(\delta > \delta_m)$ denotes the RBS cross-section integrated above the acceptance limit [65]. The corresponding beam lifetime due to RBS is given by

$$\tau_{\mathrm{RBS}} \;=\; \frac{N_b}{n_{\mathrm{IP}}\,L_{\mathrm{inst}}\,\sigma_{\mathrm{RBS}}}, \tag{2.55}$$

[6]The accuracy of the Equivalent Photon Approximation compared with full QED calculations is typically within 5%. This level of accuracy is acceptable, as the relevant beam parameters are usually not known with better than 5% precision [66].

where N_b is the bunch population, n_{IP} is the number of interaction points, and L_{inst} is the instantaneous luminosity per IP [65].

Radiative Bhabha scattering therefore imposes an intrinsic trade-off between beam lifetime and luminosity performance: an increase in instantaneous luminosity enhances the RBS event rate and consequently reduces the beam lifetime.

2.3 Crystal collimation

Crystal collimation exploits the channeling of charged particles in bent crystals to deflect beam halo particles towards dedicated absorbers, as illustrated in Fig. 2.5. Compared to conventional collimation, relying on amorphous collimators, crystal collimation offers the potential for enhanced collimation performance and a reduced impedance contribution from the beam halo collimators.

Crystal collimation has been experimentally demonstrated at several accelerators. It was successfully tested, although never implemented in regular operation, at the Tevatron [68], demonstrating its ability to reduce beam losses in the detector region [69]. Crystal collimation has also been proposed for proton and heavy-ion beams at the LHC [1, 70], electron and positron beams at the ILC [71], and was experimentally studied at RHIC [72], where a bent crystal was tested as a collimator for heavy-ion and proton beams. Crystal collimation is now routinely employed during heavy-ion operation at the LHC [73, 74, 75, 76].

In this thesis, studies to assess the feasibility and performance of implementing crystal collimation system in the FCC-ee are presented in Chapter 7. These include a preliminary system design and a first evaluation of its expected performance.

In the remainder of this section, some fundamental principles and characteristic quantities describing the interaction of charged particles with bent crystals are introduced. These provide the theoretical basis for the studies and considerations presented in Chapter 7.

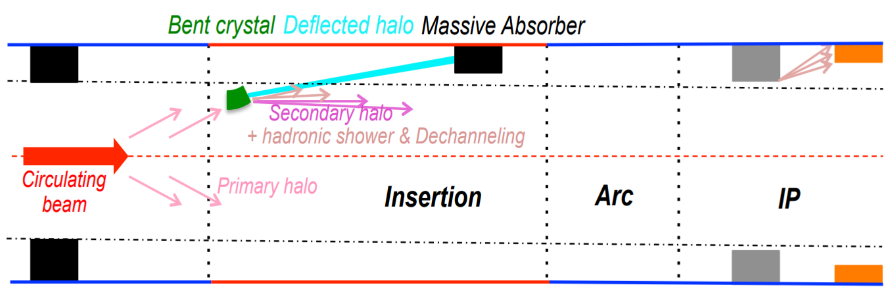

Figure 2.5. Working principle of a crystal collimation system. From [67].

Basics of crystal channeling physics

When a charged particle enters an oriented crystal at a small angle with respect to a family of lattice planes (planar case) or axes (axial case), the averaged electrostatic field of the crystal lattice forms a smooth potential that can confine its transverse motion, as illustrated in Fig. 2.6 for the planar case. In this situation, one speaks of *channeling* of the particle. For the crystal collimation studies carried out in this thesis, planar channeling is the relevant regime, and this case will therefore be the focus of the following discussion.

Planar channeling in straight crystals. In the small-angle approximation, the transverse dynamics may be described by a conserved transverse energy [78],

$$E_T = \frac{pv}{2}\,\theta^2 + U(x), \tag{2.56}$$

where p is the particle momentum, v its speed, θ the angle to the crystal planes, and $U(x)$ the interplanar potential (periodic with interplanar spacing d and depth U_0). Channeling occurs if E_T is below the barrier of $U(x)$. This defines the Lindhard critical angle [78]

$$\theta_c = \sqrt{\frac{2U_0}{pv}}, \tag{2.57}$$

which sets the approximate angular acceptance for the channeling of a particle in a straight crystal ($\sim 2\theta_c$). Within the channel the transverse motion is oscillatory, with a characteristic wavelength that increases with pv and decreases with U_0 [78].

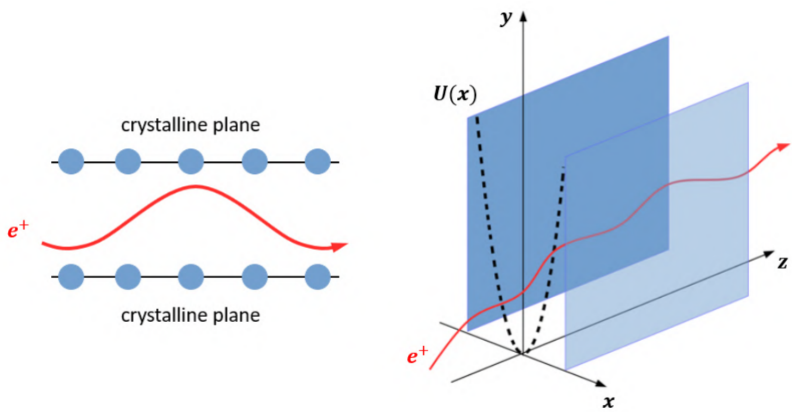

Figure 2.6. Illustration of planar channeling. The solid red line represents the path of a positively charged particle moving within the potential well formed by two neighboring crystal planes, viewed from above (left) and from the side (right). From [77].

Dechanneling. Once a particle is in the channeling state, it may lose this state due to incoherent scattering on the crystal electrons, nuclei, or lattice defects. Such scattering processes lead to a non-conservation of the transverse energy E_T. When E_T exceeds the depth of the interplanar potential well, the particle can no longer be confined within the channel and leaves the channeling regime. This process is referred to as *dechanneling* [78].

The longer a particle travels through a crystal in the channeling state, the higher the probability that such scattering events will occur, and therefore the lower the probability that the particle remains channeled. It is thus common to model the evolution of the population of channeled particles as a function of the distance traversed in the crystal by an exponentially decaying function,

$$N_{\mathrm{ch}}(z) = N_{\mathrm{ch}}(0)\, e^{-z/L_d}, \tag{2.58}$$

where $N_{\mathrm{ch}}(0)$ is the initial number of channeled particles at the crystal entrance, z is the path length inside the crystal, and L_d is the *dechanneling length*, i.e., the characteristic length describing the exponential decay of the channeled particle population [78].

Bent crystals and coherent steering. If the crystal is uniformly bent with a bending radius R, the effective potential acquires a linear term that accounts for the centrifugal force [78],

$$U_{\mathrm{eff}}(x) = U(x) + \frac{pv}{R}\, x, \tag{2.59}$$

which reduces the potential well on the inner side of the curvature.

There exists a critical value of the centrifugal term, $(pv/R)_c$, at which the potential well vanishes and channeling is no longer possible. The corresponding *critical bending radius* is defined by [78]

$$R_c = \frac{pv}{U'_{\mathrm{max}}}, \tag{2.60}$$

where U'_{max} is the maximum gradient of the planar potential.

Channeling in bent crystals therefore requires $R > R_c$. In this regime, channeled particles follow the crystal curvature and emerge with a coherent deflection approximately equal to the crystal bending angle,

$$\theta_b = \frac{L}{R}, \tag{2.61}$$

where L is the crystal length. This coherent steering is exploited in crystal collimation to deflect beam-halo particles onto dedicated absorbers. Beyond collimation, it also finds applications, for example, in beam extraction, fixed-target experiments, beam splitting, and the production of secondary particle beams.

It is important to note that the bending modifies the potential well depth and therefore reduces the channeling angular acceptance, quantified by the critical angle θ_c introduced in Eq. (2.57) for the straight crystal case. The critical angle for a bent crystal with bending radius R can be written as [78]

$$\theta_c(R) = \left(1 - \frac{R_c}{R}\right)\theta_{c,0}, \tag{2.62}$$

where $\theta_{c,0}$ is the critical angle for a straight crystal ($R \to \infty$). As can be seen from this expression, $\theta_c \to 0$ as $R \to R_c$.

The dechanneling length defined above is also affected by the bending, and can be expressed as

$$L_d(R) = L_{d,0}\left(1 - \frac{R_c}{R}\right), \tag{2.63}$$

where $L_{d,0}$ is the dechanneling length in a straight crystal.

Planar channeling of positively and negatively charged particles. In planar channeling, the particle motion depends strongly on the sign of its charge. As illustrated in Fig. 2.6, positively charged particles oscillate between adjacent crystal planes, while negatively charged particles move along trajectories that cross the planes. The corresponding transverse trajectories of both cases in the x–z plane, where x denotes the transverse coordinate and z the penetration depth into the crystal, are shown in Fig. 2.7(a).

Under channeling conditions, positively charged particles are repelled from the atomic nuclei and therefore penetrate more deeply into the crystal compared to the unaligned orientation. Negatively charged particles, on the other hand, are attracted toward regions of higher nuclear density, which increases their interaction probability compared to the positive-charge case [79]. As a consequence of this attraction, negatively charged particles experience more frequent close encounters with the crystal atoms, leading to enhanced scattering and therefore a significantly shorter dechanneling length than for positively charged particles [80].

The continuous interplanar potential governing the transverse motion can be approximated by a harmonic potential well for positively charged particles, as illustrated in Fig. 2.7(c). For negatively charged particles, the situation is reversed: since they are attracted to the nuclei, the potential changes sign and becomes non-harmonic, exhibiting a minimum near the mid-plane between two atomic planes, as shown in Fig. 2.7(d). As a result, the transverse dynamics and phase-space trajectories of positively and negatively charged particles differ substantially, as illustrated in Fig. 2.7(b).

Volume reflection in bent crystals. When particles traverse a bent crystal at an incidence angle larger than the critical channeling angle, they are not captured into the channeling regime but can still undergo coherent deflection due to the averaged electrostatic field of the bent crystal planes. In this case, the particle approaches the maximum of the effective potential and is turned by the field of the bent planes in a direction opposite to the crystal curvature. This process is known as *volume reflection* [80, 79].

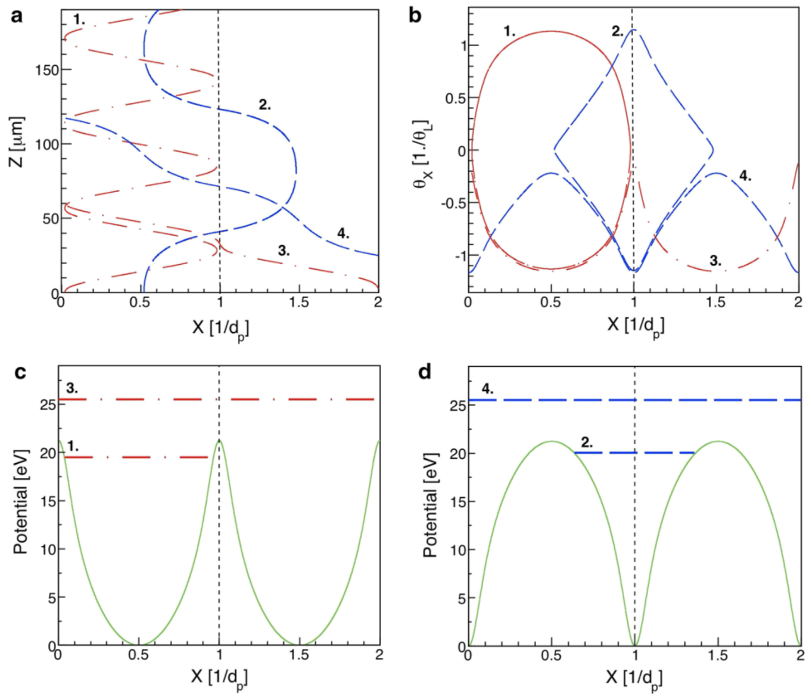

Figure 2.7. Transverse trajectories and potentials for 400 GeV/c particles interacting with Si(110) planes (dotted lines). Curves 1 and 2 correspond to channeled particles, while curves 3 and 4 represent over-barrier trajectories. Dashed (dot-dashed) lines refer to negative (positive) particles. (a) Trajectories as a function of transverse position x and penetration depth z. (b) Trajectories in phase space, i.e. transverse position x versus transverse angle θ_x. (c–d) Continuous planar potential (solid line) and transverse energies for positive and negative particles, respectively. The quantity d_p is the interplanar distance. From [79].

For positively charged particles, the mean deflection angle in volume reflection is typically of the order of $(1.0–1.5)\,\theta_c$, while for negatively charged particles it is smaller, around $(0.8)\,\theta_c$ [79].

Electromagnetic radiation in crystals. When high-energy electrons and positrons interact with oriented crystals, they can emit electromagnetic radiation as a result of their coherent interaction with the periodic crystal lattice. Two main radiation mechanisms are distinguished: *coherent bremsstrahlung*, which occurs for over-barrier particles traversing the crystal at angles larger than the channeling critical angle, and *channeling radiation*, which is emitted by particles captured in the channeling regime and oscillating in the averaged interplanar or axial electric field [78]. In both cases, the radiation intensity can be strongly enhanced with respect to amorphous materials.

Chapter 3

Simulation tools

The study of collimation in the FCC-ee relies on advanced simulation tools capable of modeling both beam dynamics and particle–matter interactions with collimators. These tools enable accurate predictions of beam loss patterns and collimation performance, providing essential input for the design and optimization of collimation systems. While they do not directly provide estimates of detector background levels, the output of these simulations—specifically the spatial and kinematic distributions of beam losses—serves as a crucial input for subsequent background evaluation studies. This chapter presents the simulation frameworks employed in this work, outlining their capabilities, underlying physics models, and their application to FCC-ee collimation studies. In addition, for benchmarking purposes, the same tools are also applied to SuperKEKB. In this context, a dedicated software framework developed for the Belle II experiment is used to simulate detector backgrounds, and its relevant features are also described in this chapter.

3.1 Xsuite

Xsuite [81, 82] is the primary simulation framework employed in the collimation studies presented in this thesis. It is a modern and modular collection of Python-based tools developed at CERN, designed to simulate beam dynamics in particle accelerators. Xsuite aims to unify and extend the capabilities of previously domain-specific tools, offering a coherent, flexible, and high-performance environment suitable for a wide range of accelerator physics applications.

A key feature of Xsuite is its modular architecture, which enables seamless integration between its core components and with other accelerator-specific or general-purpose Python tools. This design supports the simulation of complex scenarios within a single, cohesive framework.

The core modules of Xsuite are structured as individual Python packages, each dedicated to a specific aspect of accelerator modeling:

- **Xtrack**: The central tracking engine, supporting symplectic tracking through both thin and thick element maps. It also includes tools for beamline definition, optics computations, and optics matching.

- **Xpart**: Handles the creation and manipulation of particle ensembles, including routines to generate distributions that are matched to the local optics parameters.

- **Xfields**: Provides models for collective effects, including space charge, beam–beam interactions, and electron cloud. It supports both analytical field calculations and Particle-In-Cell (PIC) approaches.

- **Xwakes**: Enables the modeling of wakefields and impedances, allowing the inclusion of these effects in beam-dynamics simulations.

- **Xcoll**: A dedicated module for simulating interactions between beam particles and beam–intercepting devices such as collimators [83, 84]. It supports coupling with external Monte Carlo codes such as BDSIM/Geant4 and FLUKA for detailed particle–matter interaction simulations.

- **Xdeps**: Manages symbolic variables and deferred expressions, supporting advanced parameter control and configuration management.

- **Xobjects**: Provides the memory management infrastructure and supports code compilation and execution across different computing platforms, including CPUs and GPUs.

In the context of this thesis, the most relevant feature of Xsuite is the interface provided by Xcoll to the BDSIM/Geant4 framework, which allows online simulation—i.e., during tracking—of particle–matter interactions with collimators. This interface has been central to the design and performance assessment of the FCC-ee collimation system, enabling detailed modeling of different beam loss scenarios. A more detailed description of the Xsuite–BDSIM interface is provided in Section 3.3.

3.2 BDSIM

BDSIM (Beam Delivery SIMulation) [85, 86] is a C++ software package developed for the simulation of radiation transport and particle–matter interactions in particle accelerators and beamlines. It combines standard high-energy physics libraries—Geant4 [87, 88, 89], ROOT [90], and CLHEP [91]—to construct accelerator models that support both beam tracking and particle–matter interaction physics.

BDSIM integrates accelerator-specific tracking routines with the physics models provided by Geant4, enabling simulations where both long-range beam transport and particle–material interactions are relevant. This makes it well suited for studies involving energy deposition, radiation transport, and the production of secondary particles in components such as collimators, absorbers, and beamline elements.

Geant4 is the Monte Carlo toolkit at the core of these simulations. It allows particles, defined by initial conditions such as position and momentum, to be tracked through complex three-dimensional geometries built from user-defined volumes and materials. As particles traverse these geometries, Geant4 models their interactions with matter using a comprehensive set of physics processes—including electromagnetic, hadronic, and nuclear interactions—while generating and tracking all secondary particles produced.

In this thesis, BDSIM is employed through the interface provided by the Xcoll module in Xsuite. This setup enables the modeling of beam–collimator interactions during tracking, combining the beam dynamics capabilities of Xsuite with the detailed particle–matter interaction modeling of Geant4 through BDSIM.

3.3 Xsuite–BDSIM coupling

Xsuite and BDSIM can be used together to perform simulations that combine particle tracking with particle-matter interactions. While BDSIM includes both tracking and particle-matter interaction capabilities, its internal tracking is not symplectic. This, combined with the use of a Cartesian coordinate system required by Geant4, limits its applicability for long-term tracking in large circular accelerators such as the FCC-ee. In such cases, the tracking becomes both computationally inefficient and insufficiently accurate over the full ring.

To address this, an interface between Xsuite and BDSIM [92, 93, 94] has been developed in the form of `collimasim` [95], a Python library providing Python–C++ bindings bindings to BDSIM. `collimasim` is used in Xsuite through the Xcoll module.

In an Xsuite–BDSIM simulation, the accelerator lattice is defined in Xsuite, and selected collimator volumes are modeled in 3D using BDSIM. During tracking, Xsuite tracks particles through the lattice until they reach a collimator. At that point, the particles are transferred to the corresponding BDSIM model, where a full Monte Carlo particle–matter interaction simulation is performed. Surviving primary particles and produced secondaries are then sent back to

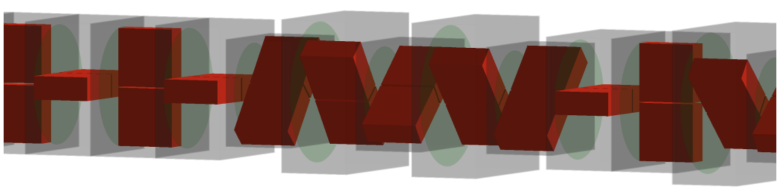

Figure 3.1. A visualization of an example BDSIM model used for collimator interactions, showing the collimator models (red) and the isolated cells (grey) [92].

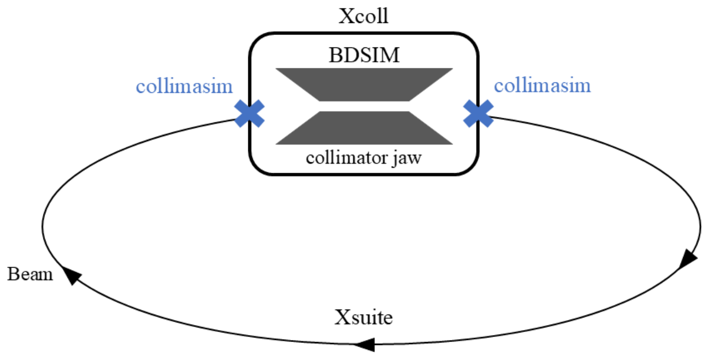

Figure 3.2. Conceptual scheme of the Xsuite–BDSIM coupling simulation framework. During a simulation run, particle tracking through the magnetic lattice is performed by Xsuite. When a collimator region is reached, the particle distribution is passed to BDSIM, which performs a full Monte Carlo simulation of particle–matter interactions. The resulting primary and secondary particles are then transferred back to Xsuite for continued tracking until the next collimator is encountered. The interface between the two codes is provided by the `collimasim` library via the Xcoll module.

Xsuite for further tracking. The BDSIM Monte Carlo model for the collimators consists of individual 3D geometry models (one for each collimator), each enclosed in a box of infinite absorber to eliminate cross-talk, as illustrated in Fig. 3.1. These geometries are generated at run time according to the collimator orientation and opening specified in the input. The schematic of the Xsuite–BDSIM coupling simulation framework is shown in Fig. 3.2, while Fig. 3.3 illustrates the structure of the corresponding software components. The conceptual scheme is similar to the historical SixTrack–FLUKA coupling [96] used in earlier LHC collimation studies.

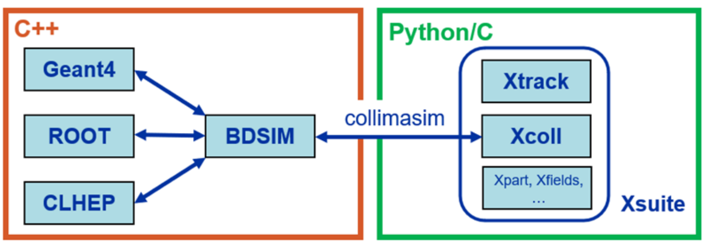

Figure 3.3. Schematic representation of the software components involved in the Xsuite–BDSIM coupling.

For the simulations presented in this thesis, BDSIM is configured with the Geant4 reference physics list `FTFP_BERT`, which is the recommended option for collider physics applications [97]. Collimators are modeled as simple rectangular blocks of material using BDSIM `jcol` elements. These represent two opposing jaws, with the size in the non-collimation plane fixed to the default value of 20 cm, see Fig. 3.1, while the active length in the collimation plane is set according to the jaw under consideration. The surrounding tank and other mechanical details are not included in the collimator geometry, as they are not expected to significantly affect, to first order, the beam–collimator interaction or the resulting loss patterns relevant for this work.

3.4 basf2

For simulations of the signals in the Belle II detector at SuperKEKB, the Belle II Analysis Software Framework (`basf2`) [98, 99] is used. `basf2` is a modular, object-oriented framework developed in C++ with Python bindings, designed to support data processing and analysis for the Belle II experiment. It covers the full data-processing chain of the experiment, including event generation, detector simulation, reconstruction, and user-level analysis. It integrates a wide range of external libraries and tools, offering a flexible and extensible architecture optimized for the high-performance processing of large-scale high-energy physics datasets.

Among its many components, the background module is particularly relevant to the work presented in this thesis. This module enables the estimation of radiation dose rates in the Belle II radiation monitoring system, based on the spatial and kinematic distributions of particle losses in the inner beam pipe. As detailed in Chapter 4, this functionality is instrumental in comparing background levels from beam losses simulated with Xsuite–BDSIM to those measured experimentally by the Belle II detector, thereby supporting the validation of the Xsuite–BDSIM simulation framework for collimation and background studies in electron–positron colliders.

3.5 Simulation developments

3.5.1 Beam-gas scattering routine

As part of this thesis, a simulation routine was developed to model electron/positron beam–residual gas interactions when performing particle tracking in Xsuite [100]. The developed routine implements bremsstrahlung and Coulomb scattering processes using realistic pressure profiles and arbitrary gas mixtures provided as input. For simulations of operating machines, measured pressure profiles can be used as input, while for future machines under design—such as the FCC-ee—simulated profiles derived from vacuum studies with tools like SYNRAD++ and MOLFLOW [101, 102] are employed. The inclusion of this routine in Xsuite–BDSIM tracking simulations allows simultaneous evaluation of beam–gas lifetimes, collimation, and aperture losses.

The core of the implementation is a Python module named `Xgas` [103], which uses a Monte Carlo approach to sample beam–gas interactions during particle tracking. Its main components are:

- `BeamGasManager`: class that initializes the simulation with residual gas data—including atomic densities and gas composition—as well as interaction models; it also manages the tracking logic and handles data logging;
- `BeamGasElement`: Xsuite custom element placed at discrete beamline locations, acting as a lumped scattering center for beam-gas interactions;
- `BremsstrahlungCalculator`: class that contains the bremsstrahlung physics model and implements the corresponding sampling algorithm.
- `CoulombScatteringCalculator`: class that contains the Coulomb scattering physics model and implements the corresponding sampling algorithm.

The physics models (differential cross-sections) for bremsstrahlung and Coulomb scattering are described in Section 2.2.2.

Simulation methodology

When a tracking simulation including beam–residual gas interactions modeled with `Xgas` is performed, the simulation proceeds as follows. For each beam particle that is tracked, a number of mean free paths to the next interaction is sampled from an exponential distribution,

$$n_\lambda = -\ln(\text{random}(0,1)). \tag{3.1}$$

where `random(0,1)` denotes a uniformly distributed random number in the interval $(0,1)$. This expression arises because the probability for a particle to traverse a given distance without interacting decreases exponentially with path length [104]. The corresponding cumulative distribution function (CDF) of the exponential law is

$$F(n_\lambda) = 1 - e^{-n_\lambda}. \tag{3.2}$$

In the inverse transform sampling method, a uniform random variable $u \in (0,1)$ is equated to the CDF, $u = F(n_\lambda)$, and then inverted to obtain

$$n_\lambda = -\ln(u). \tag{3.3}$$

This procedure maps the uniform random variable u into an exponentially distributed one. Expressed in units of mean free paths, n_λ represents a dimensionless measure that can be directly compared to the normalized path length accumulated during tracking.

As particles are tracked through the ring, the normalized traversed path length $n_{\lambda,ij}$ is accumulated as

$$n_{\lambda,ij} = \frac{\Delta s_{ij}}{\lambda_j}, \tag{3.4}$$

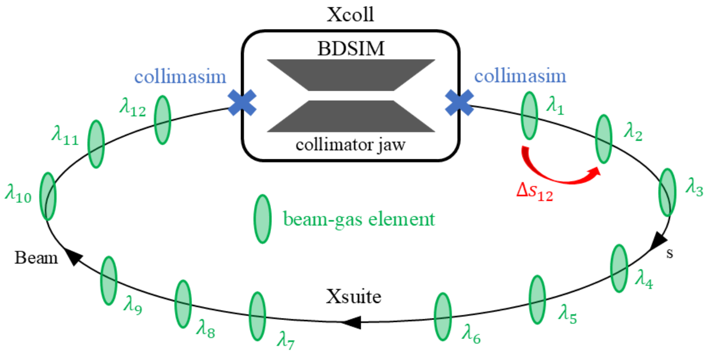

Figure 3.4. Schematic representation of an Xsuite–BDSIM simulation including beam–gas scattering during tracking. Interactions are sampled using a Monte Carlo approach based on the accumulated normalized path length between discrete scattering centers. An interaction is triggered when this accumulated value exceeds a randomly sampled threshold mean free path.

where Δs_{ij} is the path length traversed between beam-gas elements i and j, and

$$\lambda_j = \frac{1}{n_j \sigma_j}, \tag{3.5}$$

is the local mean free path, with n_j the atomic density and σ_j the total cross-section at location j.

If the accumulated normalized path length at the next beam-gas element exceeds n_λ, an interaction is triggered; otherwise, tracking continues and the remaining number of mean free paths is updated as

$$n'_\lambda = n_\lambda - n_{\lambda,ij}. \tag{3.6}$$

Once an interaction is triggered, the gas species and the type of interaction—bremsstrahlung or Coulomb scattering—are selected probabilistically, based on their respective contributions to the total cross-section. The user can choose to include both interaction processes in the simulation or isolate the effect of a specific process by selectively disabling one of them. This flexibility is particularly useful in scenarios where the cross-section of one process significantly exceeds that of the other, causing it to dominate the simulated beam–gas interactions. In such cases, selectively enabling each process in separate simulations can provide clearer insights into the contributions of the less probable interaction.

After determining the interaction type and the gas species involved, the particle's momentum and energy deviation are updated using values sampled from the corresponding differential cross-section, with rejection sampling applied to reproduce the correct distributions.

A schematic representation of an Xsuite–BDSIM simulation including beam–gas scattering is shown in Fig. 3.4. This illustrates the integration of beam–gas interactions into Xsuite tracking.

Since particle accelerators typically operate under ultra-high vacuum (UHV) conditions, the mean free path associated with residual gas in the vacuum chamber can reach extremely large values. As a result, observing a statistically significant number of beam–gas interactions in a tracking simulation would require tracking a particle distribution over an impractically large number of turns, leading to excessive computational demands. Moreover, because the ultimate goal of these simulations is to evaluate beam lifetimes and beam loss patterns resulting from beam–gas interactions, it is not sufficient to merely trigger interactions: a meaningful fraction of these must also lead to actual beam losses.

To address this, a cross-section biasing technique is applied: the cross-sections are scaled by a global biasing factor (BF), such that the average mean free path becomes equal to a target number of machine turns, thereby increasing the interaction probability.

The average mean free path before biasing is computed from the individual mean free paths λ_k of each gas species k, defined as

$$\lambda_k = \frac{1}{\bar{n}_k \, \sigma_k}, \tag{3.7}$$

where $\bar{n}_k$ is the average atomic density of species k, computed as the mean over the machine circumference, and σ_k is its total interaction cross-section. These are combined into a total average mean free path λ_{avg} using the harmonic sum:

$$\frac{1}{\lambda_{\text{avg}}} = \sum_k \frac{1}{\lambda_k}. \tag{3.8}$$

The biasing factor BF is then defined such that the biased mean free path becomes equal to a target number of machine turns (the default value is set to 1):

$$\text{BF} = \frac{\lambda_{\text{avg}}}{L_{\text{target}}}, \tag{3.9}$$

where $L_{\text{target}} = n_{\text{turn}} \cdot C$, with C the machine circumference and n_{turn} the desired mean free path expressed in units of machine turns. Finally, all cross-sections are scaled uniformly by the biasing factor:

$$\sigma_k \to \sigma_k^{\text{biased}} = \text{BF} \cdot \sigma_k. \tag{3.10}$$

This procedure artificially increases the interaction rate in the simulation while maintaining the correct relative contributions of the different gas species and processes.

In practice, beam–gas interactions are enabled only during this first, artificially biased turn. From the second turn onward, they are disabled to study the downstream transport and possible loss of the scattered particles. This approach mimics the single-interaction regime expected under realistic UHV conditions. Additionally, to prevent unphysical multiple interactions introduced by the biasing—given that the likelihood of multiple beam–gas interactions for a single particle in realistic scenarios is extremely low—each particle is restricted to undergo at most one interaction during the simulation.

The true beam lifetime can then be reconstructed from the survival fraction of the tracked particles f_{surv} as:

$$\tau \approx -\frac{T_{\mathrm{rev}} \cdot \mathrm{BF}}{\ln(f_{\mathrm{surv}})}, \tag{3.11}$$

where T_{rev} is the revolution period. This expression is derived under the assumption that beam–gas interactions cause the beam intensity $N(t)$ to decay exponentially with time:

$$\frac{N(t)}{N_0} = f_{\mathrm{surv}}(t) = \exp\left(-\frac{t}{\tau}\right), \tag{3.12}$$

where N_0 is the initial number of particles, t is time, and τ is the beam–gas lifetime. In the biased simulation, the interaction probability is artificially increased, effectively compressing the timescale of the simulation by a factor equal to the biasing factor BF. The simulated time corresponds to $T_{\mathrm{rev}} \cdot \mathrm{BF}$, and the survival fraction $f_{\mathrm{surv}} = N(t)/N_0$ observed at the end of the simulation is used in Eq. (3.11) to recover the true (unbiased) beam lifetime.

In addition to cross-section biasing, a further strategy is applied to enhance simulation efficiency by increasing the fraction of beam–gas interactions that result in actual particle losses. Specifically, the sampling of energy deviations (for bremsstrahlung) and scattering angles (for Coulomb scattering) is restricted to ranges where the resulting perturbations are likely to exceed the machine's acceptance limits. For example, bremsstrahlung events causing only minimal energy loss—well within the momentum acceptance—are unlikely to lead to particle losses and can be omitted. Similarly, Coulomb scattering events producing very small angular deflections have negligible impact on particle trajectories and may be excluded.

To maintain physical accuracy, when applying these restrictions, the total cross-section is computed by integrating the differential cross-section over the selected interval of energy deviations or scattering angles. This total cross-section is then used to determine the interaction probability and mean free path, ensuring consistency in the Monte Carlo simulation.

To further mitigate artifacts introduced by the artificial biasing—specifically the tendency of interactions to cluster near a common initial tracking location—the simulation is divided into multiple parallel runs. In each run, the tracking starting point is randomly assigned to one of the inserted beam–gas scattering centers. This randomization ensures uniform spatial sampling of interaction points along the ring and leads to more accurate estimates of beam loss distribution.

Suitable cutoffs for energy and angle can be initially estimated based on the machine's momentum acceptance and dynamic aperture. These values can then be refined through simulation scans over different threshold parameters, identifying the point at which the number of simulated beam-gas-induced losses saturates—indicating that all loss-inducing interactions are being captured.

Interaction events and their locations can be logged element-wise and saved to dedicated output called beam-gas logs for offline analysis.

The modular structure of the implementation facilitates future extensions, such as incorporating dynamic vacuum models or adding other beam–gas interaction processes.

3.5.2 Touschek scattering routine

As will be discussed in more detail in Chapter 4, an essential aspect in the development and application of novel simulation tools—such as the Xsuite–BDSIM framework used in this work—is their validation against existing codes and, most importantly, experimental data. Since the FCC-ee is an electron–positron collider, the most relevant benchmarking opportunities arise from comparisons with data from presently operating e^+e^- machines, such as SuperKEKB. In the context of collimation and beam-loss simulations, typical observables available for comparison include measured beam lifetimes and beam-induced background levels in the experimental detectors.

However, a key difference between the FCC-ee and current e^+e^- colliders lies in the beam energy: while the FCC-ee is designed for beam energies between 45.6 GeV and 182.5 GeV, SuperKEKB operates at significantly lower energies (4–7 GeV). At these lower energies, Touschek scattering is typically the dominant mechanism limiting the beam lifetime, in contrast to higher-energy machines where Touschek losses are suppressed and other processes prevail.

Therefore, to enable meaningful benchmarking of collimation and beam-loss simulations against experimental data from presently operating low-energy e^+e^- machines such as SuperKEKB, it is necessary to model Touschek scattering and the resulting particle losses accurately. This requirement motivated the development of a dedicated Touschek-scattering routine, carried out as part of this thesis, for use in Xsuite-based simulations.

The implementation of the Touschek–scattering routine developed in this work is organized into the following components:

- `TouschekManager`: Python class that serves as the main controller for the Touschek–scattering simulation. It validates input parameters (e.g., Twiss and momentum-aperture tables, beam parameters), configures `TouschekScattering` elements (see below), and orchestrates the full beamline setup.
- `TouschekCalculator`: Python class that provides the physics back-end for computing Touschek–scattering rates via the Piwinski formula (see Eq. (2.46)).
- `TouschekScattering`: Xtrack beam element (hybrid Python/C structure) that acts as the Monte Carlo generator and selector for Touschek-scattered particles.

Simulation methodology

The implementation of the Touschek scattering routine is based on the approach by Xiao and Borland [61, 105], originally developed for the ELEGANT [106] beam dynamics code. This method uses a Monte Carlo sampling scheme combined with the Piwinski formalism to evaluate the Touschek scattering rate and to generate the kinematic parameters of the scattered particles. In this thesis, their procedure is re-implemented within an Xsuite-based framework. To ensure reproducible benchmarking against ELEGANT, the Monte Carlo draws use an ELEGANT-like random number generator that reproduces the same random streams, initialized from a user-provided integer seed.

In the simulation routine, the integral expression for the Touschek scattering rate (see Eq. (2.45)) is evaluated using the general Monte Carlo approximation of an integral of a function $f(\vec{x})$, in which N events are randomly sampled from the phase-space volume V:

$$\int_V f(\vec{x})\, d\vec{x} \approx \frac{V}{N} \sum_{i=1}^{N} f(\vec{x}_i). \tag{3.13}$$

Using this technique, the Touschek scattering rate for particles with momentum deviation $|\delta| = |\Delta P/P_0|$ greater than a threshold δ_m can be computed as [106, 105]:

$$R_{\mathrm{MC}}(|\delta| > \delta_m) = \frac{V}{N} \sum_{i=1}^{M} \left[\frac{v^*}{\gamma^2} \frac{d\sigma^*}{d\Omega^*} \sin\Theta^* \rho(\vec{x}_1)\rho(\vec{x}_2) \right]_i = \sum_{i=1}^{M} r_i, \tag{3.14}$$

where V is the total sampled (11-dimensional) phase-space volume, N is the total number of simulated scattering events, and M is the number of scattered particles with $|\delta| > \delta_m$.[1] The quantities with asterisks refer to the center-of-mass frame: v^* is the particle velocity, Θ^* is the scattering angle, and $d\sigma^*/d\Omega^*$ is the Møller differential cross-section (see Eq. (2.40)). The Lorentz factor is denoted by γ, and $\rho(\vec{x}_1)$ and $\rho(\vec{x}_2)$ are the phase-space densities of the interacting particles. The term r_i represents the contribution to the total rate from the i-th scattering particle with $|\delta| > \delta_m$.

For sufficiently large N, the Monte Carlo result converges to the true scattering rate.

When the threshold δ_m is set equal to the local momentum acceptance δ_a, Eq. (3.14) gives the Touschek beam loss rate.

Monte Carlo integration is applied by generating a series of random scattering events, each involving a pair of particles sampled from the bunch distribution.

The sampling is performed in normalized phase space, under the assumption of a Gaussian-distributed bunch and in absence of X-Y coupling. In this space,

[1] A scattering event can generate one or two particles with $|\delta| > \delta_m$; in Eq. (3.14), each particle with $|\delta| > \delta_m$ is counted individually.

nine uniformly distributed random numbers are drawn within the following intervals:

- $[-n_x\sqrt{\varepsilon_x},\, n_x\sqrt{\varepsilon_x}]$: two values assigned to the normalized horizontal position X_1 and slope X_1' of particle 1;
- $[-n_y\sqrt{\varepsilon_y},\, n_y\sqrt{\varepsilon_y}]$: two values assigned to the normalized vertical position Y_1 and slope Y_1' of particle 1;
- $[-n_z\sqrt{\varepsilon_z},\, n_z\sqrt{\varepsilon_z}]$: two values assigned to the normalized longitudinal coordinate Z_1 and relative momentum deviation $\delta_1 = \Delta p_1/p_0$ of particle 1.

Here, n_x, n_y and n_z are user-defined parameters that determine the phase-space region from which the coordinates of the scattering particles are sampled. The default values are

$$n_x = n_y = n_z = 3,$$

meaning the sampling extends up to three beam sigmas from the beam core. The parameters ε_x, ε_y, and ε_z denote the horizontal, vertical, and longitudinal geometric emittances, respectively.

In total, this provides the 6D normalized coordinates $(X_1, X_1', Y_1, Y_1', Z_1, \delta_1)$ of the first scattering particle.

Then, three additional uniformly distributed random numbers are generated:

- one in $[-n_x\sqrt{\varepsilon_x},\, n_x\sqrt{\varepsilon_x}]$ assigned to X_2';
- one in $[-n_y\sqrt{\varepsilon_y},\, n_y\sqrt{\varepsilon_y}]$ assigned to Y_2';
- one in $[-n_z\sqrt{\varepsilon_z},\, n_z\sqrt{\varepsilon_z}]$ assigned to δ_2.

The spatial coordinates of the second particle are assumed to match those of the first, since they are assumed to scatter at the same point:

$$x_2 = x_1, \quad y_2 = y_1, \quad z_2 = z_1.$$

At this stage, applying the relations that map between normalized and real phase-space coordinates (see Eq. (2.4)), and including dispersive effects, yields

$$\textbf{Particle 1}\ \begin{cases} x_1 = \sqrt{\beta_x}\, X_1 + \delta_1 D_x, \\ x_1' = \dfrac{X_1' - \alpha_x X_1}{\sqrt{\beta_x}} + \delta_1 D_x', \\ y_1 = \sqrt{\beta_y}\, Y_1 + \delta_1 D_y, \\ y_1' = \dfrac{Y_1' - \alpha_y Y_1}{\sqrt{\beta_y}} + \delta_1 D_y'. \end{cases}$$

$$\textbf{Particle 2} \begin{cases} X_2 = \dfrac{x_1 - \delta_2 D_x}{\sqrt{\beta_x}}, \\ x'_2 = \dfrac{X'_2 - \alpha_x X_2}{\sqrt{\beta_x}} + \delta_2 D'_x, \\ Y_2 = \dfrac{y_1 - \delta_2 D_y}{\sqrt{\beta_y}}, \\ y'_2 = \dfrac{Y'_2 - \alpha_y Y_2}{\sqrt{\beta_y}} + \delta_2 D'_y. \end{cases}$$

where β_x, β_y are the horizontal and vertical beta functions, α_x, α_y are the corresponding Twiss alpha functions, and D_x, D_y and D'_x, D'_y are the horizontal and vertical dispersion functions and their derivatives, respectively.

After this step, a complete set of phase-space coordinates for each of the two scattering particles has been defined, namely $(x, y, z, x'_1, y'_1, \delta_1, x'_2, y'_2, \delta_2)$.

Although the procedure has been described for a single scattering event, the same approach is applied to generate an arbitrary number of events in the simulation.

With these information, the (Gaussian) phase-space density ρ for each of the scattering particles can be computed as

$$\rho = \frac{N_p}{8\pi^3 \varepsilon_x \varepsilon_y \varepsilon_z} \exp\left(-\frac{z^2}{2\sigma_z^2} - \frac{\delta^2}{2\sigma_\delta^2}\right) \times \exp\left(-\frac{x_\beta^2 + (\alpha_x x_\beta + \beta_x x'_\beta)^2}{2\sigma_{\beta,x}^2} - \frac{y_\beta^2 + (\alpha_y y_\beta + \beta_y y'_\beta)^2}{2\sigma_{\beta,y}^2}\right), \quad (3.15)$$

where the terms x_β, x'_β, y_β, and y'_β represent the betatron components of the transverse positions and slopes (i.e., with the dispersive contributions removed), and $\sigma_{\beta,x}$, $\sigma_{\beta,y}$, σ_z, and σ_δ are the respective RMS beam sizes, bunch length and energy spread.

To simulate the scattering process, two additional random numbers are generated: one uniformly in the interval $(0, \pi/2]$ to define the polar scattering angle Θ^*, and another in $[0, 2\pi]$ for the azimuthal angle Ψ^*, both in the center-of-mass (c.m.) frame. Using these angles, the corresponding Møller differential cross-section is computed.

The phase-space volume V from which the events are sampled—appearing in Eq. (3.14)—is evaluated as:

$$V = \frac{\pi^2}{\sqrt{\beta_x \beta_y \beta_z}} \cdot (2n_x\sqrt{\varepsilon_x})^3 \left(2n_y\sqrt{\varepsilon_y}\right)^3 (2n_z\sqrt{\varepsilon_z})^3 \quad (3.16)$$

Next, the scattering is applied to all generated particle pairs. To correctly simulate the relativistic kinematics of the scattering process, each particle pair is transformed from the laboratory frame to its center-of-mass frame using a Lorentz boost. In this frame, the polar and azimuthal scattering angles Θ^* and Ψ^* are sampled, and the particle momenta are rotated accordingly. The resulting

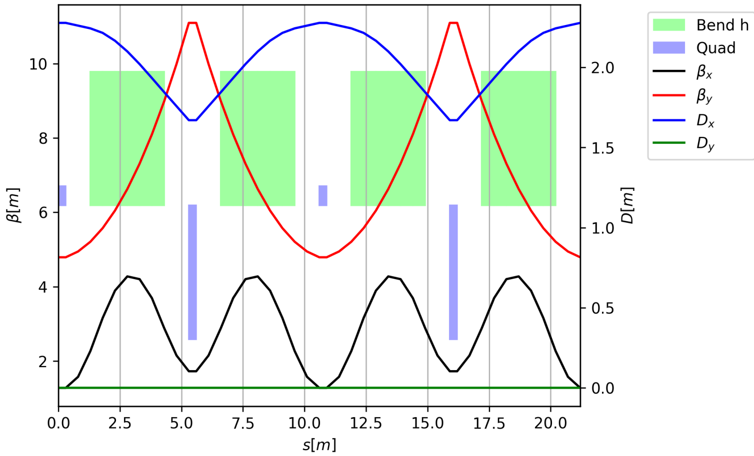

Figure 3.5. Layout and optics for the 21.2 m circumference toy ring available among the Xsuite example beam lines.

post-scattering momenta are then transformed back to the laboratory frame. This ensures full conservation of momentum and energy for each scattering event, and provides a correct treatment of the (relativistic) effect.

After scattering, the new phase-space coordinates of the particles in the lab frame are available. If either particle's final momentum deviation—i.e., $|\delta_1|$ or $|\delta_2|$—exceeds a user-defined threshold δ_m, then the particle and its associated scattering rate contribution r_i are recorded for further processing. This threshold δ_m serves as a lower bound on momentum deviation, below which particle losses are not expected to occur in tracking simulations.

By repeating this process for a large number of samples, the Monte Carlo integration of Eq. (3.14) converges to a stable estimate of the Touschek scattering rate for events with $|\delta| > \delta_m$.

Similarly to what was done in Ref. [61], to verify the accuracy of the Monte Carlo scattering rate simulation, both the Piwinski formula and the Monte Carlo routine were applied to a *toy ring* available among the Xsuite example beam lines, assuming a Gaussian-distributed beam. Figure 3.5 shows the optical functions and layout of the toy ring and Fig. 3.6 the local Touschek scattering rate computed with the Piwinski formula and with the Monte Carlo routine for an electron bunch with population of 4×10^9 particles per bunch, transverse emittances of $\epsilon_x = 10$ nm (horizontal) and $\epsilon_y = 0.1$ nm (vertical), an RMS bunch length $\sigma_z = 4$ mm, and an RMS energy spread $\sigma_\delta = 0.01\%$. As seen from the plot, the agreement between the Piwinski formula and the Monte Carlo result is excellent.

The comparison of Touschek lifetimes predicted by the Piwinski formula with experimental data has been extensively validated in the literature. Since the Monte Carlo simulation implemented here shows excellent agreement with

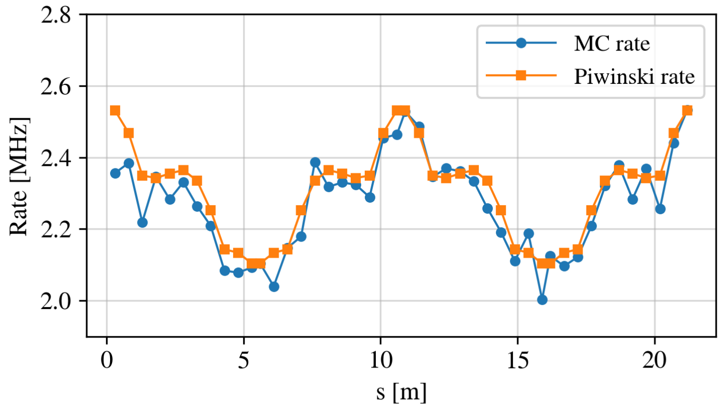

Figure 3.6. Comparison between local Touschek scattering rates obtained via the Piwinski formula and Monte Carlo simulation. The level of agreement improves with increasing the number of simulated scattering events N; for the case shown here, $M = 2 \times 10^7$ events were simulated at each scattering location. Reliable convergence is typically achieved for $M \gtrsim 5 \times 10^6$.

the Piwinski method, it is therefore expected to achieve a comparable level of agreement with the experimental measurements reported in those studies.

The simulation of beam losses from Touschek scattering in Xsuite is carried out in several steps, as illustrated in Fig. 3.7.

A lumped-element approach is used to model beam loss. The accelerator lattice is divided into a series of small segments, by placing `TouschekScattering` elements at different locations. The number and spacing of these elements should be chosen such that the optical functions vary slowly between adjacent elements.

At each `TouschekScattering` element, the distribution of scattered particles is sampled using the Monte Carlo procedure described above. The scattered particles are then tracked from the position of the corresponding `TouschekScattering` element. The scattering rate associated with each of these particles is scaled according to the total scattering rate integrated over the section between the current and the previous `TouschekScattering` element.

In the tracking phase, we are only interested in scattered particles with momentum deviation $|\delta| > \delta_m$, where δ_m is defined as a user-specified threshold smaller than the local momentum acceptance δ_a. By choosing $\delta_m < \delta_a$ (typically with a safety factor of 0.8–0.9), we ensure that particles with nonzero betatron amplitudes—which can be lost at smaller momentum deviations than the on-orbit acceptance—are also taken into account, so that potentially lost particles are not missed.

To accurately study beam losses from Touschek scattering, the local momentum acceptance $\delta_a(s)$ must first be estimated using Xsuite tracking simulations. At arbitrary reference locations s, a set of test particles is generated on the closed orbit with varying momentum deviations δ. These particles are then

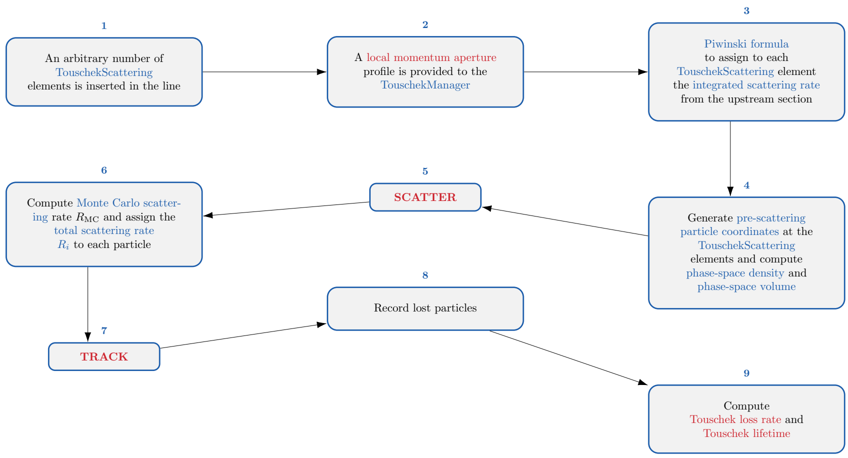

Figure 3.7. Workflow of Touschek scattering beam loss simulation using Xsuite.

tracked for a fixed number of turns—typically of the order of 1000—to evaluate their long-term stability. The largest momentum deviation for which a particle remains stable throughout the tracking is recorded as the local momentum aperture δ_a at location s. Figure 3.8 illustrates the resulting momentum aperture profile along the SuperKEKB LER lattice used for the studies presented in Chapter 4. The threshold δ_m is subsequently defined as a fraction $a_0\delta_a$, where $a_0 < 1$ is a safety factor set by the user to avoid underestimating beam losses.

While the local scattering rate could be calculated using Monte Carlo integration, doing so for the entire machine would be computationally expensive. Instead, Piwinski formula is used to rapidly estimate the total Touschek scattering rate R_P over each lattice section. This is then used to normalize and scale the Monte Carlo-generated scattered particle distributions at the `TouschekScattering` elements.

Each scattered particle generated at a given `TouschekScattering` element and associated with a local rate contribution r_i (as defined in Eq. (3.14)) is assigned a total scattering rate weight R_i as follows:

$$R_i = \frac{r_i}{\sum r_i} \cdot \int R_{\mathrm{P}}, \tag{3.17}$$

where R_{P} is the local Touschek scattering rate calculated via Piwinski formula, and the integral is taken over the upstream section between the current and previous `TouschekScattering` element.

In this way, the ensemble of scattered particles at each `TouschekScattering` accurately represents the total scattering rate originating from the corresponding section of the accelerator. The full beam-loss profile is then obtained by tracking all scattered particles through the machine and recording the locations at which

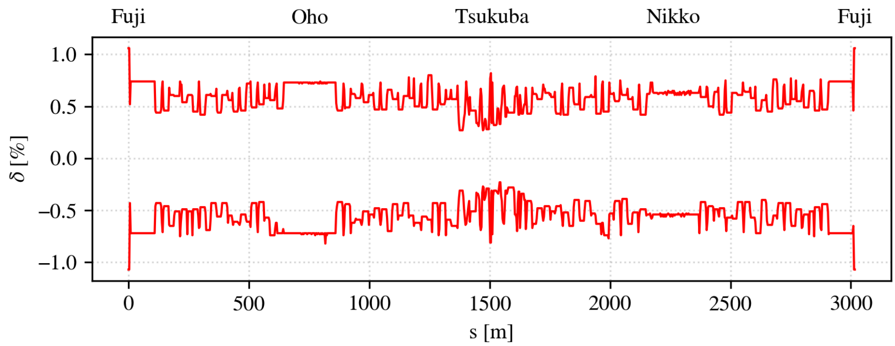

Figure 3.8. Local momentum acceptance δ_a along the SuperKEKB LER ring (2020-06-23_1.2A_0.8x60_nb_1576_cw_80) obtained with Xsuite tracking.

they are lost. The total beam loss rate is finally obtained as the sum of all R_i corresponding to lost particles.

The Touschek lifetime τ_T can then be computed from the total bunch population N_b and the total beam loss rate $\sum R_i$ as

$$\tau_T = \frac{N_b}{\sum R_i}. \tag{3.18}$$

As noted in Ref. [61], obtaining a reliable estimate of the scattering rate requires a large number of Monte Carlo events, typically $M \gtrsim 5 \times 10^6$. In addition, the accelerator lattice must be divided into a sufficiently large number of sections, N_s, to accurately resolve the spatial variation of the beam optics. As a result, the total number of particles that must be tracked scales with $M \times N_s$, which can lead to substantial computational demands.

To address this challenge, the same simulation speed-up strategy proposed in Ref. [61] is adopted. Since only a small subset of the simulated scattering events contributes the majority of the total scattering rate—while many low-weight events represent rare, low-probability interactions—an efficient approach is to track only the most significant particles. In practice only the highest-weight subset that accumulates a fraction $1 -$ `ignored_portion` of the total simulated weight at each `TouschekScattering` is retained, with `ignored_portion` $= 0.01$ by default (i.e. keep 99%). This method provides a good accuracy–efficiency trade-off [61].

As part of the development and validation of the Touschek scattering routine, dedicated simulations were performed on the toy ring introduced earlier using both Xsuite and ELEGANT. The results obtained with the two codes were found to be in excellent agreement in terms of the computed local momentum acceptance profiles, Touschek lifetimes, and spatial distributions of Touschek losses. This consistency provides strong validation of the implementation of the routine within the Xsuite framework carried out in this work.

Chapter 4

Simulation tool benchmark

As presented in the previous chapter, the Xsuite–BDSIM coupling was originally developed to address the FCC-ee collimation simulation needs. Given the novelty of this simulation framework, a key aspect is its validation against experimental data. This chapter presents the first benchmarking of Xsuite–BDSIM collimation and beam loss simulations against measurements from an operating e^+e^- collider: SuperKEKB.

SuperKEKB is an ideal testbed for this purpose, as it shares several relevant features with the FCC-ee design, including operation at high beam currents sustained by continuous top-up injection, an ultra-low emittance regime, and the implementation of a crab-waist collision scheme.

The results presented in this chapter aim to assess the reliability and predictive capabilities of the Xsuite–BDSIM framework for collimation and background studies in electron–positron colliders. In addition, a complementary benchmark with measured beam loss patterns at the Large Hadron Collider (LHC) is also presented at the end of this chapter.

4.1 Benchmark with measured backgrounds at SuperKEKB

At SuperKEKB, beam losses are a major challenge for the Belle II detector, as they can cause backgrounds that degrade detector performance, trigger beam aborts, or even damage sensitive components. To mitigate them, SuperKEKB employs movable collimators that intercept halo particles before they reach the interaction region (IR). Radiation levels in the IR are monitored by dedicated detectors integrated into Belle II. These measurements provide continuous diagnostics and enable correlation studies between background levels and machine conditions.

Beam-induced background simulations are essential to predict background levels and ensure safe operation as the collider approaches its luminosity goal. At SuperKEKB, beam-induced background simulations are historically performed using the SAD [107] tracking code, with the inclusion of Geant4-parametrized collimator interactions. This approach has shown excellent agreement with experimental data from dedicated background studies [108, 109].

As part of this thesis, the Xsuite–BDSIM simulation framework has been benchmarked against background measurements carried out at SuperKEKB/Belle II in June 2020 [108, 110]. In particular, simulated and measured dose rates were compared at one of the IR diamond radiation monitors during a vertical collimator scan in the LER. This study represents the first ever validation of Xsuite-based simulations for collimation and background modeling at a lepton collider.

In this benchmark we target single-beam losses in the SuperKEKB LER (positron ring) under the June 2020 conditions. In Xsuite, the dominant beam loss sources are modeled as (i) particles scattered on residual gas (Coulomb and bremsstrahlung) and (ii) final-state positrons from Touschek scattering. These primaries are then tracked for multiple turns through the full nonlinear lattice, with particle–matter interactions in the collimators simulated in BDSIM/Geant4. A limitation of the experimental configuration is the absence of ring-wide beam loss monitors; therefore, the comparison is performed at Belle II only using highly sensitive radiation monitors in the interaction region, where beam-induced backgrounds provide a precise proxy for local losses. This makes the study directly relevant for validating the end-to-end Xsuite–BDSIM prediction chain used for collimation and background modeling.

4.1.1 SuperKEKB beam-induced backgrounds

The primary single-beam background sources relevant to this study are Touschek and beam–gas scattering [108, 109]. These processes generate off-momentum or large-amplitude particles that deviate from the nominal orbit, forming a beam halo. When these halo particles interact with the machine aperture—such as collimators or vacuum chamber walls—they produce secondary particles that can propagate toward the interaction region and contribute to detector backgrounds. These background-inducing particles not only increase detector occupancy but can also degrade sensor performance over time due to accumulated radiation dose and neutron fluence, particularly in subsystems like the silicon vertex detectors.

SuperKEKB operates with significantly higher beam currents and much smaller vertical emittances than its predecessor KEKB, resulting in an overall increase in beam-induced backgrounds. Touschek scattering becomes particularly significant due to the ultra-low vertical emittance. The Touschek scattering rate scales with the square of the beam current and is inversely proportional to the number of bunches and the transverse beam size, making it especially relevant in the high-current, low-emittance regime of SuperKEKB. To mitigate its impact near the interaction region, dedicated horizontal collimators have been installed close to the IR to intercept Touschek-scattered particles before they reach Belle II.

Beam–gas scattering remains a major background source due to interactions

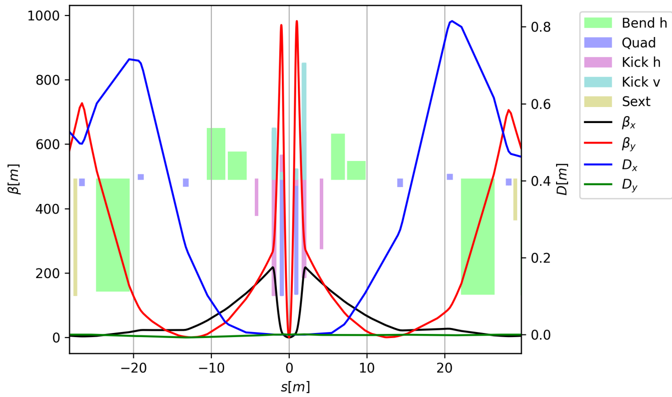

Figure 4.1. SuperKEKB LER interaction region optics and layout.

with residual gas molecules in the vacuum chamber. In particular, Coulomb scattering events may lead to vertical beam losses in the IR because of the large vertical beta functions near the final focus quadrupoles, see Fig. 4.1. Although vacuum scrubbing reduces overall pressure, beam–gas backgrounds are still relevant for background studies, especially under less-than-ideal vacuum conditions.

To mitigate these effects, SuperKEKB employs several background suppression strategies. Movable collimators are used to intercept halo particles upstream of the detector region in both the LER and HER, as described in more detail in Section 4.1.2. Vacuum scrubbing is employed to reduce residual gas pressure and thus suppress beam–gas interactions.

In addition to active collimation, extensive passive shielding is installed to protect the Belle II detector from secondary showers. Tungsten shields are mounted around the final focusing quadrupoles (QCS), where beam losses are expected to be most severe due to the high beta functions. Additional tungsten shielding is positioned just outside the interaction point beam pipe and inside the vertex detector, placed outside the acceptance region for physics signals to avoid interference with measurements.

Synchrotron radiation (SR) backgrounds, while not the focus of this work, are also addressed through dedicated engineering measures. The IP beam pipe, whose profile for the Low-Energy positron Ring is shown in Fig. 4.8, is carefully shaped to prevent upstream SR from striking the central beryllium section. A tapered collimation section and ridge structures on the beam pipe surface effectively stop or deflect both direct and reflected SR. Moreover, the use of separate QCS magnets for each ring in SuperKEKB—unlike the shared magnet scheme at KEKB—reduces SR backscattering from outgoing beam orbits by allowing nearly straight beam trajectories through the IR.

Other background mechanisms, such as injection-related losses, may con-

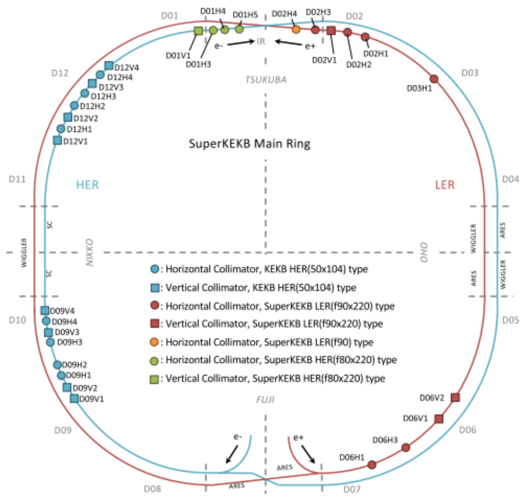

Figure 4.2. SuperKEKB collimator layout as of June 2020 [108].

tribute during top-up cycles but are not considered here, as this work focuses on steady-state single-beam operation. Similarly, two-beam processes like radiative Bhabha scattering are excluded, as they only occur during collisions.

Accordingly, this study focuses exclusively on Touschek and beam–gas scattering as the dominant sources of single-beam backgrounds under the relevant operating conditions.

4.1.2 SuperKEKB collimation

This section provides an overview of the SuperKEKB collimation system as it was configured in June 2020, corresponding to the period during which the experimental study presented in this chapter was conducted. A comprehensive and up-to-date description of the SuperKEKB collimation system, including more recent upgrades, can be found in Refs. [21, 111].

The SuperKEKB collimation system [29] is designed to intercept beam halo particles before they reach the interaction region (IR), thereby reducing beam-induced backgrounds and protecting sensitive detector components. Each ring is divided into twelve sections (D01–D12), and hosts a set of movable collimators placed at high-beta locations. The placement is chosen based on their phase advance relative to the IR to ensure optimal cleaning efficiency.

As of June 2020, the High Energy Ring (HER) and Low Energy Ring (LER) were equipped with 20 and 10 collimators, respectively, as illustrated in Fig. 4.2. All LER collimators are of the newer SuperKEKB type, while all HER collimators are inherited from KEKB. A summary of the collimator specifications for the LER and HER is provided in Tables 4.1 and 4.2, respectively.

SuperKEKB-type collimators feature two movable jaws made of copper, with high-Z tips made from tungsten (W) or tantalum (Ta), depending on

Table 4.1. SuperKEKB LER collimator types and specifications (as of June 2020).

Name	Type	Orientation	Bulk material	Tip material	Tip length [mm]
D06H1	SuperKEKB	Hor.	Cu	W	10.0
D06H3	SuperKEKB	Hor.	Cu	W	10.0
D06V1	SuperKEKB	Ver.	Cu	Ta	5.0
D06V2	SuperKEKB	Ver.	Cu	Ta	5.0
D03H1	SuperKEKB	Hor.	Cu	W	5.0
D02H1	SuperKEKB	Hor.	Cu	W	5.0
D02H2	SuperKEKB	Hor.	Cu	W	5.0
D02V1	SuperKEKB	Ver.	Cu	W	5.0
D02H3	SuperKEKB	Hor.	Cu	W	10.0
D03H4	SuperKEKB	Hor.	Cu	W	10.0

Table 4.2. SuperKEKB HER collimator types and specifications (as of June 2020).

Name	Type	Orientation	Bulk material	Tip material	Tip length [mm]
D09V1	KEKB	Ver.	Al	Ti	40.0
D09V2	KEKB	Ver.	Al	Ti	40.0
D09H1	KEKB	Hor.	Cu	Ti	80.0
D09H2	KEKB	Hor.	Cu	Ti	80.0
D09H3	KEKB	Hor.	Cu	Ti	80.0
D09V3	KEKB	Ver.	Al	Ti	40.0
D09H4	KEKB	Hor.	Cu	Ti	80.0
D09V4	KEKB	Ver.	Cu	Ti	40.0
D12V1	KEKB	Ver.	Cu	Ti	40.0
D12H1	KEKB	Hor.	Cu	Ti	80.0
D12V2	KEKB	Ver.	Cu	Ti	40.0
D12H2	KEKB	Hor.	Cu	Ti	80.0
D12H3	KEKB	Hor.	Cu	Ti	80.0
D12V3	KEKB	Ver.	Cu	Ti	40.0
D12H4	KEKB	Hor.	Cu	Ti	80.0
D12V4	KEKB	Ver.	Cu	Ti	40.0

the specific device. These tips typically have a length of 10 mm, although shorter tips are also used in certain cases. For instance, the LER vertical collimator D06V1—central to this study—was installed during the 2019–2020 winter shutdown and features a 5 mm Ta tip. A schematic overview of the SuperKEKB-type collimator layout and jaw geometry is shown in Fig. 4.3.

In contrast, the KEKB-type collimators used in the HER consist of a single movable jaw, typically with a longer tip (up to 80 mm) made of titanium (Ti). The bulk jaw material varies depending on the orientation: aluminum (Al) is used for vertical collimators, and copper (Cu) for horizontal ones. Their design is illustrated in Fig. 4.4.

Each jaw is mounted within a dedicated collimator vacuum chamber and can be positioned with sub-100 µm precision via motorized actuators. However, the mechanical alignment between the collimator chamber and the beamline reference—typically defined by the nearest quadrupole magnet—can vary significantly. Alignment uncertainties are estimated to range from 200–500 µm

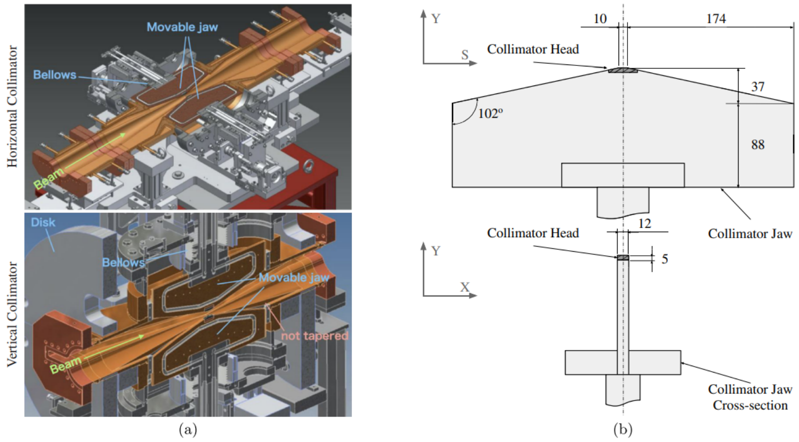

Figure 4.3. SuperKEKB-type collimators. (a) Conceptual drawing of the collimator assembly for horizontal and vertical configurations. (b) Schematic of a SuperKEKB-type collimator jaw with a 10 mm long high-Z tip. All dimensions are in mm. Figure adapted from [108].

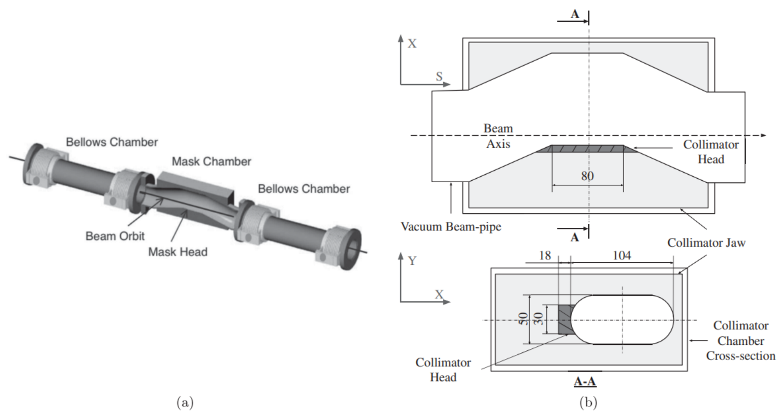

Figure 4.4. KEKB-type collimators. (a) Conceptual drawing of a KEKB-type collimator assembly. (b) Schematic of a horizontal KEKB-type collimator chamber with an 80 mm long Ti head. All dimensions are in mm. Figure adapted from [108].

for vertical SuperKEKB-type collimators and from 500–1000 µm for horizontal SuperKEKB-type and all KEKB-type devices. This can result in a notable offset between the actual beam center and the nominal collimator position.

Collimator settings are carefully tuned during dedicated machine studies, during which the jaws can be incrementally moved inward to probe their influence on beam lifetime, radiation monitors, and detector backgrounds. For this purpose, dose rate monitors—such as diamond sensors positioned around the IR beam pipe—provide direct observables for benchmarking beam loss simulations.

Horizontal and vertical collimators serve distinct purposes. Horizontal collimators are particularly effective at intercepting Touschek-scattered particles, while vertical collimators primarily mitigate beam–gas Coulomb scattering. The vertical collimators must often be closed down to apertures of the order of 1 mm, requiring high-precision actuation and control.

However, such narrow apertures introduce significant impedance contributions to the machine, which can trigger collective instabilities. In particular, the Transverse Mode Coupling Instability (TMCI) sets an upper threshold on the bunch current [108]. This imposes a constraint on how tightly collimator jaws can be closed.

As a result, the collimation system must balance multiple operational constraints: tighter settings improve halo interception and reduce IR backgrounds, but at the cost of reduced beam lifetime, lower injection efficiency, and potential stability issues. Wider settings alleviate these constraints but reduce collimation effectiveness. Since SuperKEKB uses continuous top-up injection, high injection efficiency is essential to minimize trigger veto dead time in Belle II. Consequently, collimator optimization involves empirical tuning informed by measured background rates, injection performance, and loss monitor signals.

4.1.3 SuperKEKB background study

On June 27, 2020, a dedicated single-beam background study was conducted at SuperKEKB to validate simulation tools for beam loss and background predictions [108]. The study involved a stepwise scan of the vertical collimator D06V1 in the LER (e^+ ring), while recording radiation dose rates at selected Belle II radiation monitors.

D06V1 had been installed earlier that year, during the 2019–2020 winter shutdown, and was specifically designed to intercept beam–gas-scattered particles in the vertical plane before they could reach the interaction region. At the time of the study, it featured a tantalum (Ta) head with a 5 mm long tip (see Table 4.1). The collimator was chosen for this experiment because it was expected to suppress the dominant IR background contribution from vertical beam–gas Coulomb scattering in the LER.

During the scan, the D06V1 jaw position was varied symmetrically in discrete steps, and radiation levels were recorded by the diamond detector named QCS-FW, located at +56.8 cm from the interaction point (IP) in the forward direction of the positron beam. This detector is positioned near the final focusing quadrupole QCS, a region characterized by large vertical beta functions, and is highly sensitive to losses caused by off-momentum or missteered particles.

To protect Belle II detector subsystems during the aperture manipulation, high voltage was turned off in all sub-detectors. This ensured that background measurements could be safely acquired without risking damage to sensitive electronics.

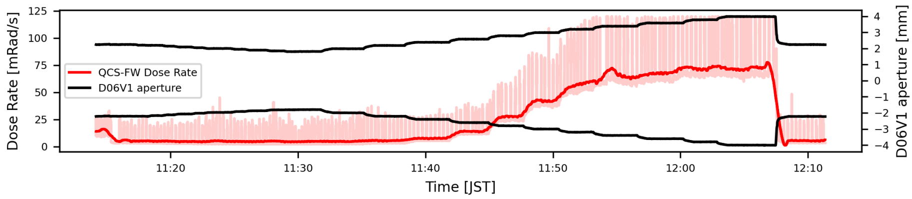

Figure 4.5. Measured dose rate at the QCS-FW diamond detector during the June 27, 2020 SuperKEKB LER background study, shown as a function of time and overlaid with the D06V1 collimator aperture. The raw dose rate (light red) is displayed alongside a smoothed trend (solid red).

The evolution of the D06V1 aperture and the corresponding QCS-FW dose rate are shown in Fig. 4.5. The plotted data highlight the correlation between vertical collimator settings and measured background levels in the IR, offering a clear benchmark for validating simulation predictions.

The main beam and machine parameters from measurements taken during the study are summarized in Table 4.3.

Table 4.3. SuperKEKB LER beam and machine parameters during the June 27, 2020 background study [108].

Parameter	**Value**
Beam momentum p	4.0 GeV/c
Beam current I	200 mA
Number of bunches N_b	978
Horizontal emittance ε_x	3.3 nm
Vertical emittance ε_y	22 pm
Bunch length σ_z	5.0 mm
Inj. rep.	12.5 Hz
Hor./Ver. Tune Q_x/Q_y	45.525/43.581

4.1.4 Simulation setup

In this study, Xsuite–BDSIM was used to simulate beam losses at SuperKEKB/Belle II. Touschek and beam–gas scattering were modeled using the dedicated routines developed as part of this thesis, as described in Chapter 3.

To reproduce the June 2020 background study in simulation, the first step involved converting the lattice description from SAD (native to SuperKEKB) to Xsuite. This required a careful optics rematching strategy to account for the native differences between the two frameworks. Details on this conversion procedure and on achieving consistent lattice representation across optics codes can be found in Refs. [112, 113].

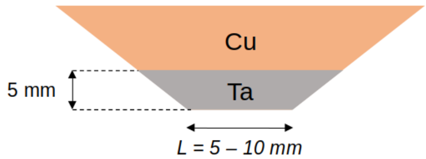

(a)

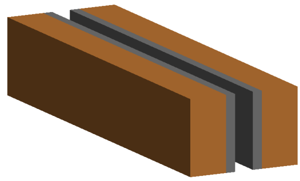

(b)

Figure 4.6. (a) Schematic layout of a jaw of a SuperKEKB-type collimator, consisting of a copper body with a short high-Z tip made of tantalum (Ta) or tungsten (W), typically 5–10 mm in length. (b) View of the CollimatorTipJaw element ("jcoltip") implemented in BDSIM, used to realistically reproduce the two-material structure of SuperKEKB-type collimators in simulation.

Accurate modeling of the LER SuperKEKB-type collimators was also essential. A new collimator geometry ("jcoltip") was implemented in BDSIM to reproduce the two-material structure of these devices, consisting of a copper body and a high-Z tip, as shown in Fig. 4.6. The Xsuite–BDSIM interface via Xcoll was extended accordingly to support this new geometry.

Separate simulations were carried out for eight different D06V1 collimator settings and for each of the three single-beam background processes: beam–gas Coulomb scattering, beam–gas bremsstrahlung, and Touschek scattering.

For beam–gas simulations, 1500 scattering centers were uniformly distributed around the LER. As explained in Chapter 3, cross-section biasing was applied during the first turn to increase the probability of beam–gas interactions. Scattered particles were then tracked for 999 additional turns without further interactions to simulate their transport through the lattice.

A realistic pressure profile corresponding to a beam current of 200 mA was used as input. This profile was obtained by linearly interpolating between two measured pressure profiles: one at zero beam current (p_0) and one at 1.2 A ($p_{1.2\,\mathrm{A}}$), using the relation

$$p_{200\,\mathrm{mA}} = p_0 + \left(\frac{200}{1200}\right)(p_{1.2\,\mathrm{A}} - p_0).$$

To better estimate the effective pressure experienced by the beam—accounting for the limited conductance between the vacuum chamber and Cold Cathode Gauges (CCGs)—the dynamic component was scaled by a factor of three:

$$p_{\mathrm{eff}} = p_0 + 3 \times (p_{200\,\mathrm{mA}} - p_0).$$

The resulting effective pressure distribution p_{eff} as a function of longitudinal coordinate s around the ring, see Fig. 4.7, was used in all beam–gas simulations. Following established SuperKEKB practice, the residual gas was assumed to consist of a single atomic species with atomic number $Z = 7$, corresponding to a nitrogen-equivalent gas.

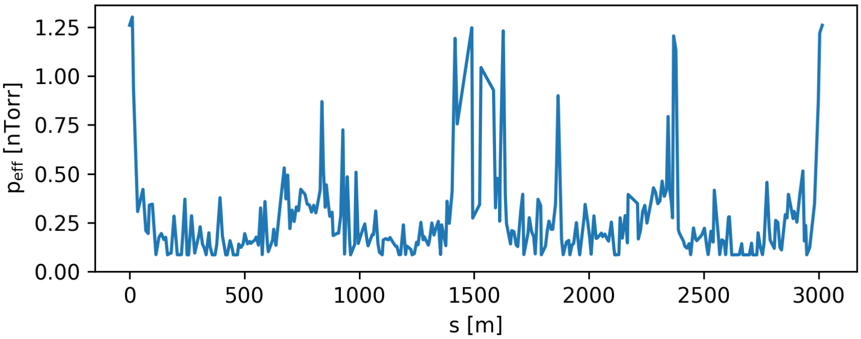

Figure 4.7. Effective pressure profile $p_{\mathrm{eff}}(s)$ used in the beam–gas simulations for the SuperKEKB LER, corresponding to a beam current of 200 mA. The profile was obtained by interpolating between measurements at 0 A and 1.2 A and scaling the dynamic component by a factor of three to account for conductance limitations between the beam pipe and pressure gauges.

Touschek simulations employed 1000 scattering centers uniformly spaced around the ring. At each center, scattered particles were generated and tracked for 1000 turns.

Approximately 10^7 primary particles were simulated per beam–gas case, and between 2×10^7 and 3×10^7 particles per Touschek case.

All simulations included the full nonlinear lattice, a detailed beam pipe aperture profile, and realistic collimator geometries modeled in BDSIM/Geant4. Synchrotron radiation and machine errors were not included. The omission of synchrotron radiation is justified by the relatively short simulation time (1000 turns), which corresponds to roughly a quarter of the LER damping time and is therefore not expected to significantly impact the results.

For each case, particle losses within ±4 m of the interaction point (Belle II region) were recorded and used as input for `basf2` simulations to calculate the dose rate at the QCS-FW diamond detector. The beam pipe aperture profile in this region—critical for accurately determining loss locations—is shown in Fig. 4.8. Contributions from all background sources were then summed to determine the total dose rate for each D06V1 collimator aperture.

Finally, following Ref. [108], a vertical alignment offset of 150 µm was applied to the D06V1 collimator in the simulation to better match the experimentally observed response in the QCS-FW detector.

4.1.5 Results

The simulation results were compared with the experimental data collected during the D06V1 vertical collimator scan on June 27, 2020 [108]. Figure 4.9 shows the relative dose rate measured by the QCS-FW diamond detector as a function of the D06V1 aperture, expressed in units of the vertical beam size

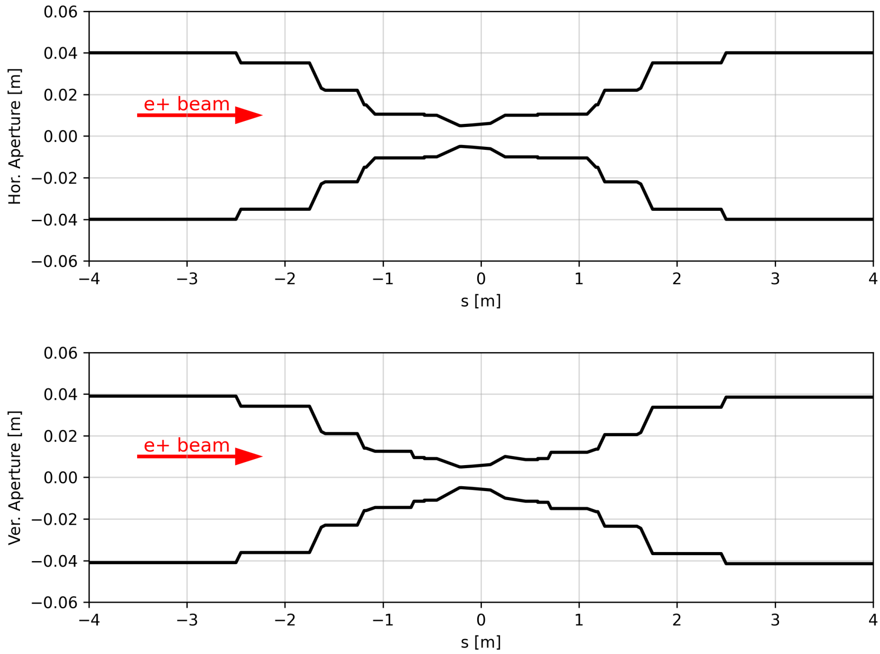

Figure 4.8. Beam pipe aperture profiles in the SuperKEKB LER within ±4 m of the interaction point (Belle II region), used for identifying local particle loss locations. Top: horizontal aperture; bottom: vertical aperture.

$\sigma_{\beta V}$. The predictions obtained using the Xsuite–BDSIM framework are overlaid for direct comparison.

To enable a meaningful comparison, both datasets were processed following the normalization procedure described in Ref. [108]. Specifically, the dose rate measured at small apertures (below 52 $\sigma_{\beta V}$), where the collimator absorbs most stray particles, was averaged and used as a pedestal. This baseline value was subtracted from all data points. The resulting values were then normalized to the average dose rate measured at large apertures (above 92 $\sigma_{\beta V}$), where the background contribution saturates.

As shown in Fig. 4.9, the Xsuite-based simulations reproduce the general shape and features of the measured curve with excellent accuracy, including the steep increase in dose rate between 60 and 80 $\sigma_{\beta V}$, followed by saturation at larger apertures.

Figure 4.9 corresponds to Fig. 16(a) in Ref. [108], which compares the same normalized experimental dataset with normalized dose rates predicted by SAD–Geant4 simulations. The results presented here demonstrate that Xsuite–BDSIM achieves a comparable level of agreement, showing an excellent capability to model collimation, local beam losses, and beam backgrounds in e^+e^- machines.

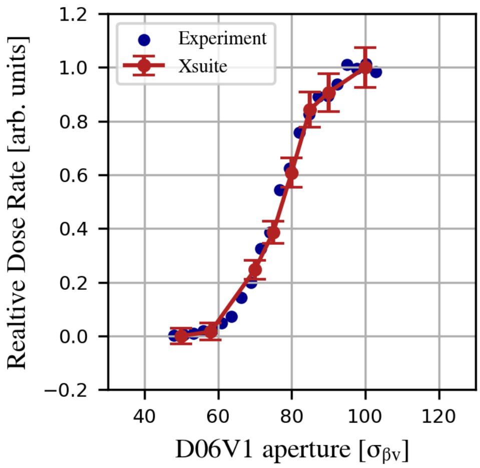

Figure 4.9. Comparison of simulated and measured relative dose rates in the QCS-FW diamond detector as a function of D06V1 collimator aperture, expressed in units of vertical beam size $\sigma_{\beta V}$. Simulated values were obtained with Xsuite–BDSIM, including beam–gas and Touschek background sources.

In absolute terms—i.e., before applying the normalization procedure—the ratio between the measured and simulated dose rates (commonly referred to as the Data/MC ratio in SuperKEKB and Belle II background studies) is approximately between 3 and 4. This level of agreement is consistent with previous results obtained using independent SAD–Geant4 simulations [108], and is considered excellent given the various uncertainties in the modeling. These include the assumption of a single nitrogen-equivalent gas species with $Z = 7$, the extrapolation of the residual gas pressure profile to a 200 mA beam current as discussed in Section 4.1.4, the absence of machine imperfections such as magnet misalignments and field errors, and possible uncertainties in how accurately `basf2` models the actual QCS-FW diamond detector response.

This level of agreement confirms the reliability of the entire simulation chain, including the SAD-to-Xsuite lattice conversion, the two-material collimator implementation in BDSIM, and the dedicated routines for Touschek and beam–gas scattering. It also supports the applicability of the framework to operational background predictions and future studies at SuperKEKB and other future lepton colliders.

4.2 Benchmark with measured beam loss patterns at the LHC

Given the potential limitation of the SuperKEKB benchmark outlined in Sec. 4.1—namely the absence of ring-wide beam loss monitors and the comparison restricted to beam-induced background signals at the Belle II region—a complementary benchmark with measured beam loss patterns at the LHC is presented in this section. This section summarizes the work by the author of this thesis that is reported in more detail in Ref. [114].

4.2.1 Setup

The benchmark targets the comparison between simulated and measured loss maps recorded during the 2022 LHC Run 3 commissioning. The scenario considered corresponds to LHC Beam 1, horizontal betatron collimation losses (B1H) impacting on the primary betatron collimator TCP.C6L7.B1, protons at 6.8 TeV beam energy in physics conditions with collision optics, and $\beta^* = 30$ cm at IP1 (ATLAS) and IP5 (CMS).

In the simulation, primary protons impacting the TCP.C6L7.B1 collimator jaws were generated with a maximum impact parameter $b = 1$ μm [37]. The impact parameter b corresponds to the transverse depth into the collimator jaw at which a particle hits the surface (further details are provided in Chapter 6, Sec. 6.1). A total of 2×10^7 primary protons were tracked for 700 turns using Xsuite through the full nonlinear LHC lattice. Particle–matter interactions in the collimators were modeled with BDSIM/Geant4. Beam loss locations were recorded during tracking, and the loss distribution along the longitudinal coordinate s was binned in 10 cm intervals to produce the loss maps, showing the beam loss distribution along the LHC ring.

The simulation was then compared with the measured loss map, obtained using pilot bunches in the LHC with an intensity of approximately 10^{10} protons each. For this measurement, a pilot bunch was excited transversely using the LHC transverse damper (ADT) [115], and the resulting losses were recorded by the system of ionization-chamber Beam Loss Monitors (BLMs) distributed around the full 27 km circumference [116, 117]. From the BLM signals, position-resolved loss distributions were reconstructed.

4.2.2 Results

Figures 4.10 and 4.11 show the comparison between the simulated and measured loss maps for the full LHC ring and for the IR7 insertion (betatron collimation insertion), respectively. The measured loss maps are expressed in terms of the normalized BLM signal,

$$\frac{\mathrm{BLM}_i}{\mathrm{BLM}_{\mathrm{TCP}}},$$

where BLM_i is the signal from the i-th BLM, and $\mathrm{BLM}_{\mathrm{TCP}}$ is the BLM signal of the impacted primary collimator TCP.C6L7.B1 (which corresponds to the maximum among all BLM signals). The simulated loss maps, are expressed in terms of the cleaning inefficiency η, defined as

$$\eta = \frac{E_{\mathrm{lost},\,\Delta s}}{E_{\mathrm{lost}}^{\mathrm{TCP}}\,\Delta s}, \tag{4.1}$$

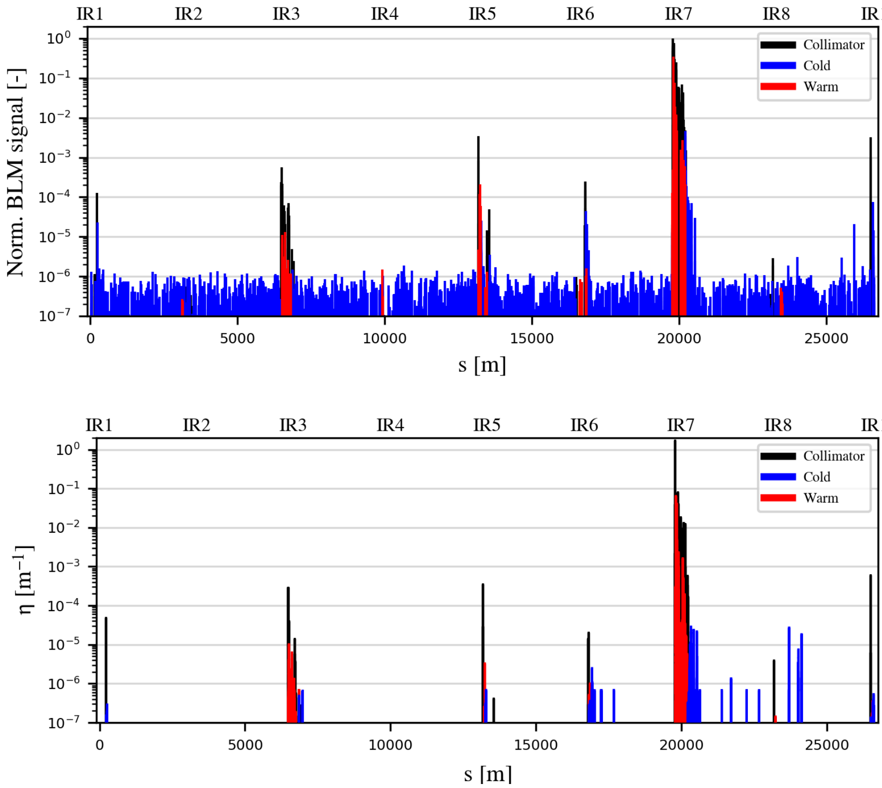

Figure 4.10. Comparison between measured and simulated LHC Run 3 (2022) B1H loss maps for the full 27 km ring. Top: measured loss map reconstructed from Beam Loss Monitor (BLM) signals. Bottom: loss map simulated with Xsuite–BDSIM.

where $E_{\mathrm{lost},\,\Delta s}$ is the energy lost from particles within each 10 cm bin, $E_{\mathrm{lost}}^{\mathrm{TCP}}$ is the energy lost on the impacted primary collimator TCP.C6L7.B1, and $\Delta s = 10$ cm is the bin width. For collimators only, the cleaning inefficiency η is instead normalized to the collimator length, rather than to 10 cm.

It should be noted that the simulation reports the energy of the particles impacting on the machine aperture, which is treated as a black absorber, while the BLMs measure the secondary-shower signal outside the cryostat. The proportionality between these two quantities is location dependent, as it is determined by the local geometry and material composition of the elements between the vacuum chamber and the BLMs. Consequently, quantitative agreement is not expected to be better than at the level of typically about a factor 10 [37].

Within this caveat, the agreement is generally good. The main loss locations are reproduced, and in particular, the clusters of cold losses in the dispersion

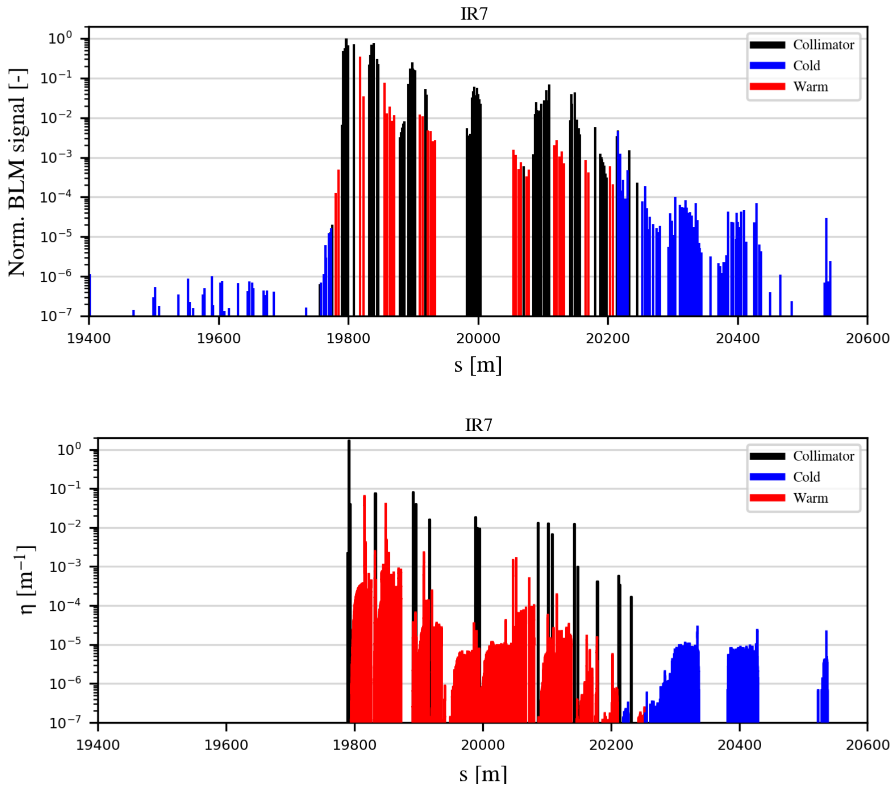

Figure 4.11. Comparison between measured and simulated LHC Run 3 (2022) B1H loss maps for the IR7 insertion (betatron collimation insertion). Top: measured loss map reconstructed from Beam Loss Monitor (BLM) signals. Bottom: loss map simulated with Xsuite–BDSIM.

suppressors downstream of IR7 are clearly visible in both simulation and measurement. In contrast, warm-loss peaks at collimators and resistive magnets appear relatively larger in the BLM data, consistent with the fact that the BLMs also intercept showers generated upstream. A fully quantitative BLM-level comparison would require an additional simulation stage to propagate showers through a detailed 3D geometry model of the magnets and cryostat, as performed in dedicated FLUKA-based studies [37, 118].

Overall, the LHC benchmark demonstrates that Xsuite–BDSIM reproduces the measured loss patterns around the ring with satisfactory accuracy. It complements the localized SuperKEKB validation by exercising the same prediction chain against distributed losses in a hadron collider, thereby broadening the scope of the benchmarking effort.

Chapter 5

Collimation system design

This chapter presents the design of the FCC-ee beam halo collimation system developed in this thesis work. For completeness, the main features of the synchrotron radiation (SR) collimation system will also be briefly introduced in a dedicated section.

The discussion focuses on the FCC-ee Z operation mode, featuring a beam energy of 45.6 GeV. Despite being the lowest-energy operating point, the Z mode features the highest beam current and total stored beam energy, making it the most challenging scenario from a collimation point of view. This motivates its selection as the primary focus of the study. Nevertheless, the methodologies and principles outlined in this chapter are general and apply to all FCC-ee operation modes.

5.1 FCC-ee halo collimation system

The motivations for implementing a beam halo collimation system in the FCC-ee have been discussed in Section 1.2.1. This section presents the design of the FCC-ee halo collimation system developed as part of this thesis work, detailing its layout, integration, operational principles, and design parameters.

The primary function of the halo collimation system is to protect the machine's aperture bottlenecks from beam losses under various operating conditions, and to keep experimental backgrounds caused by these losses at acceptable levels. In the FCC-ee, beam halo collimation is foreseen to be implemented in one of the long straight sections—also referred to as technical insertions. Specifically, the system is currently envisaged to be located in the insertion at Point F (PF), as illustrated in Fig. 1.2. In the collider layout studied in this thesis, this insertion is foreseen to host both the betatron and off-momentum collimation systems.

To achieve effective betatron and off-momentum halo cleaning within the same insertion, the optics must be carefully designed to provide the appropriate conditions for collimation in well-defined regions where the corresponding

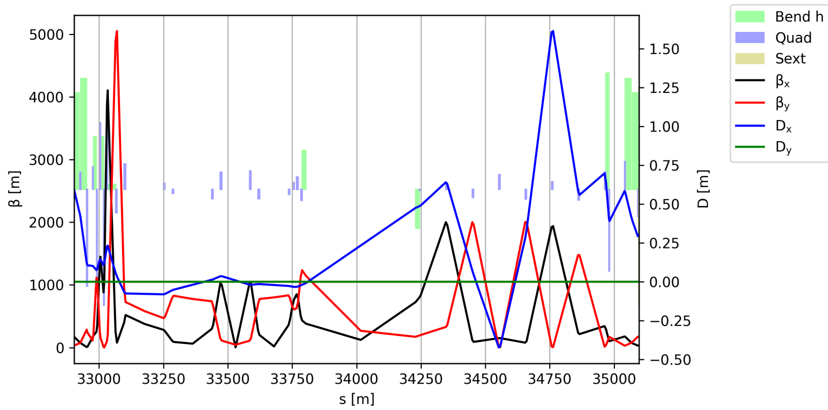

Figure 5.1. Optical functions of the FCC-ee V23 collimation insertion at Point F (PF). The optics provide high beta functions with low dispersion for efficient betatron collimation in the first half of the insertion, and a dispersion bump for off-momentum collimation in the second half.

betatron or off-momentum collimators will be placed. This requires a careful optics matching strategy that ensures the collimation insertion can fulfill its functional requirements without compromising the collider performance. Ideally, the integration of dedicated technical insertion optics — whether for collimation, injection/extraction, or RF systems — should be fully transparent to collider operation, preserving key performance indicators such as dynamic aperture (DA), momentum acceptance (MA), and equilibrium emittance.

In the initial design phase of the FCC-ee collimation section, the adopted strategy was to develop dedicated optics in PF capable of fulfilling the functional requirements for both betatron and off-momentum collimation. This approach aimed to achieve efficient cleaning performance while maintaining mechanical jaw openings within acceptable limits to respect impedance constraints. An example of such a dedicated optics configuration is shown in Fig. 5.1, corresponding to the collimation optics developed for the FCC-ee V23 layout (2023) in the Z operation mode.

This configuration enabled a two-stage, split-function collimation system within the same insertion: betatron collimation was implemented in the first half of the insertion, while off-momentum collimation was implemented in the second half, downstream of the central beam crossing point. In the betatron collimation section, the optics was optimized to maximize the beta functions while keeping dispersion low; in contrast, the off-momentum region featured minimized beta functions and a local dispersion bump.

As will be demonstrated in Chapter 6, a two-stage system—consisting of both primary and secondary collimators—was adopted because it offers significantly improved collimation performance compared to a single-stage system relying only on primaries. Although this optics configuration satisfied the

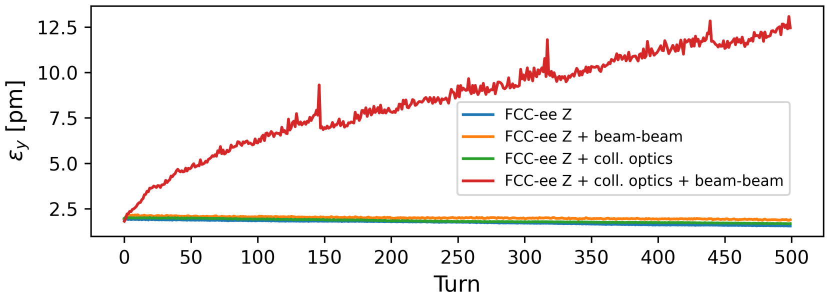

Figure 5.2. Simulated vertical emittance evolution vs. turn number for different configurations. The plot shows that a significant vertical emittance blow-up occurs only when both the dedicated collimation insertion optics and beam-beam interactions are present.

collimation requirements well, it was found during this thesis work—specifically when including beam-beam interactions at the four interaction points during particle tracking—that the dedicated collimation optics in PF induced a significant vertical emittance blow-up. This effect is illustrated in Fig. 5.2, which shows the evolution of the simulated vertical emittance over time for different machine configurations. This study was performed with Xsuite simulations, tracking a Gaussian-distributed beam matched to the equilibrium beam parameters at collision and initialized at the center of the RF section in Point H (PH). To generate a nonzero vertical emittance in the absence of imperfections or misalignments, vertical wigglers were included; these create local vertical dispersion and were tuned in strength to reproduce the desired lattice emittance. The rms vertical emittance was computed from the macroparticle coordinates at each passage through PH and recorded as a function of turn number. The results indicate that the emittance degradation occurs only when both the dedicated collimation optics and beam-beam effects are simultaneously present.

This phenomenon was traced back to the fact that the inclusion of the collimation insertion optics breaks the ideal four-fold super-periodicity of the lattice, thereby introducing new resonances. The beam-beam interactions, in turn, enlarge the beam's tune footprint, increasing the likelihood of resonance crossing — ultimately leading to the observed vertical emittance growth. The effect does not occur if either the collimation insertion optics or the beam-beam interactions are excluded. Similar studies performed with the specialized injection optics in PB revealed the same emittance blow-up mechanism, further supporting this interpretation.

In addition to the vertical emittance blow-up, the inclusion of the dedicated collimation optics in PF also led to a sizeable reduction in the machine's momentum acceptance (MA), as illustrated in Fig. 5.3.

These findings have played a critical role in guiding the further development of the FCC-ee optics. They highlight how the introduction of new resonances—arising from the breaking of the lattice's super-periodicity—can impose stringent constraints on the design of technical insertion optics. It is

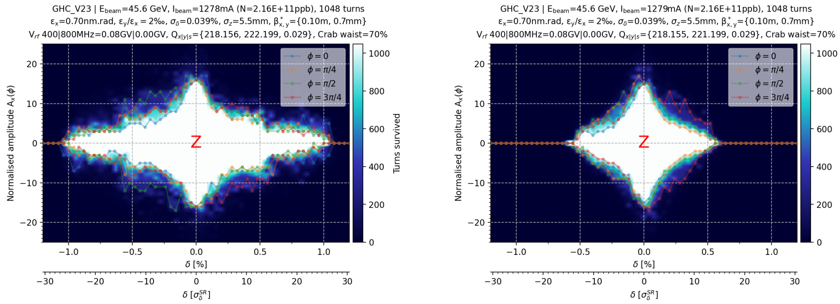

Figure 5.3. Impact of dedicated collimation optics on the machine momentum acceptance (MA) for the FCC-ee Z operation mode. Left: MA with the standard lattice. Right: MA with collimation insertion optics in PF, showing a clear reduction.

worth stressing that this does not imply that specialized optics in technical insertions are fundamentally incompatible. Rather, it reinforces a key design principle already noted: technical insertion optics must be fully transparent to the machine performance.

To address the limitations observed with dedicated collimation optics, an alternative approach was proposed by the optics developers: adopting a collider optics in which all technical insertions share the same optics layout. This *universal insertion optics* preserves the perfect four-fold super-periodicity of the ring and avoids the issues previously encountered, as demonstrated in Fig. 5.4. The corresponding optics layout for the universal insertions is shown in Fig. 5.5.

The FCC-ee V25.2 (2025) layout, which implements universal technical insertion optics for injection/extraction, collimation, and RF, has therefore been adopted as the baseline for this thesis. This is the optics configuration considered for the remainder of the discussion and forms the basis for the results presented in the following chapters.

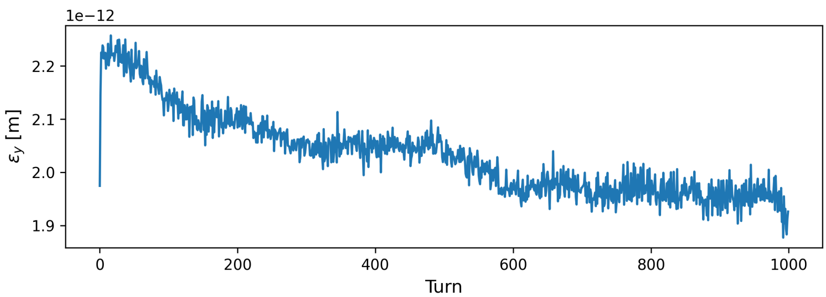

Figure 5.4. Vertical emittance evolution vs. turn number for the FCC-ee Z V25.2 lattice including beam-beam interactions. The lattice features universal technical insertion optics for injection/extraction, collimation, and RF, preserving four-fold super-periodicity and preventing vertical emittance blow-up.

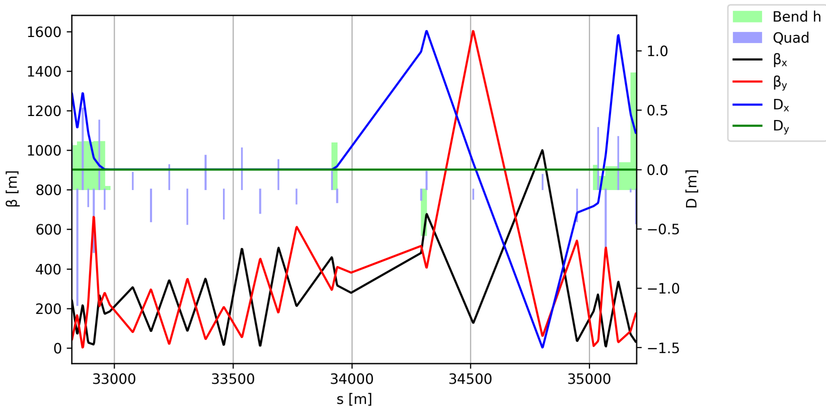

Figure 5.5. Optical functions of the FCC-ee V25.2 GHC lattice (Z-mode) with universal technical insertion optics for injection/extraction, collimation, and RF.

5.1.1 Design of a collimation system layout for the FCC-ee

Once the FCC-ee optics layout is established—whether based on dedicated or universal technical insertion optics—the design of the collimation system within the PF insertion proceeds through a series of key steps carried out as part of this thesis work.

Aperture and momentum bottlenecks

The first step in designing a collimation system layout is to identify the aperture and momentum bottlenecks of the machine. This requires detailed knowledge of the beam pipe aperture profile as well as its tolerances on manufacturing and alignment, beam optics, and the imperfections on optics and orbit. By combining these two elements, one can compute the minimum normalized transverse aperture in both the horizontal and vertical planes, as well as the minimum momentum aperture. These define the limiting regions—commonly referred to as the aperture and momentum bottlenecks—that the collimation system must be designed to protect.

The minimum normalized transverse aperture $A_n^{\min}$ is defined as:

$$A_n^{\min} = \min\left(\frac{A_u(s)}{\sigma_u(s)}\right), \tag{5.1}$$

where $A_u(s)$ is the local physical half-aperture at the longitudinal location s, and $\sigma_u(s)$ is the corresponding local RMS beam size. In the ideal case, the beam size is given by:

$$\sigma_u(s) = \sqrt{\epsilon_u \, \beta_u(s) + D_u^2(s) \, \sigma_\delta^2}, \tag{5.2}$$

Table 5.1. Assumed FCC-ee parameters for maximum closed orbit distortion, beta-beating factor, and parasitic dispersion factor.

Parameter	Value
Maximum closed orbit distortion, $\Delta_{\max}u$	250 μm
Beta-beating factor, β_{beat}	1.2
Parasitic dispersion factor, D_{par}	1.0

where ϵ_u is the emittance in plane u, $\beta_u(s)$ is the beta function, $D_u(s)$ is the dispersion function, and σ_δ is the relative RMS momentum spread.

However, this idealized estimate can overstate the actual available aperture, since it neglects imperfections such as orbit drifts, beta-beating, and parasitic dispersion. These arise from sources like magnet misalignments, field errors, and alignment tolerances.

To obtain a realistic estimate of the transverse aperture bottleneck—also referred to as the minimum *beam stay clear* (BSC)—one must account for possible machine imperfections. In this context, the minimum normalized aperture becomes:

$$A_n^{\min} = \min\left(\frac{A_u(s) - \Delta_{\max}u}{\tilde{\sigma}_u(s)}\right), \tag{5.3}$$

where $\Delta_{\max}u$ is the maximum expected closed orbit excursion, and $\tilde{\sigma}_u(s)$ is the effective beam size corrected for optics distortions:

$$\tilde{\sigma}_u(s) = \sqrt{\epsilon_u\, \beta_u(s)\, \beta_{\text{beat}} + [D_u(s)\, D_{\text{par}}]^2\, \sigma_\delta^2}. \tag{5.4}$$

Here, β_{beat} represents the maximum expected beta-beating factor, and D_{par} accounts for parasitic dispersion.

The nominal values for $\Delta_{\max}u$, β_{beat}, and D_{par} assumed in this thesis are summarized in Table 5.1. These values are based on mechanical tolerances and optics correction studies carried out for the FCC-ee [119, 120, 121].

Disclaimer on aperture bottleneck evaluation. The method adopted here for the evaluation of the minimum BSC is a simplified approach compared to more sophisticated methods available, for instance in MAD-X [122, 123], which provides a dedicated `APERTURE` computation routine accounting for detailed mechanical and alignment tolerances and performing angular scans to detect possible aperture bottlenecks in skew planes. However, dedicated checks performed for the FCC-ee case considered here have confirmed that, with the present tolerance assumptions, these additional effects have a negligible influence on the resulting minimum BSC value, as the dominant contributions arise from the closed-orbit distortion and β-beating, and that a 1D aperture calculation can fully reproduce the bottleneck found in a 2D study for the present FCC-ee optics and beam pipe geometry. Should future revisions of the mechanical or alignment tolerances introduce larger impacts on the evaluated minimum BSC, a more complete aperture analysis *à la* MAD-X may become warranted.

The minimum linear momentum aperture is defined as:

$$\delta_{\min} = \min\left(\frac{A_x}{|D_x| \cdot D_{\mathrm{par}}}\right), \tag{5.5}$$

where A_x is the mechanical aperture in the horizontal plane, D_x is the horizontal dispersion function, and D_{par} is the parasitic dispersion factor. Only the horizontal plane is considered in this context, as the beam bending and associated energy-dependent orbit deviations occur in this plane only.

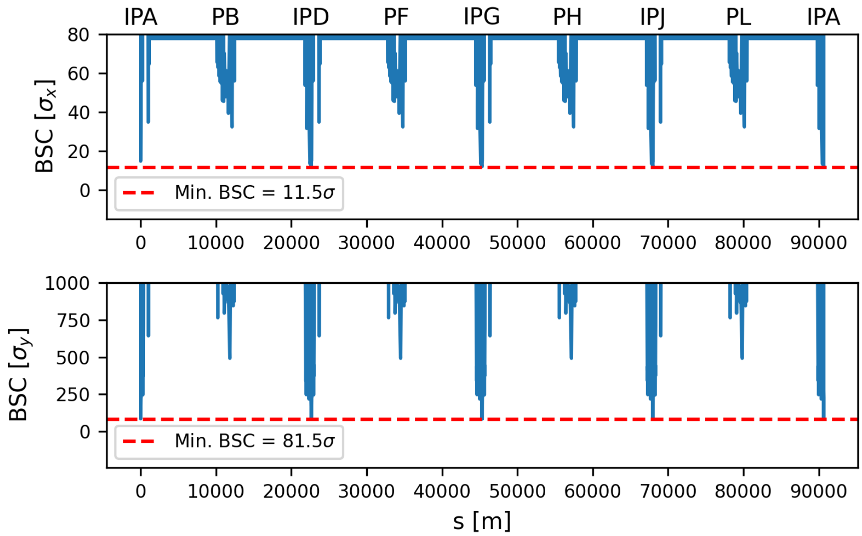

Figure 5.6. Beam-stay-clear (BSC) along the FCC-ee ring in the horizontal and vertical planes for the Z operation mode. The minima in each plane define the aperture bottlenecks.

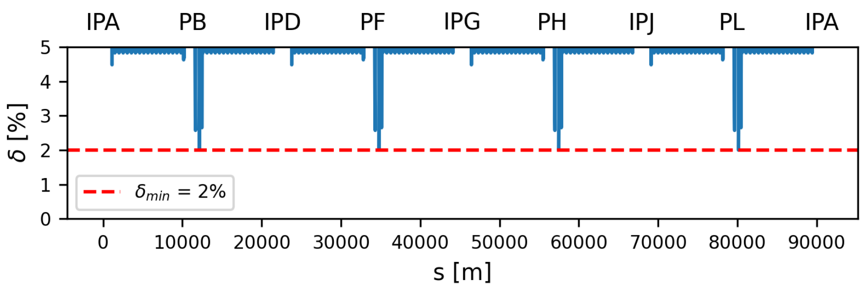

Figure 5.7. Linear momentum aperture along the FCC-ee ring for the Z operation mode. The minimum defines the momentum bottleneck.

Table 5.2. Minimum normalized BSC and linear momentum aperture for the FCC-ee Z operation mode. Also shown are the lattice elements where each minimum occurs.

	Value	Plane	At element
Min. BSC	$11.5\sigma_x$	H	QC2L2
Min. BSC	$81.5\sigma_y$	V	QC1L2
$\delta_{\rm min}$	2.0%	H	QI2

To illustrate these concepts in the context of the FCC-ee, the computed beam-stay-clear (BSC) along the ring in both the horizontal and vertical planes for the Z operation mode is shown in Fig. 5.6. Similarly, Fig. 5.7 shows the corresponding profile of the linear momentum aperture. From these results, the limiting locations—i.e., the longitudinal positions where the minimum BSC or momentum aperture occurs—can be identified. These values are summarized in Table 5.2, which reports the minimum horizontal and vertical BSC, the minimum momentum aperture, and the lattice element at which each minimum is reached. The values of these minima constitute the reference inputs for the definition of the collimator settings discussed in the following section.

The minimum BSC in the horizontal plane is found at the QC2L2 quadrupoles, while the vertical-plane minimum occurs at the QC1L2 quadrupoles. These quadrupoles are part of the FCC-ee final focus system. For reference, the interaction region optics for the Z operation mode is shown in Fig. 5.8. As seen in the figure, the aperture bottlenecks coincide with the locations of the largest beta functions, as expected from the inverse scaling of the normalized aperture with beam size.

The momentum bottleneck is instead found at the QI2 quadrupoles, located in the technical straight sections. These quadrupoles correspond to the regions where the largest negative horizontal dispersion D_x is reached, as shown in Fig. 5.5.

Collimator settings

After identifying the aperture and momentum bottlenecks, the next step is to define the collimator settings—that is, the normalized apertures at which each collimator will be positioned.

In general, collimators must be set with apertures smaller than those of the corresponding bottlenecks to ensure effective protection.

For betatron collimation, the collimators must impose a transverse cut that sets the new limiting aperture for on-momentum particles. This cut must be sufficiently small, with adequate margins, to effectively protect the aperture bottlenecks from beam halo losses, while avoiding a significant reduction of the beam lifetime due to interception of stable particles from the beam core.

Similarly, for momentum collimation, the collimators must define a momentum cut that is small enough to protect the momentum bottleneck, but not

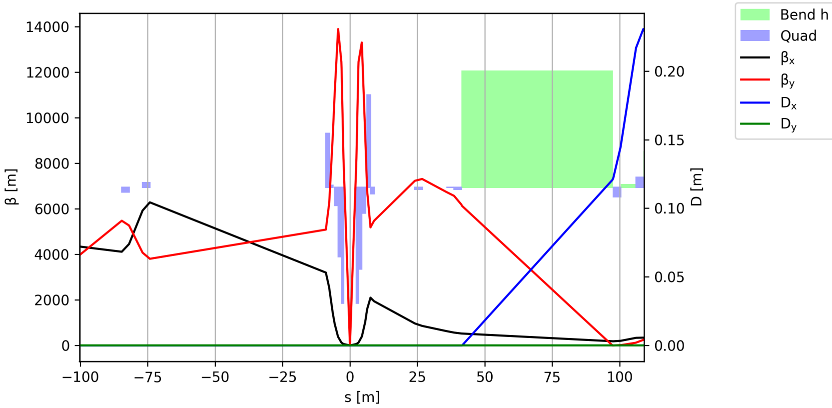

Figure 5.8. Optical functions in the FCC-ee interaction region for the Z operation mode (V25.2 GHC lattice). The highest beta functions occur in the final focus quadrupoles, QC2L2 and QC1L2, where the horizontal and vertical aperture bottlenecks are also located.

so small as to significantly reduce the momentum acceptance and compromise beam lifetime.

The retraction—i.e., the difference in normalized aperture between a collimator and the aperture bottleneck it protects—must be feasible from an operational standpoint. Experience at the LHC indicates that absolute retractions in the range of 100–300 µm can be reliably achieved. In the FCC-ee, this corresponds approximately to $1\sigma_x$ in the horizontal plane and $15\sigma_y$ in the vertical plane.

In a single-stage collimation system, individual collimators directly protect the aperture bottlenecks. In a multi-stage system—such as the one foreseen for the FCC-ee, additional secondary collimators are inserted between the primaries and the bottlenecks in a hierarchical arrangement. Each stage must be separated by a sufficient retraction margin to maintain the intended collimation hierarchy, while still respecting mechanical and operational constraints.

Based on the bottleneck values summarized in Table 5.2, and taking into account the minimum retraction margins discussed earlier, the collimator settings selected for the FCC-ee V25.2 GHC optics in the Z operation mode are: $9.5\sigma_x$ and $10.5\sigma_x$ for the horizontal primary and secondary betatron collimators, respectively; and $50,\sigma_y$ and $65,\sigma_y$ for the vertical primary and secondary betatron collimators, respectively. For momentum collimation, the selected settings are $18\sigma_x$ and $28\sigma_x$ for the primary and secondary collimators, respectively. The aperture of the primary momentum collimator corresponds to a momentum cut of 1.1%, which lies just outside the machine momentum acceptance of 1.0% reported in Table 1.2.

Collimator placement

Once the halo collimator settings are defined, suitable locations for the collimators must be selected within the dedicated collimation insertion at Point F (PF). The primary betatron collimators, being the closest to the circulating beam in terms of normalized aperture, are typically placed at locations where the beta function is maximized and also where the dispersion is small. This choice serves multiple purposes: it increases the physical jaw opening for a given normalized aperture—thereby reducing the collimator's impedance contribution—and it results in a more transversely spread-out beam halo at the collimator location. The latter is beneficial both for cleaning efficiency and for mitigating local energy deposition in the collimator material. A more distributed impact profile reduces the risk of excessive localized heating, which can induce thermal stresses and potentially damage the collimator jaws.

For the primary off-momentum collimator, a different placement criterion applies: it is typically located where the normalized dispersion, $D_x/\sqrt{\beta_x}$, is maximized. This enhances the off-momentum to betatron cleaning efficiency and reduces the impedance contribution by allowing for a wider physical jaw opening at a given momentum cut.

Secondary collimators — both for betatron and off-momentum cleaning — are then placed at locations that satisfy optimal phase advance conditions with respect to their corresponding primaries. These optimal phase advances are derived to maximize the efficiency of a two-stage collimation system, as described in Ref. [124]. The goal is to ensure that any particle scattered at the primary collimator with a deflection angle equal to or larger than a certain threshold is intercepted by a downstream secondary collimator. This improves halo cleaning efficiency by reducing the number of particles potentially leaking to sensitive regions of the machine.

For a one-dimensional (1D) case—either purely horizontal or purely vertical—with a primary collimator opening of $n_1\,\sigma$ and a secondary opening of $n_2\,\sigma$, the optimal primary-to-secondary phase advance μ_{opt} is given by [124]:

$$\mu_{\text{opt}} = \arctan\left(\frac{\sqrt{n_2^2 - n_1^2}}{n_1}\right), \tag{5.6}$$

for positively scattered particles (i.e., with positive scattering angle θ) from the primary collimator. For negatively scattered particles (i.e., $\theta < 0$), the optimal phase advance becomes:

$$\mu_{\text{opt}} = \pi - \arctan\left(\frac{\sqrt{n_2^2 - n_1^2}}{n_1}\right). \tag{5.7}$$

It is important to note that the solutions for μ_{opt} are periodic with period π. Therefore, the full set of optimal phase advances can be expressed as:

$$\mu_{\text{opt}} = \arctan\left(\frac{\sqrt{n_2^2 - n_1^2}}{n_1}\right) + n\pi \quad \text{for } \theta > 0, \tag{5.8}$$

$$\mu_{\rm opt} = \pi - \arctan\left(\frac{\sqrt{n_2^2 - n_1^2}}{n_1}\right) + n\pi \quad \text{for } \theta < 0, \tag{5.9}$$

where $n = 0, 1, 2, \ldots$.

These multiple solutions offer flexibility in selecting practical locations for the secondary collimators, especially when constrained by physical layout or integration issues. In practice, the most convenient solution (typically with $n = 0$ or $n = 1$) is chosen to balance phase advance optimization with mechanical feasibility.

Since scattered particles can exit the primary collimator with either positive or negative angles, two secondary collimators are placed per primary collimator — one positioned at a phase advance $\mu_{\rm opt}$ as given by Eq. (5.8), and the other at a phase advance $\mu_{\rm opt}$ as given by Eq. (5.9). This ensures interception of particles in both scattering directions, thereby maximizing the collimation efficiency and phase space coverage.

This concept is illustrated in Fig. 5.9, which shows a schematic example of a two-stage collimation system. A two-sided primary collimator (TCP) is placed at a phase advance $\phi = 0$, while two two-sided secondary collimators, TCS.1 and TCS.2, are positioned at phase advances $\mu_{\rm opt,1}$ and $\mu_{\rm opt,2}$, corresponding to the optimal phase advances for positively and negatively scattered particles, respectively, as given by Eqs.(5.8) and (5.9) with $n = 0$.

Alternatively, TCS.1 and TCS.2 can also be placed at equivalent phase locations corresponding to higher-order solutions of the same equations with $n > 0$. In the figure, the positions of TCS.1 and TCS.2 with $n = 1$ are also shown, labeled as TCS.1* and TCS.2*, respectively. The trajectories of particles scattered with positive ($\theta > 0$), negative ($\theta < 0$), and zero ($\theta = 0$) scattering angles are included.

As can be seen, the scattered particles reach their maximum transverse amplitude at the locations of TCS.1 and TCS.2. This implies that the particles impact the secondary collimators with maximum depth into the jaw material, which in turn maximizes the probability of absorption. Equivalently, these are also the locations where the minimum scattering angle θ required to reach a normalized amplitude of n_2 at the secondary collimator is achieved.

To provide additional flexibility in the positioning of secondary collimators — particularly given the preference for locations where the local beta functions are sufficiently high to keep the physical gaps acceptable for impedance constraints — small deviations from the exact optimal phase advances can be tolerated. Within the framework of the FCC-ee collimation system design developed in this thesis, a maximum deviation of $\pm 20°$ from the ideal values given by Eqs. (5.8) and (5.9) has been considered acceptable.

The collimator settings and placement strategies outlined in this section impose requirements on the optics functions and phase advances at the collimator locations. These requirements are summarized in Table 5.3 for the betatron collimators and Table 5.4 for the momentum collimators.

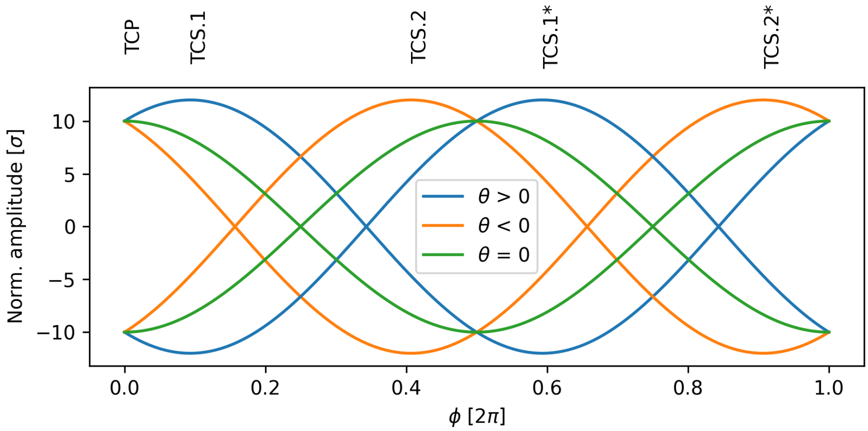

Figure 5.9. Schematic representation of a two-stage collimation layout. A two-sided primary collimator (TCP) is placed at phase advance $\phi = 0$, and two secondary collimators, TCS.1 and TCS.2, are positioned at the optimal phase advances $\mu_{\text{opt},1}$ and $\mu_{\text{opt},2}$ for intercepting positively and negatively scattered particles, respectively (with $n = 0$). Alternative secondary collimator positions corresponding to higher-order phase advance solutions ($n = 1$) are also shown as TCS.1* and TCS.2*. The trajectories of particles scattered at the TCP with positive ($\theta > 0$), negative ($\theta < 0$), and zero ($\theta = 0$) angles are illustrated. As shown, the scattered particles reach their maximum normalized amplitude at the locations of the secondary collimators, resulting in maximum impact depth and enhanced absorption efficiency.

Table 5.3. Betatron collimator placement requirements. TCP: Primary collimator, TCS: Secondary collimator, H: Horizontal, V: Vertical, σ: betatron RMS beam size. These collimators must protect the horizontal and vertical aperture bottlenecks.

Collimator	Setting	Optics Requirement	Phase Advance Requirement	Note
TCP.H	9.5σ	$D_x \approx 0$, β_x max	—	—
TCS.H1	10.5σ	Highest possible β_x	[5.2°, 45.2°] from TCP.H (25.2° ideal)	Valid also at $+n\pi$
TCS.H2	10.5σ	Highest possible β_x	[134.8°, 174.8°] from TCP.H (154.8° ideal)	Valid also at $+n\pi$
TCP.V	50σ	$D_y \approx 0$, β_y max	—	—
TCS.V1	65σ	Highest possible β_y	[19.7°, 59.7°] from TCP.V (39.7° ideal)	Valid also at $+n\pi$
TCS.V2	65σ	Highest possible β_y	[120.3°, 160.3°] from TCP.V (140.3° ideal)	Valid also at $+n\pi$

Table 5.4. Momentum collimator placement requirements. TCP: Primary collimator, TCS: Secondary collimator, HP: Horizontal-momentum, σ: betatron RMS beam size. These collimators must protect the momentum bottleneck.

Collimator	Setting	Optics Requirement	Phase Advance Requirement	Note
TCP.HP	18σ	$D_x/\sqrt{\beta_x}$ max	—	—
TCS.HP1	28σ	High $D_x/\sqrt{\beta_x}$	[30°, 70°] from TCP.HP (50° ideal)	Valid also at $+n\pi$
TCS.HP2	28σ	High $D_x/\sqrt{\beta_x}$	[110°, 150°] from TCP.HP (130° ideal)	Valid also at $+n\pi$

FCC-ee PF collimation layout

The FCC-ee V25.2 GHC optics has been developed to meet the collimation requirements outlined in this section. The optics of the PF insertion, together with the proposed collimator layout fulfilling all spatial and optical constraints, is presented in Fig. 5.10. The choices of collimator jaw materials and lengths, along with the rationale behind them, are outlined later in Section 5.3 (see also Table 5.5).

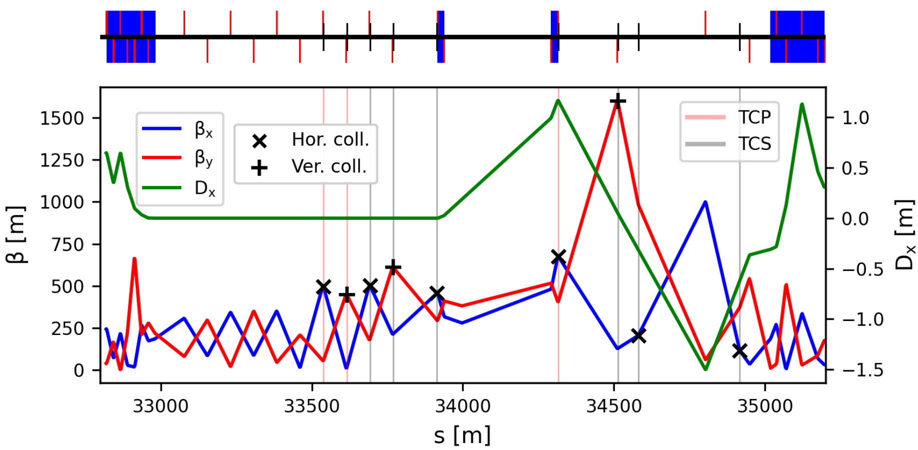

Figure 5.10. Optics functions and proposed collimator layout in the PF insertion of the FCC-ee V25.2 GHC optics (Z-mode). The placement of primary and secondary collimators satisfies the required optical functions and phase advance constraints.

Tertiary collimators for local protection

In addition to the halo collimators placed in the PF insertion (i.e., the primary and secondary collimators for betatron and momentum collimation), the FCC-ee collimation system also includes a set of tertiary collimators for local protection.

The primary role of the PF collimators is to provide global machine protection and to localize losses within the PF insertion, thereby preventing excessive radiation doses elsewhere in the ring and reducing the risk of experimental backgrounds. This assumes that beam loss processes occur on timescales slow enough (i.e., multi-turn losses) for halo particles to be intercepted and removed by the localized collimation system. However, this assumption does not always hold. In particular, fast beam loss mechanisms can cause particles to be lost within a single or only a few turns, without sufficient time for interception by the PF collimators. As a result, such particles may be lost elsewhere in the machine, potentially causing damage to sensitive components. In addition, even with the two-stage collimation system in PF, a fraction of halo particles is expected to leak out of the insertion and may be lost elsewhere in the ring.

When losses occur outside the PF insertion, they are most likely to manifest near existing aperture restrictions. In the FCC-ee, the tightest aperture constraints are found in the vicinity of the experimental interaction regions—especially at the final focus quadrupoles and the synchrotron radiation (SR) collimators, described in Section 5.2.

These regions are particularly sensitive for two reasons. First, SR collimators are optimized for photon absorption and are therefore typically less robust than the halo collimators against direct beam impacts. Second, even if they are not physically damaged by beam losses, their proximity to the detectors makes them a potential source of secondary particle showers, which can increase experimental backgrounds and compromise physics performance.

To mitigate these risks, additional tertiary halo collimators have been included into the FCC-ee collimation system. Specifically, two collimators—one for the horizontal and one for the vertical plane—are installed upstream of each interaction region hosting SR collimators and an experimental detector. Their locations are chosen to be in phase (at a phase advance that is a multiple of π) with the aperture bottlenecks in the final focus system and the SR collimators. Since these elements sit at different individual phases, it is not possible to be exactly in phase with all of them simultaneously. Instead, candidate drift spaces upstream of the IP were scanned, and the TCT positions were selected by minimizing the phase mismatch across all protected elements while respecting practical installation margins. This ensures that any particle on a loss trajectory toward these sensitive components is intercepted first by the tertiary collimators. Following this procedure, the horizontal tertiary collimator (TCT.H) is placed approximately 700 m upstream of the interaction point (IP), while the vertical tertiary collimator (TCT.V) is located about 460 m upstream. The optics layout of the FCC-ee interaction region over the region extending from 800 m upstream of the IP to the IP itself is shown in Fig. 5.11, together with the placement of the tertiary collimators.

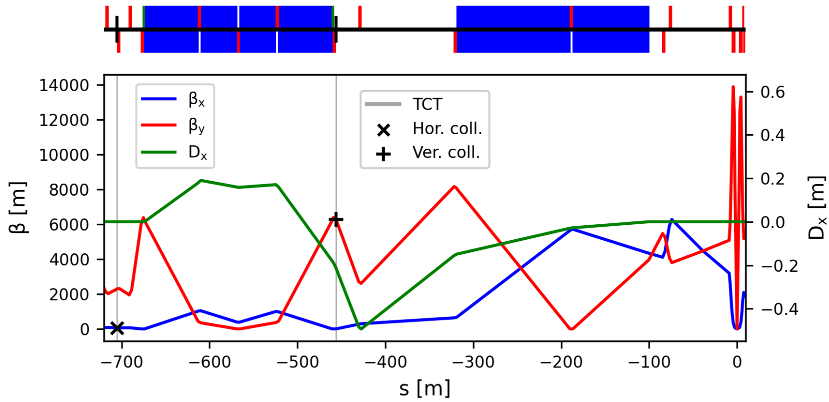

Figure 5.11. Optical functions in the FCC-ee interaction region (Z operation mode) over the upstream section extending from −720 m to the interaction point (IP). The locations of the horizontal and vertical tertiary collimators (TCT.H and TCT.V) are indicated. Their placement is chosen to be in phase with the aperture bottlenecks in the final focus system and the SR collimators, ensuring effective local protection of the interaction region.

The tertiaries act as local primary collimators, directly shielding critical components. As such, they are not required to be retracted relative to the secondary collimators in PF and are set to the same normalized apertures: $10.5\sigma_x$ in the horizontal plane and $65\sigma_y$ in the vertical plane. Nevertheless, the system is designed such that the majority of primary beam losses are intercepted within the PF insertion, with the tertiary collimators providing an additional layer of protection only for residual or fast-loss particles escaping the main collimation system in PF.

As will be shown in the following chapter, these tertiary collimators are essential for providing effective local protection to the FCC-ee interaction regions.

Shower absorbers

In addition to the primary and secondary collimators installed in the PF insertion, the FCC-ee collimation system includes shower absorbers [11], which play a key complementary role to the secondary collimators in managing secondary particle showers produced by the interaction between the beam halo and the primary collimators.

When high-energy electrons or positrons strike the jaws of the primary collimators, intense electromagnetic showers are initiated. Due to possible shallow impacts on the primary collimator jaws and the rather extended longitudinal development of these showers, FLUKA Monte Carlo simulations [125, 126] have shown that only a small fraction of the incident energy is absorbed by the jaws themselves [127, 128]. The majority of the energy escapes as secondary photons, electrons, and positrons, with a large portion reaching downstream vacuum

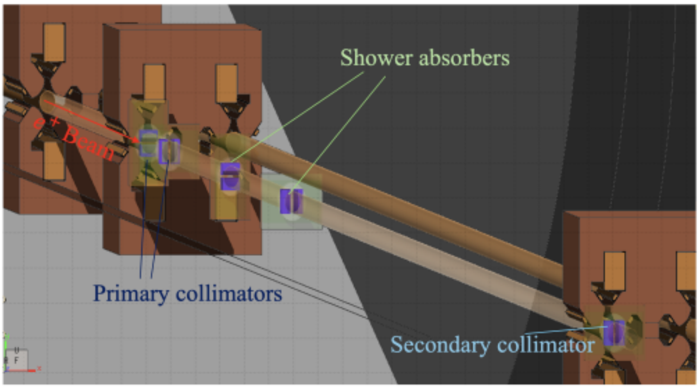

Figure 5.12. Geometry of the FLUKA model used to simulate energy deposition in the FCC-ee V23 GHC betatron collimation section. Primary and secondary collimators, as well as horizontal and vertical shower absorbers, are shown. Courtesy of S. Marin [127, 128].

chambers, secondary collimators, or surrounding structures.

This uncontrolled energy leakage results in significant power deposition in the environment—up to nearly 50% of the total beam loss energy—posing concerns for equipment integrity, tunnel activation, and radiation protection.

To address these challenges, dedicated shower absorbers have been proposed and studied. These are placed between the primary and secondary betatron collimators and are designed to intercept the shower particles before they reach downstream components. The absorbers adopt the same structural design as the secondary collimators but are set with wider jaw openings to avoid interfering with the collimation hierarchy. The absorber material is currently assumed to be TZM, a molybdenum-based alloy.

FLUKA simulations by the SY-STI group at CERN [127, 128] have shown that a configuration with just two optimized shower absorbers—one horizontal and one vertical—can reduce the fraction of energy deposited in the environment from nearly 50% to about 15%. This significantly enhances the overall effectiveness of the collimation system and reduces potential long-term radiation effects. The optimal configuration studied for an earlier FCC-ee collimation optics layout (V23, shown in Fig. 5.1) placed the first absorber about 20 m downstream of the primary collimators, and the second another 20 m further downstream. The layout of the FLUKA geometry model used to perform these simulations—corresponding to the FCC-ee V23 GHC betatron collimation section—is shown in Fig. 5.12. The figure illustrates the longitudinal arrangement of the primary and secondary collimators, along with the two shower absorbers inserted between them. Increasing the number of absorbers yielded diminishing returns, and since each additional absorber contributes to the total impedance, it was deemed unnecessary to add more than two absorbers at this stage.

Although the detailed absorber design and layout will evolve with future updates to the collimation optics, the inclusion of shower absorbers is expected to remain a fundamental feature of the FCC-ee halo collimation system. Their function is complementary to the core design developed in this thesis and forms a crucial part of the overall strategy to mitigate beam loss effects, particularly from a radiation protection standpoint.

5.2 FCC-ee SR collimation system

The design of the synchrotron radiation (SR) collimation system for the FCC-ee is not part of this thesis work. Nevertheless, its main scope and characteristics are briefly outlined here, based on the studies presented in Refs. [129, 130, 131], to provide sufficient context for the broader FCC-ee collimation strategy.

In the FCC-ee, synchrotron radiation is expected to be the dominant source of machine-induced background impacting the detectors. An effective SR collimation system is therefore essential both to reduce the flux of SR photons reaching the experimental regions and to mitigate power deposition in the inner beam pipe of the interaction regions (IRs) caused by SR losses.

The SR collimation system consists of a set of movable collimators and fixed masks, installed upstream of each interaction point. The layout was initially developed for the FCC-ee Conceptual Design Report (CDR) [9] and has been refined in subsequent iterations to follow updates in the machine layout and optics. In its latest configuration—corresponding to the FCC-ee lattice version V25.2 GHC—the system includes six movable SR collimators (TCRs), four horizontal and two vertical, and two fixed masks (TCRMs), one with a circular aperture and the other with a rectangular one. The SR collimation layout is shown in Fig. 5.13.

As shown in Fig. 5.13, the movable collimators are strategically placed at key locations. One horizontal collimator (TCR.H.WL) is installed immediately downstream of the last dipole upstream of the interaction point. A second horizontal collimator (TCR.H2.C0) is located midway along the drift region between the last dipole and the beginning of the final focus system. Additional collimators—both horizontal and vertical (TCR.H.C0 and TCR.V.C0)—are placed just downstream of the first final focus quadrupole (QC0), while others (TCR.H.C2 and TCR.V.C2) are located upstream of the second quadrupole (QC2). These collimators are primarily intended to intercept SR photons generated in the upstream arcs and final focus magnets before they reach the experimental region.

Unlike the halo collimators installed in the PF insertion, the SR collimators are not designed to intercept charged particles. Their apertures are instead matched to the estimated physical aperture bottlenecks and are not retracted for active protection.

Following the movable SR collimators, two fixed masks are installed as final shielding elements near the detector. The first (TCRM.C2) is a circular mask placed between the QC1 and QC2 quadrupoles, with an aperture of 15 mm. The second (TCRM.C1) is a rectangular mask installed just downstream

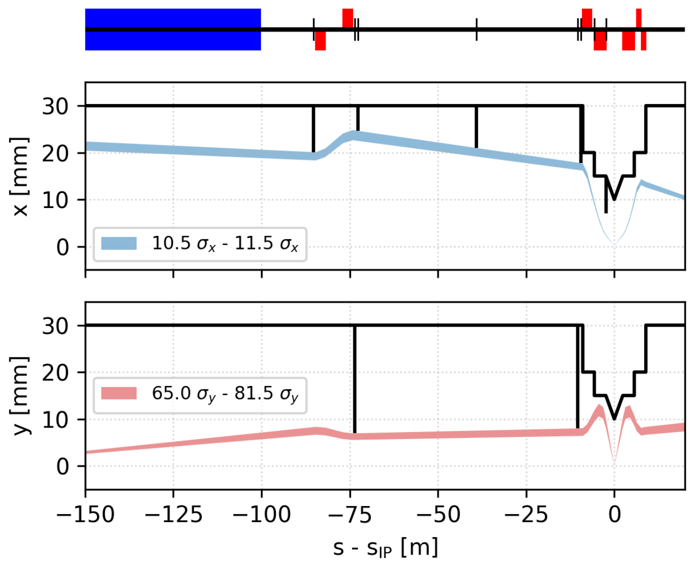

Figure 5.13. Layout of the FCC-ee synchrotron radiation (SR) collimation system for the V25.2 GHC lattice. The system includes six movable SR collimators (TCRs) and two fixed masks (TCRMs). Collimators are positioned to intercept SR photons from upstream arcs and final focus magnets, while the masks provide final shielding near the detector.

of QC1 and closest to the interaction point, featuring a 7 mm horizontal aperture and a 13 mm vertical aperture. These masks are designed to intercept residual SR photons not caught by the upstream collimators, as well as SR photons originating in QC2 and QC1. However, under realistic operating conditions—such as with magnet misalignments or orbit excursions—a small fraction of scattered photons may still reach the detector. Ongoing studies are assessing the impact of this residual SR-induced background on sub-detector performance and are informing further optimization of the mask design.

At present, the movable SR collimators are assumed to be 10 cm long and made of Inermet 180, a tungsten-based heavy alloy with high photon absorption capability. The fixed masks are also made of Inermet 180 but are shorter, with lengths of 2 cm (TCRM.C2) and 6 cm (TCRM.C1). These specifications are subject to refinement as detailed energy deposition and thermo-mechanical studies progress.

5.3 FCC-ee halo collimator design parameters

This section summarizes the main design parameters assumed for the beam halo collimators in the FCC-ee, including their material composition, jaw length, and the criteria guiding these choices.

Designing beam-intercepting devices, such as collimators, for the FCC-ee presents a unique set of challenges. The FCC-ee operates in an unprecedented regime for lepton colliders, with the highest stored beam energy ever considered for an e^+e^- machine. The combination of large stored beam energy and extremely small transverse beam sizes results in exceptionally high energy density, which imposes stringent requirements on the robustness and effectiveness of the collimators. Even a small fraction of the beam intercepted under abnormal or accidental conditions can cause significant energy deposition, risking damage to both sensitive machine components (e.g., superconducting magnets) and the collimators themselves.

Moreover, impedance-driven instabilities are a critical performance concern in the FCC-ee. All machine components must therefore be carefully designed to minimize their contribution to the overall beam-coupling impedance. Collimators are particularly relevant in this context, as they are known to be major contributors to impedance.

Beyond survivability and impedance, another essential functional requirement for the collimators is efficient absorption of beam halo particles and the electromagnetic showers they produce. This ensures that the intercepted energy is effectively dissipated and does not propagate downstream, where it could jeopardize sensitive components, raise radiation levels, or create experimental backgrounds.

Unfortunately, these design goals often conflict. For instance, highly robust materials—such as carbon-based composites—offer excellent resistance to thermal shock and mechanical damage but typically exhibit low density and poor electrical conductivity. This limits their effectiveness in stopping high-energy particles and results in higher impedance contributions. Conversely, dense metallic materials with good electrical conductivity—desirable for efficient energy absorption and low impedance—are generally more susceptible to direct beam impacts. Their high density leads to energy being deposited in small volumes, which can cause localized overheating, thermal stress, and material failure.

As a result, selecting the optimal collimator material and geometry involves carefully balancing these competing requirements. The choices made for the FCC-ee build on best practices and operational experience from previous machines such as LEP, the LHC, and SuperKEKB, while being specifically adapted to the unique challenges posed by the FCC-ee.

The following subsections describe the current assumptions for collimator materials and jaw lengths, along with the rationale behind these design choices.

Collimator materials

The choice of material for each type of halo collimator in the FCC-ee must balance several competing demands, including robustness against direct beam impacts, effectiveness in absorbing secondary particles, and minimization of impedance.

The primary and tertiary local protection collimators (TCPs and TCTs), being potentially exposed to direct high-intensity beam losses, must be made from highly robust materials. Carbon-based materials such as carbon-fibre composites (CFC), graphite, and molybdenum carbide–graphite (MoGr) are considered suitable candidates for these roles due to their high thermal shock resistance and capacity to withstand intense beam impacts. Among these, MoGr [132] offers an attractive compromise, providing approximately an order of magnitude higher electrical conductivity than conventional graphite, while retaining comparable robustness.

For the secondary collimators (TCSs), which are not exposed to direct beam impacts but must efficiently absorb out-scattered particles and shower debris from the primaries, higher-density and higher-Z materials are preferred. Molybdenum (Mo) and TZM (a titanium–zirconium–molybdenum alloy) are considered as candidate materials, offering improved stopping power and reduced energy leakage, along with better electrical conductivity compared to carbon-based materials.

In the tracking studies presented in this thesis, MoGr has been assumed as the jaw material for the TCPs and TCTs, while Mo is used for the TCSs.

Collimator lengths

The assumed jaw lengths for the FCC-ee halo collimators are 25 cm for the primary collimators (TCPs) and 30 cm for the secondary collimators (TCSs). These values are motivated by estimates from earlier studies, such as those presented in Refs. [114], and are consistent with previous experience from LEP and analytical considerations relevant to FCC-ee.

At LEP, a length corresponding to approximately two radiation lengths was found to be suitable for primary collimators [133]. This provided a good balance between avoiding excessive heating of the collimator blocks due to showering electrons and positrons, and ensuring that traversing particles would lose sufficient energy to fall outside the machine's momentum acceptance.

For the FCC-ee secondary collimators, the length requirement is more stringent. Analytical estimates indicate that the collimators must be capable of fully stopping an $e^{\pm}$ of up to 182.5 GeV—the beam energy in the FCC-ee $t\bar{t}$ operation mode—under normal incidence [114]. This motivates a longer jaw length for the TCSs compared to the TCPs.

While these values serve as first-order estimates, a more refined determination of the optimal collimator length is typically carried out through dedicated tracking simulations. In these studies, the length of each collimator type is varied parametrically, and key figures of merit for collimation performance—such as cleaning efficiency, energy loss in critical components, and leakage to sensitive regions—are monitored as a function of the collimator length. This allows identification of the point beyond which further increasing the length yields diminishing returns. The selection of an optimal collimator length must also take into consideration impedance requirements, which favor collimator lengths that are as short as possible. Examples of such parametric studies and their outcomes can be found in Ref. [134].

Mechanical design

Although the mechanical design of the collimators lies outside the scope of this thesis, it is assumed that the collimators will follow a layout similar to that of the LHC, with two independently movable jaws per collimator, each equipped with built-in beam position monitors (BPMs). Separate motors are assumed for the upstream and downstream ends of each jaw, enabling precise control of the jaw tilt angle. A minimum motor step of 5 µm—consistent with the LHC collimator system—is tentatively assumed, though this value will be refined as the FCC-ee design evolves.

The collimator parameters and settings for all FCC-ee collimators, including the SR collimators and shower absorbers, are summarized in Table 5.5.

Table 5.5. Summary of collimator parameters and settings for the FCC-ee Z operation mode. The momentum cut is not reported for collimators located in regions with negligible dispersion. All collimators are assumed to feature two movable jaws and integrated beam position monitors (BPMs). The tertiary collimators (TCTs) and synchrotron radiation collimators (TCRs) are replicated at each of the four interaction points (IPs), resulting in a total of 43 collimators per beam: 9 PF halo collimators, 2 PF shower absorbers, 8 TCTs, and 24 TCRs. Abbreviations: TCP – Target Collimator Primary; TCS – Target Collimator Secondary; TCSA – Target Collimator Shower Absorber; TCT – Target Collimator Tertiary (local protection); TCR – Target Collimator Radiation (SR collimator); H – horizontal betatron; V – vertical betatron; HP – horizontal-momentum.

Name	Plane	Material	Length [cm]	Gap [σ]	Gap [mm]	δ_{cut} [%]
TCP.H.B1	H	C-based	25	9.5	5.6	–
TCP.V.B1	V	C-based	25	50	1.4	–
TCS.H1.B1	H	Mo-based	30	10.5	6.2	–
TCS.V1.B1	V	Mo-based	30	65	2.2	–
TCS.H2.B1	H	Mo-based	30	10.5	6.5	–
TCS.V2.B1	V	Mo-based	30	65	3.6	–
TCSA.H.B1	H	Mo-based	30	15	3.6	–
TCSA.V.B1	V	Mo-based	30	91	1.6	–
TCP.HP.B1	H	C-based	25	18	12.5	1.1
TCS.HP1.B1	H	Mo-based	30	28	11.0	3.5
TCS.HP2.B1	H	Mo-based	30	28	8.3	1.3
TCT.H.B1	H	C-based	25	10.5	2.4	–
TCT.V.B1	V	C-based	25	65	7.3	–
TCR.H.WL.B1	H	W-based	10	11.5	20.4	–
TCR.V.C0.B1	V	W-based	10	81.5	7.1	–
TCR.H.C0.B1	H	W-based	10	11.5	25.0	–
TCR.H2.C0.B1	H	W-based	10	11.5	21.3	–
TCR.V.C2.B1	V	W-based	10	81.5	8.2	–
TCR.H.C2.B1	H	W-based	10	11.5	18.0	–

It is worth noting that a detailed evaluation of the impedance contribution of the FCC-ee collimators to the overall machine impedance budget is beyond the scope of this thesis. Nevertheless, the design studies presented here have been periodically shared with the BE-ABP impedance team at CERN, which is assessing these effects in parallel studies. Although a complete picture of the FCC-ee impedance budget is not yet available—since several components still need to be modeled [135]—estimates for the FCC-ee optics version V25.2 GHC, considering the collimation layout discussed in this chapter, indicate that the impedance contribution from the collimation system has increased in this optics version and might be too high and, as a consequence, there is a risk for impedance-driven instabilities [135], even when mitigation strategies based on feedback systems and optimized chromaticity are applied—strategies that had proven effective in earlier design iterations [135].

This change in behavior in the V25.2 GHC optics has been traced primarily to the vertical primary betatron collimator (TCP.V.B1) [136], which gives the largest impedance contribution. This is mainly due to its very small half gap of approximately 1.4 mm—the smallest among all collimators (see Table 5.5)—a consequence of the extremely low vertical emittance foreseen for the FCC-ee (about 2 pm) and the relatively low beta-function values in the FCC-ee V25.2 GHC betatron collimation section, which in turn are a consequence of the new universal insertion optics. The material choice, constrained by robustness requirements to be carbon-based, further contributes to its high impedance due to its low electrical conductivity.

This is a known issue, and several mitigation strategies are under study. One ongoing effort focuses on optimizing the collimator geometry, for instance through improved taper transitions between the vacuum chamber and the collimator jaws [136], to minimize impedance. This work is being carried out by the impedance team in the BE-ABP group. In parallel, increasing the beta functions in the betatron collimation sections has been proposed, as this would allow larger physical gaps for the same collimator settings, thereby reducing impedance. First results from new optics iterations show promising potential for achieving this without compromising collider performance [137].

Moreover, since the settings of the primary betatron collimators are determined by the minimum beam stay-clear (BSC) of the machine, an increase in the BSC—achievable by enlarging the physical aperture at the current aperture bottleneck locations (i.e., in the final focus systems)—could enable more relaxed collimator settings. Discussions in this direction have already started [138].

Alternative solutions that could help reduce impedance are also being explored. One promising approach is crystal collimation, where thin bent crystals deflect halo particles toward dedicated absorbers featuring gaps that are typically larger than those of conventional secondary collimators; exploratory studies conducted as part of this thesis are presented in Chapter 7. Another option is nonlinear collimation (NLC), a scheme successfully implemented at SuperKEKB [111, 139, 140], where sextupole pairs generate closed nonlinear kicks that drive halo particles to large amplitudes. Therefore, they can be intercepted by a (nonlinear) collimator kept at a larger physical gap than without the nonlinear kicks, hence reducing the impedance. NLC has demonstrated impedance reduction at SuperKEKB [139, 140] and is being considered for other future lepton colliders, such as the Super Tau-Charm Facility [141]. Given its potential benefits, it is foreseen to study the applicability of nonlinear collimation to the FCC-ee in future work.

In summary, while the present impedance contribution from the FCC-ee collimation system is higher than desirable, the issue has been clearly identified, its causes understood, and several viable mitigation strategies are under active development. The outcomes of this work provide essential input to these ongoing optimization efforts and will guide future iterations of the collimation and optics design toward a solution compatible with impedance constraints.

Chapter 6

FCC-ee collimation performance

The performance of the FCC-ee collimation system is critical for ensuring the safe and reliable operation of the collider. Building on the system design and layout presented in Chapter 5, this chapter presents a detailed evaluation of the system performance based on tracking simulations.

The primary objectives of the simulations are to quantify the collimation cleaning efficiency and to assess the level of protection provided to sensitive components, such as superconducting magnets (e.g., the final focus quadrupoles), the interaction region (IR), and the experimental detectors. The simulations also offer insight into local beam loss patterns and energy loss in the collimators and downstream elements, providing a first assessment of potential risks related to component damage, magnet quenches, or background generation. They are also used to guide the optimization of key collimator design parameters, including jaw material, length, and geometry.

The studies presented in this chapter are based on high-statistics Xsuite-BDSIM multi-turn tracking simulations, described in Chapter 3, performed with realistic machine optics (GHC V25.2) and collimator settings. Several loss scenarios were considered: generic beam halo losses (Section 6.1), off-momentum losses (Section 6.2), beam-gas scattering (Section 6.3), Touschek scattering (Section 6.4), and beam-beam interaction losses (Section 6.5). For a complete assessment of the collimation performance, fast beam losses due to, e.g., failures or accidental conditions need to be investigated in addition to the sources of regular beam losses shown here. This goes beyond the scope of this thesis work and will be examined closely in the future. First preliminary results are found in Ref. [36]. However, this thesis also includes an initial collimation performance evaluation for a *generic failure scenario*, performed using the optimized collimation layout established in this work. This study, serving as a generic proxy for fast accidental losses such as asynchronous dumps, injection failures, or sudden beam loss events, is presented in Section 6.6.

The analysis focuses on the FCC-ee Z operation mode, which represents the most challenging scenario from a collimation point of view due to the highest stored beam energy. All simulations presented in this chapter are performed for the positron beam (Beam 1, B1), for which a complete magnetic lattice description is available at the time of writing. The magnetic lattice of the counter-rotating electron beam (Beam 2, B2) is expected to be specular-symmetric, and at the FCC-ee beam energies considered here the particle–matter interaction processes relevant for beam–collimator interactions are equivalent for electrons and positrons. The collimation performance obtained for B1 is therefore expected to be representative of that for B2.

6.1 Generic beam halo losses

The first beam loss scenario considered in this study is the so-called *generic beam halo* loss scenario. This scenario is used to evaluate the performance of the collimation system in the presence of a slow, continuous loss mechanism, where the transverse amplitude of the beam particles increases gradually over many turns. In such case, the beam halo is progressively populated by particles diffusing outward from the beam core.

Given the slow nature of this loss mechanism—characterized by a gradual, diffusive increase of the transverse particle amplitudes over many turns, as can arise from operational setting errors, orbit drifts, or certain classes of beam instabilities—the first element encountered by the halo particles as they reach large transverse amplitudes is one of the primary collimators, which by design correspond to the smallest normalized aperture of the machine in each plane (see Chapter 5 and Table 5.5). This forms the basis of the simulation approach adopted here: modeling the full halo dynamics is challenging, as it depends on the interplay of various machine imperfections — such as magnetic errors, dynamic aperture, and noise in feedback or RF systems. Moreover, simulating the diffusion process would require tracking particles over an extremely large number of turns, making it computationally inefficient for large parameter scans. While such simulations are feasible and are occasionally performed for dedicated studies or validation tests, a more practical and efficient approach is adopted here: simulations begin directly at the point where halo particles impact a primary collimator.

A matched beam halo distribution impinging on the jaws of a primary collimator is therefore generated. This distribution serves as the initial condition for the simulation. The simulation then proceeds with the BDSIM Monte Carlo scattering engine, which models the particle–matter interactions at the collimator. The particles scattered out from the primary collimator are tracked through the machine for a number of turns — typically around 500 — which is sufficient, as most particles are lost within the first few turns due to the large initial amplitudes and the initial interaction with the collimator.

Losses on the beam pipe aperture or other collimators are recorded, and the resulting longitudinal loss distribution along the machine is analysed through

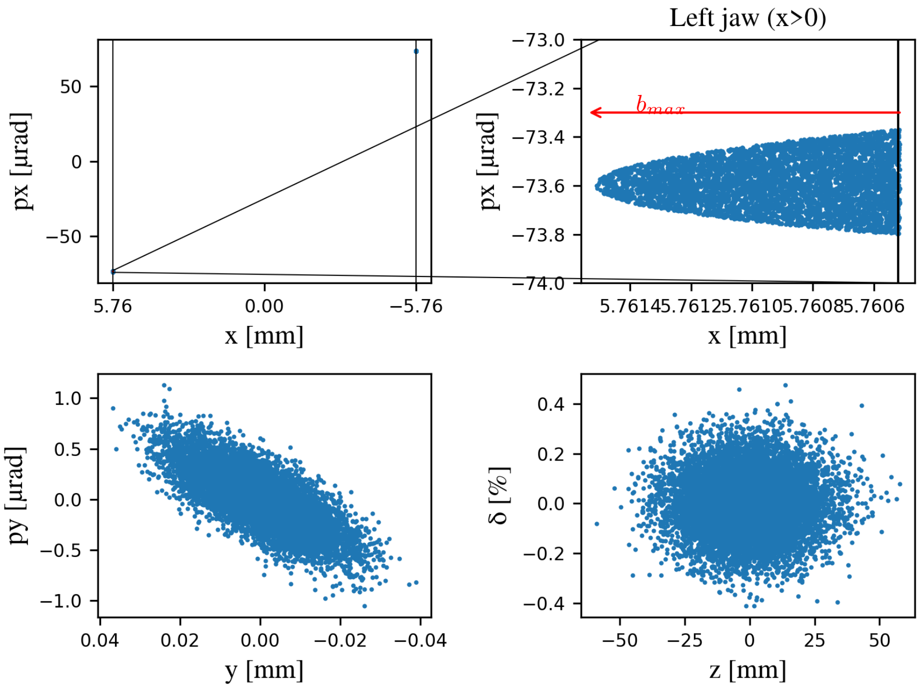

Figure 6.1. Example of a direct halo particle distribution impacting on the horizontal primary collimator TCP.H.B1 in the FCC-ee V25.2 GHC in the Z operation mode. The upper-left plot shows the particle distribution in horizontal phase space (x–p_x), with collimator jaws indicated by vertical black lines at $x = \pm 5.76$ mm (corresponding to $\pm 9.5\,\sigma_x$). A zoom-in on the left jaw region ($x > 0$) is shown in the upper-right inset, where the maximum impact parameter b_{max} is indicated by a red arrow. The bottom plots show the same distribution in vertical phase space (y–p_y, bottom left) and longitudinal phase space (z–δ, bottom right). The distribution is generated using the equilibrium beam parameters at collision for the FCC-ee Z mode, as listed in Table 1.2.

loss maps, i.e., histograms showing the number of particle losses as a function of the longitudinal coordinate s.

The exact shape of the impacting halo distribution is not known a priori. In these simulations, a standard assumption is made: as in LHC collimation studies [37], a uniform distribution is generated in transverse phase space at the primary collimator, extending from the collimator jaw edge up to a specified maximum impact depth (or *impact parameter* b). An illustration of such a distribution is shown in Fig. 6.1.

To ensure conservative results, and since b is not known in detail as it depends on the diffusion speed, the maximum impact parameter b_{max} is typically set to the *critical impact parameter* b_{crit}, corresponding to the impact parameter that yields the worst-case cleaning performance. This value is determined from dedicated impact parameter scans, as discussed in Section 6.1.2. However, in the

FCC-ee studies presented here, no clear critical value has been identified: the collimation performance was observed to degrade monotonically with decreasing impact parameter. As explained in detail in Section 6.1.2, this behavior is attributed to the limited vertical dynamic aperture of the FCC-ee lattice used in the studies presented here, rather than to an intrinsic limitation of the collimation system. It should also be noted that impact parameters significantly smaller than the micrometer scale are not considered realistic, as effects such as collimator jaw surface roughness or flatness become non-negligible at that level. For these reasons, a maximum impact parameter of 1 μm is adopted in the simulations presented here. Studies of collimation performance including realistic surface-roughness effects are left as future work. First studies on this matter from the energy-deposition point of view are presented in Ref. [142].

An intrinsic feature of this simulation strategy is that beam losses are evaluated on a per-particle basis, without explicitly modeling the time evolution of the loss process. This allows the resulting loss distributions to be rescaled *a posteriori* to different beam loss rates corresponding to different assumed beam lifetimes. In the studies presented here, a conservative assumption is adopted for the loss rate: the beam lifetime is assumed to drop to 5 minutes, which is approximately one third of the nominal lifetime expected during regular FCC-ee operation in the Z operation mode (about 17 minutes, see Table 1.2). This choice ensures that the simulated conditions represent a pessimistic scenario. If the collimation system proves effective under these conditions, its performance can be expected to be satisfactory under nominal or less severe circumstances.

Simulation setup

Based on the considerations discussed above, two Xsuite-BDSIM simulations were set up for the FCC-ee positron beam (Beam 1, B1) at a beam energy of 45.6 GeV, corresponding to the Z operation mode. One simulation was configured to model generic horizontal betatron collimation losses (referred to as B1H), and the other to model generic vertical betatron collimation losses (B1V). The initial direct halo distributions were generated at the locations of the corresponding primary collimators: TCP.H.B1 for the horizontal case and TCP.V.B1 for the vertical case.

The distributions were generated using the equilibrium beam parameters at collision, as listed in Table 1.2. Since the simulations do not include beam–beam interactions, the vertical geometric emittance at collision — equal to 1.9 pm — was artificially preserved during tracking through the inclusion of vertical wigglers. These wigglers were configured to introduce local vertical dispersion and tuned in strength to reproduce the desired equilibrium vertical emittance.

Each simulation used a total of 5×10^6 macroparticles. The particles were tracked for 500 machine turns in the full nonlinear FCC-ee lattice (V25.2 GHC [15], Z operation mode), which includes the crab-waist collision scheme, a detailed model of the machine aperture, and the complete collimation system. The collimators were modelled in BDSIM/Geant4, as described in Chapter 3. Synchrotron radiation effects — including both radiation damping and quantum

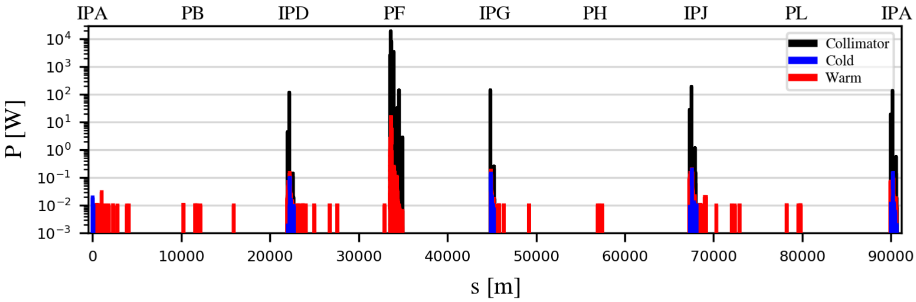

Figure 6.2. Loss map for the full FCC-ee ring for the B1H generic halo loss scenario. The plot shows the power load along the full machine, binned in 10 cm intervals, assuming a beam lifetime of 5 minutes.

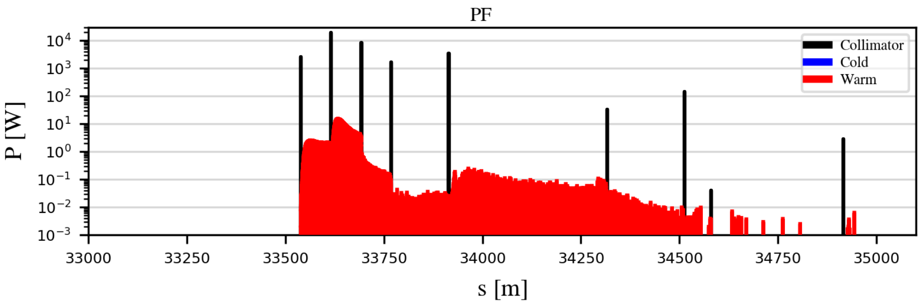

Figure 6.3. Loss map in the PF collimation insertion for the B1H generic halo loss scenario. The collimator region is zoomed in to highlight the distribution and efficiency of the local cleaning.

excitation — were included throughout the machine, along with the effects of RF cavities and magnet tapering. For synchrotron radiation, a stochastic quantum excitation model was used, where each particle receives individual random energy kicks during tracking, in contrast to simplified mean models that only reproduce average energy loss and damping without including excitation effects.

Beam loss locations were recorded during tracking, and the loss distribution along the longitudinal coordinate s was binned in 10 cm intervals to produce the loss maps for the generic halo loss scenarios. The results are presented and discussed in the following section.

Results

The simulation results for the generic beam halo loss scenario are presented in the form of loss maps in Figs. 6.2, 6.3, and 6.4 for generic horizontal betatron collimation losses (B1H), and in Figs. 6.5, 6.6, and 6.7 for generic vertical betatron collimation losses (B1V). These are power load distribution loss maps, showing the local loss power in each 10 cm bin along the machine. The power

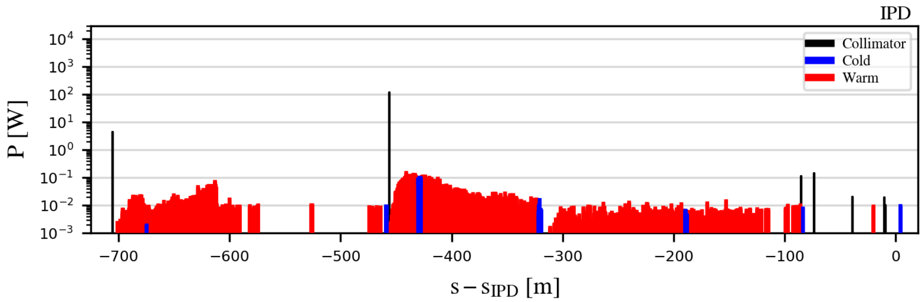

Figure 6.4. Loss map in the downstream interaction region (IPD) for the B1H generic halo loss scenario. The plot spans from 725 m upstream of IPD to 20 m downstream. Losses in this region are particularly critical due to the presence of final focus quadrupoles and detector components.

loads have been computed by summing, in each bin, the total energy of all particles lost in that bin and dividing this quantity by the assumed beam lifetime of 5 minutes. A different binning scheme is used for collimators only, where each collimator is represented by a single bin corresponding to its physical length (see Table 5.5).

The performance of the FCC-ee collimation system for generic betatron halo losses can be assessed from the loss maps shown in Figs. 6.2–6.4 for B1H and Figs. 6.5–6.7 for B1V. In both cases, more than ∼98 % of the beam losses are intercepted and confined within the collimation insertion located in PF. This demonstrates that the collimation system is effective in localizing losses in the dedicated collimation region, while strongly suppressing losses elsewhere in the ring.

The cleaning performance is consistent across planes: in both B1H and B1V, losses on the tertiary collimators (TCTs) are suppressed by approximately two orders of magnitude relative to those in PF. Synchrotron radiation (SR) collimators downstream of the TCTs experience even lower power loads, suppressed by 4 to 5 orders of magnitude. Since collimators upstream of the interaction points — including the TCTs and the synchrotron radiation (SR) collimators — may contribute to experimental background, their losses should be suppressed as much as possible. The acceptable loss limits on these collimators will need to be determined in future studies, including detailed shower simulations from the collimators to the experimental detector. All other elements outside the PF insertion show losses reduced by more than five orders of magnitude.

Zoomed views of the PF insertion are shown in Figs. 6.3 and 6.6. In both scenarios, the peak power loads on the collimators range from 100 W to 20 kW. Additional power loads, up to approximately 10 W, are observed on elements located between the primary (TCP) and secondary (TCS) collimators.

As expected, in B1H, the majority of losses are intercepted by the horizontal betatron collimators, while in B1V they are absorbed primarily by the vertical ones. In both cases, however, the off-momentum collimators in the second half

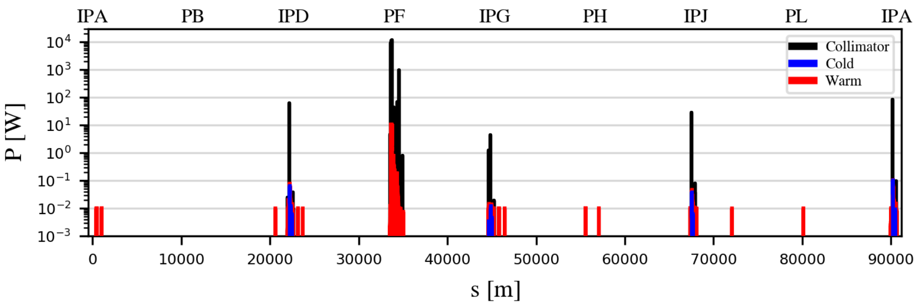

Figure 6.5. Loss map for the full FCC-ee ring for the B1V generic halo loss scenario. The plot shows the power load distribution along the full machine, binned in 10 cm intervals, assuming a beam lifetime of 5 minutes.

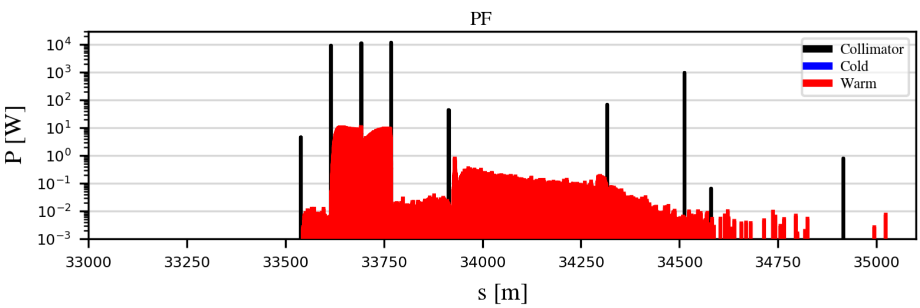

Figure 6.6. Loss map in the PF collimation insertion for the B1V generic halo loss scenario. The collimator region is zoomed in to highlight the distribution and efficiency of the local cleaning.

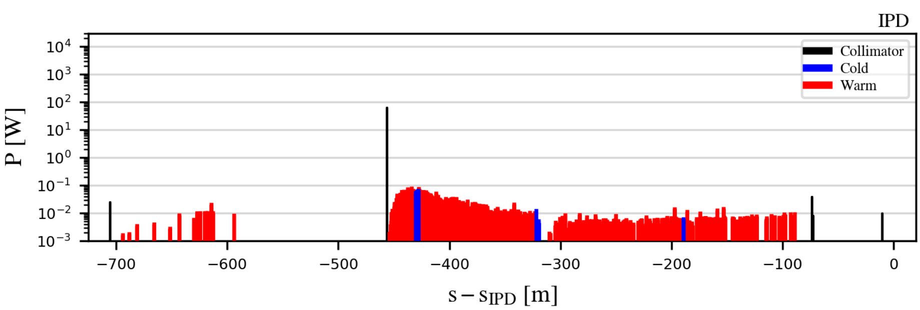

Figure 6.7. Loss map in the downstream interaction region (IPD) for the B1V generic halo loss scenario. The plot spans from 725 m upstream of IPD to 20 m downstream. Losses in this region are particularly critical due to the presence of final focus quadrupoles and detector components.

of the insertion intercept a non-negligible number of scattered particles. The highest power load among these is observed on the horizontal off-momentum primary collimator TCP.HP.B1, with a peak power load of approximately 30 W in B1H and 100 W in B1V. These losses are attributed to off-momentum particles that have lost energy in upstream interactions with the betatron collimators.

Clear signs of interplane scattering are also observed. In B1H, the highest individual power load in the insertion is recorded on the vertical primary collimator TCP.V.B1, caused by vertical scattering of particles initially interacting with TCP.H.B1. Conversely, in B1V, small horizontal losses appear on TCP.H.B1. This occurs because TCP.V.B1 is positioned downstream of TCP.H.B1, meaning that particles reaching TCP.H.B1 in B1V do so after one or more machine turns.

In both planes, the secondary collimators experience higher power loads than the primaries. This trend is consistent with the assumed collimator design parameters: the primary collimators are made of low-density carbon-based material (MoGr), whereas the secondaries are based on higher-density molybdenum alloys (Mo). The 30 cm length assumed for the Mo-based secondaries corresponds to roughly 30 radiation lengths, compared to less than 2 radiation lengths for the 25 cm C-based primaries. These differences explain the significantly higher absorption capacity of the secondary collimators.

It should be noted that the simulations presented here do not yet include the dedicated shower absorbers foreseen between the primary and secondary betatron collimators in PF. Their future inclusion is expected to reduce the observed clusters of warm losses in this region by concentrating power loads onto the absorber blocks. This would help to lower material activation and radiation levels in surrounding equipment.

Zoomed-in loss maps of the interaction region around IPD are shown in Figs. 6.4 and 6.7. In both B1H and B1V, this region is particularly sensitive due to the presence of superconducting elements — such as the final focus quadrupoles and crab sextupoles — as well as experimental detector components. The maximum power loads on the TCTs reach up to 100 W. Losses on superconducting magnets are minimal, with the most exposed of such elements being the crab sextupoles upstream of the IPs, where power loads remain below 100 mW.

Similar to PF, small clusters of warm losses are observed downstream of the TCTs in both planes. This indicates that additional shower absorbers will likely be required in this region as well, to localize these losses and lower radiation levels in potentially critical areas.

Overall, these results indicate that, under the assumed conditions, the FCC-ee collimation system provides effective protection to sensitive components. The system successfully confines the majority of losses within the PF collimation insertion and limits power loads on superconducting and detector regions to acceptable levels. While dedicated energy deposition and thermo-mechanical studies are still required to determine whether the observed loads are fully tolerable, the values obtained here are likely within operational limits.

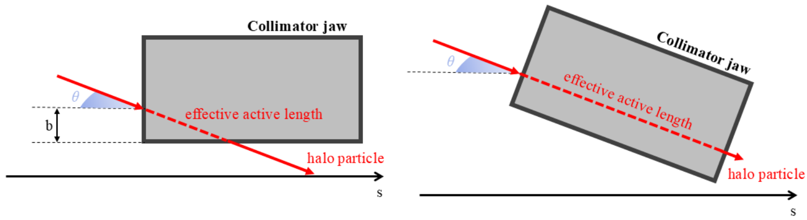

Figure 6.8. Conceptual illustration of the effect of collimator angular alignment. Left: A halo particle impacts the collimator jaw with a nonzero angle θ, interacting with only a fraction of its length. Right: When the collimator jaw is aligned with θ, the particle trajectory is parallel to the jaw surface, allowing interaction along the full length and maximizing absorption efficiency.

6.1.1 Collimator angular alignment

As observed in previous studies [114, 143, 144, 134] and confirmed by the simulations presented here, angular alignment of the primary collimators can significantly improve the performance of the FCC-ee halo collimation system.

Beam halo particles typically strike the primary collimator jaws with a non-zero angle, rather than parallel to the jaw surface. This angle of incidence depends on the local optical functions at the collimator location. For a primary collimator set at a transverse cut n_{TCP} (in units of the RMS beam size), the angle at which particles intersect the collimator jaw is

$$\theta = -n_{\mathrm{TCP}} \cdot \alpha_u \sqrt{\frac{\epsilon_u}{\beta_u}}, \tag{6.1}$$

where α_u and β_u are the Twiss parameters in the transverse plane u, and ϵ_u is the geometric emittance in that plane.

Because of this non-zero incidence angle, halo particles interact with only a fraction of the full collimator jaw length. Under the simplified assumption of straight-line particle trajectories through the jaw material, the effective length inside the collimator traversed by particles with impact parameter b is approximately

$$L_{\mathrm{eff}} \approx \frac{b}{\sin\theta}, \tag{6.2}$$

where b is the impact parameter, and θ is given by Eq. (6.1).

To mitigate this effect, the primary collimators can be angularly aligned to the local beam divergence, thereby maximizing the effective interaction length seen by halo particles. This ensures that particles interact with a larger (ideally full) jaw length, enhancing the absorption efficiency of the collimator. A conceptual illustration of this principle is shown in Fig. 6.8.

To quantify the performance gain, new simulations were carried out with the primary collimators tilted to match the beam divergence at their locations. Specifically, the horizontal primary collimator TCP.H.B1 was aligned to the

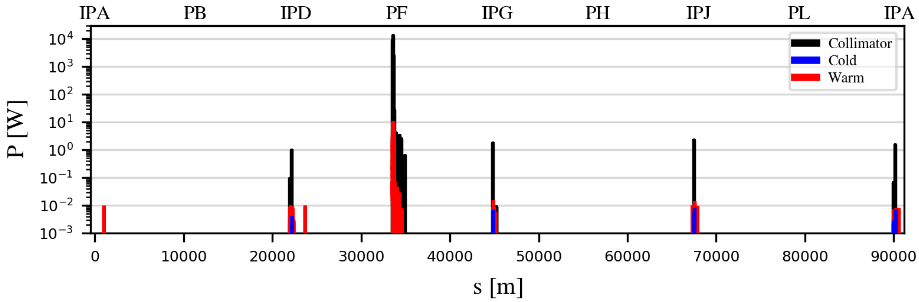

Figure 6.9. Loss map for the full FCC-ee ring for the B1H scenario with angularly aligned primary collimators. The plot shows the power load distribution binned in 10 cm intervals, assuming a beam lifetime of 5 minutes.

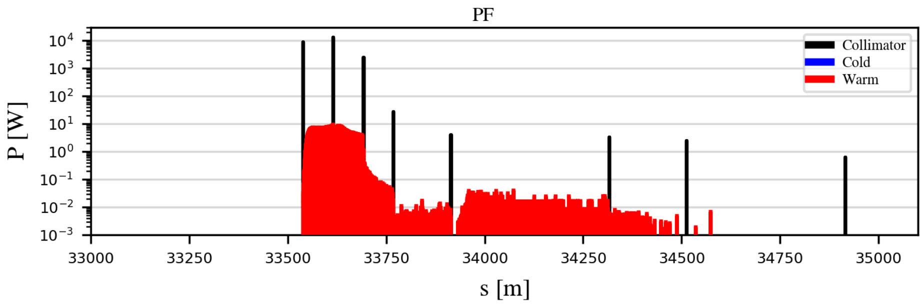

Figure 6.10. Loss map in the PF collimation insertion for the B1H scenario with angularly aligned primary collimators.

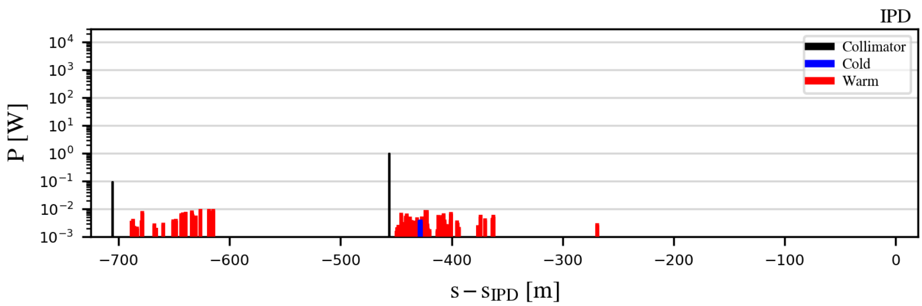

Figure 6.11. Loss map in the interaction region (IPD) for the B1H scenario with angularly aligned primary collimators.

local beam divergence of 63.7 μrad in the B1H case, while the vertical collimator TCP.V.B1 was aligned to a vertical divergence of 7.7 μrad in the B1V case.

The resulting loss maps are shown in Figs. 6.9, 6.10, and 6.11. These figures show the power load distribution for the B1H scenario with angularly aligned primary collimators, assuming a beam lifetime drop to 5 minutes.

The results clearly demonstrate a substantial improvement in collimation performance due to angular alignment. In particular, the power load on the TCTs upstream of the IPs is reduced by nearly two orders of magnitude compared to the case with untilted primary collimators illustrated in Figs. 6.2–6.4. This enhanced suppression of leakage losses highlights the importance of angular alignment for optimal system performance.

The specifications for the mechanical design of the FCC-ee collimators have been updated based on these results. Therefore, the collimator design, as discussed in Chapter 5, should include the capability to tilt the jaws via independent motorized actuators on either side. This allows precise angular positioning of the jaws with respect to the local beam divergence.

Although the performance gain is most pronounced for the primary collimators, a similar strategy is expected to benefit other collimators in the system — including secondary and tertiary collimators — albeit with reduced sensitivity due to the much larger impact parameters involved. Taking the horizontal plane as an example, the typical maximum impact parameters are on the order of 10 mm for the secondary collimators, as shown in Figs. 6.12 and 6.13, and around 100 μm for the tertiary collimators, as illustrated in Fig. 6.14. The larger impact parameters at the TCS compared to the TCT are explained by the higher horizontal β-function at the TCS locations relative to those of the TCTs, as can be seen in Figs. 5.10 and 5.11. Accordingly, and based on these findings, the current design foresees the inclusion of angular adjustment mechanisms for all collimators, enabling full exploitation of this performance enhancement across the system.

What has been presented so far corresponds to an idealized scenario in which the primary collimator jaws are perfectly angularly aligned with the local beam divergence. While this setup provides an upper bound on the achievable collimation performance, it represents a best-case configuration that is not fully achievable in practice. In a realistic machine environment, small deviations from the optimal angular setting are inevitable due to factors such as mechanical tolerances, actuator precision, misalignment, and deviations from the ideal optics.

To evaluate the robustness of the collimation system to such deviations, a dedicated set of simulations was performed in which the tilt angle of the primary collimators was varied around the optimal value. This parametric study allows quantifying the degradation in performance as a function of angular misalignment.

The resulting dependence of collimation performance on tilt deviation is presented in Fig. 6.15. The performance is evaluated in terms of the global inefficiency, defined as:

$$\text{global inefficiency} = \frac{\text{losses outside PF}}{\text{total losses}}, \tag{6.3}$$

where PF denotes the collimation insertion. A smaller value of global inefficiency indicates more effective loss containment within the collimation region, and thus better overall collimation performance.

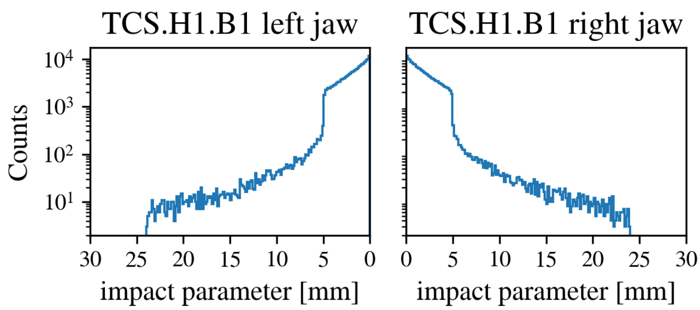

Figure 6.12. Impact parameter distribution on the horizontal secondary collimator TCS.H1.B1 for horizontal betatron losses (B1H), simulated with an untilted primary collimator TCP.H.B1 and a 1 µm maximum impact parameter.

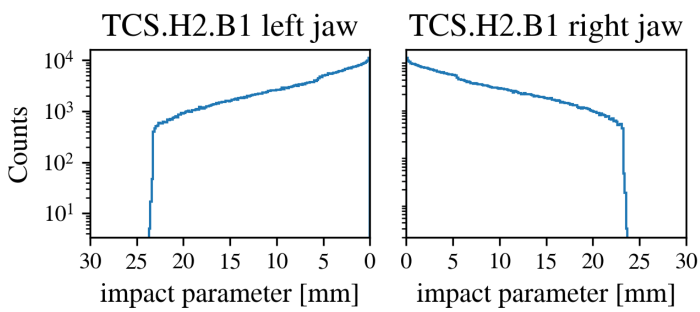

Figure 6.13. Impact parameter distribution on the horizontal secondary collimator TCS.H2.B1 for horizontal betatron losses (B1H), simulated with an untilted primary collimator TCP.H.B1 and a 1 µm maximum impact parameter.

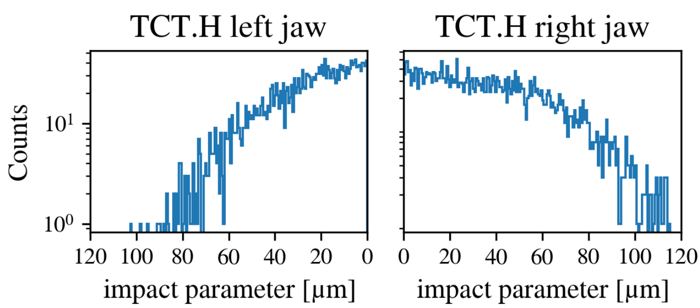

Figure 6.14. Impact parameter distribution on the horizontal tertiary collimator TCT.H upstream of IPJ for horizontal betatron losses (B1H), simulated with an untilted primary collimator TCP.H.B1 and a 1 µm maximum impact parameter.

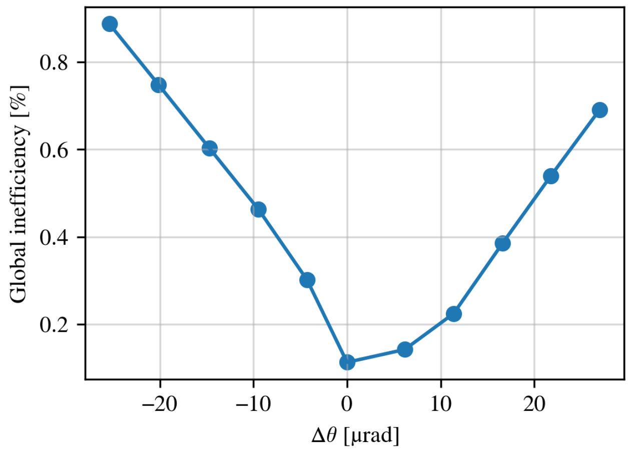

Figure 6.15. Global inefficiency as a function of primary collimator tilt deviation $\Delta\theta$. The minimum inefficiency is reached at the ideal tilt alignment ($\Delta\theta = 0$ μrad), with performance degrading as the deviation increases.

As shown in Fig. 6.15, any deviation from the ideal tilt angle results in a measurable increase in global inefficiency. For example, a deviation of 5 μrad leads to an increase in inefficiency by nearly a factor of 3, while a deviation of 10 μrad yields a degradation of almost a factor of 5. A more detailed view of this trend is shown in Fig. 6.16, where the factor increase in global inefficiency relative to the ideal tilt case is plotted as a function of tilt deviation. Three curves are presented, corresponding to the maximum, average, and minimum observed inefficiency increase across the set of horizontal betatron collimation (B1H) studies, alongside a reference line representing the inefficiency increase with no tilt applied.

This analysis confirms that while angular precision is important, the system remains relatively robust: even with tilt deviations as large as 25 μrad, the collimation performance remains significantly better than in the un-tilted case. At this extreme, the inefficiency is still improved by approximately a factor of 3 relative to the case with parallel collimator jaws. For reference, in the LHC collimator design, a minimum motor step size of 5 μm is implemented, corresponding to an angular resolution of approximately 5 μrad for a 1 m-long jaw. While the active jaw length of FCC-ee collimators is expected to be shorter, the full collimator tank — including tapers to reduce impedance — will be significantly longer. This allows placing the actuators farther apart, enabling angular alignment precision comparable, or even better, to that achieved in the LHC. These results underline both the importance of implementing angular alignment and the tolerable range of deviations that can be accommodated without dramatic performance loss.

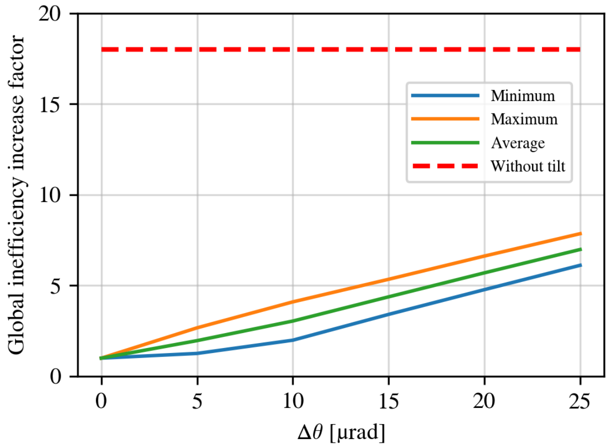

Figure 6.16. Factor increase in global inefficiency as a function of tilt deviation. The maximum, average, and minimum inefficiency factors are shown relative to the ideal tilt case. The blue horizontal line indicates the inefficiency level with no tilt applied.

6.1.2 Impact parameter scan

The impact parameter b—defined as the transverse distance between the edge of the collimator jaw and the incoming particle trajectory—plays a key role in determining the interaction between beam halo particles and the collimator material, and thus in shaping the overall collimation performance.

Smaller impact parameters correspond to shallower, more grazing interactions, resulting in shorter effective path lengths through the jaw material. This, in turn, leads to fewer particle–matter interactions, smaller angular kicks, and an increased probability for particles to escape interception by halo collimators and leak towards downstream regions. Conversely, larger impact parameters correspond to deeper penetrations into the jaw material, where particles receive stronger kicks and are more efficiently absorbed within the collimation insertion.

To quantify the dependence of the FCC-ee collimation performance on this parameter, a dedicated series of simulations was carried out for the B1H case (i.e., horizontal betatron collimation losses for the FCC-ee positron Beam 1), systematically varying the maximum impact parameter b_{max} of the direct halo distribution on the horizontal primary collimator TCP.H.B1. The purpose of this study was to investigate whether a *critical impact parameter* could be identified—i.e., a value of b_{max} at which the global collimation performance reaches a minimum—and to understand how the system efficiency varies for different impact parameters.

The simulations were performed using the same setup and parameters as in the generic beam halo study (Section 6.1). The only parameter varied was the maximum impact parameter b_{max}, which was scanned from 2 μm down to 0.01 µm. Each simulation tracked 5×10^6 macroparticles for 500 turns in the full nonlinear FCC-ee lattice, including synchrotron radiation effects, RF cavities, a full aperture model, and collimators modeled in BDSIM/Geant4.

The results of the scan are presented in Fig. 6.17, which shows the behavior of the *global inefficiency* (defined in Eq. (6.3)) as a function of the maximum impact parameter b_{max}.

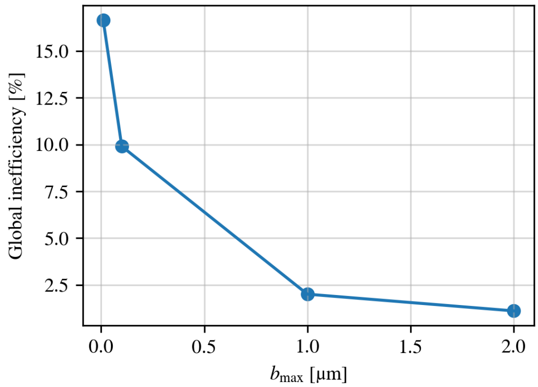

Figure 6.17. Global inefficiency as a function of the maximum impact parameter b_{max} for the FCC-ee positron beam (B1) in the Z operation mode. Each point corresponds to an Xsuite–BDSIM tracking simulation of 5×10^6 macroparticles for 500 turns in the full nonlinear FCC-ee lattice (V25.2 GHC). A monotonic increase in global inefficiency is observed with decreasing b_{max}, indicating that shallower particle–jaw interactions lead to less effective confinement of losses within the PF collimation insertion. No critical impact parameter is observed within the studied range.

A clear monotonic trend is observed: the global inefficiency increases (i.e., the collimation performance worsens) monotonically with decreasing b_{max}, indicating that shallower halo–primary collimator interactions systematically lead to poorer confinement of beam losses within the collimation insertion in PF. The reasons for this trend are discussed in detail below.

This trend differs from that typically observed in LHC studies [37], where a critical impact parameter is found around 1 µm—corresponding to a minimum in collimation cleaning performance—beyond which the efficiency improves again as b_{max} increases. In that case, when b_{max} is smaller than the critical value, the impact with the primary collimator is too shallow to immediately produce a loss. Instead, the particle receives a weak perturbation that allows it to survive one or more turns in the ring until it eventually re-encounters the primary collimator at a larger impact parameter and is then efficiently removed. This mechanism results in the observed improvement in cleaning performance for $b_{\text{max}} < b_{\text{max,crit}}$.

In the FCC-ee case, no such turning point is observed: the global inefficiency increases continuously as b_{max} becomes smaller.

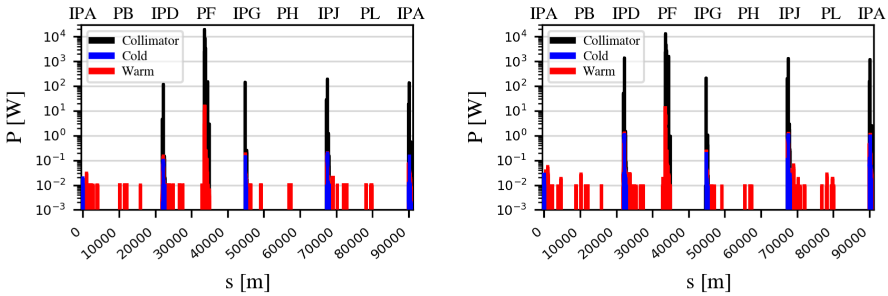

Figure 6.18. Full-ring loss maps for the B1H impact-parameter scan: **left** $b_{\max} = 1\ \mu\text{m}$, **right** $b_{\max} = 0.01\ \mu\text{m}$. Power loads are shown per 10 cm bin assuming a 5 minute beam lifetime. As $b_{\max}$ decreases, losses at the TCTs upstream of the IPs increase, with a concurrent rise at TCP.H.B1.

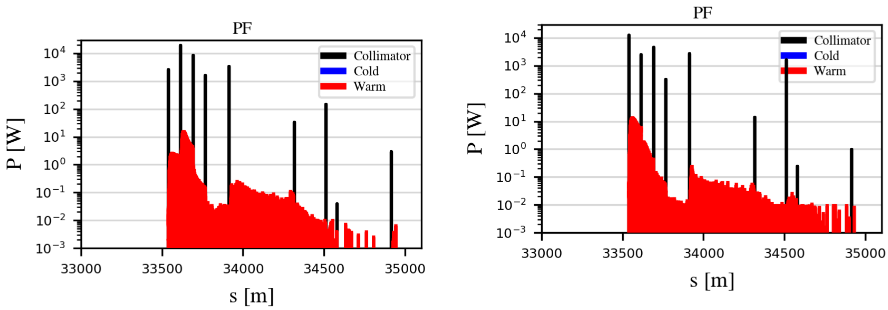

Figure 6.19. Loss maps in the PF collimation insertion for the B1H impact-parameter scan: **left** $b_{\max} = 1\ \mu\text{m}$, **right** $b_{\max} = 0.01\ \mu\text{m}$. Power loads (single-bin per collimator; 10 cm bins elsewhere) assume a 5 minute lifetime. Smaller $b_{\max}$ yields higher losses at TCP.H.B1 and reduced loads on the horizontal secondaries, consistent with increased leakage downstream.

Loss maps obtained in the scan are reported in Figs. 6.18–6.20 for two representative cases with $b_{\max} = 1\ \mu\text{m}$ and $b_{\max} = 0.01\ \mu\text{m}$. By comparing the loss maps obtained for different $b_{\max}$ values, several trends can be observed.

First, a comparison of the full-ring loss maps (Fig. 6.18) shows that the overall increase in losses for smaller impact parameters occurs mainly at the tertiary collimators (TCTs) located upstream of each interaction point. This effect can be seen in more detail in Fig. 6.20. In addition, the losses at the horizontal primary collimator TCP.H.B1 itself increase as $b_{\max}$ decreases, as shown in Fig. 6.19, indicating the presence of a multi-turn re-impact mechanism similar to that observed in LHC collimation studies. However, as shown in Fig. 6.17, since the global inefficiency continuously increases with decreasing $b_{\max}$, this effect appears to be counteracted by the concurrent rise in losses at the TCTs as $b_{\max}$ is reduced.

Focusing on the PF collimation insertion (Fig. 6.19), it is also observed that the losses at the secondary horizontal betatron collimators decrease for

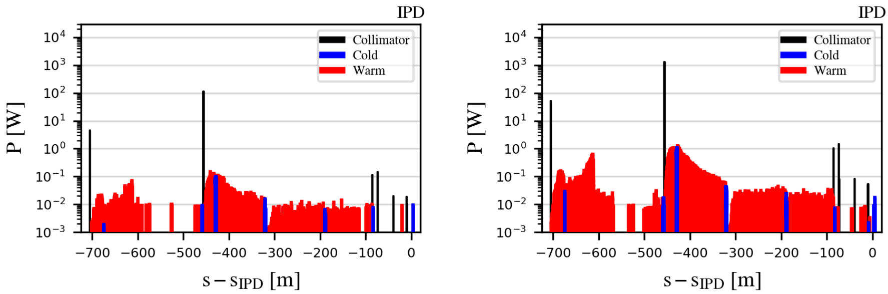

Figure 6.20. Loss maps of the interaction region around IPD for the B1H impact-parameter scan: **left** $b_{\text{max}} = 1$ µm, **right** $b_{\text{max}} = 0.01$ µm. The plotted region spans from 725 m upstream of IPD to 20 m downstream. TCT losses grow markedly as b_{max} decreases, highlighting increased leakage toward the interaction regions.

smaller impact parameters. In contrast, in the vertical plane, losses at the primary vertical betatron collimator TCP.V.B1 decrease with decreasing b_{max}, while losses at the downstream secondary vertical collimators TCS.V1.B1 and TCS.V2.B1 increase.

These trends can be explained as follows. For smaller and smaller b_{max}, the angular kicks acquired by the particles interacting with the primary collimator become too small to be intercepted by one of the downstream secondary collimators (or by another collimator in PF in a different plane). As a result, an increasing fraction of these weakly scattered particles escapes interception in the PF insertion and travels further downstream. As opposed to the LHC case, where particles exiting the collimation insertion can come back and interact with the primary again on a later turn, many of the particles escaping PF in FCC-ee typically end up outside of the dynamic aperture, causing them to be lost on the TCTs. This behavior is explained in detail below.

As a representative example, the left (positive-x) jaw of TCP.H.B1 has been considered. In linear optics, the transport between the primary collimator location s_0 and a downstream point s can be written as

$$x(s) = \sqrt{\frac{\beta_x}{\beta_{x,0}}}\,(\cos\Delta\mu_x + \alpha_{x,0}\sin\Delta\mu_x)\,x_0 + \sqrt{\beta_x\,\beta_{x,0}}\,\sin\Delta\mu_x\,(p_{x,0} + \Delta p_x), \tag{6.4}$$

where x_0 and $p_{x,0}$ denote the horizontal position and normalized transverse momentum of the particle at the entrance of TCP.H.B1, and Δp_x represents the horizontal kick imparted by the interaction with the collimator jaw. The parameters $\beta_{x,0}$ and $\alpha_{x,0}$ are the Twiss parameters at the location of TCP.H.B1, while β_x is the beta function at the downstream observation point (e.g., TCS.H1.B1 or TCS.H2.B1). The angle $\Delta\mu_x$ corresponds to the horizontal betatron phase advance between the two locations.

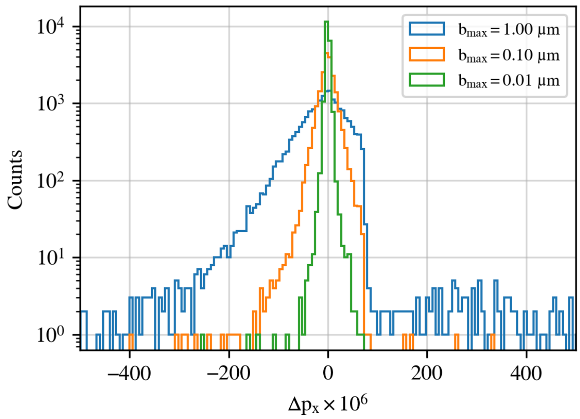

Figure 6.21. Horizontal kick distributions of the outgoing particles from TCP.H.B1 for different impact parameters.

By inverting Eq. (6.4) and imposing the amplitude conditions at the start (TCP.H.B1) and at the end of the transport (TCS.H1.B1 or TCS.H2.B1), it is possible to compute the range of horizontal kicks for which a particle will *not* be intercepted by one of the horizontal secondary collimators. This results in the following window:

$$\Delta p_x \in (-5.48 \times 10^{-6}, +6.52 \times 10^{-6}) . \tag{6.5}$$

By tracking the direct halo distributions with varying impact parameters through the TCP.H.B1 collimator, the outgoing particle distributions can be recorded and the horizontal kicks Δp_x imparted to the particles can be analyzed. The resulting distributions are shown in Fig. 6.21 for $b_{\text{max}} = 1$ µm, $b_{\text{max}} = 0.1$ µm, and $b_{\text{max}} = 0.01$ µm.

From Fig. 6.21, it is evident that the horizontal kick distribution progressively narrows as b_{max} decreases. More specifically, the fraction of particles scattered within the angular window defined in Eq. (6.5) increases with decreasing b_{max}. This implies that a larger number of particles interacting with TCP.H.B1 receive kicks too small to reach the downstream horizontal secondary collimators, thereby bypassing the horizontal betatron collimation system in PF. Consequently, a greater fraction of these particles leaks beyond PF and is eventually lost further downstream (e.g., on the TCTs), leading to a higher global inefficiency as b_{max} is reduced.

The above example provides a simplified, semi-analytical demonstration that for smaller b_{max}, a larger fraction of particles can bypass the horizontal betatron collimation system. However, since additional collimators are also present in PF—in the vertical and horizontal-momentum planes—a full quantitative assessment requires detailed particle tracking including all collimator interactions.

This was performed using Xsuite–BDSIM. Direct halo distributions with varying b_{max} values were tracked from the TCP.H.B1 primary collimator to the

Table 6.1. Number of particles escaping the PF collimation insertion for different impact parameters $b_{\max}$. Each case corresponds to 10^5 primary positrons interacting with the positive-x jaw of TCP.H.B1.

$b_{\max}$ [μm]	**Particles escaping PF**
1.0	5 084 (5.1%)
0.1	30 320 (30.3%)
0.01	86 318 (86.3%)

end of the PF collimation insertion. At the end of the tracking, the number of surviving particles was recorded. The results are summarized in Table 6.1.

In this study, 10^5 primary positrons were generated to interact with the left (positive-x) jaw of TCP.H.B1 for three different impact parameters: 1 μm, 0.1 μm, and 0.01 μm. As expected, with decreasing impact parameter, the number of particles escaping the PF collimation region increases significantly.

However, it is important to stress that a larger fraction of particles escaping the PF collimation insertion is not, by itself, sufficient to explain the observed increase in losses at the TCTs for smaller $b_{\max}$. More precisely, this increase cannot be fully explained by considering linear optics alone.

In a purely linear optics regime, particles that bypass the halo collimation system in PF should not be intercepted by the TCTs, since these are set at the same normalized betatron amplitude as the secondary collimators (TCSs), as detailed in Chapter 5. Therefore, to account for the observed rise in TCT losses, nonlinear effects must play a role.

This can occur if the particles escaping the halo collimation system in PF lie outside the dynamic aperture (DA). In that case, they occupy a nonlinear and chaotic region of phase space where linear optics no longer apply. Nonlinear beam dynamics then dominate, leading to chaotic and unpredictable trajectories in which the transverse amplitudes of these particles can grow rapidly. As a consequence, particles escaping the PF collimation system are eventually lost on the first aperture restrictions they encounter—namely, the TCTs.

Hence, the observed increase in global inefficiency with decreasing $b_{\max}$ most likely originates from nonlinear dynamics and dynamic-aperture exceedance of the particles escaping the collimation system in PF.

To confirm this interpretation, the direct halo distributions (each consisting of 10^5 particles) with varying $b_{\max}$ values (1 μm, 0.1 μm, and 0.001 μm) were tracked using Xsuite–BDSIM up to an endpoint at the end of the collimation insertion PF, chosen as the dispersion-free location corresponding to the point where the horizontal dispersion D_x crosses zero downstream of the momentum collimation section.

At this endpoint, the normalized betatron amplitudes of the particles were computed as

$$A_x^{\text{norm}} = \sqrt{\left(\frac{x}{\sigma_x}\right)^2 + \left(\frac{p_x}{\sigma_{p_x}}\right)^2}, \tag{6.6}$$

$$A_y^{\mathrm{norm}} = \sqrt{\left(\frac{y}{\sigma_y}\right)^2 + \left(\frac{p_y}{\sigma_{p_y}}\right)^2}. \tag{6.7}$$

Here, x and y denote the transverse particle positions at the endpoint, while p_x and p_y are the corresponding normalized transverse momenta. The quantities σ_x and σ_y represent the local horizontal and vertical beam sizes, and σ_{p_x} and σ_{p_y} are the corresponding rms beam divergences.

The resulting particle distributions were then plotted in the $(A_x^{\mathrm{norm}}, A_y^{\mathrm{norm}})$ plane. An approximate yet representative XY dynamic aperture (DA) boundary[1] was superimposed on the same plot for reference. The corresponding results are shown in Fig. 6.22.

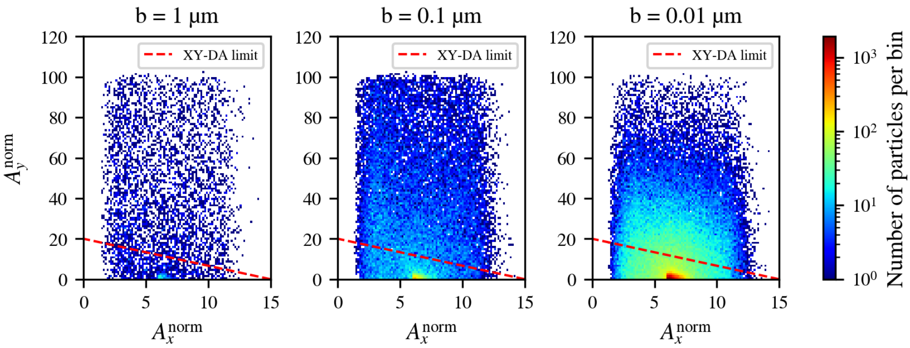

Figure 6.22. Normalized amplitude distributions $(A_x^{\mathrm{norm}}, A_y^{\mathrm{norm}})$ of particles escaping the PF collimation system for different $b_{\max}$ values. The dashed line indicates the approximate XY dynamic aperture limit.

As shown in Fig. 6.22, a substantial fraction of the particles escaping the PF collimation system lie outside the XY-DA limit. Moreover, the number of particles beyond the DA boundary increases significantly as $b_{\max}$ decreases. This confirms that the degradation of the global cleaning performance for smaller impact parameters originates from nonlinear beam dynamics and dynamic-aperture exceedance of the particles escaping the PF collimation system.

To further quantify this effect, the number of particles found outside the XY-DA limit was counted for each $b_{\max}$. The results, summarized in Table 6.2, show that the fraction of particles exceeding the dynamic aperture increases markedly with decreasing $b_{\max}$, confirming the strong correlation between smaller impact parameters, DA exceedance, and the rise in global inefficiency.

In summary, this study demonstrates that the observed increase in losses on the TCTs with decreasing impact parameter $b_{\max}$ originates primarily from a limitation of the machine's dynamic aperture, most notably in the vertical plane, as illustrated in Fig. 6.22. As will be shown later in this chapter, the same limited vertical DA also amplifies beam–residual gas Coulomb-scattering losses, highlighting its crucial role in shaping both halo- and beam–gas–induced loss

[1]The precise XY-DA contour is reported later in this chapter; see Fig. 6.38 for comparison.

Table 6.2. Fraction of particles escaping the PF collimation insertion and fraction lying outside the dynamic aperture (DA) for different impact parameters b_{max}. Each case corresponds to 10^5 primary positrons interacting with the positive-x jaw of TCP.H.B1.

b_{max} [μm]	**Particles escaping PF**	**Particles outside DA**
1.0	5 084 (5.1%)	4 004 (4.0%)
0.1	30 320 (30.3%)	21 984 (22.0%)
0.01	86 318 (86.3%)	40 836 (40.8%)

patterns. Since this behaviour arises mainly from a DA constraint rather than from an intrinsic limitation of the collimation system itself, it is expected that continued optimization of the FCC-ee lattice design—including improvements to the dynamic aperture—will progressively mitigate this effect. With an enlarged DA, the increased TCT losses observed at smaller b_{max} values should become less significant, and multi-turn re-impacts on primary collimators would emerge more clearly, making it possible to identify a critical impact parameter. An example of such an improved optics configuration is the FCC-ee lattice with *Local Chromatic Correction* (LCC) optics, which is currently being developed in parallel to the *Global Hybrid Correction* (GHC) optics considered in this thesis. For the time being, however, a maximum impact parameter of $b_{\mathrm{max}} = 1$ μm is retained as the standard reference for evaluating the FCC-ee collimation system performance against generic beam halo losses.

6.1.3 Single-stage halo collimation

As mentioned in Chapter 5, the halo collimation insertion in PF adopts a two-stage collimation system with one primary and two secondary collimators per plane[2] because it offers improved cleaning performance compared to a single-stage system relying only on primary collimators. To provide a direct comparison with the results presented earlier in this chapter for the two-stage system, this section reports the FCC-ee collimation performance for the *generic beam halo* loss scenarios when the secondary collimators in PF are removed. The goal is to visualize the change in beam loss patterns and leakage outside the halo collimation insertion in PF when only the primary collimators are present.

Simulation setup

The simulation setup is the same as that described in Section 6.1 for the B1H and B1V cases (FCC-ee V25.2 GHC [15], Z operation mode). The only modification is the removal of the secondary collimators in PF. The same initial direct halo distributions are used, generated at TCP.H.B1 for the horizontal

[2]Horizontal, vertical, and momentum

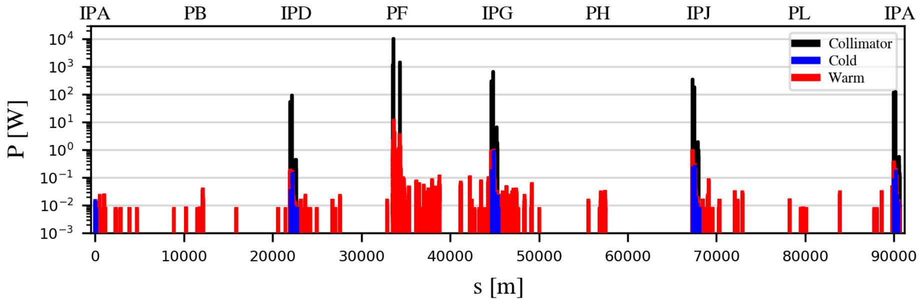

Figure 6.23. Loss map for the full FCC-ee ring for the B1H generic halo scenario *without* secondary collimators in PF. Power loads are binned in 10 cm intervals and normalized to a 5 minute beam lifetime.

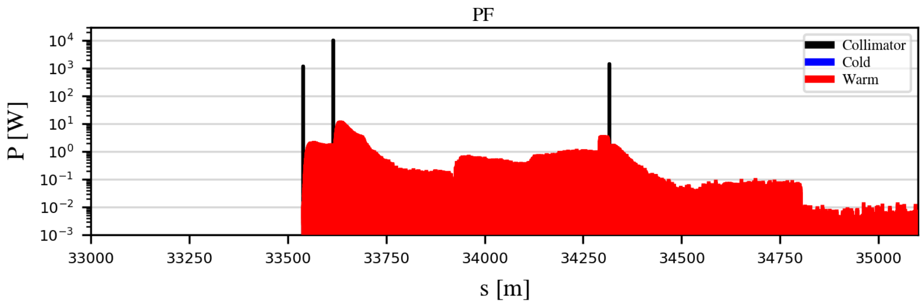

Figure 6.24. Zoomed view of B1H losses in the PF insertion *without* secondary collimators. Larger clusters of aperture losses appear due to the absence of secondary collimators.

case (B1H) and at TCP.V.B1 for the vertical case (B1V). Tracking includes synchrotron radiation with damping and quantum excitation, RF cavities, magnet tapering, a detailed aperture model, and BDSIM/Geant4 collimator interactions, as in the baseline study. Particles are tracked for 500 turns, and losses are binned longitudinally in 10 cm intervals, with collimators shown as single bins corresponding to their physical length (Table 5.5). Power loads are reported under the same conservative lifetime assumption used for the generic halo studies (5 minutes).

Results

Figures 6.23 and 6.24 show the loss maps for the B1H case when only the primary collimators are installed in PF. A clear degradation of the overall cleaning performance is observed with respect to the two-stage baseline configuration (Figs. 6.2–6.4). The most evident change is the significant increase in loss leakage outside the halo collimation insertion, particularly on the tertiary collimators (TCTs) located upstream of the interaction regions. Although the peak power loads on the most exposed TCTs do not increase dramatically—with the vertical

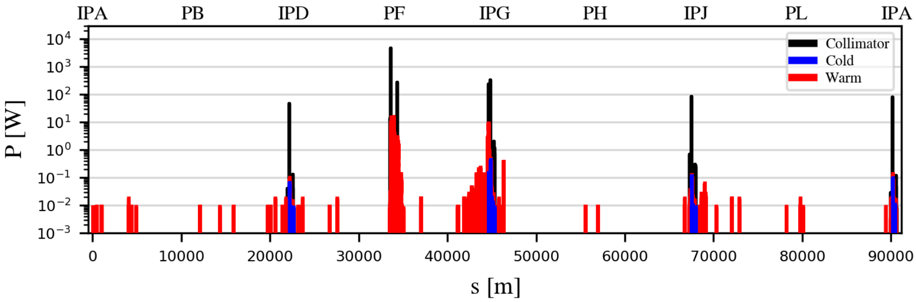

Figure 6.25. Loss map for the full FCC-ee ring for the B1V generic halo scenario *without* secondary collimators in PF. Power loads are binned in 10 cm intervals and normalized to a 5 minute beam lifetime.

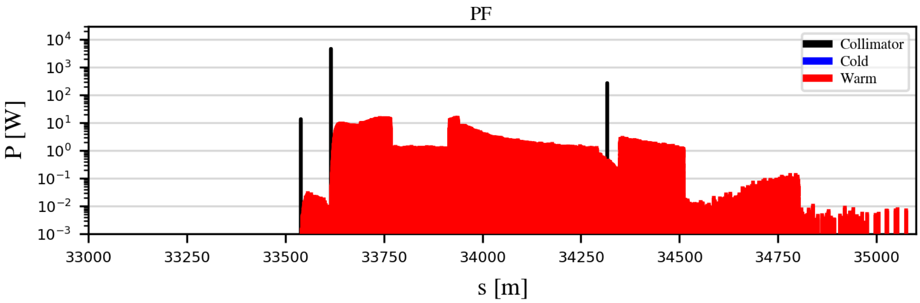

Figure 6.26. Zoomed view of B1V losses in the PF insertion *without* secondary collimators. Larger clusters of aperture losses appear due to the absence of secondary collimators.

TCT upstream of IPG featuring an increase of roughly a factor of two—the removal of the secondary collimators causes all TCTs, including those that were less exposed in the two-stage configuration, to intercept comparable levels of losses. An overall increase in losses is also observed on the SR collimators located downstream of the TCTs. This results in higher and less localized losses in the IRs. This effect is particularly undesirable, since losses on IR collimators can generate secondary showers directed toward the experimental detectors. In general, it is a design goal of the collimation system to concentrate losses on collimators placed far from the detectors—such as those in PF—rather than on elements in the vicinity of the experiments, where particle showers may cause unwanted backgrounds that degrade the quality of experimental data.

In addition to the increased leakage toward the interaction regions, the loss maps reveal larger aperture losses within the PF insertion itself and in the arcs between PF and IPG, as well as between IPG and PH. The absence of relatively dense (Mo-based) secondary collimators leads to a larger fraction of scattered halo particles escaping the primary collimator jaws and impacting surrounding components. This translates into higher power deposition in the environment, raising potential concerns for equipment integrity, tunnel

Table 6.3. Global inefficiency (Eq. (6.3)) for single-stage and two-stage (baseline) halo collimation in PF.

Case	Single-stage	Two-stage	Increase factor
B1H	12.0%	2.0%	6
B1V	8.9%	0.6%	16

activation, and radiation protection.

Figures 6.25 and 6.26 show the corresponding results for the vertical case (B1V). The overall picture is similar to that observed for B1H: the removal of the secondary collimators results in larger leakage outside the PF insertion and increased losses on the TCTs and SR collimators, as well as larger aperture losses in PF and in the arcs. It is particularly worth noting that, in the B1V case, the maximum power loads on the collimators upstream of IPG increase by approximately two orders of magnitude compared to the two-stage configuration, highlighting the crucial role of the secondary collimators in absorbing particles out-scattered from the primary collimators.

Global inefficiency. To quantify the overall impact, the global inefficiency defined in Eq. (6.3) has been evaluated for the single-stage and two-stage configurations. For B1H, the global inefficiency increases from 2.0% (two-stage) to 12.0% (single-stage), i.e. by a factor of 6. For B1V, it increases from 0.6% (two-stage) to 8.9% (single-stage), i.e. by a factor of 16. These figures confirm quantitatively the trends visible in the loss maps: removing the secondary collimators substantially degrades loss localization in PF and increases leakage toward the interaction regions.

The observed degradation when removing the secondary collimators is consistent with the collimator material and length choices discussed in Chapter 5. In the two-stage system, the combination of relatively short ($\lesssim 2\ X_0$) low-density C-based primary collimators, with X_0 being the radiation length, followed by longer (on the order of 30 X_0) higher-density Mo-based secondary collimators, provides robust initial interception and efficient downstream absorption of scattered debris. Without the secondary stage, a larger fraction of the scattered halo is lost onto warm elements in PF and leaks toward the IR, increasing the load on the TCTs, SR collimators, and nearby components. This comparison therefore supports the design choice of a two-stage halo collimation system in PF to maximize cleaning efficiency and minimize leakage toward sensitive regions of the machine.

6.2 Off-momentum losses

This section presents an evaluation of the collimation performance of the proposed FCC-ee collimation system against off-momentum particle losses, i.e. losses originating from particles that acquire large transverse amplitudes as a consequence of a momentum offset Δp with respect to the reference momentum

p_0.

To investigate this mechanism, a dedicated *RF sweep* simulation has been set up. In this simulation, the RF-cavity frequency is slowly varied during tracking. When the sweep is sufficiently slow, the RF bucket remains stable and follows the frequency shift, effectively moving its center to a non-zero momentum deviation $\delta = \Delta p/p_0$ while keeping the particles captured. As a result, the average momentum offset of the tracked bunch is progressively increased, thereby populating the off-momentum halo in a controlled, quasi-adiabatic way. This scenario could represent both a slow failure of the RF system and other relatively slow beam-loss processes that lead to significant off-momentum losses.

As the bunch drifts to larger δ values, particles with sufficiently large momentum deviations eventually reach transverse amplitudes that exceed the physical or dynamic aperture, leading to losses. These losses are recorded during tracking to assess how efficiently the collimation system confines off-momentum losses away from sensitive regions. The RF-sweep functionality used here is implemented in the Xcoll package, developed specifically to study off-momentum losses and the associated collimation performance.

Simulation setup

Based on the RF-sweep setup described above, an Xsuite–BDSIM simulation was performed for the FCC-ee positron beam (Beam 1, B1) at a beam energy of 45.6 GeV (Z operation mode). The initial distribution was a matched Gaussian bunch at the beginning of the arc section between IPA and PB, using the equilibrium collision parameters in Table 1.2. Since beam–beam interactions were not included, the vertical geometric emittance at collision—1.9 pm—was preserved by means of vertical wigglers introducing local D_y and tuned to reproduce the target equilibrium value.

A total of 5×10^6 macroparticles were tracked for 6000 turns in the full nonlinear FCC-ee lattice (V25.2 GHC [15]), including the crab-waist collision scheme, a detailed aperture model, and the complete collimation system. Collimators were modeled in BDSIM/Geant4. Synchrotron radiation (radiation damping, quantum excitation) and lattice tapering were included. For SR, a stochastic quantum-excitation model was used, i.e. each particle receives individual random energy kicks at each step.

The RF sweep was configured to shift the RF frequency by 300 Hz over 6000 turns, i.e. +0.05 Hz/turn (toward negative δ in this study). This corresponds to moving the bucket center by

$$\Delta\delta \simeq -2.63\% \quad \text{over the full sweep,}$$

i.e. a per-turn change of $\sim -4.38 \times 10^{-6}$. In bucket units, this is a shift of ~ 0.55 bucket heights. By the end of the sweep the bunch center reached $\delta \approx -2.6\%$. This value is significantly larger than the momentum acceptance of the machine (about 1%); therefore, all particles are expected to be lost over the course of the simulation.

Beam-loss positions were recorded throughout tracking, and the longitudinal loss distribution was binned in 10 cm intervals to produce loss maps for the off-momentum scenario. The corresponding results are presented following section.

Results

The off-momentum loss maps are shown in Figs. 6.27 and 6.28. The plots show the longitudinal distribution of beam losses, expressed as power loads in 10 cm bins. Power loads are obtained by summing, in each bin, the energy of all lost macroparticles and normalizing consider a beam lifetime drop to 5 minutes. Collimators are displayed with a single bin corresponding to their physical length.

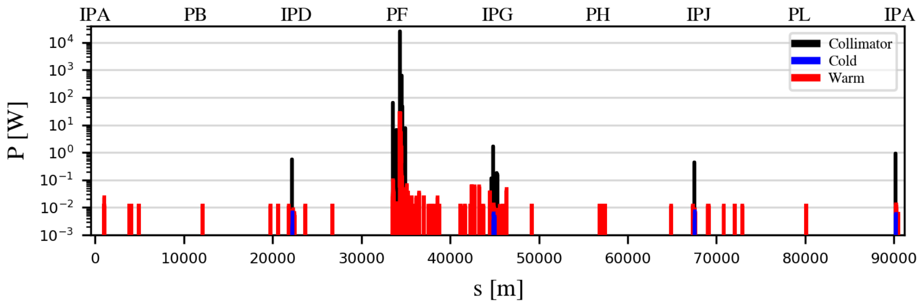

Figure 6.27. Longitudinal distribution of off-momentum losses in the FCC-ee (full ring) from the RF-sweep simulation. Losses are shown as local power loads in 10 cm bins, assuming a 5 minute beam lifetime. Most losses are intercepted in the PF collimation insertion, confirming the effectiveness of the off-momentum collimation system.

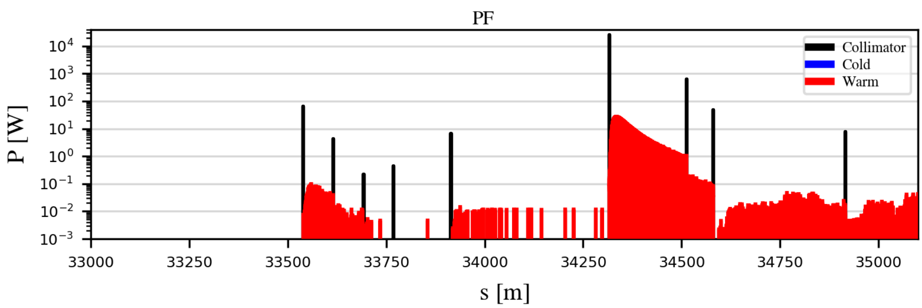

Figure 6.28. Zoomed view of the PF collimation insertion for the off-momentum scenario. Losses are concentrated in the off-momentum collimation section, with minimal leakage outside the collimation insertion.

The first losses appear around turn 1700, when the RF bucket center is $\delta \approx -0.75\%$. From that point, losses rise rapidly; by turn 2400 (bucket center at $\delta \simeq -1.05\%$) the entire bunch is lost.

As intended, the first losses occur at the machine momentum bottleneck, which by design is the primary off-momentum collimator TCP.HP.B1. The loss maps show that the vast majority of losses, i.e. more than 99 %, are intercepted in the second half of the PF insertion, corresponding to the off-momentum collimation section. The most exposed device is the primary off-momentum collimator TCP.HP.B1, with a peak load of ∼35 kW. Downstream, the secondary off-momentum collimators TCS.HP1.B1 and TCS.HP2.B1, together with the secondary vertical betatron collimator TCS.V2.B1, absorb the remaining debris, with loads up to several hundred watts. TCS.V2.B1 intercepts a non-negligible fraction of particles scattered vertically in the interaction with TCP.HP.B1. Noticeable warm losses appear between the primary and secondary off-momentum collimators, driven by out-scattering at TCP.HP.B1; these remain well confined within PF.

Lower losses are also observed on the horizontal and vertical primary betatron collimators, TCP.H.B1 and TCP.V.B1 (both below 100 W). Residual losses on the vertical TCTs upstream of the IPs are strongly suppressed—by about four orders of magnitude relative to TCP.HP.B1. Outside PF, losses are negligible across the ring.

Overall, the off-momentum loss pattern confirms that the FCC-ee collimation system effectively localizes off-momentum losses in the dedicated section. Compared to the generic betatron-halo case (Section 6.1), off-momentum losses are even better confined within PF, with significantly reduced leakage toward the interaction regions. The absolute power levels are comparable to those in the halo case, while the spatial confinement is improved. As in the betatron-collimation studies, performance is expected to benefit further from angular tilts of the collimator jaws, maximizing the effective interaction length of the off-momentum halo with the material.

6.3 Beam-gas losses

Although in the FCC-ee the beam lifetime is limited by radiative Bhabha scattering at the interaction points, a precise understanding of beam–gas interactions remains essential. These interactions may influence local loss patterns, contribute to experimental background, and place constraints on the design and performance of both the vacuum and collimation systems [11, 114, 145, 143, 144, 134].

In this section, we present a study of beam losses arising from beam–gas interactions in the FCC-ee. The results are obtained using the dedicated beam-gas Monte Carlo routine developed in the context of this thesis and described in Chapter 3. The validity of this simulation routine has been benchmarked through comparison with experimental background measurements at SuperKEKB, showing very good agreement, as discussed in Chapter 4.

This study provides quantitative estimates of both the beam lifetime contributions and the spatial loss distribution associated with beam–gas interactions, under realistic FCC-ee operating conditions. The relative importance of

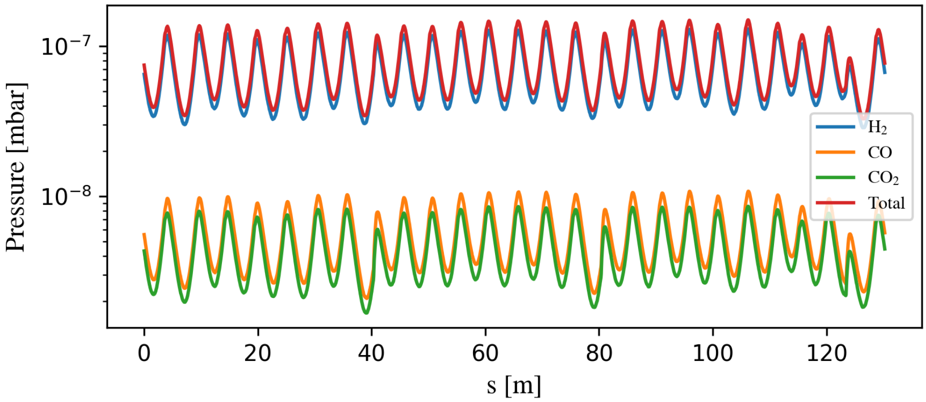

Figure 6.29. Residual gas pressure profile in a representative FCC-ee arc section, obtained from SYNRAD++ and MOLFLOW simulations after 1 hour of beam conditioning at nominal Z-mode current [147].

bremsstrahlung and Coulomb scattering processes is examined, with particular attention to their impact on loss localization, collimation performance, and implications for detector backgrounds.

Simulation setup

Beam–gas losses in the FCC-ee have been evaluated using the Xsuite-BDSIM simulation framework, with the setup described in Chapter 3. Simulations were performed for the positron beam (B1) at a beam energy of 45.6 GeV, corresponding to the FCC-ee (V25.2 GHC [15]) Z operation mode.

The vacuum pressure profile used as input to the simulations was based on SYNRAD++ and MOLFLOW [101, 102] calculations, performed by vacuum experts under a pessimistic assumption of only 1 hour of beam conditioning at nominal Z-mode current [146]. In these simulations, the dominant gas load arises from photon-stimulated desorption (PSD) induced by synchrotron radiation, as is typical for electron storage rings. A NEG-coated vacuum chamber has been considered. These calculations were originally carried out for two representative sections of the FCC-ee V23 lattice: a 130 m-long arc cell [147] (see Fig. 6.29) and the machine–detector interface (MDI) region [148], extending from about −600 m to about +250 m relative to the interaction point (see Fig. 6.30). Although these calculations were based on an earlier lattice version (V23), no significant differences in vacuum performance are expected for the more recent V25.2 lattice, and the profiles have therefore been retained for the present study.

To construct a full-ring pressure profile, the arc pressure profile was periodically repeated to cover the full FCC-ee arcs and stitched together with the MDI pressure profile. For the long straight sections (LSS), a flat pressure of 5×10^{-10} mbar was assumed, based on guidance from vacuum experts. This relatively low value is justified by the near-absence of bending magnets in the

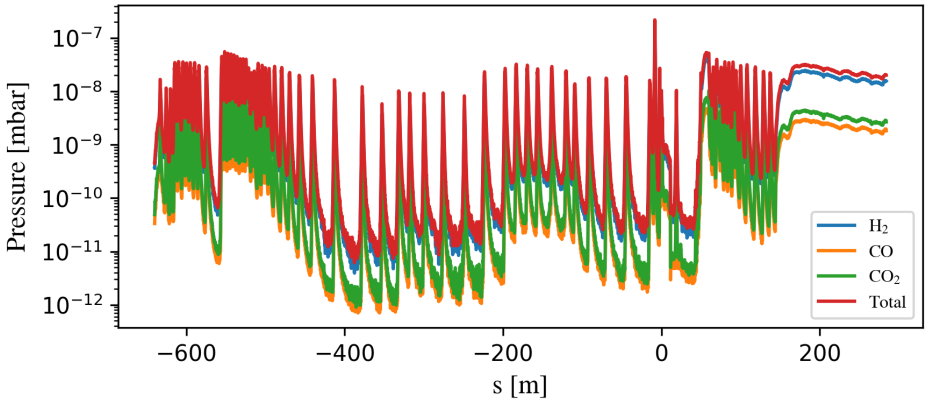

Figure 6.30. Residual gas pressure profile in the machine–detector interface (MDI) region of the FCC-ee, derived from SYNRAD++ and MOLFLOW simulations after 1 hour of beam conditioning at nominal Z-mode current [148].

LSS, which results in significantly lower synchrotron radiation (SR) photon flux compared to the arcs. Since photo-stimulated desorption (PSD) by SR photons is the dominant source of residual gas in the beam pipe, pressure levels in the LSS are expected to be substantially lower than in the arcs. A notable exception to this assumption is the collimation insertion (PF), where sizable local beam losses on collimators, shower absorbers, and nearby components may cause local pressure rises. A more detailed evaluation of pressure conditions in this region is planned for future work.

The assumed residual gas composition in the FCC-ee vacuum chamber was taken to be 85% H_2, 10% CO, and 5% CO_2, consistent with typical gas compositions observed in modern synchrotron light sources.

The resulting pressure profile for the full FCC-ee ring, constructed as detailed above, is shown in Fig. 6.31.

Beam–residual gas interactions were simulated using the dedicated routine described in Section 3.5.1, with bremsstrahlung and Coulomb scattering processes treated in separate runs. A total of 22,500 beam–gas scattering centers were placed uniformly along the 90.7 km ring, corresponding to an average spacing of approximately 4 m. Each simulation tracked 10^7 primary particles over 1000 turns.

As described in Section 3.5.1, the first turn was artificially biased to correspond to one effective mean free path using cross-section scaling, thereby increasing the probability of interactions. To avoid unphysical clustering of interactions near a common starting location due to this biasing, the simulations were split into 1000 independent parallel runs of 10^4 particles each, and the starting location in each run was randomly assigned among the 22,500 scattering centers. Following the biased first turn, particles were tracked for an additional 999 turns without further beam–gas interactions, allowing the study of the propagation and loss distribution of beam–gas scattered particles.

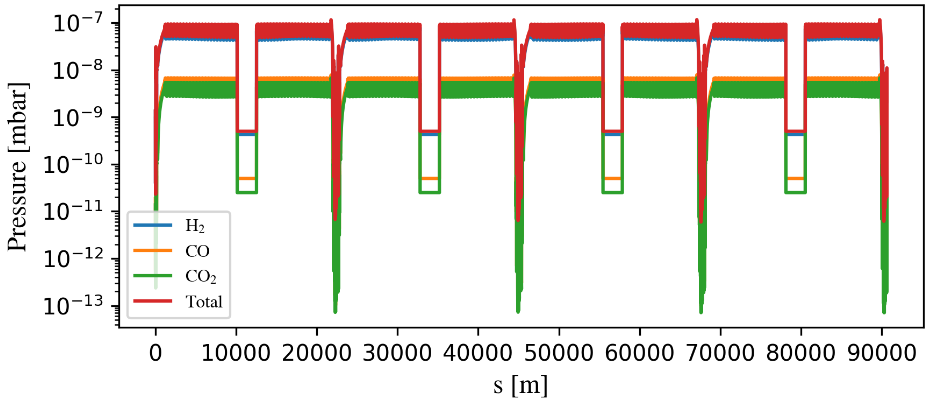

Figure 6.31. Full-ring residual gas pressure profile for the FCC-ee Z operation mode. The profile combines arc and MDI regions from SYNRAD++/MOLFLOW simulations with flat pressures of 5×10^{-10} mbar assumed in the long straight sections (LSS).

Synchrotron radiation effects—including damping, quantum excitation, and energy recovery in RF cavities—have been included, as well as magnetic lattice tapering. The simulations also included a detailed aperture model, as well as collimator geometries modeled using BDSIM/Geant4.

Beam loss positions have been recorded and binned longitudinally in 10 cm intervals to generate loss maps, showing the beam loss distribution along the FCC-ee ring.

6.3.1 Beam-Gas bremsstrahlung losses

Results

The performance of the FCC-ee collimation system in mitigating beam-gas bremsstrahlung losses is demonstrated in Figs. 6.32–6.34, which show the distribution of beam–residual gas bremsstrahlung losses in the FCC-ee. The losses are presented as power loads, assuming the full stored beam energy in the Z-mode and the effective simulated machine time t_{sim}, which—given the cross-section biasing applied on the first simulated turn as explained in Section 3.5.1—can be computed as

$$t_{\text{sim}} = (\text{BF} + n_{\text{turns}} - 1) \cdot T_{\text{rev}}, \tag{6.8}$$

where BF is the cross-section biasing factor introduced in Section 3.5.1, n_{turns} the number of simulated machine turns, and T_{rev} the machine revolution period. Since in most cases BF $\gg n_{\text{turns}}$, the effective simulated machine time can be well approximated by $t_{\text{sim}} \approx \text{BF} \cdot T_{\text{rev}}$. For aperture losses, the longitudinal bin size is 10 cm, while for collimators it corresponds to the respective collimator length (see Table 5.5).

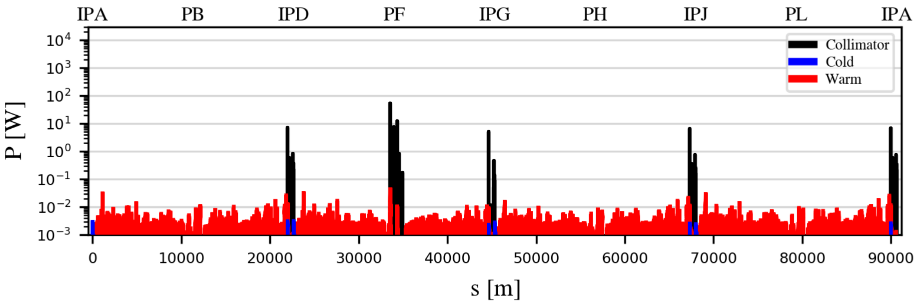

Figure 6.32. Longitudinal distribution of beam–gas bremsstrahlung losses in the FCC-ee (full ring). Losses are shown as power loads, assuming the simulated beam–gas bremsstrahlung lifetime under pessimistic vacuum conditions after only 1 h of beam conditioning at nominal Z-mode current.

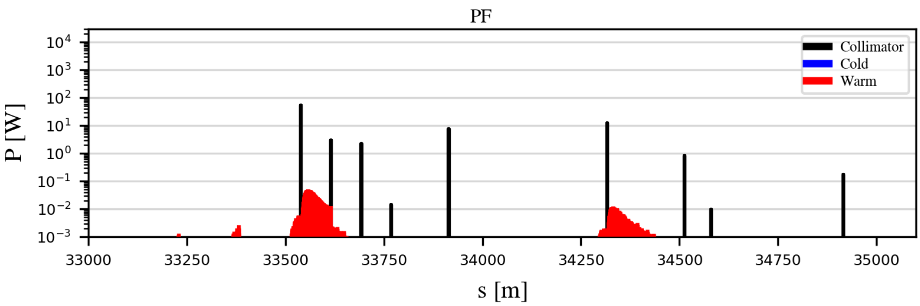

Figure 6.33. Zoomed view of beam–gas bremsstrahlung losses in the PF collimation insertion. Losses are concentrated on the horizontal primary collimator TCP.H.B1 and the off-momentum primary collimator TCP.HP.B1, consistent with the predominantly off-momentum nature of bremsstrahlung-induced losses.

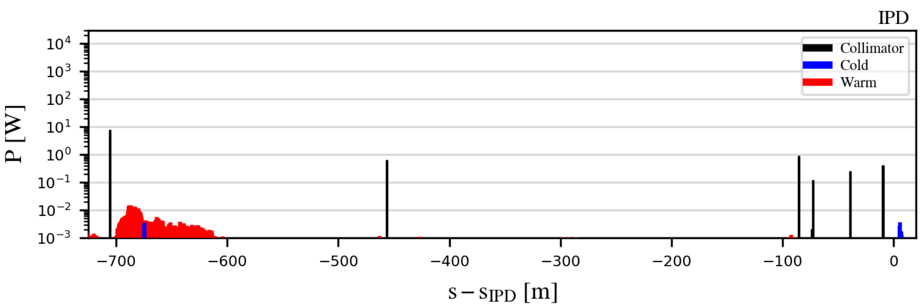

Figure 6.34. Zoomed view of beam–gas bremsstrahlung losses in the interaction region around IPD. Residual losses are mainly absorbed by the horizontal TCTs, with secondary power loads below a few mW on superconducting magnets and around 1 W on downstream SR collimators.

From the same simulation, the beam–gas bremsstrahlung lifetime under the pessimistic vacuum assumption of 1 hour of beam conditioning at full Z-mode current is estimated to be 274 minutes.

From Fig. 6.32, it is clear that the highest beam–gas–induced losses are observed on the beam halo collimators in the PF insertion, confirming that the system effectively localizes losses in the dedicated collimation section and suppresses them elsewhere in the ring.

A closer view of the PF insertion is shown in Fig. 6.33, which indicates that most losses are intercepted by the horizontal primary collimator TCP.H.B1 and the off-momentum primary collimator TCP.HP.B1, with peak power loads of approximately 100 W and 10 W, respectively. This loss pattern is consistent with the inelastic nature of bremsstrahlung interactions, which primarily cause off-momentum losses. Consequently, the losses tend to concentrate in the horizontal plane, where the dispersion function is non-zero.

Lower losses—approximately one order of magnitude lower than those on the primary collimators—are also observed on the tertiary collimators (TCTs) upstream of the interaction points, particularly the horizontal ones (TCT.H). This is again attributed to the inelastic nature of bremsstrahlung interactions. A zoomed view of the interaction region around IPD is shown in Fig. 6.34. This region is particularly sensitive due to the presence of superconducting magnets, such as the final focus quadrupoles and crab sextupoles, as well as nearby experimental detector components. As seen in Fig. 6.34, the maximum power loads on the TCTs reach up to 10 W, while losses on superconducting magnets remain below a few mW. Power loads on synchrotron radiation collimators downstream of the TCTs are even lower, with maxima around 1 W.

Overall, the results indicate that, even under the pessimistic vacuum conditions considered (i.e., after only 1 hour of beam conditioning at full nominal Z-mode current), the FCC-ee collimation system performs effectively. Beam–gas bremsstrahlung losses are confined to the dedicated collimation regions, and losses in sensitive regions are limited to acceptable levels. While detailed energy deposition and thermo-mechanical studies will be required to fully assess tolerability, the simulated power loads are likely within operational limits.

It can therefore be concluded that, under the studied conditions, beam-gas bremsstrahlung interactions are not expected to represent a limiting factor for FCC-ee performance.

6.3.2 Beam-Gas Coulomb scattering losses

Results

The performance of the FCC-ee collimation system in mitigating beam-gas Coulomb scattering losses is illustrated in Figs. 6.35–6.37, which show the spatial distribution of Coulomb-induced losses around the ring. The losses are expressed as power loads, assuming the full stored beam energy in the Z-mode and the effective simulated machine time t_{sim}, computed in the same way as

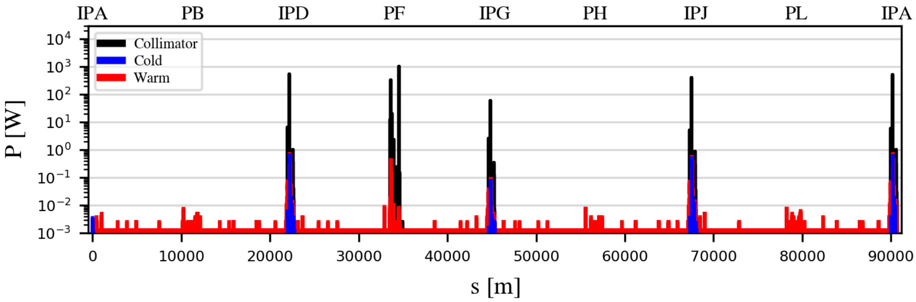

Figure 6.35. Longitudinal distribution of beam-gas Coulomb scattering losses in the FCC-ee (full ring). Losses are shown as power loads, assuming the simulated beam-gas Coulomb scattering lifetime under pessimistic vacuum conditions after only 1 h of beam conditioning at nominal Z-mode current.

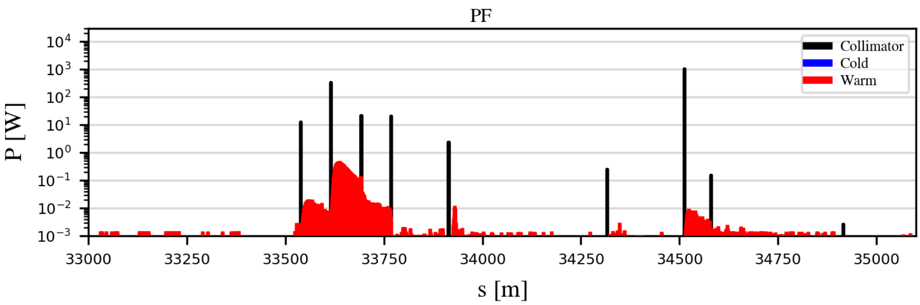

Figure 6.36. Zoomed view of Coulomb scattering losses in the PF collimation insertion. Losses are dominated by vertical angular kicks intercepted by the vertical betatron collimators.

described for the bremsstrahlung case in Section 6.3.1

$$t_{\mathrm{sim}} = (\mathrm{BF} + n_{\mathrm{turns}} - 1) \cdot T_{\mathrm{rev}}. \tag{6.9}$$

As before, since in most cases $\mathrm{BF} \gg n_{\mathrm{turns}}$, this reduces to $t_{\mathrm{sim}} \approx \mathrm{BF} \cdot T_{\mathrm{rev}}$. For aperture losses, the longitudinal bin size is 10 cm, while for collimators it corresponds to the respective collimator length (see Table 5.5).

Under the pessimistic vacuum assumption of 1 hour of beam conditioning at full Z-mode current, the beam–gas Coulomb scattering lifetime is estimated to be 42 minutes, i.e. more than a factor of six shorter than the bremsstrahlung lifetime reported in Section 6.3.1. The beam–gas lifetimes are summarized in Table 6.4.

As shown in Fig. 6.35, Coulomb scattering losses are approximately equally intercepted by the halo collimators in the PF insertion and the tertiary collimators (TCTs) upstream of the interaction regions. This contrasts with the bremsstrahlung case discussed in Section 6.3.1, where losses were primarily absorbed by the PF collimators and were about one order of magnitude lower at the TCTs.

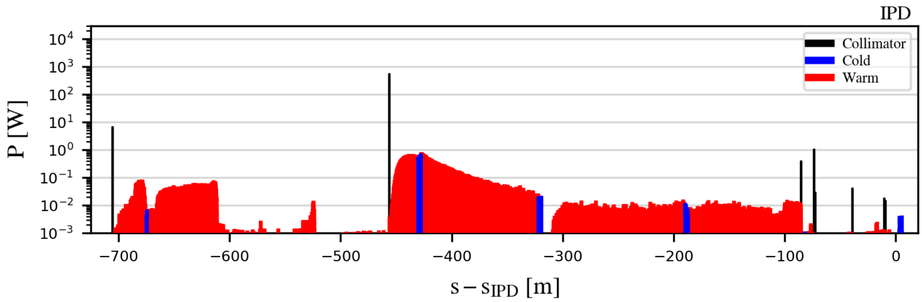

Figure 6.37. Zoomed view of Coulomb scattering losses in the interaction region around IPD. Significant losses are observed on the vertical TCTs, with secondary showers extending downstream.

This distribution arises from the sensitivity of the studied FCC-ee Z-mode lattice (V25.2 GHC) to vertical angular deflections. As shown in Fig. 6.38, this lattice features a limited vertical dynamic aperture of about 25 units of normalized betatron amplitude, making it susceptible to relatively small kicks. In the arcs, where most beam–gas interactions occur, the vertical rms divergence is approximately $\sigma_{p_y} \approx 0.3$ µrad. A typical vertical kick of 10 µrad from Coulomb scattering thus corresponds to a $30\sigma_{p_y}$ deflection—enough to immediately drive the particle beyond the DA limit.

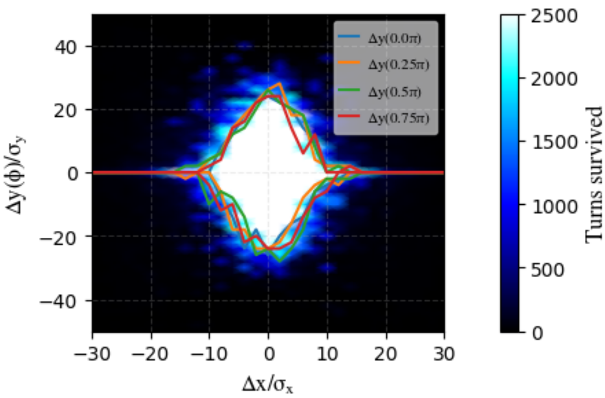

Figure 6.38. Transverse dynamic aperture (DA-XY) for the FCC-ee V25.2 GHC Z operation mode, including the effect of synchrotron radiation: damping, quantum excitations, RF cavities and lattice tapering.

Once outside the DA, the motion of these particles becomes chaotic and no longer follows the linear optics of the lattice. Their subsequent trajectories are therefore largely unpredictable, and it is no longer guaranteed that they will be intercepted at the smallest normalized aperture of the ring (i.e., at the primary collimators in the PF insertion). Particles entering this chaotic regime can quickly acquire very large transverse amplitudes and be lost at various downstream locations. This mechanism explains why Coulomb-induced losses are observed with comparable magnitude at the tertiary collimators (TCTs) and the primary collimators, despite the larger normalized aperture of the TCTs. The resulting loss pattern is thus a direct manifestation of nonlinear dynamics beyond the DA limit and highlights the importance of dynamic aperture optimization for minimizing beam losses close to the interaction regions.

This sensitivity is further amplified near the interaction regions, where the vertical beta function β_y reaches several kilometers, as shown in Fig. 5.8, reducing σ_{p_y} even further and resulting in losses from even smaller deflections. By contrast, horizontal kicks are less critical due to the larger beam divergence in that plane, and Coulomb-induced losses remain predominantly vertical. As also discussed in Chapter 4, the tendency for Coulomb interactions to cause vertical losses is consistent with observations at SuperKEKB, owing to the similarities between the two machines.

This is reflected in the collimator loss pattern. As shown in Fig. 6.36, the vertical primary collimator TCP.V.B1 and the vertical secondary collimator TCS.V2.B1 exhibit peak power loads of about 1 kW. The vertical TCTs upstream of the interaction points, visible in Fig. 6.37, intercept losses at the level of hundreds of W. These values are roughly an order of magnitude higher than those observed for bremsstrahlung losses, consistent with the shorter beam-gas Coulomb scattering lifetime.

Beyond the collimators, Fig. 6.37 also reveals sizable secondary particle showers downstream of the vertical TCTs. Notably, the superconducting crab sextupoles located in this region are exposed to power loads of up to 1 W, although these values remain well below critical thresholds.

While the overall power loads remain within tolerable limits, the results underscore a non-negligible contribution of Coulomb scattering to beam losses at FCC-ee beam energies, contrary to the common expectation that bremsstrahlung would dominate under such conditions.

The observed high rate of losses on the vertical TCTs—located approximately 400 m upstream of the interaction points—raises some concerns regarding potential experimental background contributions. To assess this impact, the results of these simulations have been provided as input to FLUKA-based studies, which simulate full particle shower development and transport through the interaction region environment, including collimators, magnets, beam pipe, and detector components.

In conclusion, although beam-gas Coulomb scattering was previously considered a minor contributor at FCC-ee beam energies, under specific machine conditions such as limited vertical dynamic aperture, it may lead to significant losses with distinct spatial patterns. Nevertheless, no showstoppers have been identified, and the FCC-ee collimation system still provides effective mitigation, containing the majority of the losses within the dedicated collimation regions.

Table 6.4. FCC-ee V25.2 GHC Z-mode beam–gas lifetimes from tracking simulations under a pessimistic vacuum scenario (1 hour of beam conditioning at nominal current), and projections for a fully conditioned machine obtained by scaling linearly with the expected $\sim 100\times$ reduction in residual gas pressure.

Process	1 h conditioning [min]	Fully conditioned (×100) [min]
Bremsstrahlung	274	27 400
Coulomb scattering	42	4 200

6.4 Touschek scattering losses

This section presents a study of beam losses arising from Touschek scattering in the FCC-ee. While this mechanism plays a major role in limiting the beam lifetime and contributing to background levels in several existing electron–positron colliders, it is not expected to significantly impact the FCC-ee performance. This is primarily due to the higher beam energies foreseen in all FCC-ee operation modes, which strongly suppress Touschek scattering losses, as discussed in Chapter 2.

Despite this, Touschek scattering remains relevant in the context of this thesis for two key reasons. First, as discussed in earlier chapters, an important component of the FCC-ee design effort involves benchmarking the employed simulation tools against data from currently operating colliders. Since Touschek scattering plays a significant role in existing e^+e^- colliders such as SuperKEKB—used in this thesis as a reference machine for benchmarking the Xsuite-BDSIM simulation tool, as presented in Chapter 4—it was essential to implement a dedicated Touschek scattering simulation routine, as described in Chapter 3. Second, once such a routine is available, applying it to the FCC-ee comes at minimal cost. Therefore, a quantitative evaluation remains valuable to confirm this expectation and ensure that no unforeseen beam loss scenarios are overlooked.

The remainder of this section presents a study of Touschek losses in the FCC-ee Z operation mode, using the simulation routine developed in the context of this thesis.

Simulation setup

The Touschek scattering routine developed as part of this thesis and described in Chapter 3 has been used to evaluate beam losses from Touschek scattering in the FCC-ee. The routine has been integrated into the Xsuite-BDSIM simulation framework.

Simulations were performed for the positron beam (B1) at a beam energy of 45.6 GeV, corresponding to the FCC-ee (V25.2 GHC [15]) Z operation mode. This represents the most critical case for Touschek scattering in the FCC-ee, since the Touschek loss rate decreases rapidly with increasing beam energy, as shown in Eq. (2.46).

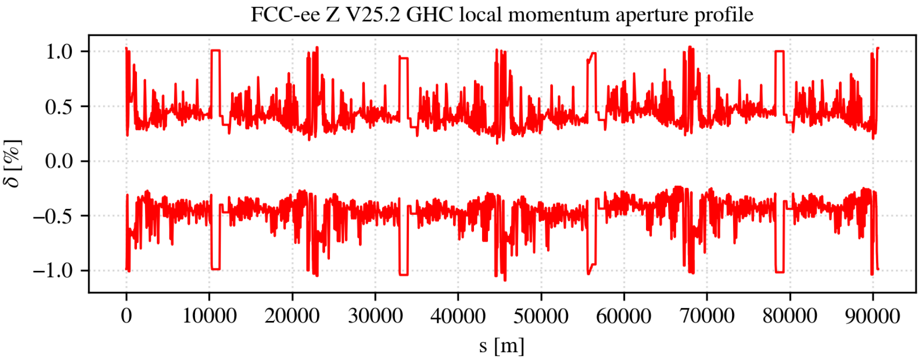

Figure 6.39. Local momentum aperture profile for the FCC-ee (V25.2 GHC) *Z* operation mode, obtained from Xsuite tracking.

To simulate the worst-case scenario for Touschek losses, the study was carried out assuming nominal beam intensity while adopting the most pessimistic conditions in terms of bunch parameters. These correspond to the configuration with the highest 6D phase-space density, which in the FCC-ee occurs in the absence of collisions at the interaction points (single-beam mode). As shown in Table 1.2, when beams are stored without collisions, the vertical geometric emittance ϵ_y (lattice vertical emittance in the table), the bunch length σ_z, and the energy spread σ_δ are each reduced by approximately a factor of three. Altogether, these reductions yield much denser bunches in 6D phase space, thereby enhancing the Touschek scattering and associated losses.

It should be emphasized that such a configuration does not represent a standard operation mode: the FCC-ee is not foreseen to store single beams at full nominal intensity. Nevertheless, exploring this overly pessimistic case provides a robust safety margin—if Touschek scattering is shown not to be performance-limiting under these extreme conditions, it can be confidently excluded as a concern in realistic operating scenarios.

For completeness, simulations were also performed for a more realistic configuration with bunch parameters corresponding to colliding beams. This allows a quantitative comparison and illustrates the extent to which Touschek losses are alleviated under nominal collision conditions.

The local momentum aperture profile for the FCC-ee (V25.2 GHC) *Z* operation mode was obtained through tracking, following the procedure described in Section 3.5.2. The resulting profile, used as input for the Touschek scattering simulation, is shown in Fig. 6.39.

A total of 1610 Touschek scattering centers were used in the simulation. Given the 90.7 km circumference of the FCC-ee, using uniformly spaced scattering centers—as done in the SuperKEKB simulations in Chapter 4—would be computationally prohibitive. It is worth remembering that to obtain physically meaningful results, the placement of Touschek scattering centers must resolve the local variations of the optical functions. Accordingly, a non-uniform distribution of scattering centers was adopted: larger spacing was used in regions with slowly varying optics (such as the arcs), while denser sampling was applied in regions where the optics vary rapidly, such as the interaction regions.

A total of 3×10^7 Touschek-scattered macroparticles were tracked over 1000 machine turns. Synchrotron radiation effects—including damping, energy recovery in the RF cavities, and magnetic lattice tapering—were included in the simulation. Quantum excitation was not included. This choice is motivated by the fact that in this simulation framework, each macroparticle is assigned a weight corresponding to its contribution to the total Touschek scattering rate. Including quantum excitation could introduce losses due to secondary mechanisms unrelated to Touschek scattering itself (e.g., photon emission driving particles beyond the momentum aperture), which would bias the result. For this reason, only deterministic SR effects were included.

The simulation included a detailed aperture model and realistic collimator geometries implemented via BDSIM/Geant4. Beam loss locations, along with the corresponding Touschek rate contribution of each macroparticle, were recorded and binned longitudinally in 10 cm intervals to generate loss maps, representing the Touschek scattering losses along the FCC-ee ring.

Results

The results of the Touschek scattering simulations are presented here for two selected configurations: the pessimistic nominal-intensity single-beam mode (no collisions) and the more realistic nominal-intensity colliding-beam mode, representative of the nominal FCC-ee operating conditions. It should be noted that beam–beam interactions are not explicitly included in the colliding-beam configuration; the simulations are performed for a single beam, but with the larger equilibrium emittances, bunch length, and energy spread corresponding to colliding-beam conditions.

For the single-beam mode, the spatial distribution of Touschek losses is shown in Figs. 6.40–6.42. The losses are expressed as power loads, assuming the full stored beam energy in the Z operation mode. The power load in each bin is obtained by summing the energies of all lost macroparticles in that bin, weighted by their corresponding Touschek scattering rate factors R_i (see Eq. (3.17)). For aperture losses, the longitudinal bin size is 10 cm, while for collimators it corresponds to the respective collimator length.

As shown in Fig. 6.40, Touschek losses are distributed across the full ring, as expected from the continuous intrabunch nature of the scattering mechanism. Nonetheless, the highest losses are observed on the halo collimators in the PF insertion. Figure 6.41 shows that peak local power loads in this region reach values at the kW level, with the highest losses observed on the horizontal primary betatron collimator TCP.H.B1 and the primary off-momentum collimator TCP.HP.B1. This is consistent with the expectation that Touschek scattering predominantly induces losses in the horizontal plane, as it causes large energy deviations in the scattered particles.

Outside of the PF insertion, the Touschek-induced power loads are suppressed by more than one order of magnitude. As shown in Fig. 6.42, residual

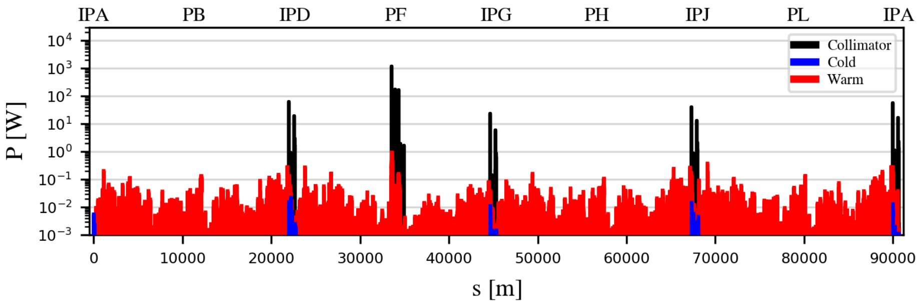

Figure 6.40. Longitudinal distribution of Touschek scattering losses in the FCC-ee (full ring) for the pessimistic single-beam configuration (no collisions). Losses are shown as local power loads in 10 cm bins, obtained by summing the energies of lost macroparticles weighted by their Touschek scattering rates R_i.

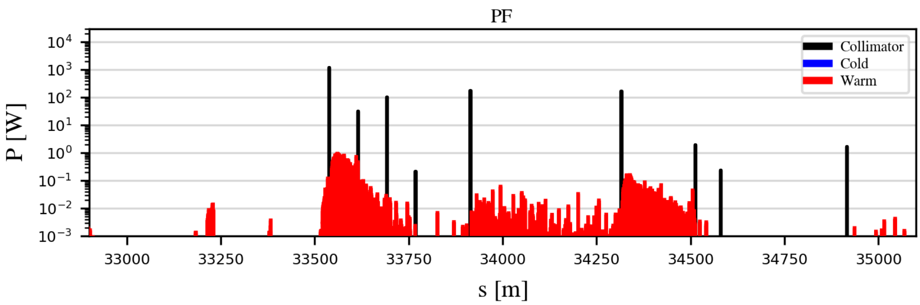

Figure 6.41. Zoomed view of Touschek scattering losses in the PF collimation insertion for the single-beam configuration. Peak loads occur on the horizontal primary betatron collimator TCP.H.B1 and on the primary off-momentum collimator TCP.HP.B1, consistent with the predominantly off-momentum character of Touschek scattering losses.

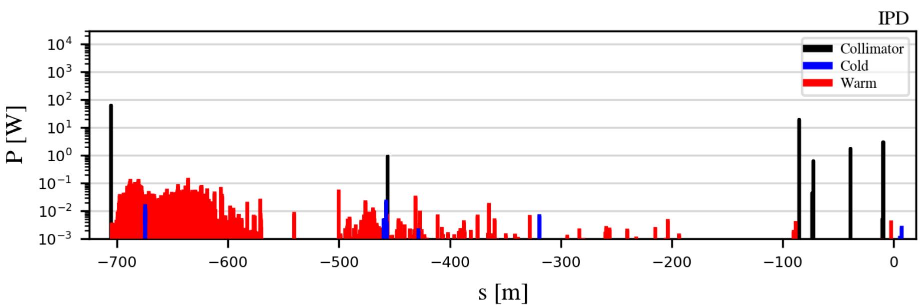

Figure 6.42. Zoomed view of Touschek scattering losses in the interaction region around IPD for the single-beam configuration. Residual losses are mainly intercepted by the TCTs and SR collimators; loads on superconducting elements remain negligible.

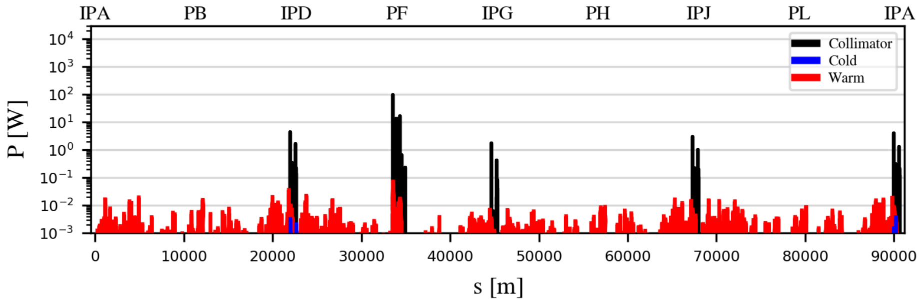

Figure 6.43. Longitudinal distribution of Touschek scattering losses in the FCC-ee (full ring) for the nominal colliding-beam configuration. Owing to the reduced phase-space density in the collision regime, the overall Touschek losses decrease markedly with respect to the single-beam case, while losses remain well localized in the PF insertion.

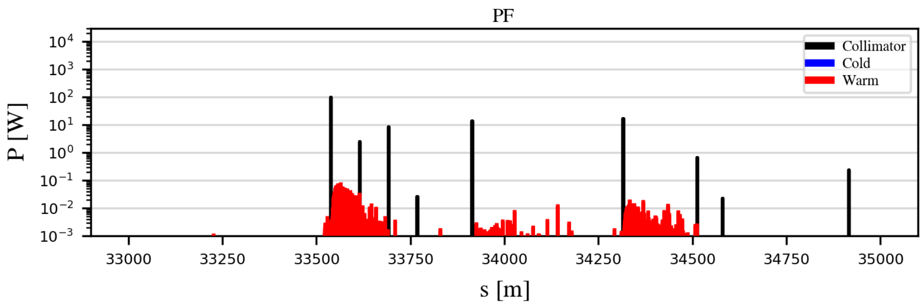

Figure 6.44. Zoomed view of Touschek scattering losses in the PF collimation insertion for the colliding-beam configuration. The halo collimators efficiently intercept the reduced Touschek-scattered particles; peak loads are significantly lower than in the single-beam case and remain concentrated on TCP.H.B1 and TCP.HP.B1.

losses are mostly localized on the tertiary collimators and SR collimators. Losses on magnets or other critical components remain minimal, with peak power levels on the order of one watt or below. A small amount of Touschek losses is recorded near the detector region; although further dedicated simulations are required to quantify the corresponding experimental background contribution, the overall impact is expected to be negligible compared to other dominant background sources such as synchrotron radiation or radiative Bhabha scattering.

The simulation yields a Touschek lifetime of about 1 hour for the Z operation mode in this pessimistic case. This confirms that, even under extreme conditions, Touschek scattering does not pose a limitation to the beam lifetime in the FCC-ee.

In the more realistic colliding-beam configuration, the reduced phase-space density results in a significantly lower Touschek scattering probability and, consequently, reduced associated losses, as shown in Figs. 6.43–6.45. In this

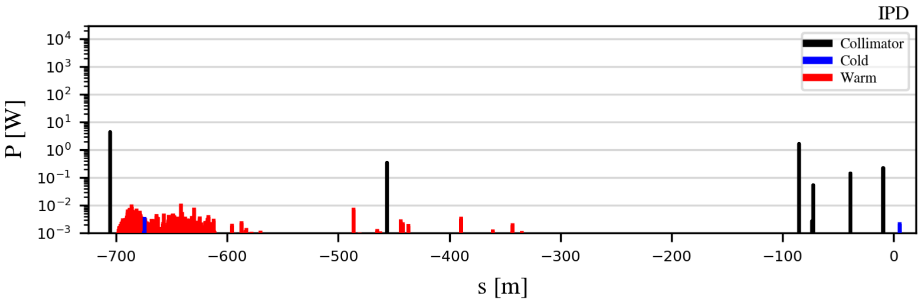

Figure 6.45. Zoomed view of Touschek scattering losses in the interaction region around IPD for the colliding-beam configuration. Only small residual losses are observed on the TCTs, with no appreciable loads on superconducting magnets or detector-adjacent components.

scenario, the simulation yields a Touschek lifetime of about 13 hours, further confirming that Touschek scattering is not expected to represent a performance-limiting effect in the FCC-ee.

It is worth noting that the Touschek lifetimes obtained from these simulations are in good agreement with those computed using Piwinski's analytical formula (see Eq. (2.47)). Furthermore, the 13 h Touschek lifetime obtained for the realistic colliding-beam configuration is consistent with earlier analytical estimates made for the FCC-ee Conceptual Design Report [9], which predicted a Touschek lifetime in the range of 15–30 h for the Z operation mode [149].

In the colliding-beam configuration, the lower phase-space density leads to a substantial reduction of Touschek-induced losses along the ring. As seen in Figs. 6.43–6.45, the power deposition is uniformly reduced by about one order of magnitude relative to the single-beam case, while the spatial loss pattern is preserved: losses remain mostly intercepted in the PF insertion, with the horizontal primary (TCP.H.B1) and the primary off-momentum (TCP.HP.B1) collimators capturing the majority of Touschek-scattered particles. Residual leakage toward the interaction regions is further suppressed, and loads on the TCTs and nearby warm elements remain modest. No significant losses are observed on superconducting magnets.

Altogether, these results confirm that Touschek scattering is not a performance-limiting effect in the FCC-ee, and that the proposed FCC-ee collimation system appears fully appropriate to handle the associated Touschek losses. The pessimistic single-beam case demonstrates large safety margins, while the colliding-beam case provides additional reassurance that Touschek-induced losses and lifetimes will remain well within acceptable limits for all FCC-ee operation modes.

Table 6.5. Summary of simulated Touschek lifetimes in the FCC-ee Z operation mode for the two configurations considered. Values are obtained with the Touschek-scattering rotuine described in Sec. 6.4, assuming a bunch population of $N_b = 2 \times 10^{11}$ particles. The single-beam case corresponds to the pessimistic, high phase-space-density configuration (no collisions), whereas the colliding-beams case represents realistic nominal collision conditions. The assumed bunch parameters for both configurations are reported in Table 1.2.

Configuration	**Touschek Lifetime [h]**
Single-beam (no collisions)	$\sim$1
Colliding-beams	$\sim$13

6.5 Beam-beam losses

Beam–beam interactions at the collision points represent one of the dominant mechanisms of particle loss in high-luminosity e^+e^- colliders. At FCC-ee, they contribute directly to the so-called *luminosity lifetime*, i.e. the rate at which particles are removed from the stored beams due to hard scattering processes in the collisions. The main channel is radiative Bhabha scattering, but additional effects such as beamstrahlung (BS) and beam–beam kicks may also influence single-turn trajectories and ultimately the final loss location of halo particles. In fact, in the FCC-ee these three processes — radiative Bhabha scattering, beamstrahlung, and beam–beam kicks — are the main contributors to the beam lifetime in nominal operation, and they can produce distinct beam loss patterns. Moreover, large beam–beam kicks can in some cases drive particles directly onto the collimators. This is a new regime in which it becomes important to include these effects in studies of the collimation performance.

In this section, we present dedicated simulation studies of beam–beam induced losses in the FCC-ee (V25.2 GHC [15]) Z operation mode. The aim is to evaluate the resulting multi-turn beam dynamics, to quantify the beam losses from spent-beam particles, and to assess the effectiveness of the collimation system in localizing these losses and protecting sensitive regions of the machine.

The simulations presented here were performed using the beam–beam models available in Xsuite, specifically those implemented in the Xfields package. The development and integration of these models into Xsuite are described in Ref. [150]. These models have been benchmarked against established simulation tools, showing very good agreement [151]. An important advantage of these models is their modularity, which enables seamless integration with other studies — such as collimation studies — thereby offering a unified simulation framework to address the demanding requirements of complex machines like the FCC-ee. This makes it possible to simulate beam losses caused by beam–beam effects, including their interaction with the collimation system, as presented in this section.

Simulation setup

For the studies presented in this section, the positron beam (B1) was simulated at a beam energy of 45.6 GeV, corresponding to the FCC-ee Z operation mode, which represents the most critical case in terms of stored beam energy and beam–beam effects. A total of 10^7 macroparticles were tracked in the full FCC-ee nonlinear lattice for 1000 turns.

Synchrotron radiation effects — including damping, quantum excitation, and energy recovery in RF cavities — were included, together with magnetic lattice tapering. The simulations also incorporated a detailed aperture model, collimator geometries modeled using BDSIM/Geant4, and weak–strong beam–beam interactions (beam–beam kicks, beamstrahlung, and radiative Bhabha scattering) at each interaction point. In the weak–strong beam–beam model, dynamic effects during tracking are applied only to the strong beam.

The initial particle distribution was a Gaussian bunch, matched at the center of the RF section in PH. The initial emittances and bunch length were set to the equilibrium values in collision, as reported in Table 1.2.

After 1000 turns, beam loss positions were recorded and binned longitudinally in 10 cm intervals to generate loss maps, showing the beam loss distribution along the FCC-ee ring.

Results

The results of the beam–beam loss simulations for the FCC-ee Z operation mode are shown in Figs. 6.46–6.48. Losses are presented as power loads, assuming the full stored beam energy in the Z-mode and the effective simulated machine time

$$t_{\mathrm{sim}} = n_{\mathrm{turns}} \cdot T_{\mathrm{rev}}, \tag{6.10}$$

where n_{turns} is the number of simulated turns and T_{rev} the revolution period of the machine. The beam lifetime from the simulation is 14 minutes, in good agreement with the nominal expectation of 17 minutes reported in Table 1.2, which assumes no physical aperture limitations. For aperture losses, the longitudinal bin size is 10 cm, while for collimators it corresponds to the respective collimator length (see Table 5.5).

As shown in Fig. 6.46, losses are predominantly concentrated in the vicinity of the interaction regions, with distinct clusters observed downstream of the interaction points (IPs). These local losses originate directly from beam–beam interactions and cannot be intercepted by the collimation system in PF or by any other collimators, as the scattered particles do not survive long enough to reach them. In addition, losses of comparable magnitude are observed on the halo collimators in PF and on the tertiary collimators (TCTs). These correspond to particles driven into the halo by beam–beam interactions at earlier turns and subsequently intercepted.

The zoomed view of the PF insertion in Fig. 6.47 shows that the highest recorded loads in this region occur on the primary halo collimators, confirming that the system is effective in intercepting non-local beam–beam losses, i.e.,

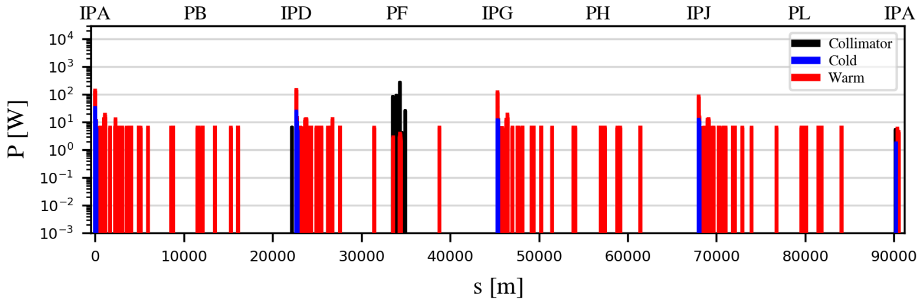

Figure 6.46. Longitudinal distribution of beam–beam induced losses in the FCC-ee (full ring). Losses are shown as power loads, normalized to the simulated beam lifetime in collision (luminosity lifetime).

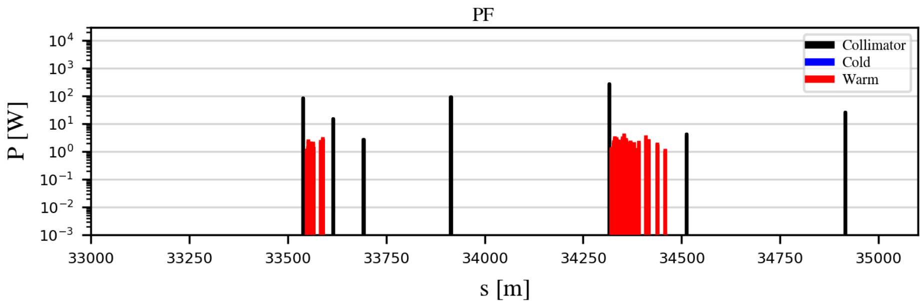

Figure 6.47. Zoomed view of beam–beam induced losses in the PF collimation insertion. The halo collimators intercept scattered particles driven into the beam halo by beam–beam interactions.

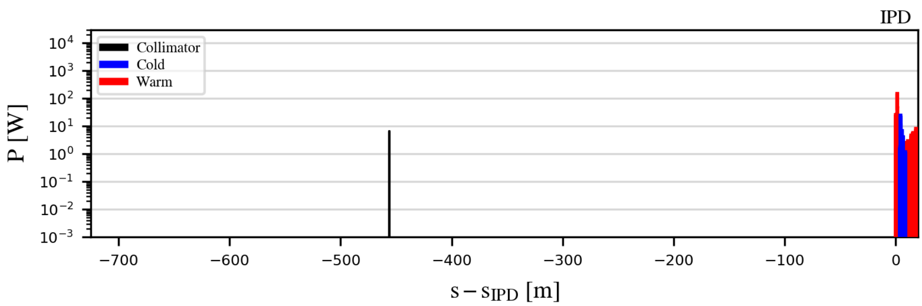

Figure 6.48. Zoomed view of beam–beam induced losses in the interaction region around IPD. Local cold losses are observed on the downstream final-focus quadrupoles and crab sextupoles, while no losses are recorded upstream of the IP.

losses originating from beam–beam interactions at the IPs but occurring at locations well away from the interaction point. Similarly, the TCTs upstream of the IPs contribute to the cleaning performance by absorbing a fraction of scattered particles. Notably, no losses are recorded between the TCTs and the

IPs, demonstrating that elements such as synchrotron-radiation collimators and upstream magnets remain unaffected by beam–beam–induced losses.

A zoomed view of the interaction region around IPD is provided in Fig. 6.48. Losses are observed on the final-focus quadrupoles and crab sextupoles located downstream of the IP, while no losses are recorded upstream. The absence of losses upstream of the IP is particularly reassuring, as it excludes any direct exposure of the synchrotron-radiation collimators or incoming superconducting magnets to beam–beam debris.

It should be emphasized, however, that in this simulation setup—covering 1000 turns and tracking 10^7 macroparticles—only a small fraction of the initial particles is actually lost. As can be seen from the rather noisy character of the loss maps in Figs. 6.46–6.48, the limited number of lost macroparticles leads to large statistical fluctuations. Consequently, the statistical uncertainty on the estimated power load from beam–beam losses is very high, reaching up to 100% in bins where only a single macroparticle is lost. Therefore, no quantitative conclusions are drawn here regarding the absolute power loads. A dedicated high-statistics study of beam–beam induced losses, based on biased radiative Bhabha generation, is presented in the next subsection to address this limitation.

Overall, the results indicate that the FCC-ee collimation system provides effective mitigation of beam–beam induced losses around the ring. The majority of non-local beam–beam losses are intercepted within the dedicated collimation regions, while unavoidable local losses downstream of the IPs are present and merit more detailed analysis, as discussed in the following section. An important outcome of these studies is that the proposed collimator settings are compatible with the large transverse kicks experienced by particles in the beam–beam interaction, allowing such particles to be efficiently intercepted without compromising the collimation hierarchy. Although beam–beam losses do not appear, in first approximation, to pose a limitation for machine performance, the possibility of backgrounds arising in the detector regions warrants further investigation. As the FCC-ee design progresses, the addition of dedicated collimators downstream of the IPs—similar to the physics-debris collimators employed at the LHC—may be considered to further suppress these losses.

Improved statistical sampling of beam–beam losses through biased radiative Bhabha generation

While the multi-turn weak–strong beam–beam simulations described above provide a description of the beam dynamics on a realistic timescale—with the simulated number of turns directly corresponding to the real machine time—the number of macroparticles undergoing hard interactions within this period remains very small. As a result, the statistical sample of lost particles is limited, and many longitudinal bins in Figs. 6.46–6.48 contain only one or two loss events, leading to large statistical fluctuations. To obtain high-statistics loss maps, one would need to track for a substantially larger number of turns, which would significantly increase the computational cost. Although the current simulations reproduce the overall loss mechanisms and beam lifetime, their limited statistics hinder a detailed quantitative assessment of localized power loads, especially in the regions downstream of the IPs and in the tails of the loss distribution outside PF.

To overcome this limitation, a dedicated high-statistics study was devised, focusing exclusively on the beam–beam process dominating beam–beam losses at the FCC-ee, namely radiative Bhabha (RB) scattering. In this complementary approach, the beam–beam model was configured to include only the RB process, while the corresponding cross-section was artificially increased by a fixed bias factor in order to enhance the occurrence of RB scattering events. This procedure ensures that nearly all tracked macroparticles undergo a single RB interaction when passing through the interaction point, providing a statistically rich sample of post-scattering trajectories. The resulting outgoing particles ("RB debris") were then extracted immediately downstream of the interaction point and used as input distributions for subsequent multi-turn tracking in the full machine.

For each of the four FCC-ee interaction points, an independent sample of RB-scattered positrons was generated using this biased configuration. Each sample was initialized with the nominal optical functions, equilibrium emittances, and bunch length in collision, consistent with the parameters reported in Table 1.2. A total of N_{RB} macroparticles (of order 10^6 per IP) were generated. These post-interaction macroparticles were then tracked for 100 turns in the full nonlinear FCC-ee lattice (V25.2 GHC, Z mode), including synchrotron radiation effects, RF cavities, magnet tapering, and a detailed aperture and collimator model, with collimators implemented in BDSIM/Geant4. No further beam–beam interactions were applied during this tracking, as the aim was to study the propagation and loss locations of the RB debris produced in single RB scattering events.

The total energy lost in each longitudinal bin was converted into steady-state power considering the total stored beam energy $E^{\mathrm{tot}}_{\mathrm{stored}} \approx 17.7$ MJ and the design luminosity lifetime associated with radiative Bhabha scattering, $\tau_{\mathrm{RB}} \approx 22$ min, as reported in Table 1.2. The corresponding steady-state total power loss due to RB scattering is then $P^{\mathrm{tot}}_{\mathrm{loss}} = E^{\mathrm{tot}}_{\mathrm{stored}}/\tau_{\mathrm{RB}} \approx 13.4$ kW. The relative energy-loss distribution obtained from the simulation, i.e. the fraction of simulated beam energy lost in each longitudinal bin, was scaled by this total power to obtain the physical power-loss profile:

$$P_j = \frac{E_j^{(\mathrm{sim})}}{E_{\mathrm{tot}}^{(\mathrm{sim})}} \frac{E_{\mathrm{stored}}}{\tau_{\mathrm{RB}}}, \tag{6.11}$$

where $E_j^{(\mathrm{sim})}$ is the total simulated energy loss in bin j and $E_{\mathrm{tot}}^{(\mathrm{sim})}$ is the total simulated energy loss over the full ring. This normalization ensures that the integrated power over all bins reproduces the expected steady-state RB power loss at design luminosity.

The resulting loss maps are presented in Figs. 6.49–6.51.

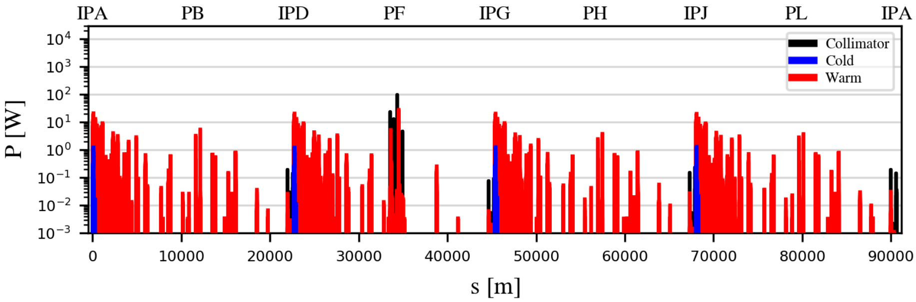

Figure 6.49. Longitudinal distribution of RB-induced losses in the FCC-ee (full ring). Losses are shown as power loads, normalized to the RB lifetime. The loss map represents the superposition of RB-induced losses from all interaction points.

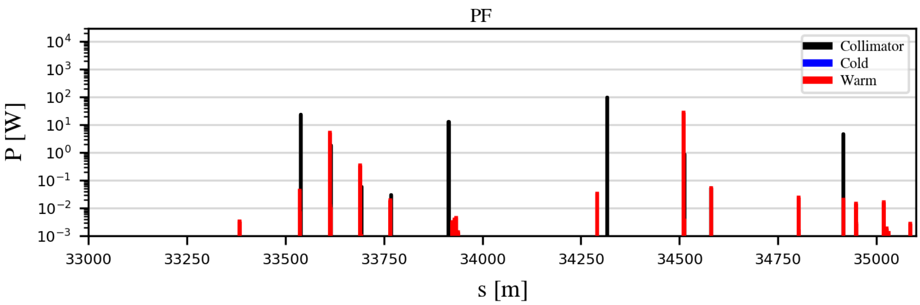

Figure 6.50. Zoomed view of RB-induced losses in the PF collimation insertion.

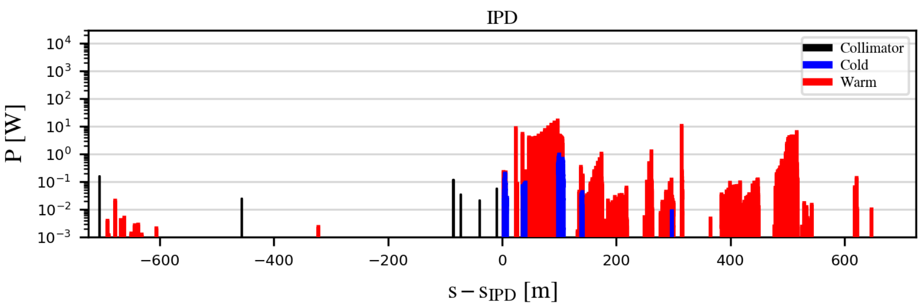

Figure 6.51. Zoomed view of RB-induced losses in the interaction region around IPD.

The loss maps shown in Figs. 6.49–6.51 provide a high-statistics representation of the steady-state power deposition resulting from radiative Bhabha (RB) scattering at design luminosity. Compared to the multi-turn weak–strong beam–beam simulations presented earlier, where the limited number of hard interactions resulted in large statistical fluctuations, the biased RB generation method yields a smoother and quantitatively reliable loss profile across the full machine.

At a global level, the RB-induced losses are localized within the regions already identified in the unbiased simulation: approximately 90 % of the losses occur in the sections downstream of the interaction points, with the remaining ∼10 % intercepted by the halo collimation system in PF.

In the PF collimation insertion (Fig. 6.50), the halo collimators intercept a sizable fraction of RB debris particles. These correspond to RB-scattered particles that survive long enough to reach the collimation insertion in PF. The most loaded collimators are the primary off-momentum collimator TCP.HP.B1 and the horizontal primary collimator TCP.H.B1, with peak power loads of approximately 100 W and 10 W, respectively. This is consistent with expectations from RB scattering, which generates particles with significant momentum deviations and therefore leads predominantly to losses in the horizontal plane. This confirms that the existing collimation system provides effective interception of long-range RB debris.

Most losses, however, remain concentrated in the vicinity of the interaction regions. The zoomed view around IPD in Fig. 6.51 reveals distinct clusters immediately downstream of the IP, corresponding to particles with large energy losses in the RB process that are lost very soon after scattering. These losses primarily impact the first few elements of the final-focus system downstream of the IP—namely the superconducting quadrupoles of the final-focus doublet, the crab sextupoles, and the first warm dipoles. The main cluster of losses starts around 50 m downstream of the IP, corresponding to the location of the first warm dipole, where the horizontal dispersion D_x begins to grow. The dispersion is also large at the downstream crab sextupole, which explains the enhanced losses observed on these elements at $s \approx +150$ m from the IPs. The simulated peak power loads on cold elements are of the order of 1 W on the crab sextupoles and about 0.1 W on the superconducting quadrupoles of the final-focus doublet. Higher power loads, up to 10–20 W, are observed on the warm magnets downstream of the IP, mainly in the dipoles. These values are consistent with the estimates from the unbiased simulation (Fig. 6.48) but are now statistically well resolved.

It is worth noting that the losses on the superconducting quadrupoles of the final focus immediately downstream of the IP are essentially unavoidable, as they cannot be intercepted by collimators placed between the IP and these magnets. This is due to the very limited space available and to the fact that these quadrupoles are integrated within the Machine–Detector Interface (MDI) structures, which involve a complex cryostat and support assembly. What can be done instead—and has in fact been proposed following dedicated energy-deposition studies—is to include a thin layer of tungsten shielding, a few millimeters thick, inside the beam pipe of these quadrupoles [152]. The function of this shielding is to protect the superconducting coils from energy deposition caused by interactions between the RB debris and the magnet material, thereby reducing the risk of quenches induced by local heating. For the nearby crab sextupoles and other warm magnets downstream of the IP, the situation is more flexible: if required, additional local absorbers or collimators could be strategically placed to intercept RB debris and confine the losses. The optimal design and placement of such protective devices should be investigated in future studies.

Outside the interaction regions, the biased study confirms that RB debris losses in the arcs and long straight sections are not a concern, with power loads typically of a few watts or less.

In summary, the biased RB study provides a statistically enhanced representation of the expected loss pattern, reducing statistical fluctuations and enabling a clearer identification of hot spots for beam–beam losses outside the main collimation insertion. In particular, it allows for a more precise quantification of the losses downstream of the IPs and in the arcs, which are otherwise obscured by statistical noise in the unbiased simulations. Overall, the simulations indicate that collisional beam–beam losses are not expected to be performance-limiting for the FCC-ee, and that the proposed collimation system design appears adequate to handle these losses.

6.6 Generic failure scenario

In addition to the regular beam loss mechanisms discussed in the previous sections, accidental or failure-induced beam losses can represent critical operational scenarios for the FCC-ee. Such events may arise, for instance, from asynchronous beam dumps, impedance-driven instabilities, injection failures, sudden RF trips, or interactions with dust particles in the beam pipe, as observed at SuperKEKB [153]. Although a full characterization of these failure modes requires dedicated studies for each specific case—such as those reported in Ref. [36] for impedance-driven instabilities following a feedback-system failure—it is nevertheless useful to evaluate the collimation system response to a simplified, representative failure scenario.

To this end, a *generic failure scenario* has been simulated to assess the system performance under fast beam-loss conditions. The study models a Gaussian bunch impacting the horizontal primary collimator TCP.H.B1 with an impact parameter of one σ_x[3], where σ_x is the horizontal rms beam size at the TCP.H.B1 location, thereby representing a generic proxy for any sudden beam–collimator interaction caused by a machine failure.

This study complements the steady-state beam-loss analyses presented earlier in this chapter by exploring an extreme, time-localized loss scenario representative of accidental beam impacts.

Simulation setup

The study was performed for the FCC-ee (V25.2 GHC [15]) Z operation mode at a beam energy of 45.6 GeV. An Xsuite–BDSIM simulation was carried out with a total of 10^7 macroparticles, tracked for 1000 turns in the full nonlinear FCC-ee lattice. The simulation included synchrotron radiation effects (damping,

[3]An impact parameter of one σ_x corresponds to a *deep impact* condition on the primary collimator, i.e. a direct and significant interception of the beam with the collimator jaw.

quantum excitation, and magnetic lattice tapering) and RF cavities, with the physical beam-pipe aperture limitations and all collimators modeled in BDSIM/Geant4. Particle losses during tracking were recorded in longitudinal bins of 10 cm.

The initial condition represents a fast-failure proxy: a matched Gaussian bunch was prepared immediately upstream of the horizontal primary betatron collimator TCP.H.B1, using the equilibrium emittances and bunch length at collision (see Table 1.2). The bunch was generated around the closed orbit and then horizontally displaced so that its centroid impacted the *left* (positive-x) jaw of TCP.H.B1 with an impact parameter of $1\,\sigma_x$, where σ_x is the local horizontal rms beam size at TCP.H.B1.

Each of the 10^7 macroparticles represents a fraction of the real beam population. This approach allows evaluating loss scenarios involving an arbitrary number of bunches deeply impacting TCP.H.B1 *a posteriori*, by rescaling the results according to the corresponding macroparticle weighting. In the present study, the results have been rescaled to represent the impact of **40 bunches** at full nominal intensity, which corresponds to the estimated damage threshold for a molybdenum–graphite (MoGr) primary collimator according to detailed FLUKA energy-deposition studies performed by the CERN SY-STI group for similar deep-impact conditions [154].

Results

The resulting loss maps are presented in Figs. 6.52 and 6.53, corresponding to the impact of 40 bunches at full nominal intensity. These plots show the longitudinal distribution of energy deposition from particle losses on the collimators and on the beam-pipe aperture along the full FCC-ee ring (Fig. 6.52), as well as a zoomed view of the PF collimation insertion (Fig. 6.53). For aperture losses, the longitudinal bin size is 10 cm, while for collimators it corresponds to the respective collimator length (see Table 5.5). It is important to recall that, unlike the collimators—whose materials are explicitly modeled and for which the interaction of beam particles with the jaw material is simulated through detailed Monte Carlo particle–matter interactions using BDSIM/Geant4—the beam pipe is treated in the simulation as a black absorber. In this model, any particle touching the physical aperture limit of the beam pipe is instantaneously registered as lost at that location, without further shower development being simulated.

As can be seen from Figs. 6.52 and 6.53, the vast majority of the energy deposition—exceeding 99 %—occurs locally within the PF collimation insertion. The primary collimator TCP.H.B1, which directly intercepts the incoming bunches, absorbs the largest fraction of the total energy stored in the 40 bunches. With the total stored energy per bunch being about 1.5 kJ, the total stored energy in 40 bunches amounts to 58.8 kJ. Of this total, 24.5 kJ are lost in the simulation, with 22.8 kJ deposited in TCP.H.B1—corresponding to roughly 38.8% of the total energy stored in 40 bunches and about 93% of the total energy lost.

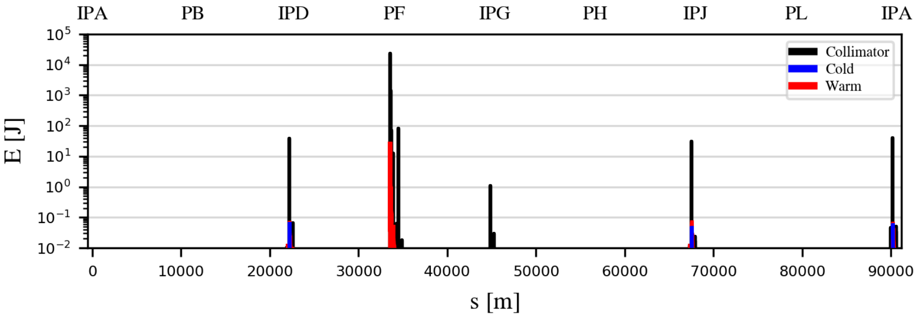

Figure 6.52. FCC-ee generic failure scenario loss map, corresponding to 40 bunches at full nominal intensity impacting the left jaw of the horizontal primary collimator TCP.H.B1 with an impact parameter of 1 σ_x. The plot shows the power deposition along the full ring.

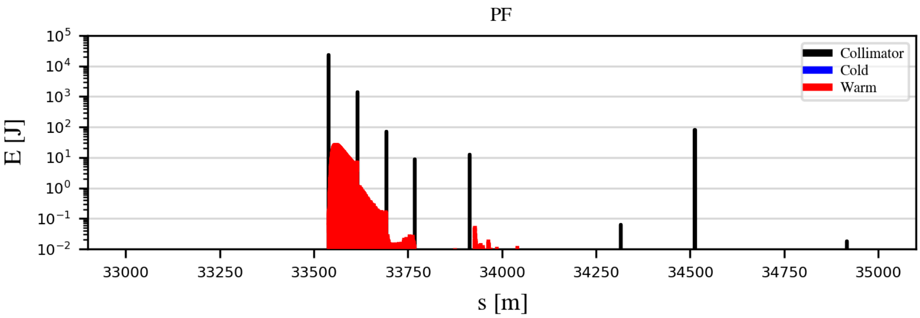

Figure 6.53. Zoomed view of the loss distribution in the PF collimation insertion for the generic failure scenario with 40 bunches impacting TCP.H.B1.

Downstream of TCP.H.B1, lower losses are registered on other collimators. The vertical betatron primary collimator TCP.V.B1 is the most exposed among these, with recorded losses of about 1.4 kJ (approximately 5.7% of the total energy lost). The secondary betatron collimators, both horizontal and vertical, are less exposed and register losses in the range of 10–100 J.

Outside the PF insertion, only a very small fraction of the total lost energy is detected, amounting to less than 1% of the total energy lost. Within this small fraction, most of the losses are registered on the vertical tertiary collimators upstream of the IPs, where the recorded losses are at most of the order of a few tens of joules. This demonstrates that the halo collimation system in PF is capable of suppressing losses on the TCTs by about three orders of magnitude with respect to the maximum losses registered in PF.

Losses on the beam-pipe aperture occur almost exclusively between the collimators within the PF insertion. The most loaded region is the beam-pipe section between the horizontal primary betatron collimator TCP.H.B1 and the vertical primary betatron collimator TCP.V.B1, where losses of up to a few tens of joules are recorded. Input from energy-deposition studies performed by the CERN SY-STI group [155] indicates that the estimated damage threshold of the Cu beam pipe for fast beam-loss events depends strongly on the spatial loss distribution. For localized, direct impacts on the beam pipe, a fraction of a single FCC-ee bunch (of the order of 10^{10} $e^{\pm}$) would already be sufficient to reach the melting point of copper. However, for distributed losses—as expected for particle losses occurring downstream of the primary collimators as a consequence of beam–collimator interactions—the melting threshold corresponds to several $\times 10^{13}$ $e^{\pm}$/m. Even assuming a conservative (pessimistic) threshold of 1×10^{13} $e^{\pm}$/m, this translates, in the units reported in the loss maps presented here, to approximately 7 kJ within a 10 cm bin. This value is more than two orders of magnitude above the maximum losses of only a few tens of joules recorded on the beam pipe downstream of the impacted collimators. One can therefore confidently conclude that the maximum beam-pipe losses remain well below any critical threshold. This confirms that, even under such failure-like conditions, no damage to the Cu vacuum chamber is expected, and that the directly impacted primary collimator remains the only potentially vulnerable component.

From these results, one can also estimate that, to reach the Cu melting threshold in such a failure scenario, an increase by a factor of approximately 350 in the energy lost on the beam pipe would be required. In terms of the number of bunches deeply impacting the TCP, this corresponds to about $40 \times 350 \approx 1400$ bunches, which is higher than the 12000 bunches foreseen to be stored in the FCC-ee in the Z-operation mode.

Overall, these results confirm the robustness of the FCC-ee halo collimation system under failure-like conditions. Despite the severity of the simulated impact, the losses remain almost entirely confined within the PF collimation section, with the impacted primary collimator intercepting nearly all of the lost energy. Since all downstream collimators experience loads reduced by orders of magnitude, the corresponding impacting distributions are significantly more diffuse than at the first impacted element, and the losses on the beam-pipe aperture remain well below critical thresholds. It can therefore be concluded that, in such a failure scenario, the only potentially damaged device would be the directly impacted primary collimator, confirming that the present collimation system provides effective protection against this class of accidental beam-loss events. It should nevertheless be stressed that, for a fully conclusive assessment, failure scenarios leading to more severe losses or involving qualitatively different impact conditions should be investigated using dedicated initial conditions representative of those specific cases. In addition, the potential risk of primary particle impacts on the secondary collimators during certain failures—for instance, if a coherent orbit oscillation were out of phase with the primary collimator—should be examined in future studies.

Chapter 7

Crystal Collimation for the FCC-ee

The design principles and performance of the FCC-ee collimation system have been described in the previous chapters. What has been discussed so far corresponds to what is considered, at the time of writing of this thesis, the baseline design for the FCC-ee collimation system.

As part of this thesis, a bent-crystal-assisted collimation scheme has also been explored as a possible alternative to the present baseline design. The aim is to investigate whether such a scheme could further improve collimation performance and address the unique challenges posed by the FCC-ee. This chapter presents the first studies aimed at assessing the feasibility of implementing a crystal-based collimation system in the FCC-ee.

First studies on crystal collimation for the FCC-ee were performed as part of this thesis work and have been published in Ref. [156]. These studies were conducted using the FCC-ee lattice version V23 GHC, which included dedicated collimation optics (see Fig. 5.1). In this chapter, an updated study is presented based on the same methodology but using the more recent FCC-ee lattice version V25.2 GHC, featuring universal straight-section optics. This is the reference version adopted throughout the rest of this thesis. The main design principles and analysis procedures remain unchanged; only the lattice version, simulation setup, and results have been updated accordingly.

7.1 FCC-ee crystal collimation system

As an alternative to the baseline design described in Chapter 5, which relies on conventional amorphous primary collimators, the use of bent crystals as primary halo deflectors has been explored.

As outlined in more detail in Section 2.3, this approach exploits channeling in bent crystals, whereby beam halo particles are guided along crystallographic planes and coherently steered toward designated absorbers. Compared to conventional amorphous collimators, this method offers the potential for enhanced collimation efficiency and for reducing the impedance contribution of the halo collimators.

The principle is as follows: bent crystals are installed in the collider and oriented such that the crystalline planes are parallel to the incoming halo trajectories. Halo particles entering within the critical channeling angle θ_c, defined in Eq. (2.57), are captured in the potential well between planes and follow the crystal curvature—i.e., they are *channeled*. After accumulating a significant angular deviation, these particles exit the crystal and are directed onto a downstream secondary collimator, which acts as an absorber.

In the first exploratory studies carried out as part of this thesis, the channeling of 45.6 GeV (FCC-ee Z operation mode) electrons and positrons in bent Si crystals with planar orientations (110) and (111) was investigated.

The location of the FCC-ee horizontal primary betatron collimator, TCP.H.B1, was selected as the candidate site for a horizontal, two-sided bent crystal collimator. The remainder of the halo collimation system layout was preserved, with the horizontal betatron secondary collimators serving as absorbers for the channeled beam halo. As described in detail in Chapter 5, the positions of the secondary collimators were already optimized in the baseline amorphous collimation system design. Maintaining these optimized conditions in the crystal collimation scheme ensures that halo particles which are not channeled, and are instead scattered amorphously, will still be effectively intercepted by the secondary collimators.

7.2 Crystal collimator parameter selection

In order to assess the feasibility of bent-crystal collimation in the FCC-ee, it is essential to determine a suitable set of parameters for the crystal collimator. The most relevant are the crystal length l and the bending angle θ, which together define the crystal bending radius $R = l/\theta$.

The choice of these parameters requires a careful balance between competing effects. On the one hand, large bending radii are desirable to provide a smooth deflection of the particles, thereby enhancing the probability that halo particles will remain in the channeling state for the full length of the crystal. On the other hand, crystals that are too long increase the probability of nuclear interactions, which, by increasing the dechanneling rate, reduce the channeling efficiency. Shorter crystals therefore tend to perform better in this respect.

The optimal performance of the system thus results from a compromise: the crystal must be long enough to achieve the desired bending with a sufficiently smooth deflection, while at the same time not exceeding the length at which nuclear interactions become detrimental. For this reason, a range of candidate parameters has been explored in this thesis.

7.2.1 Crystal bending angle

The first parameter considered is the bending angle of the crystal. This quantity directly determines the impact parameter of the channeled halo particles on the downstream absorbers. Larger bending angles produce larger deflections, which in turn increase the distance between the channeled trajectories and the machine reference orbit when they reach the absorber. From the point of view of collimation performance, this is highly beneficial, as it allows the absorbers to be potentially placed at a larger physical half-gap while still effectively intercepting the channeled beam halo. A larger impact parameter also helps to reduce sensitivity to misalignments and to uncertainties in the optics. However, increasing the bending angle also implies either a longer crystal or a smaller bending radius, and both of these factors tend to reduce the channeling efficiency. For this reason, a range of bending angles has been investigated.

Three bending angles were considered, following the first studies reported in Ref. [156]: 50 μrad, 100 μrad, and 150 μrad. These values span from relatively modest deflections, which maximize channeling efficiency, to stronger bends that enhance the impact parameter but come at the expense of efficiency. To estimate the effect of these bending angles on the particle trajectories, the standard formalism of transverse beam dynamics can be applied. The horizontal displacement of a particle deflected by a crystal with bending angle θ is given by

$$\begin{aligned} x(s) = {} & \sqrt{\frac{\beta_x(s)}{\beta_x(s_{cr})}} \left(\cos\Delta\mu_x + \alpha_x(s_{cr}) \sin\Delta\mu_x\right) x(s_{cr}) \\ & + \sqrt{\beta_x(s)\,\beta_x(s_{cr})}\, \sin\Delta\mu_x \left(x'(s_{cr}) + \theta\right), \end{aligned} \tag{7.1}$$

where $\beta_x(s)$ and $\beta_x(s_{cr})$ are the horizontal beta functions at the observation point and at the crystal location, respectively, $\alpha_x(s_{cr})$ is the corresponding Twiss α-parameter at the crystal location, and $\Delta\mu_x$ is the betatron phase advance between the two points. The quantities $x(s_{cr})$ and $x'(s_{cr})$ denote, respectively, the horizontal position and angle of the particle at the crystal location. The second term of Eq. (7.1) contains the contribution of the angular deflection imparted by the crystal. It is this term, which depends on the bending angle θ, that determines the separation of the channeled trajectories from the reference orbit.

By applying Eq. (7.1) to the FCC-ee optics, the transverse trajectories of halo particles deflected by 50, 100, and 150 μrad can be computed. The resulting trajectories are shown in Fig. 7.1 for halo particles deflected by the left jaw (positive x) of the crystal collimator. Trajectories for halo particles deflected by the right jaw (negative x) are specular.

As explained in detail in Chapter 5, the secondary collimator TCS.H1.B1 is located at a position optimized for the interception of halo particles outscattered at the primary horizontal collimator TCP.H.B1 with positive scattering angles ($\theta > 0$), while TCS.H2.B1 is placed at a location optimized for the interception

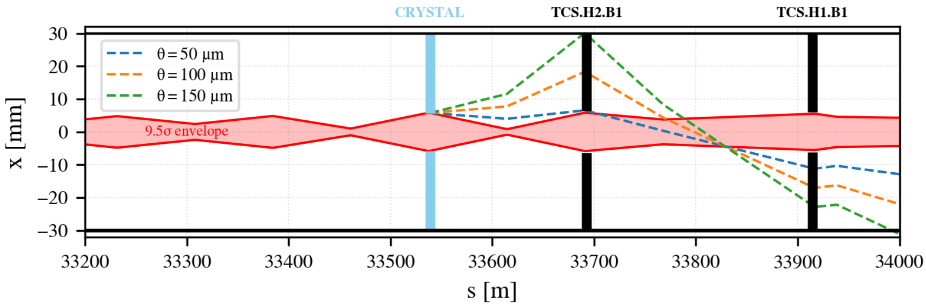

Figure 7.1. Horizontal beam envelope (9.5σ) in the betatron collimation section in PF. Dashed lines: particle trajectories deflected by a crystal with 50, 100, or 150 μrad bending angle.

of particles outscattered with negative scattering angles ($\theta < 0$). This can be observed quantitatively in Fig. 7.1, where the trajectory for $\theta = 50$ μrad nearly misses TCS.H2.B1 but intercepts TCS.H1.B1 with a sizeable impact depth.

In the crystal-collimation configuration, the primary amorphous collimator TCP.H.B1 is replaced by a bent crystal designed to impart a controlled positive angular kick ($\theta > 0$) to the halo particles. Therefore, one could, in principle, rely solely on TCS.H1.B1 as the absorber, potentially removing TCS.H2.B1. However, not all particles incident on the crystal are channeled: a fraction is unavoidably deflected by angles different from the nominal bending angle, and some particles can even be deflected at angles of opposite sign with respect to the bending one. For this reason, in these first studies it was considered more prudent to keep the FCC-ee collimation layout unchanged—except for replacing the primary with the crystal—to ensure good cleaning performance also for the non-channeled halo particles.

Additionally, as can also be seen in Fig. 7.1, for sufficiently large θ values ($\theta \geq \hat{\theta} \approx 47$ μrad), where $\hat{\theta}$ denotes the minimum deflection required for a particle to reach the left (positive-x) jaw of TCS.H2.B1, halo particles deflected by the crystal will first impact on TCS.H2.B1 rather than on TCS.H1.B1 only. Therefore, keeping the current layout of the secondary collimators offers an additional layer of protection in the crystal-collimation configuration.

To clarify the interception mechanism, the impact locations of halo particles for different deflection cases are summarized below. The example refers to halo particles impinging on the left (positive-x) jaw of the crystal collimator:

- **Negative deflection angle ($\theta < 0$):** particles are directed toward negative x and are intercepted by the right (negative-x) jaw of TCS.H2.B1.

- **Small positive deflection angle ($0 < \theta < \hat{\theta}$):** particles are deflected toward positive x but not enough to reach the left (positive-x) jaw of TCS.H2.B1; they are therefore intercepted by the right (negative-x) jaw of TCS.H1.B1.

- **Large positive deflection angle ($\theta \geq \hat{\theta}$):** particles are deflected toward positive x and are intercepted by the left (positive-x) jaw of TCS.H2.B1.

These different cases are illustrated in Fig. 7.2.

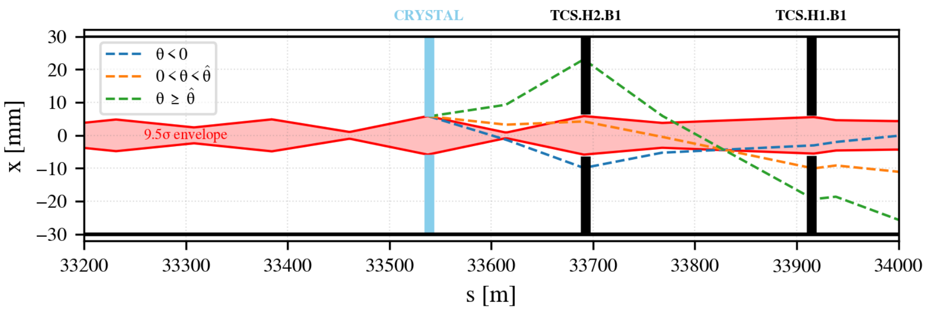

Figure 7.2. Trajectories of halo particles in the FCC-ee betatron collimation section for different deflection angles θ imparted by the crystal collimator. The 9.5σ beam envelope is shown in red. Dashed blue, orange, and green lines correspond, respectively, to halo particles deflected with negative angles ($\theta = -20$ µrad), small positive angles ($0 < \theta = 40$ µrad $< \hat{\theta}$), and large positive angles ($\theta = 120$ µrad $\geq \hat{\theta}$).

7.2.2 Crystal length

The second key parameter is the crystal length. This must be chosen in such a way that the bending radius $R = l/\theta$ is sufficiently large to allow channeling to occur smoothly. A lower bound is set by the so-called *critical radius*, R_c, which represents the minimum curvature radius for which the interplanar potential still provides a stable channeling well. An approximate expression for R_c is [67]:

$$R_c \approx \frac{E}{U'(x_{max})},$$

where E is the beam energy and $U'(x_{max})$ is the maximum gradient of the planar potential. For silicon crystals in the (110) and (111) orientations, $U'(x_{\mathrm{max}}) \simeq 5$ GeV/cm [78]. Inserting $E = 45.6$ GeV (FCC-ee Z operation mode) yields a critical radius of roughly $R_c \approx 9$ cm. To guarantee stable channeling, the bending radius R of the crystal must therefore be several times larger than this value. A conservative requirement of $R > 3R_c$ has been adopted in this study.

To explore the performance across a broad parameter space, six different crystal lengths were considered, ranging from 50 µm up to 500 µm. Combined with the candidate bending angles, these values correspond to bending radii between the tens of centimeters and the meter scale, thus comfortably above the critical threshold.

For reference, the bent crystals installed in the LHC collimation system feature a bending angle of about 50 μrad and a length of 4 mm, corresponding to a bending radius of approximately 80 m. Given the critical radius at the LHC beam energy is about 14 m, this configuration operates at roughly six times the critical radius—consistent with the conservative stability margin adopted here.

7.2.3 Critical angle

Another important figure of merit for crystal collimation is the critical channeling angle, θ_c. This angle defines the maximum angle of a halo particle with respect to the crystal plane that still allows it to be captured in the channeling regime. It is a function of the beam energy and the crystal bending parameters, and can be approximated as

$$\theta_c = \left(1 - \frac{R_c}{R}\right)\sqrt{\frac{2U_0}{E}},$$

where U_0 is the depth of the interplanar potential well, about 20 eV for the Si orientations of interest [78]. For the FCC-ee Z mode with 45.6 GeV beam energy, this expression yields critical angles of order 20 μrad or larger for all parameter combinations considered. This is significantly larger than the angular spread of the beam halo at the candidate crystal collimator location, which is typically of the order of 1 μrad or less. The large margin between θ_c and the halo divergence indicates that channeling conditions in the FCC-ee can be robustly maintained during operation. Importantly, this conclusion also holds for the highest-energy FCC-ee operation mode at 182.5 GeV ($t\bar{t}$ mode), where the critical angle is reduced by about a factor of two but still remains an order of magnitude larger than the typical beam halo angular spreads. It is also worth noting that channeling is successfully achieved in the LHC crystal collimation system during heavy-ion operation, where the critical angle is as small as about 2 μrad [75]. By comparison, the FCC-ee conditions are more favorable.

7.2.4 Channeling simulations

With the parameter space of bending angles and crystal lengths defined, dedicated channeling simulations were performed to quantify the expected efficiencies. The simulations were carried out using BDSIM, which, as described in detail in Chapter 3, provides a particle-tracking framework including detailed particle–matter interactions. In particular, BDSIM allows the use of the Geant4 crystal channeling module [79], which has been extensively validated against experimental data. The version available in BDSIM 1.7.7 was used for this work. Although this version does not yet incorporate certain advanced features such as channeling radiation and strong-field effects [157], it provides a reliable baseline for studying channeling efficiencies at the FCC-ee beam energies.

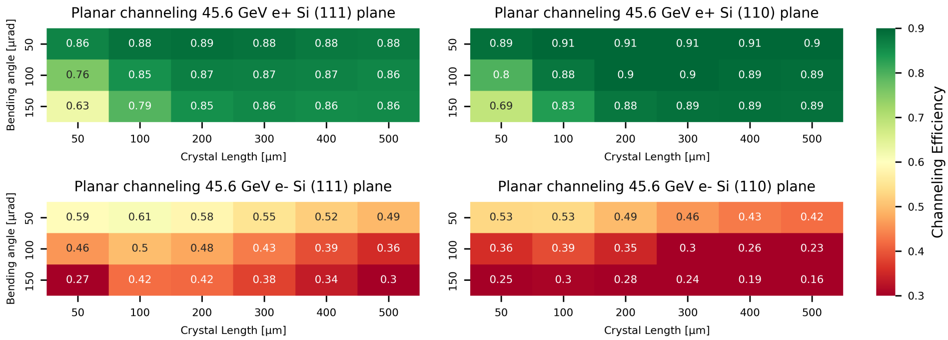

Figure 7.3. Heat maps of channeling efficiency for various Si planar orientations, bending angles, and crystal lengths.

The simulations were performed for both electrons and positrons at 45.6 GeV, using silicon crystals in the (110) and (111) planar orientations. A Gaussian distribution was generated in both transverse planes with $\sigma_{x,y} = 1$ µm and angular spreads $\sigma_{x',y'} = 1$ µrad. The electric fields of the Si crystal planes were taken from Ref. [158]. For each parameter set, the channeling efficiency ϵ_{ch} was computed as

$$\epsilon_{ch} = \frac{n_{ch}}{n_{tot}},$$

where n_{ch} is the number of particles exiting the crystal with a deflection angle within $[\theta - \theta_c,\, \theta + \theta_c]$, and n_{tot} is the total number of incident particles.

The results of these simulations are summarized in Fig. 7.3. They reveal clear trends with bending angle, length, and particle type.

The selection of the optimal crystal parameters requires a trade-off between channeling efficiency and the achieved impact depth (or impact parameter) at the downstream absorbers. The quantity that ultimately determines the collimation performance is the absorption efficiency in the absorbers, which depends on both factors: a higher channeling efficiency ensures that more halo particles are coherently deflected, while a larger impact parameter increases the likelihood that these particles are ultimately removed by the absorbers. To fully exploit the present layout of absorbers (secondary collimators), as discussed in Section 7.2.1, the condition is to have a sufficiently large positive deflection, $\theta > \hat{\theta}$, so that the channeled trajectories are intercepted by TCS.H2.B1, while the other possible trajectories are also intercepted, either by TCS.H2.B1 or by TCS.H1.B1. This constrains the practical choice for the bending angle (among the scanned ones) to 100 or 150 µrad. However, in the present optics version, as shown in Fig. 7.1, a deflection of 150 µrad is too strong, causing the channeled trajectories to intercept the beam-pipe aperture between the crystal and TCS.H2.B1. Consequently, $\theta = 100$ µrad is identified as the most suitable choice, offering a sufficiently large deflection to maximize absorption at the absorbers while maintaining good channeling efficiency and adequate aperture margins.

Table 7.1. First candidate parameters and settings for the FCC-ee (Z) horizontal betatron crystal collimation system.

Type	Count	Plane	Material	l [mm]	θ [μrad]	Half-gap [σ (mm)]	α_x	β_x [m]	TCP–TCS $\Delta\mu_x$ [deg]
e^+ beam									
crystal-TCP	1	H	Si (110)	0.2	100	9.5 (5.6)	6.3	496	-
absorber-TCS	2	H	Mo	300	–	10.5 (6.2, 6.5)	2.5, -1.2	501, 457	152.5, 193.8
e^- beam									
crystal-TCP	1	H	Si (111)	0.1	100	9.5 (5.6)	6.3	496	-
absorber-TCS	2	H	Mo	300	–	10.5 (6.2, 6.5)	2.5, -1.2	501, 457	152.5, 193.8

It should be noted that intermediate bending angles between 50 and 150 μrad could, in principle, provide an even better balance between efficiency and impact parameter, and their exploration is left for future studies involving full tracking simulations with varying crystal lengths and bending angles aimed at optimizing the overall cleaning performance. Moreover, bending angles below approximately 47 μrad, for which the channeled halo would miss TCS.H2.B1 and instead impact TCS.H1.B1, could also be investigated. A comprehensive assessment of these configurations through dedicated tracking simulations over a broader range of crystal parameters is therefore proposed as future work.

For the above reasons, the crystal parameters adopted in this study were, for electrons, a crystal with $\theta = 100$ μrad and $l = 100$ μm in the (111) orientation, which achieves a single-pass channeling efficiency of about 50%. For positrons, a crystal with $\theta = 100$ μrad and $l = 200$ μm in the (110) orientation, which achieves a single-pass channeling efficiency of almost 90%. These parameter choices represent a realistic and balanced starting point for the design of a crystal-collimation system for the FCC-ee.

The resulting candidate parameters for the FCC-ee crystal collimation system are summarized in Table 7.1.

It is worth adding that the simulation setup used here has been validated by reproducing, with good agreement, the results of the 6.3 GeV electron beam channeling experiment conducted at SLAC [159]. Additionally, while the SLAC experiment reported a channeling efficiency of approximately 22% for a 6.3 GeV electron beam, the BDSIM simulations performed here yield significantly higher efficiencies. This difference is consistent with expectations based on the scaling behavior of the dechanneling length [160], i.e., the characteristic length of the exponential decay of a population of channeled particles due to scattering with crystal nuclei and electrons. In our case, the crystal parameters for electron beam channeling are $l = 100$ μm and $\theta = 100$ μrad, corresponding to a bending radius of $R = 1$ m. In contrast, the SLAC experiment used a shorter crystal of $l = 60$ μm and a larger bending angle of $\theta = 400$ μrad, resulting in a much smaller bending radius of $R = 0.15$ m. The dechanneling length increases linearly with beam energy for a given set of crystal parameters (l, θ, $R = l/\theta$), and linearly with R for a fixed beam energy. In this work, both the beam energy and the bending radius are significantly larger—each by a factor of about seven—compared to the SLAC experiment. Therefore, a longer dechanneling length is expected, and a higher channeling efficiency is in line with expectations, despite the $\approx 70\%$ longer crystal considered in this study.

7.3 Crystal collimation performance assessment

Once optimal crystal collimator parameters for the electron and positron beams were identified, two further BDSIM simulations (one per beam type) were conducted, simulating a realistic FCC-ee halo beam impacting on a two-sided bent-crystal collimator with a maximum impact parameter of 1 μm. The impacting distribution corresponds to the same *direct halo* distribution used for the generic beam halo loss scenario discussed in Section 6.1 and shown in Fig. 6.1.

The channeled halo distributions emerging from the crystal were then used as input to perform collimation tracking in the full FCC-ee ring, using the Xsuite–BDSIM simulation setup.

In these simulations, a channeled beam halo consisting of 5×10^6 macroparticles (45.6 GeV e^- or e^+) was tracked in the full nonlinear FCC-ee lattice for one machine turn, accounting for the effects of synchrotron radiation (damping and quantum excitations), RF cavities, magnetic lattice tapering, and incorporating a detailed aperture model as well as collimators modelled in BDSIM/Geant4. The simulation output is the distribution of beam losses on collimators and machine apertures around the ring.

It should be noted that the tracking was limited to one machine turn because of a current limitation of the Xsuite–BDSIM coupling, which does not yet support crystal collimators (with crystal channeling physics) in a multi-turn tracking setup. For this reason, a decoupled simulation approach was adopted: first, a BDSIM simulation including crystal channeling physics was used to generate the channeled halo distributions; these were then imported into the Xsuite–BDSIM framework for one-turn tracking with amorphous collimator interactions. A full implementation of crystal collimators within the Xsuite–BDSIM coupling is foreseen in the near future. Nevertheless, for the present studies, this one-turn approach still provides meaningful results: in simulations based on direct-halo distributions impacting a primary (or crystal) collimator, the vast majority of particles are lost within the first turn. Therefore, the resulting beam-loss patterns already offer a representative picture of the overall collimation-cleaning performance and allow for a reliable comparison between the investigated crystal-collimation system and the baseline system relying on amorphous collimators.

The same type of simulation was performed for the standard amorphous-collimator-based collimation system, and the one-turn collimation cleaning performance was compared.

The results of this comparison are reported in Fig. 7.4 as loss maps, showing the *local cleaning inefficiency* around the ring, defined as $\eta = N_{\mathrm{loss},\Delta s}/(N_{\mathrm{tot}}\Delta s)$, where $N_{\mathrm{loss},\Delta s}$ is the integrated number of particles lost in $[s, s + \Delta s]$, and N_{tot} is the total number of simulated macroparticles. In Fig. 7.4 only the loss map for the e^+ beam is shown for the amorphous case, as for the e^- beam the collimation performance is equivalent.

Figure 7.4 shows that the one-turn collimation-cleaning performance of the crystal-collimation system is improved compared to that of the amorphous-

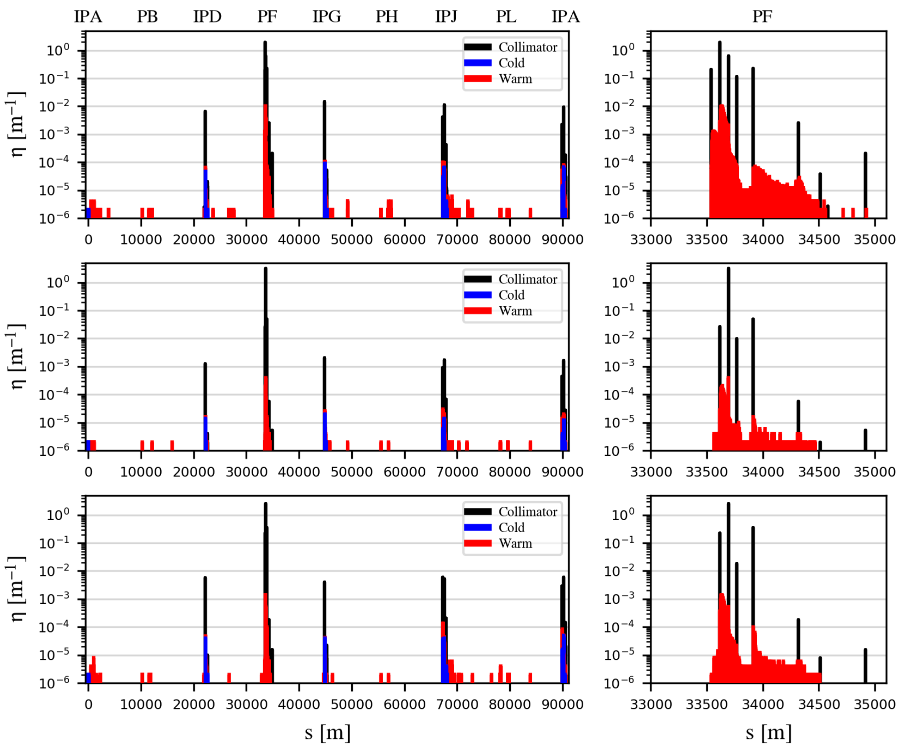

Figure 7.4. Loss maps for horizontal betatron collimation losses: full FCC-ee ring (left) and PF halo collimation insertion (right) for e^+ beam with standard collimation (top), e^+ beam with crystal collimation (middle), and e^- beam with crystal collimation (bottom).

collimation system for both electron and positron beams. Notably, crystal collimation of the positron beam halo reduces the maximum losses at the tertiary collimators (TCTs) upstream of each interaction point by about one order of magnitude. The reduction of TCT losses for crystal collimation of the electron beam halo is less pronounced, with the maximum TCT losses reduced by roughly a factor of two. This smaller improvement in the collimation-cleaning performance for the electron beam is expected and consistent with the significantly lower channeling efficiencies for electrons compared to positrons, as shown in Fig. 7.3.

Examining more closely the beam-loss patterns in the collimation insertion PF in Fig. 7.4, several additional observations can be made. First, in the crystal-collimation configuration, no losses are registered on the crystal collimator itself for either beam type, indicating that channeled particles are effectively steered toward the absorbers. Second, a clear reduction of losses is observed at the primary vertical collimator TCP.V.B1: the reduction amounts to about two orders of magnitude for the positron case and to approximately one order

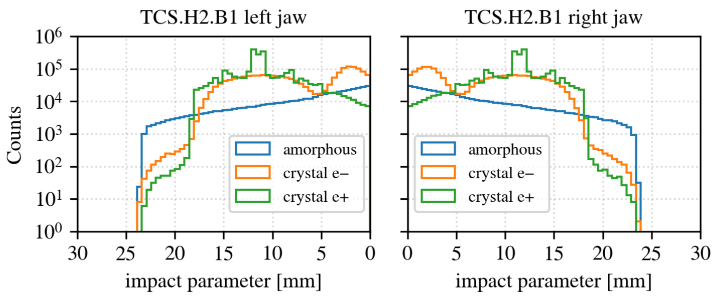

Figure 7.5. Impacting distributions on the TCS.H2.B1 absorber.

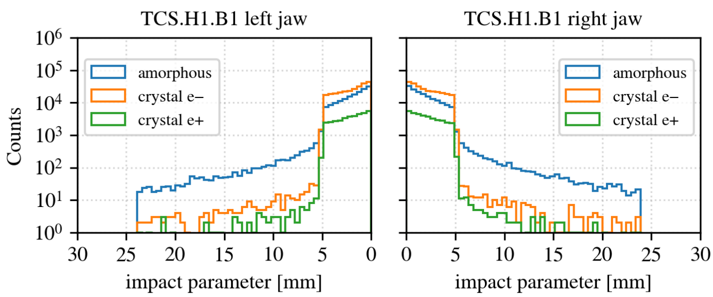

Figure 7.6. Impacting distributions on the TCS.H1.B1 absorber.

of magnitude for the electron case. This improvement arises because, with channeling, halo particles are coherently steered toward the absorbers in the horizontal collimation plane, resulting in far fewer particles being amorphously scattered into the orthogonal (vertical) plane. The smaller reduction observed in the electron case is again consistent with the lower channeling efficiency of electrons. At the same time, in the crystal-collimation configuration for both beams, a significant increase in losses is observed on the first absorber in the collimation plane, TCS.H2.B1, as expected from the channeled trajectories. Specifically, the losses on TCS.H2.B1 increase by about a factor of four compared to the amorphous-collimation case for both e^- and e^+ beams.

A larger asymmetry in the losses between the two absorbers, TCS.H2.B1 and TCS.H1.B1, is also evident in the crystal-collimation case. This reflects the fact that most of the beam-halo particles are deflected toward TCS.H2.B1, while a smaller fraction is deflected by the crystal at negative angles, thereby being directed toward TCS.H1.B1. The losses on TCS.H1.B1 are higher for the electron beam than for the positron beam, consistent with the lower electron channeling efficiency and the consequently larger number of particles exiting the crystal with a negative deflection angle.

Furthermore, the crystal-collimation system registers fewer off-momentum losses compared to the amorphous-collimation system. This reduction likely originates from the smaller fraction of out-scattered off-momentum particles from the collimators, due to both the increased interaction of the beam halo with high-density absorbers rather than amorphous low-density TCPs, and the larger average impact parameter on the TCS.H2.B1 absorber achieved with crystal collimation (see Fig. 7.5). Finally, in the crystal-collimation configuration for both beam types, a substantial reduction—by up to more than one order of magnitude—is observed in local aperture losses within the PF collimation insertion. This reduction is particularly advantageous in mitigating radiation levels in a region that is otherwise a hotspot for activation.

Figures 7.5 and 7.6 show the impact distributions on the absorbers TCS.H2.B1 and TCS.H1.B1 for all studied cases. In the amorphous-collimation configuration, the distributions extend smoothly from the absorber edge up to a maximum impact parameter of about 25 mm on both TCS.H2.B1 and TCS.H1.B1. In contrast, in the crystal-collimation cases, distinct channeling peaks, the onset of dechanneling tails, and additional peaks corresponding to non-channeled particles negatively deflected onto the opposite TCS.H2.B1 jaw[1] are visible on TCS.H2.B1. The latter contribution is more pronounced for the electron beam, consistent with its lower channeling efficiency compared to the positron beam. These distributions provide a clear explanation for the superior cleaning performance of the crystal-collimation system relative to the amorphous system, as well as for the better performance observed for the positron beam compared to the electron beam. The main performance gain of crystal collimation lies in increasing the impact parameter of the channeled halo particles on the downstream absorbers. In the present study, the average impact parameter on TCS.H2.B1 increases from 6.9 mm in the amorphous-collimation case to 7.4 mm for crystal collimation of the electron beam, and to 10.9 mm for crystal collimation of the positron beam.

Finally, an additional observation from Figs. 7.5 and 7.6 is that, in the crystal-collimation configuration, the impacting distributions are more spatially concentrated. While this better localization at larger impact parameters is beneficial for cleaning efficiency—and potentially advantageous from an impedance standpoint if the absorber mechanical gaps can be increased to reduce impedance while maintaining effective collimation—it may also pose challenges in terms of local energy deposition on the absorbers. Dedicated future studies will therefore be required to assess whether the absorbers can safely withstand the energy deposition associated with such localized impact distributions.

7.4 FCC-ee crystal collimation summary

In this thesis, the feasibility and performance of a bent-crystal collimation system have been explored as an alternative to the baseline amorphous collimation system in the FCC-ee. The channeling of electrons and positrons in bent Si crystals along the (110) and (111) planar orientations has been investigated.

[1] These correspond to particles following the blue trajectory shown in Fig. 7.2.

Simulations identified optimal crystal orientations and initial crystal parameters—such as bending angle and length—to maximize channeling efficiency while maintaining compatibility with the FCC-ee collimation optics. The initial working points were selected to be Si(111) with $(\theta, l) = (100\ \mu\text{rad}, 100\ \mu\text{m})$ for the e^- beam and Si(110) with $(\theta, l) = (100\ \mu\text{rad}, 200\ \mu\text{m})$ for the e^+ beam, achieving channeling efficiencies of approximately 50% and 90%, respectively.

Collimation-tracking simulations showed that the one-turn cleaning efficiency of the crystal-collimation system is improved relative to the amorphous baseline. Additionally, significant reductions (up to a factor of 10) in local aperture losses within the halo-collimation insertion were observed for both beam types, which is advantageous for reducing radiation levels. The studies presented in this thesis have so far evaluated the crystal-collimation performance for electron and positron beams only against generic beam-halo losses. For a complete assessment of the crystal-collimation performance, it will be necessary to extend the analysis to other regular beam-loss scenarios and, more importantly, to abnormal and failure scenarios, in order to determine whether a crystal-based system can provide a sufficient level of machine protection. Furthermore, a full evaluation should include the study of cleaning inefficiency using multi-turn simulations.

If the performance of the crystal-collimation system is confirmed by these additional studies, crystal collimation of electron and positron beams could be considered a promising strategy also for existing e^+e^- colliders such as SuperKEKB [18] and DAΦNE [161], as well as for future Higgs or Tau–Charm factories.

Future work should focus on assessing multi-turn collimation performance, using the latest channeling simulation routines (including channeling radiation and strong-field effects), and extending the studies to additional beam-loss scenarios—both regular and abnormal—to fully evaluate the capabilities of a crystal-based collimation system. Further efforts should also explore other channeling processes such as axial channeling and (multiple) volume reflection. In addition, dedicated studies are required to evaluate whether the absorbers can withstand the energy deposition from channeled beam halos; these studies will guide the optimization of absorber design parameters, including material and length.

Chapter 8

Conclusions

This thesis presents a comprehensive design and performance study of the beam collimation system for the Future Circular electron–positron Collider (FCC-ee), a proposed next-generation lepton collider aiming to push the frontiers of precision physics by delivering unprecedented luminosities. The combination of high stored beam energy and ultra-low emittances expected in the FCC-ee represents a completely new operational regime for lepton machines, introducing unique beam-loss and collimation challenges for this class of accelerators.

The goal of this work was to design a beam collimation system capable of ensuring both the efficient reduction of beam losses in the interaction regions—to minimize the risk of unwanted experimental backgrounds—and the reliable protection of machine components, while accommodating the unique constraints imposed by its demanding beam parameters and beam-dynamics regime. Achieving this required not only conceptual and analytical design efforts, but also the development and validation of advanced simulation tools able to model beam losses and collimation processes under realistic machine conditions.

In this context, dedicated simulation routines to model beam–residual gas interactions and Touschek scattering were developed. While similar capabilities exist in other codes, the distinctive feature of these implementations is their native integration within the Xsuite framework. This allows these effects to be combined self-consistently with others, such as online Monte Carlo particle–matter interactions in collimators and, where relevant, beam–beam interactions, enabling beam-loss and collimation studies of unprecedented complexity.

Beyond the development of simulation tools, this thesis has delivered the first end-to-end validation of Xsuite-based collimation and background simulations at a lepton collider, using data from a machine study performed at SuperKEKB. In this benchmark, the simulations accurately reproduced the beam-induced background dose-rate evolution measured in the Belle II detector during a vertical collimator scan. To complement this validation, the same simulation tool was also benchmarked against measured beam-loss patterns with protons from the LHC. Together, these studies provide a direct validation of key ingredients relevant for simulation-based FCC-ee predictions.

On the design side, this thesis proposes for the FCC-ee a multi-stage halo collimation system implemented in the PF technical insertion. The system is based on primary and secondary betatron and off-momentum collimators, complemented by shower absorbers and by tertiary collimators upstream of the interaction regions, with settings chosen to protect the identified aperture and momentum bottlenecks while respecting operational and integration constraints and minimizing impedance as far as permitted by the present optics configuration. Together, these elements provide global halo cleaning in PF and additional local protection of the final-focus systems and synchrotron-radiation collimators against residual or fast beam losses.

A detailed quantitative evaluation of the impedance contribution of the FCC-ee collimators was beyond the scope of this thesis. First studies indicate that the present baseline may lead to excessive impedance, driven primarily by the vertical primary betatron collimator. However, this limitation is well understood, and several mitigation paths are already under study, including geometry optimization, optics modifications, and alternative collimation schemes such as crystal or nonlinear collimation. An actionable roadmap is therefore in place to converge on a collimation and optics design compatible with impedance constraints.

The performance of the proposed FCC-ee halo collimation system was evaluated through an extensive simulation campaign covering the main regular beam-loss mechanisms expected during operation. In addition, a dedicated study was performed for a generic failure scenario, representing a proxy for sudden beam–collimator interactions caused by machine failures. All studies were carried out for the FCC-ee Z operation mode, which is the most challenging from a collimation standpoint due to the highest stored beam energy.

Overall, the FCC-ee baseline collimation system proposed in this work is shown to provide robust protection and efficient cleaning, with strong resilience to both regular and accidental beam-loss scenarios that are well represented by the generic failure proxy studied here. The results establish comfortable performance margins, validate the design choices, and highlight clear paths for further improvement.

Beyond the baseline collimation system relying on conventional amorphous collimators, this thesis also explored crystal collimation as a possible alternative strategy for the FCC-ee. Bent-silicon crystals were investigated as replacements for the horizontal primary collimator jaws, and first crystal-collimator parameters were identified.

Tracking simulations of generic beam-halo losses indicate that a crystal-based system can achieve higher one-turn cleaning efficiency than the baseline amorphous system, especially for the positron beam, while offering the potential for a reduced impedance contribution. These results suggest that crystal collimation is technically feasible and performance-wise promising for the FCC-ee. However, a complete assessment will require further multi-turn studies over a broader range of beam-loss scenarios, including abnormal and failure conditions. If confirmed, crystal collimation could represent a viable evolution of the FCC-ee collimation baseline and a potential upgrade path for other high-luminosity e^+e^- colliders such as SuperKEKB or future Higgs and τ–Charm factories.

Future studies will include a full quantitative assessment of the collimation performance across all FCC-ee operation modes as part of the forthcoming technical design phase, complementing the studies presented in this thesis for the most critical Z operation mode. Furthermore, beyond the present baseline GHC optics used throughout this thesis, the collimation performance should also be evaluated for alternative optics and layouts, such as the Local Chromatic Correction (LCC) optics [16] presently under development by the FCC-ee optics design team. Additional beam-loss mechanisms, including scattering of beam particles on thermal photons, as well as further accidental and failure scenarios—such as fast losses induced by impedance-driven instabilities, equipment failures, and sudden beam losses from beam–dust interactions (as observed at SuperKEKB)—will also be investigated.

Further assessments of tolerances to beam losses for the most sensitive machine components are recommended, including the experimental detectors, superconducting magnets, and other critical elements, to establish precise requirements and provide feedback for continued optimization of the collimation system design.

Additional studies are also foreseen on energy deposition in collimators, radiation aspects, engineering design, and impedance, for which the improvement paths outlined above should be explored.

The work presented in this thesis has combined conceptual design, simulation developments, and experimental validation into a coherent framework for designing and assessing beam-collimation system performance in high-luminosity lepton colliders. Beyond its application to the FCC-ee, the methods developed here constitute a reusable and extensible approach that can be applied to the study and optimization of collimation systems in other present and future high-luminosity e^+e^- colliders.

Bibliography

[1] O. S. Brüning, P. Collier, P. Lebrun, S. Myers, R. Ostojic, J. Poole, and P. Proudlock (editors). LHC design report v.1: The LHC main ring. Technical Report CERN-2004-003-V1, CERN, Geneva, Switzerland, 2004.

[2] *LEP Design Report, Vol. 2: The LEP Main Ring*. CERN, Geneva, Switzerland, 1984. URL `https://cds.cern.ch/record/102083`.

[3] Carlo Wyss (editor). *LEP Design Report, Vol. 3: LEP2*. CERN, Geneva, Switzerland, 1996. URL `https://cds.cern.ch/record/314187`.

[4] Ralph Aßmann, Mike Lamont, and Steve Myers. A brief history of the LEP collider. *Nucl. Phys. B Proc. Suppl.*, 109(2):17–31, 2002. doi: 10.1016/S0920-5632(02)90005-8. URL `https://cds.cern.ch/record/549223/files/sl-2002-009.pdf`. Proceedings of the 7th Topical Seminar, CERN-SL-2002-009-OP.

[5] D. Brandt, H. Burkhardt, M. Lamont, S. Myers, and J. Wenninger. Accelerator Physics at LEP. *Rep. Prog. Phys.*, 63(6):939, 2000. doi: 10.1088/0034-4885/63/6/203. URL `https://dx.doi.org/10.1088/0034-4885/63/6/203`.

[6] R. Barate et al. Observation of an Excess in the Search for the Standard Model Higgs Boson at ALEPH. *Phys. Lett. B*, 495(1):1–17, 2000. doi: 10.1016/S0370-2693(00)01269-7. URL `https://www.sciencedirect.com/science/article/pii/S0370269300012697`.

[7] G. Aad et al. Observation of a New Particle in the Search for the Standard Model Higgs Boson with the ATLAS Detector at the LHC. *Phys. Lett. B*, 716(1):1–29, 2012. doi: 10.1016/j.physletb.2012.08.020. URL `https://www.sciencedirect.com/science/article/pii/S037026931200857X`.

[8] S. Navas et al. Review of Particle Physics. *Phys. Rev. D*, 110(3):030001, 2024. doi: 10.1103/PhysRevD.110.030001. URL `https://journals.aps.org/prd/abstract/10.1103/PhysRevD.110.030001`.

[9] A. Abada et al. FCC-ee: The Lepton Collider. *Eur. Phys. J. Spec. Top.*, 228(2):261–623, 2019. doi: 10.1140/epjst/e2019-900045-4. CERN-ACC-2018-0057.

[10] A. Abada et al. FCC Physics Opportunities. *Eur. Phys. J. C*, 79(6):474, 2019. doi: 10.1140/epjc/s10052-019-6904-3. CERN-ACC-2018-0056.

[11] M. Benedikt, F. Zimmermann, B. Auchmann, W. Bartmann, J.-P. Burnet, C. Carli, A. Chancé, P. Craievich, M. Giovannozzi, C. Grojean, J. Gutleber, K. Hanke, A. Henriques, P. Janot, C. Lourenço, M. Mangano, T. Otto, J. Poole, S. Rajagopalan, T. Raubenheimer, E. Todesco, L. Ulrici, T. Watson, and G. Wilkinson (editors). Future Circular Collider Feasibility Study Report, Volume 2. Technical report, CERN, Geneva, Switzerland, 2025. URL `https://cds.cern.ch/record/2928793`.

[12] M. Benedikt. FCC Project Status. Presented at the BE-FCC Workshop, CERN, Prévessin-Moëns, France, February 2025. URL `https://indico.cern.ch/event/1498846/contributions/6311771/attachments/3012264/5311377/250211_BE_workshop_FS-Status.pdf`.

[13] M. Aiba, B. Goddard, K. Oide, Y. Papaphilippou, Á. Saá Hernández, D. Shwartz, S. White, and F. Zimmermann. Top-up injection schemes for future circular lepton collider. *Nucl. Instrum. Methods Phys. Res. A*, 880:98–106, 2018. doi: 10.1016/j.nima.2017.10.075. URL `https://www.sciencedirect.com/science/article/pii/S0168900217311646`.

[14] K. Oide, M. Aiba, S. Aumon, M. Benedikt, A. Blondel, A. Bogomyagkov, M. Boscolo, H. Burkhardt, Y. Cai, A. Doblhammer, B. Haerer, B. Holzer, J. M. Jowett, I. Koop, M. Koratzinos, E. Levichev, L. Medina, K. Ohmi, Y. Papaphilippou, P. Piminov, D. Shatilov, S. Sinyatkin, M. Sullivan, J. Wenninger, U. Wienands, D. Zhou, and F. Zimmermann. Design of Beam Optics for the Future Circular Collider e^+e^- Collider Rings. *Phys. Rev. Accel. Beams*, 19(11):111005, 2016. doi: 10.1103/PhysRevAccelBeams.19.111005. URL `https://link.aps.org/doi/10.1103/PhysRevAccelBeams.19.111005`.

[15] K. Oide. GHC Optics: Smaller β_x^* / Technical Insertion. Presented at the 206th FCC-ee Accelerator Design Meeting, April 2025. URL `https://indico.cern.ch/event/1509196/contributions/6480794/attachments/3055731/5402860/Optics_Oide_bx*_techi_250424.pdf`.

[16] P. Raimondi, S. M. Liuzzo, L. Farvacque, S. White, and M. Hofer. Local Chromatic Correction Optics for the Future Circular Collider e^+e^-. *Phys. Rev. Accel. Beams*, 28(2):021002, 2025. doi: 10.1103/PhysRevAccelBeams.28.021002. URL `https://link.aps.org/doi/10.1103/PhysRevAccelBeams.28.021002`.

[17] B. Richter, A. Skrinski, M. Tigner, and H. Wiedemann. Limitations on Performance of e^+e^- Storage Rings and Linear Colliding Beam Systems at High Energy. *Fermilab Conf.*, 1979.

[18] K. Akai, K. Furukawa, and H. Koiso. SuperKEKB Collider. *Nucl. Instrum. Methods Phys. Res. A*, 907:188–199, 2018. doi: 10.1016/j.nima.2018.08.017. URL `https://www.sciencedirect.com/science/article/pii/S0168900218309616`. Advances in Instrumentation and Experimental Methods (Special Issue in Honour of Kai Siegbahn).

[19] R. Bruce, M. A. Jebramcik, J. M. Jowett, T. Mertens, and M. Schaumann. Performance and Luminosity Models for Heavy-Ion Operation at the CERN Large Hadron Collider. *Eur. Phys. J. Plus*, 136:745, 2021. doi: 10.1140/epjp/s13360-021-01685-5. URL `https://doi.org/10.1140/epjp/s13360-021-01685-5`.

[20] S. Terui, Y. Funakoshi, H. Hisamatsu, T. Ishibashi, K. Kanazawa, Y. Ohnishi, K. Shibata, M. Shirai, Y. Suetsugu, and M. Tobiyama. Report on Collimator Damaged Event in SuperKEKB. In *Proc. IPAC'21*, number 12 in International Particle Accelerator Conference, pages 3541–3544. JACoW Publishing, Geneva, Switzerland, August 2021. doi: 10.18429/JACoW-IPAC2021-WEPAB359. URL `https://jacow.org/ipac2021/papers/wepab359.pdf`.

[21] S. Terui, T. Ishibashi, T. Abe, Y. Funakoshi, H. Nakayama, K. Ohmi, D. Zhou, A. Natochii, and N. Yoshifuji. Low-Z Collimator for SuperKEKB. *Nucl. Instrum. Methods Phys. Res. A*, 1047:167857, 2023. doi: 10.1016/j.nima.2022.167857. URL `https://www.sciencedirect.com/science/article/pii/S0168900222011494`.

[22] KEKB B-Factory Design Report. Technical Report KEK 95-7, KEK, Tsukuba, Japan, 1995.

[23] T. Abe et al. Belle II Technical Design Report, 2010. URL `https://arxiv.org/abs/1011.0352`.

[24] High Energy Accelerator Research Organization (KEK). KEK Discovers New Subatomic Particle at Belle Experiment, 2016. URL `https://www2.kek.jp/en/newsroom/2016/03/02/1630/`. Accessed: 2025-02-24.

[25] SuperB Collaboration. SuperB Technical Design Report, 2013. URL `https://arxiv.org/abs/1306.5655`.

[26] M. Zobov (on behalf of the DAΦNE Team). Crab Waist Collision Scheme: A Novel Approach for Particle Colliders. *J. Phys. Conf. Ser.*, 747(1):012090, 2016. doi: 10.1088/1742-6596/747/1/012090. URL `https://dx.doi.org/10.1088/1742-6596/747/1/012090`.

[27] M. Zobov, D. Alesini, M. E. Biagini, C. Biscari, A. Bocci, R. Boni, M. Boscolo, F. Bossi, B. Buonomo, A. Clozza, G. O. Delle Monache, T. Demma, E. Di Pasquale, G. Di Pirro, A. Drago, A. Gallo, A. Ghigo, S. Guiducci, C. Ligi, F. Marcellini, G. Mazzitelli, C. Milardi, F. Murtas, L. Pellegrino, M. A. Preger, L. Quintieri, P. Raimondi, R. Ricci,

U. Rotundo, C. Sanelli, M. Serio, F. Sgamma, B. Spataro, A. Stecchi, A. Stella, S. Tomassini, C. Vaccarezza, M. Schioppa, M. Esposito, P. Branchini, F. Iacoangeli, P. Valente, E. Levichev, P. Piminov, D. Shatilov, V. Smaluk, N. Arnaud, D. Breton, L. Burmistrov, A. Stocchi, A. Variola, B. F. Viaud, S. Bettoni, K. Ohmi, and D. Teytelman. Test of "Crab-Waist" Collisions at the DAΦNE Φ Factory. *Phys. Rev. Lett.*, 104(17):174801, 2010. doi: 10.1103/PhysRevLett.104.174801. URL https://link.aps.org/doi/10.1103/PhysRevLett.104.174801.

[28] Y. Ohnishi. Recent Performance of SuperKEKB. Presented at the 70th ICFA Advanced Beam Dynamics Workshop on High-Luminosity Circular e^+e^- Colliders (eeFACT2025), Tsukuba, Japan, March 2025. URL https://indico.jacow.org/event/75/contributions/6753/attachments/714/2653/SuperKEKB_eeFACT2025.pdf.

[29] T. Ishibashi, S. Terui, Y. Suetsugu, K. Watanabe, and M. Shirai. Movable Collimator System for SuperKEKB. *Phys. Rev. Accel. Beams*, 23(5): 053501, 2020. doi: 10.1103/PhysRevAccelBeams.23.053501. URL https://link.aps.org/doi/10.1103/PhysRevAccelBeams.23.053501.

[30] H. Wiedemann. *Particle Accelerator Physics, 3rd ed.* Springer, Berlin, 2007. doi: 10.1007/978-3-540-49045-6. URL https://cds.cern.ch/record/1083415.

[31] M. Sands. The Physics of Electron Storage Rings: An Introduction. *Conf. Proc. C*, 6906161:257–411, 1969. SLAC-R-121, SLAC-121.

[32] B. Holzer. I.3 — Transverse Beam Dynamics. In *Proc. Joint Universities Accelerator School (JUAS), Vol. 3, No. I–IV, CERN Yellow Reports: School Proceedings*. CERN, 2024. doi: 10.23730/CYRSP-2024-003.73. URL https://e-publishing.cern.ch/index.php/CYRSP/article/view/1585.

[33] A. Lasheen. I.4 — longitudinal beam dynamics. In *Proc. Joint Universities Accelerator School (JUAS), Vol. 3, No. I–IV, CERN Yellow Reports: School Proceedings*. CERN, 2024. doi: 10.23730/CYRSP-2024-003.167. URL https://e-publishing.cern.ch/index.php/CYRSP/article/view/1586.

[34] R. Ischebeck. I.10 — Synchrotron Radiation. In *Proc. Joint Universities Accelerator School (JUAS), Vol. 3, No. I–IV, CERN Yellow Reports: School Proceedings*. CERN, 2024. doi: 10.23730/CYRSP-2024-003.433. URL https://e-publishing.cern.ch/index.php/CYRSP/article/view/1608.

[35] S. Redaelli. Beam Cleaning and Collimation Systems. *CERN Yellow Reports*, 2:403–437, 2016. doi: 10.23730/CYRSP-2016-002.403. URL https://e-publishing.cern.ch/index.php/CYR/article/view/243/212.

[36] G. Nigrelli et al. Simulations of Losses from Fast Instabilities in the FCC-ee. In *Proc. IPAC'25*, pages 374–377, Taipei, Taiwan, June 2025. JACoW Publishing, Geneva, Switzerland. doi: 10.18429/JACoW-IPAC25-MOPM032. URL `https://indico.jacow.org/event/81/contributions/7347`.

[37] R. Bruce, R. W. Assmann, V. Boccone, C. Bracco, M. Brugger, M. Cauchi, F. Cerutti, D. Deboy, A. Ferrari, L. Lari, A. Marsili, A. Mereghetti, D. Mirarchi, E. Quaranta, S. Redaelli, G. Robert-Demolaize, A. Rossi, B. Salvachua, E. Skordis, C. Tambasco, G. Valentino, T. Weiler, V. Vlachoudis, and D. Wollmann. Simulations and Measurements of Beam Loss Patterns at the CERN Large Hadron Collider. *Phys. Rev. Spec. Top. Accel. Beams*, 17:081004, 2014. doi: 10.1103/PhysRevSTAB.17.081004. URL `https://link.aps.org/doi/10.1103/PhysRevSTAB.17.081004`.

[38] Geant4 Collaboration. *Geant4 Physics Reference Manual (Version 11.3, doc Rev 9.0)*, 2024. Available at: `https://geant4-userdoc.web.cern.ch/UsersGuides/PhysicsReferenceManual/html/index.html` (accessed Oct 25, 2025).

[39] M. L. Perl. Notes on the Landau–Pomeranchuk–Migdal Effect: Experiment and Theory. In *Les Rencontres de Physique de la Vallée d'Aoste: Results and Perspectives in Particle Physics*, pages 463–477, 1994. URL `https://lib-extopc.kek.jp/preprints/PDF/1994/9408/9408075.pdf`.

[40] Y.-S. Tsai. Pair Production and Bremsstrahlung of Charged Leptons. *Rev. Mod. Phys.*, 46:815–851, 1974. doi: 10.1103/RevModPhys.46.815. URL `https://doi.org/10.1103/RevModPhys.46.815`.

[41] Geant4 Collaboration. G4eBremsstrahlungRelModel. `https://gitlab.cern.ch/geant4/geant4/-/blob/geant4-11.3-release/source/processes/electromagnetic/standard/src/G4eBremsstrahlungRelModel.cc`, 2024. Accessed: Oct 25, 2025. Part of Geant4 version 11.3.0.

[42] H. A. Bethe and L. C. Maximon. Theory of Bremsstrahlung and Pair Production. I. Differential Cross Section. *Phys. Rev.*, 93(4):768–784, 1954. doi: 10.1103/PhysRev.93.768. URL `https://link.aps.org/doi/10.1103/PhysRev.93.768`.

[43] H. Davies, H. A. Bethe, and L. C. Maximon. Theory of Bremsstrahlung and Pair Production. II. Integral Cross Section for Pair Production. *Phys. Rev.*, 93(4):788–795, 1954. doi: 10.1103/PhysRev.93.788. URL `https://link.aps.org/doi/10.1103/PhysRev.93.788`.

[44] M. L. Ter-Mikaelian. *High-Energy Electromagnetic Processes in Condensed Media.* Wiley-Interscience, New York, USA, 1972.

[45] S. Klein. Suppression of Bremsstrahlung and Pair Production Due to Environmental Factors. *Rev. Mod. Phys.*, 71:1501–1538, 1999. doi: 10.1103/RevModPhys.71.1501. URL `https://doi.org/10.1103/RevModPhys.71.1501`.

[46] T. Stanev et al. Development of Ultrahigh-Energy Electromagnetic Cascades in Water and Lead Including the Landau–Pomeranchuk–Migdal Effect. *Phys. Rev. D*, 25:1291–1304, 1982. doi: 10.1103/PhysRevD.25.1291. URL `https://doi.org/10.1103/PhysRevD.25.1291`.

[47] C. Leroy and P.-G. Rancoita. *Principles of Radiation Interaction in Matter and Detection.* World Scientific, Singapore, 4th edition, 2016. doi: 10.1142/9167. URL `https://www.worldscientific.com/doi/abs/10.1142/9167`.

[48] Emilio Segrè. *Nuclei and Particles: Introduction to Nuclear and Subnuclear Physics.* Benjamin–Cummings Publishing Company, Reading, Massachusetts, USA, 2nd edition, 1977. ISBN 978-0-8053-8601-1.

[49] M. J. Boschini, C. Consolandi, M. Gervasi, S. Giani, D. Grandi, V. Ivanchenko, S. Pensotti, P. G. Rancoita, and M. Tacconi. *Nuclear and Non-Ionizing Energy-Loss for Coulomb Scattered Particles from Low Energy up to Relativistic Regime in Space Radiation Environment*, pages 9–23. 2011. doi: 10.1142/9789814329033_0002. URL `https://www.worldscientific.com/doi/abs/10.1142/9789814329033_0002`.

[50] H. A. Bethe. Molière's Theory of Multiple Scattering. *Phys. Rev.*, 89(6):1256–1266, 1953. doi: 10.1103/PhysRev.89.1256. URL `https://link.aps.org/doi/10.1103/PhysRev.89.1256`.

[51] G. Molière. Theorie der Streuung schneller geladener Teilchen. II. Mehrfach- und Vielfachstreuung. *Z. Naturforsch. A*, 3(2):78–97, 1948. doi: 10.1515/zna-1948-0203. URL `https://doi.org/10.1515/zna-1948-0203`.

[52] G. Molière. Theorie der Streuung schneller geladener Teilchen. I. Einzelstreuung am abgeschirmten Coulomb-Feld. *Zeitschrift für Naturforschung A*, 2:133–145, 1947. doi: 10.1515/zna-1947-0302. URL `https://www.degruyterbrill.com/document/doi/10.1515/zna-1947-0302/html`.

[53] W. A. McKinley and H. Feshbach. The Coulomb Scattering of Relativistic Electrons by Nuclei. *Phys. Rev.*, 74(12):1759–1763, 1948. doi: 10.1103/PhysRev.74.1759. URL `https://link.aps.org/doi/10.1103/PhysRev.74.1759`.

[54] A. V. Butkevich, R. P. Kokoulin, G. V. Matushko, and S. P. Mikheyev. Comments on Multiple Scattering of High-Energy Muons in Thick Layers. *Nucl. Instrum. Methods Phys. Res. A*, 488(1):282–294, 2002. doi: 10.1016/S0168-9002(02)00478-3. URL `https://www.sciencedirect.com/science/article/pii/S0168900202004783`.

[55] V. Ivanchenko. G4eCoulombScatteringModel. https://gitlab.cern.ch/geant4/geant4/-/blob/geant4-11.3-release/source/processes/electromagnetic/standard/src/G4eCoulombScatteringModel.cc, 2024. Accessed: Oct 25, 2025. Part of Geant4 version 11.3.0.

[56] C. Consolandi. G4eSingleCoulombScatteringModel. https://gitlab.cern.ch/geant4/geant4/-/blob/geant4-11.3-release/source/processes/electromagnetic/standard/src/G4eSingleCoulombScatteringModel.cc, 2024. Accessed: Oct 25, 2025. Part of Geant4 version 11.3.0.

[57] C. Bernardini, G. F. Corazza, G. Di Giugno, G. Ghigo, J. Haissinski, P. Marin, R. Querzoli, and B. Touschek. Lifetime and Beam Size in a Storage Ring. *Phys. Rev. Lett.*, 10(9):407–409, 1963. doi: 10.1103/PhysRevLett.10.407. URL https://link.aps.org/doi/10.1103/PhysRevLett.10.407.

[58] C. Bernardini. AdA: The First Electron–Positron Collider. *Phys. Perspect.*, 6(2):156–183, 2004. doi: 10.1007/s00016-003-0202-y. URL https://doi.org/10.1007/s00016-003-0202-y.

[59] H. Brück. Circular Particle Accelerators. Technical Report LA-TR-72-10 Rev, Los Alamos Scientific Laboratory, Los Alamos, New Mexico, USA, 1972. URL https://inspirehep.net/files/828e8e94d9e43661aa44f1968ca581eb. English translation of *Accélérateurs circulaires de particules* (Paris: PUF, 1966).

[60] A. Piwinski. The Touschek Effect in Strong Focussing Rings. Technical Report DESY 98-179, Deutsches Elektronen-Synchrotron (DESY), 1998. URL https://arxiv.org/pdf/physics/9903034.

[61] A. Xiao and M. Borland. Monte Carlo Simulation of the Touschek Effect. *Phys. Rev. Spec. Top. Accel. Beams*, 13(7):074201, 2010. doi: 10.1103/PhysRevSTAB.13.074201. URL https://link.aps.org/doi/10.1103/PhysRevSTAB.13.074201.

[62] M. A. V. García and F. Zimmermann. Beam Blow Up due to Beamstrahlung in Circular e^+e^- Colliders, 2019. URL https://arxiv.org/abs/1911.03420.

[63] K. Yokoya. Quantum Correction to Beamstrahlung Due to the Finite Number of Photons. *Nucl. Instrum. Methods Phys. Res. A*, 251(1):1–16, 1986. doi: 10.1016/0168-9002(86)91144-7. URL https://www.sciencedirect.com/science/article/pii/0168900286911447.

[64] K. Yokoya and P. Chen. Beam–Beam Phenomena in Linear Colliders. In M. Dienes, M. Month, and S. Turner, editors, *Frontiers of Particle Beams: Intensity Limitations*, pages 415–445. Springer, Berlin, Heidelberg, 1992.

ISBN 978-3-540-46797-7. URL https://www.ippp.dur.ac.uk/~gudrid/teaching/yokoya.pdf.

[65] P. Kicsiny, X. Buffat, D. Schulte, H. Burkhardt, T. Pieloni, and M. Seidel. Multiturn Simulation of Radiative Bhabha Scattering in the Equivalent Photon Approximation. *Phys. Rev. Accel. Beams*, 27(9):091001, 2024. doi: 10.1103/PhysRevAccelBeams.27.091001. URL https://link.aps.org/doi/10.1103/PhysRevAccelBeams.27.091001.

[66] P. Kicsiny. Private communication, 2025.

[67] D. Mirarchi. *Crystal Collimation for the LHC*. PhD thesis, Imperial College London, August 2015. URL https://inspirehep.net/files/4071f2ad70f407a3ad4f80e2eca42fc3.

[68] R. R. Wilson. Tevatron. *Phys. Today*, 30(10), October 1977. doi: 10.1063/1.3037746. URL https://www.osti.gov/biblio/7282652.

[69] V. D. Shiltsev. Experience with Crystals at Fermilab Accelerators. *Int. J. Mod. Phys. A*, 34(34):1943007, 2019. doi: 10.1142/S0217751X19430073. URL https://doi.org/10.1142/S0217751X19430073.

[70] R. W. Assmann, S. Redaelli, and W. Scandale. Optics Study for a Possible Crystal-Based Collimation System for the LHC. *EPAC'06 Proc.*, 2006. URL https://cds.cern.ch/record/972334. Revised version, 15 Sep 2006.

[71] A. Seryi. Future Prospects of Accelerator Science for Particle Physics. *Nucl. Instrum. Methods Phys. Res. A*, 623(1):23–28, 2010. doi: 10.1016/j.nima.2010.02.145. URL https://www.sciencedirect.com/science/article/pii/S0168900210004122.

[72] R. P. Fliller, A. Drees, D. Gassner, L. Hammons, G. McIntyre, S. Peggs, D. Trbojevic, V. Biryukov, Y. Chesnokov, and V. Terekhov. RHIC Crystal Collimation. *Nucl. Instrum. Methods Phys. Res. B*, 234(1):47–56, 2005. doi: 10.1016/j.nimb.2005.03.004. URL https://www.sciencedirect.com/science/article/pii/S0168583X05002260.

[73] D. Mirarchi, V. Avati, R. Bruce, M. Butcher, M. D'Andrea, M. Di Castro, M. Deile, B. Dziedzic, K. Hiller, S. Jakobsen, J. Kašpar, K. Korcyl, I. Lamas, A. Masi, A. Mereghetti, H. Garcia Morales, Y. Gavrikov, S. Redaelli, B. Salvachua Ferrando, P. Serrano, M. Solfaroli Camillocci, and N. Turini. Reducing Beam-Related Background on Forward Physics Detectors Using Crystal Collimation at the Large Hadron Collider. *Phys. Rev. Appl.*, 14(6):064066, 2020. doi: 10.1103/PhysRevApplied.14.064066. URL https://link.aps.org/doi/10.1103/PhysRevApplied.14.064066.

[74] M. D'Andrea, O. Aberle, A. Abramov, R. Bruce, R. Cai, M. Calviani, Q. Demassieux, K. A. Dewhurst, M. Di Castro, L. S. Esposito, Y. A. Gavrikov, S. Gilardoni, P. D. Hermes, Y. M. Ivanov, B. Lindström, A. Lechner, E. Matheson, D. Mirarchi, J.-B. Potoine, S. Redaelli, G. Ricci, R. Seidenbinder, S. Solis Paiva, L. Bandiera, V. Guidi, A. Mazzolari, M. Romagnoni, M. Tamisari, Y. Gavrikov, and Y. Ivanov. Crystal Collimation Performance at the LHC with a 6.8 TeV Proton Beam. *JACoW IPAC*, 2023:MOPL023, 2023. doi: 10.18429/JACoW-IPAC2023-MOPL023. URL `https://cds.cern.ch/record/2884756`.

[75] M. D'Andrea, O. Aberle, R. Bruce, M. Butcher, M. Di Castro, R. Cai, I. Lamas, A. Masi, D. Mirarchi, S. Redaelli, R. Rossi, and W. Scandale. Operational Performance of Crystal Collimation with 6.37 Z TeV Pb Ion Beams at the LHC. *Phys. Rev. Accel. Beams*, 27(1):011002, 2024. doi: 10.1103/PhysRevAccelBeams.27.011002. URL `https://link.aps.org/doi/10.1103/PhysRevAccelBeams.27.011002`.

[76] S. Redaelli, O. Aberle, A. Abramov, R. Bruce, R. Cai, M. Calviani, M. D'Andrea, Q. Demassieux, K. Dewhurst, M. Di Castro, L. S. Esposito, S. Gilardoni, P. D. Hermes, B. Lindström, A. Lechner, A. Masi, E. Matheson, D. Mirarchi, J.-B. Potoine, G. Ricci, V. Rodin, R. Seidenbinder, S. Solis Paiva, L. Bandiera, V. Guidi, A. Mazzolari, M. Romagnoni, M. Tamisari, Y. Gavrikov, and Y. Ivanov. Crystal Collimation of Heavy-Ion Beams at the Large Hadron Collider. *Phys. Rev. Accel. Beams*, 28(5): 051001, 2025. doi: 10.1103/PhysRevAccelBeams.28.051001. URL `https://link.aps.org/doi/10.1103/PhysRevAccelBeams.28.051001`.

[77] M. D'Andrea. *Applications of Crystal Collimation to the CERN Large Hadron Collider (LHC) and Its High-Luminosity Upgrade Project (HL-LHC)*. PhD thesis, University of Padova, February 2021. URL `http://cds.cern.ch/record/2758839`. Presented 23 Feb 2021.

[78] V. M. Biryukov, Y. A. Chesnokov, and V. I. Kotov. *Crystal Channeling and Its Application at High-Energy Accelerators*. Accelerator Physics. Springer, Berlin, Heidelberg, Germany, 1997. ISBN 978-3-540-60769-4. doi: 10.1007/978-3-662-03407-1. URL `https://doi.org/10.1007/978-3-662-03407-1`.

[79] E. Bagli, M. Asai, D. Brandt, A. Dotti, V. Guidi, and D. H. Wright. A Model for the Interaction of High-Energy Particles in Straight and Bent Crystals Implemented in Geant4. *Eur. Phys. J. C*, 74(8):2996, 2014. doi: 10.1140/epjc/s10052-014-2996-y. URL `https://doi.org/10.1140/epjc/s10052-014-2996-y`.

[80] W. Scandale and A. M. Taratin. Channeling and Volume Reflection of High-Energy Charged Particles in Short Bent Crystals: Crystal-Assisted Collimation of the Accelerator Beam Halo. *Phys. Rep.*, 815:1–107, 2019.

doi: 10.1016/j.physrep.2019.04.003. URL https://www.sciencedirect.com/science/article/pii/S0370157319301498.

[81] G. Iadarola, A. Abramov, P. Belanger, X. Buffat, R. De Maria, D. Demetriadou, L. Deniau, D. Di Croce, P. Hermes, P. Kicsiny, P. Kruyt, A. Latina, S. Łopaciuk, L. Mether, P. Niedermayer, K. Paraschou, T. Pieloni, M. Seidel, G. Sterbini, F. Van der Veken, and L. van Riesen-Haupt. Xsuite: An Integrated Beam Physics Simulation Framework. In *Proc. HB 2023*, page TUA2I1, 2024. doi: 10.18429/JACoW-HB2023-TUA2I1. URL https://cds.cern.ch/record/2882300.

[82] S. Łopaciuk et al. Empowering a Broad and Diverse Community in Beam Dynamics Simulations with Xsuite. In *Proc. IPAC'25*, 16th International Particle Accelerator Conference (IPAC'25), pages 1667–1670, Taipei, Taiwan, June 2025. JACoW Publishing, Geneva, Switzerland. doi: 10.18429/JACoW-IPAC25-WEBN1. URL https://indico.jacow.org/event/81/contributions/7141.

[83] F. Van der Veken, A. Abramov, G. Broggi, F. Cerutti, M. D'Andrea, D. Demetriadou, L. S. Esposito, G. Hugo, G. Iadarola, B. Lindström, S. Redaelli, V. Rodin, and N. Triantafyllou. Recent Developments with the New Tools for Collimation Simulations in Xsuite. In *Proc. HB 2023*, pages 474–478, 2024. doi: 10.18429/JACoW-HB2023-THBP13. URL https://cds.cern.ch/record/2901261.

[84] F. F. Van der Veken. Introducing Xcoll: A Streamlined Approach to Collimation and Beam Loss Simulations Using Xsuite. https://indico.gsi.de/event/19249/contributions/82656/attachments/48844/70973/ICAP_Xcoll.pdf, 2024. Presented at ICAP'24, Seeheim, Germany, October 2024.

[85] L. J. Nevay, S. T. Boogert, J. Snuverink, A. Abramov, L. C. Deacon, H. Garcia-Morales, H. Lefebvre, S. M. Gibson, R. Kwee-Hinzmann, W. Shields, and S. D. Walker. BDSIM: An Accelerator Tracking Code with Particle–Matter Interactions. *Comput. Phys. Commun.*, 252:107200, 2020. doi: 10.1016/j.cpc.2020.107200. URL https://www.sciencedirect.com/science/article/pii/S0010465520300400.

[86] L. J. Nevay, A. Abramov, S. T. Boogert, L. C. Deacon, H. Garcia-Morales, S. M. Gibson, R. Kwee-Hinzmann, W. Shields, J. Snuverink, and S. Walker. BDSIM: Automatic Geant4 Models of Accelerators. In *Proc. ICFA Mini-Workshop on Tracking for Collimation*, CERN, Geneva, Switzerland, 2015. doi: 10.23732/CYRCP-2018-002.45. URL https://cds.cern.ch/record/2694318.

[87] J. Allison, K. Amako, J. Apostolakis, P. Arce, M. Asai, T. Aso, E. Bagli, A. Bagulya, S. Banerjee, G. Barrand, B. R. Beck, A. G. Bogdanov, D. Brandt, J. M. C. Brown, H. Burkhardt, Ph. Canal, D. Cano-Ott,

S. Chauvie, K. Cho, G. A. P. Cirrone, G. Cooperman, M. A. Cortés-Giraldo, G. Cosmo, G. Cuttone, G. Depaola, L. Desorgher, X. Dong, A. Dotti, V. D. Elvira, G. Folger, Z. Francis, A. Galoyan, L. Garnier, M. Gayer, K. L. Genser, V. M. Grichine, S. Guatelli, P. Guèye, P. Gumplinger, A. S. Howard, I. Hřivnáčová, S. Hwang, S. Incerti, A. Ivanchenko, V. N. Ivanchenko, F. W. Jones, S. Y. Jun, P. Kaitaniemi, N. Karakatsanis, M. Karamitros, M. Kelsey, A. Kimura, T. Koi, H. Kurashige, A. Lechner, S. B. Lee, F. Longo, M. Maire, D. Mancusi, A. Mantero, E. Mendoza, B. Morgan, K. Murakami, T. Nikitina, L. Pandola, P. Paprocki, J. Perl, I. Petrović, M. G. Pia, W. Pokorski, J. M. Quesada, M. Raine, M. A. Reis, A. Ribon, A. Ristić Fira, F. Romano, G. Russo, G. Santin, T. Sasaki, D. Sawkey, J. I. Shin, I. I. Strakovsky, A. Taborda, S. Tanaka, B. Tomé, T. Toshito, H. N. Tran, P. R. Truscott, L. Urban, V. Uzhinsky, J. M. Verbeke, M. Verderi, B. L. Wendt, H. Wenzel, D. H. Wright, D. M. Wright, T. Yamashita, J. Yarba, and H. Yoshida. Recent Developments in Geant4. *Nucl. Instrum. Methods Phys. Res. A*, 835:186–225, 2016. doi: 10.1016/j.nima.2016.06.125. URL `https://www.sciencedirect.com/science/article/pii/S0168900216306957`.

[88] S. Agostinelli, J. Allison, K. Amako, J. Apostolakis, H. Araujo, P. Arce, M. Asai, D. Axen, S. Banerjee, G. Barrand, F. Behner, L. Bellagamba, J. Boudreau, L. Broglia, A. Brunengo, H. Burkhardt, S. Chauvie, J. Chuma, R. Chytracek, G. Cooperman, G. Cosmo, P. Degtyarenko, A. Dell'Acqua, G. Depaola, D. Dietrich, R. Enami, A. Feliciello, C. Ferguson, H. Fesefeldt, G. Folger, F. Foppiano, A. Forti, S. Garelli, S. Giani, R. Giannitrapani, D. Gibin, J. J. Gómez Cadenas, I. González, G. Gracia Abril, G. Greeniaus, W. Greiner, V. Grichine, A. Grossheim, S. Guatelli, P. Gumplinger, R. Hamatsu, K. Hashimoto, H. Hasui, A. Heikkinen, A. Howard, V. Ivanchenko, A. Johnson, F. W. Jones, J. Kallenbach, N. Kanaya, M. Kawabata, Y. Kawabata, M. Kawaguti, S. Kelner, P. Kent, A. Kimura, T. Kodama, R. Kokoulin, M. Kossov, H. Kurashige, E. Lamanna, T. Lampén, V. Lara, V. Lefebure, F. Lei, M. Liendl, W. Lockman, F. Longo, S. Magni, M. Maire, E. Medernach, K. Minamimoto, P. Mora de Freitas, Y. Morita, K. Murakami, M. Nagamatu, R. Nartallo, P. Nieminen, T. Nishimura, K. Ohtsubo, M. Okamura, S. O'Neale, Y. Oohata, K. Paech, J. Perl, A. Pfeiffer, M. G. Pia, F. Ranjard, A. Rybin, S. Sadilov, E. Di Salvo, G. Santin, T. Sasaki, N. Savvas, Y. Sawada, S. Scherer, S. Sei, V. Sirotenko, D. Smith, N. Starkov, H. Stoecker, J. Sulkimo, M. Takahata, S. Tanaka, E. Tcherniaev, E. Safai Tehrani, M. Tropeano, P. Truscott, H. Uno, L. Urban, P. Urban, M. Verderi, A. Walkden, W. Wander, H. Weber, J. P. Wellisch, T. Wenaus, D. C. Williams, D. Wright, T. Yamada, H. Yoshida, and D. Zschiesche. Geant4 – A Simulation Toolkit. *Nucl. Instrum. Methods Phys. Res. A*, 506(3): 250–303, 2003. doi: 10.1016/S0168-9002(03)01368-8. URL `https://www.sciencedirect.com/science/article/pii/S0168900203013688`.

[89] J. Allison, K. Amako, J. Apostolakis, H. Araujo, P. Arce Dubois, M. Asai,

G. Barrand, R. Capra, S. Chauvie, R. Chytracek, G. A. P. Cirrone, G. Cooperman, G. Cosmo, G. Cuttone, G. G. Daquino, M. Donszelmann, M. Dressel, G. Folger, F. Foppiano, J. Generowicz, V. Grichine, S. Guatelli, P. Gumplinger, A. Heikkinen, I. Hrivnacova, A. Howard, S. Incerti, V. Ivanchenko, T. Johnson, F. Jones, T. Koi, R. Kokoulin, M. Kossov, H. Kurashige, V. Lara, S. Larsson, F. Lei, O. Link, F. Longo, M. Maire, A. Mantero, B. Mascialino, I. McLaren, P. Mendez Lorenzo, K. Minamimoto, K. Murakami, P. Nieminen, L. Pandola, S. Parlati, L. Peralta, J. Perl, A. Pfeiffer, M. G. Pia, A. Ribon, P. Rodrigues, G. Russo, S. Sadilov, G. Santin, T. Sasaki, D. Smith, N. Starkov, S. Tanaka, E. Tcherniaev, B. Tome, A. Trindade, P. Truscott, L. Urban, M. Verderi, A. Walkden, J. P. Wellisch, D. C. Williams, D. Wright, and H. Yoshida. Geant4 Developments and Applications. *IEEE Transactions on Nuclear Science*, 53(1):270–278, 2006. doi: 10.1109/TNS.2006.869826. URL `https://ieeexplore.ieee.org/document/1610988`.

[90] R. Brun and F. Rademakers. ROOT – An Object Oriented Data Analysis Framework. *Nucl. Instrum. Methods Phys. Res. A*, 389(1):81–86, 1997. doi: 10.1016/S0168-9002(97)00048-X. URL `https://www.sciencedirect.com/science/article/pii/S016890029700048X`. New Computing Techniques in Physics Research V.

[91] L. Lönnblad. CLHEP – A Project for Designing a C++ Class Library for High Energy Physics. *Comput. Phys. Commun.*, 84(1):307–316, 1994. doi: 10.1016/0010-4655(94)90217-8. URL `https://www.sciencedirect.com/science/article/pii/0010465594902178`.

[92] A. Abramov, G. Broggi, R. Bruce, F. Carlier, M. Hofer, G. Iadarola, L. J. Nevay, T. Pieloni, M. Rakic, S. Redaelli, and S. M. White. Collimation Simulations for the FCC-ee. *J. Instrum.*, 19(02):T02004, 2024. doi: 10.1088/1748-0221/19/02/T02004. URL `https://dx.doi.org/10.1088/1748-0221/19/02/T02004`.

[93] A. Abramov, R. Bruce, F. S. Carlier, M. Hofer, G. Iadarola, T. Pieloni, L. J. Nevay, M. Rakic, S. Redaelli, and S. M. White. Development of Collimation Simulations for the FCC-ee. In *Proc. IPAC'22*, 13th International Particle Accelerator Conference (IPAC'22), pages 1718–1721, Bangkok, Thailand, June 2022. JACoW Publishing, Geneva, Switzerland. doi: 10.18429/JACoW-IPAC2022-WEPOST016. URL `https://jacow.org/IPAC2022/papers/WEPOST016.pdf`.

[94] B. Lindstrom et al. Xcoll–BDSIM Coupling for Beam Collimation. In *Proc. IPAC'25*, 16th International Particle Accelerator Conference (IPAC'25), pages 653–656, Taipei, Taiwan, June 2025. JACoW Publishing, Geneva, Switzerland. doi: 10.18429/JACoW-IPAC25-MOPS030. URL `https://indico.jacow.org/event/81/contributions/7413`.

[95] A. Abramov, G. Broggi, and L. J. Nevay. collimasim: Python Bindings to BDSIM for Collimation Studies in Pure Tracking Codes. `https://gitlab.cern.ch/anabramo/collimasim`.

[96] E. Skordis, V. Vlachoudis, R. Bruce, F. Cerutti, A. Ferrari, A. Lechner, A. Mereghetti, P. G. Ortega, S. Redaelli, and D. Sinuela Pastor. FLUKA Coupling to SixTrack. 2018. doi: 10.23732/CYRCP-2018-002.17. URL `https://cds.cern.ch/record/2694313`.

[97] Geant4 Collaboration. *Geant4 Physics List Guide (Version 11.3, doc Rev 9.2)*, 2025. Available at: `https://geant4-userdoc.web.cern.ch/UsersGuides/PhysicsListGuide/html/index.html` (accessed Oct 28, 2025).

[98] T. Kuhr, C. Pulvermacher, M. Ritter, T. Hauth, and N. Braun. The Belle II Core Software: Belle II Framework Software Group. *Comput. Softw. Big Sci.*, 3(1):1–11, 2018. doi: 10.1007/s41781-018-0017-9. URL `https://doi.org/10.1007/s41781-018-0017-9`.

[99] Belle II Collaboration. Belle II Analysis Software Framework (basf2). `https://doi.org/10.5281/zenodo.5574115`.

[100] G. Broggi et al. Beam Losses Due to Beam–Residual Gas Interactions in the FCC-ee. In *Proc. IPAC'25*, 16th International Particle Accelerator Conference (IPAC'25), pages 383–386, Taipei, Taiwan, June 2025. JACoW Publishing, Geneva, Switzerland. doi: 10.18429/JACoW-IPAC25-MOPM036. URL `https://indico.jacow.org/event/81/contributions/7401`.

[101] M. Ady and R. Kersevan. Recent Developments of Monte-Carlo Codes MolFlow+ and SynRad+. In *Proc. IPAC'19*, Melbourne, Australia, May 2019. doi: 10.18429/JACoW-IPAC2019-TUPMP037. URL `https://doi.org/10.18429/JACoW-IPAC2019-TUPMP037`. Paper TUPMP037.

[102] M. Ady. *Monte Carlo Simulations of Ultra High Vacuum and Synchrotron Radiation for Particle Accelerators*. PhD thesis, École Polytechnique Fédérale de Lausanne, Lausanne, Switzerland, 2016. URL `https://cds.cern.ch/record/2157666`.

[103] G. Broggi and A. Abramov. xcoll-toolkit: Assorted Tools for the xcoll Package for Collimation Simulation in Accelerator Beamlines. GitHub repository, 2025. URL `https://github.com/gbrogginess/xcoll-toolkit`.

[104] J. J. Duderstadt and L. J. Hamilton. *Nuclear Reactor Analysis*. Wiley, New York, USA, 1st edition, 1976. ISBN 978-0-471-22363-4.

[105] A. Xiao and M. Borland. Monte Carlo Simulation of Touschek Effects in a Linac Beam. In *Proc. LINAC'08*, pages 293–295, Victoria, BC, Canada,

2008. TRIUMF, Vancouver, Canada. URL https://proceedings.jacow.org/LINAC08/papers/mop092.pdf.

[106] M. Borland. ELEGANT: A Flexible SDDS-Compliant Code for Accelerator Simulation. Technical report, Argonne National Laboratory, IL, USA, August 2000. URL https://www.osti.gov/biblio/761286.

[107] Strategic Accelerator Design (SAD) Home Page. http://acc-physics.kek.jp/SAD/, 2025. Accessed: 2025-06-25.

[108] A. Natochii, S. E. Vahsen, H. Nakayama, T. Ishibashi, and S. Terui. Improved Simulation of Beam Backgrounds and Collimation at SuperKEKB. *Phys. Rev. Accel. Beams*, 24(8):081001, 2021. doi: 10.1103/PhysRevAccelBeams.24.081001. URL https://link.aps.org/doi/10.1103/PhysRevAccelBeams.24.081001.

[109] A. Natochii, T. E. Browder, L. Cao, G. Cautero, S. Dreyer, A. Frey, A. Gabrielli, D. Giuressi, T. Ishibashi, Y. Jin, K. Kojima, T. Kraetzschmar, L. Lanceri, Z. Liptak, D. Liventsev, C. Marinas, L. Massaccesi, K. Matsuoka, F. Meier, C. Miller, H. Nakayama, C. Niebuhr, A. Novosel, K. Parham, I. Popov, G. Rizzo, J. M. Roney, S. Y. Ryu, L. Santelj, S. Schneider, J. Schueler, B. Schwenker, X. D. Shi, F. Simon, S. Stefkova, M. Takahashi, H. Tanigawa, N. Taniguchi, S. Terui, S. E. Vahsen, L. Vitale, A. Vossen, Z. Wang, J. Wiechczynski, H. Windel, and K. Yoshihara. Measured and Projected Beam Backgrounds in the Belle II Experiment at the SuperKEKB Collider. *Nucl. Instrum. Methods Phys. Res. A*, 1055:168550, 2023. doi: 10.1016/j.nima.2023.168550. URL https://www.sciencedirect.com/science/article/pii/S0168900223005405.

[110] G. Broggi et al. Comparison of Xsuite Simulations with Measured Backgrounds at SuperKEKB. In *Proc. IPAC'25*, 16th International Particle Accelerator Conference (IPAC'25), pages 379–382, Taipei, Taiwan, June 2025. JACoW Publishing, Geneva, Switzerland. doi: 10.18429/JACoW-IPAC25-MOPM035. URL https://indico.jacow.org/event/81/contributions/7411.

[111] S. Terui, Y. Funakoshi, T. Ishibashi, H. Koiso, M. Masuzawa, Y. Morikawa, A. Morita, S. Nakamura, H. Nakayama, Y. Ohnishi, K. Ohmi, K. Shibata, M. Shirai, Y. Suetsugu, M. Tobiyama, R. Ueki, D. Zhou, K. Oide, and A. Natochii. Collimator Challenges at SuperKEKB and Their Countermeasures Using Nonlinear Collimator. *Phys. Rev. Accel. Beams*, 27(8):081001, 2024. doi: 10.1103/PhysRevAccelBeams.27.081001. URL https://link.aps.org/doi/10.1103/PhysRevAccelBeams.27.081001.

[112] J. Salvesen et al. Consistent Representation of Lattices Between Optics Codes for FCC-ee, SuperKEKB and More. In *Proc. eeFACT'25 – 70th ICFA Advanced Beam Dynamics Workshop on High-Luminosity Circular e^+e^- Colliders*, Tsukuba International Congress Center (EPOCHAL), Tsukuba, Japan, March 2025. Presented at eeFACT'25.

[113] J. Salvesen et al. Modelling Optics and Beam-Beam Effects of SuperKEKB with Xsuite. In *Proc. IPAC'25*, 16th International Particle Accelerator Conference (IPAC'25), pages 375–378, Taipei, Taiwan, June 2025. JACoW Publishing, Geneva, Switzerland. doi: 10.18429/JACoW-IPAC25-MOPM034. URL `https://indico.jacow.org/event/81/contributions/7317`.

[114] G. Broggi. First Study of Collimator Design for the FCC-ee. Master's thesis, Politecnico di Milano, 2022. URL `https://www.politesi.polimi.it/handle/10589/198343`. Master's thesis.

[115] W. Höfle, R. W. Assmann, S. Redaelli, R. Schmidt, D. Valuch, D. Wollmann, and M. Zerlauth. Controlled Transverse Blow-Up of High-Energy Proton Beams for Aperture Measurements and Loss Maps. In *Proc. IPAC'12, New Orleans, Louisiana, USA*, page 4059, 2012.

[116] E. B. Holzer, B. Dehning, E. Effinger, J. Emery, G. Ferioli, J. L. Gonzalez, E. Gschwendtner, G. Guaglio, M. Hodgson, D. Kramer, R. Leitner, L. Ponce, V. Prieto, M. Stockner, and C. Zamantzas. Beam Loss Monitoring System for the LHC. *IEEE Nucl. Sci. Symp. Conf. Rec.*, 2:1052, 2005. doi: 10.1109/NSSMIC.2005.1596433.

[117] E. B. Holzer et al. Development, Production and Testing of 4500 Beam Loss Monitors. In *Proc. EPAC'08, Genoa, Italy*, page 1134, 2008.

[118] A. Lechner, B. Auchmann, T. Baer, C. Bahamonde Castro, R. Bruce, F. Cerutti, L. S. Esposito, A. Ferrari, J. M. Jowett, A. Mereghetti, F. Pietropaolo, S. Redaelli, B. Salvachua, M. Sapinski, M. Schaumann, N. V. Shetty, V. Vlachoudis, and E. Skordis. Validation of Energy Deposition Simulations for Proton and Heavy-Ion Losses in the CERN Large Hadron Collider. *Phys. Rev. Accel. Beams*, 22(7):071003, 2019. doi: 10.1103/PhysRevAccelBeams.22.071003. URL `https://link.aps.org/doi/10.1103/PhysRevAccelBeams.22.071003`.

[119] M. Hofer et al. Design of a Collimation Section for the FCC-ee. In *Proc. IPAC'22*, pages 1722–1725, Bangkok, Thailand, June 2022. JACoW Publishing, Geneva, Switzerland. doi: 10.18429/JACoW-IPAC2022-WEPOST017. URL `https://jacow.org/IPAC2022/papers/WEPOST017.pdf`.

[120] M. Moudgalya. First Studies of the Halo Collimation Needs in the FCC-ee. Master's thesis, Imperial College London, Department of Physics, 2021. URL `https://inspirehep.net/files/ca5d1bb8d84d5a31f28ba39e6c4194b8`. Master's thesis.

[121] T. K. Charles, B. J. Holzer, K. Oide, and F. Zimmermann. Update on the Low Emittance Tuning of the e^+/e^- Future Circular Collider. In *Proc. IPAC'21*, pages 2601–2604, Campinas, SP, Brazil, August 2021. JACoW Publishing, Geneva, Switzerland. doi: 10.18429/

JACoW-IPAC2021-WEPAB011. URL https://jacow.org/ipac2021/papers/wepab011.pdf.

[122] MAD-X Program. http://cern.ch/mad/. CERN, Geneva, Switzerland.

[123] H. Grote, R. Ghislain, and F. Schmidt. The MAD-X Program (Methodical Accelerator Design), February 2022. URL http://madx.web.cern.ch/madx/. Accessed: April 14, 2023.

[124] J. B. Jeanneret. Optics of a Two-Stage Collimation System. *Phys. Rev. Spec. Top. Accel. Beams*, 1(8):081001, 1998. doi: 10.1103/PhysRevSTAB.1.081001. URL https://journals.aps.org/prab/abstract/10.1103/PhysRevSTAB.1.081001.

[125] C. Ahdida, D. Bozzato, D. Calzolari, F. Cerutti, N. Charitonidis, A. Cimmino, A. Coronetti, G. L. D'Alessandro, A. Donadon Servelle, L. S. Esposito, R. Froeschl, R. García Alía, A. Gerbershagen, S. Gilardoni, D. Horváth, G. Hugo, A. Infantino, V. Kouskoura, A. Lechner, B. Lefebvre, G. Lerner, M. Magistris, A. Manousos, G. Moryc, F. Ogallar Ruiz, F. Pozzi, D. Prelipcean, S. Roesler, R. Rossi, M. Sabaté Gilarte, F. Salvat Pujol, P. Schoofs, V. Stránský, C. Theis, A. Tsinganis, R. Versaci, V. Vlachoudis, A. Waets, and M. Widorski. New Capabilities of the FLUKA Multi-Purpose Code. *Front. Phys.*, 9:788253, 2022. doi: 10.3389/fphy.2021.788253. URL https://cds.cern.ch/record/2806210.

[126] G. Battistoni et al. Overview of the FLUKA Code. *Annals of Nuclear Energy*, 82:10–18, 2015. doi: 10.1016/j.anucene.2014.11.007. URL https://www.sciencedirect.com/science/article/pii/S0306454914005878.

[127] S. Marin. Collimators and Radiation Study in FCC-ee. Presented at the FCC-ee Collimation Meeting, CERN, Meyrin, Switzerland, September 2024. URL https://indico.cern.ch/event/1460411/. Available at: https://indico.cern.ch/event/1460411/contributions/6148959/attachments/2933617/5152293/slidesSTI_meeting_2.pdf.

[128] S. Marin et al. Power Deposition Studies for the FCC-ee Halo Collimation System. In *Proc. IPAC'25*, pages 486–489, Taipei, Taiwan, June 2025. JACoW Publishing, Geneva, Switzerland. doi: 10.18429/JACoW-IPAC25-MOPM069. URL https://indico.jacow.org/event/81/contributions/7237.

[129] K. André, B. Holzer, and M. Boscolo. Status of the Synchrotron Radiation Studies in the Interaction Region of the FCC-ee. In *Proc. IPAC'24*, pages 2473–2476, Nashville, TN, USA, May 2024. JACoW Publishing, Geneva, Switzerland. doi: 10.18429/JACoW-IPAC2024-WEPR09. URL https://indico.jacow.org/event/63/contributions/4511.

[130] K. Andre. Synchrotron Radiation Backgrounds. Presented at the 8th FCC Physics Workshop, CERN, Meyrin, Switzerland, January

2025. URL https://indico.cern.ch/event/1439509/. Available at: https://indico.cern.ch/event/1439509/contributions/6289585/attachments/2995407/5277333/FCC%20physics%20workshop%202025.pdf.

[131] M. Boscolo, F. Palla, G. Ammirabile, K. D. J. Andre, G. Baldinelli, P. B. de Sousa, F. Bosi, G. Broggi, R. Bruce, H. Burkhardt, M. Calviani, S. Candido, A. Ciarma, M. Dam, B. Francois, R. F. Ximenes, F. Fransesini, A. Frasca, A. Gaddi, A. Ilg, R. Kieffer, M. Koratzinos, S. Lauciani, A. Lechner, G. Lerner, G. Nigrelli, A. Novokhatski, K. Oide, A. Perillo Marcone, B. Parker, P. Raimondi, J. T. Seeman, C. Turrioni, L. Watrelot, and F. Zimmermann. Status of the FCC-ee Interaction Region Design. *EPJ Tech. Instrum.*, 12(1):4, 2025. doi: 10.1140/epjti/s40485-025-00117-3. URL https://doi.org/10.1140/epjti/s40485-025-00117-3.

[132] J. Guardia-Valenzuela, A. Bertarelli, F. Carra, N. Mariani, S. Bizzaro, and R. Arenal. Development and Properties of High Thermal Conductivity Molybdenum Carbide–Graphite Composites. *Carbon*, 135:72–84, 2018. doi: 10.1016/j.carbon.2018.04.010. URL https://www.sciencedirect.com/science/article/pii/S0008622318303555.

[133] G. von Holtey. Electron Beam Collimation at LEP Energies. In *Proc. 12th IEEE Particle Accelerator Conference (PAC'87), Washington, DC, USA*, March 1987. URL https://cds.cern.ch/record/176034/files/CM-P00065096.pdf. CERN Report CM-P00065096.

[134] G. Broggi et al. Optimizations and Updates of the FCC-ee Collimation System Design. In *Proc. IPAC'24*, pages 1192–1195, Nashville, TN, USA, May 2024. JACoW Publishing, Geneva, Switzerland. doi: 10.18429/JACoW-IPAC2024-TUPC76. URL https://indico.jacow.org/event/63/contributions/3734.

[135] M. Migliorati. Overview of Collective Effects for the Main Rings. Presented at FCC Week 2025, Vienna, Austria, May 2025. URL https://indico.cern.ch/event/1408515/contributions/6515087/attachments/3069805/5430664/2025_05_20_FCC-IS_week.pdf.

[136] D. Gibellieri. Impact of Collimators' Geometric Impedance on Beam Stability in the FCC-ee: Analysis and Optimization Techniques. Presented at FCC Week 2025, Vienna, Austria, May 2025. URL https://indico.cern.ch/event/1408515/contributions/6515086/attachments/3070936/5433965/FCCweek_Collimators_Impedance_Gibellieri_250520.pdf.

[137] P. Raimondi. LCC v105 Optics. Presented at the 212th FCC-ee Accelerator Design Meeting, CERN, Meyrin, Switzerland, September 2025. URL https://indico.cern.ch/event/1586010/contributions/6683775/attachments/3133260/5558747/LCC%20optics%20developments.pdf.

[138] G. Broggi. Collimation Considerations on IR Apertures. Presented at the FCC-ee MDI Meeting #67, CERN, Meyrin, Switzerland, June 2025. URL https://indico.cern.ch/event/1553922/contributions/6553203/attachments/3087290/5466321/FCCee_MDI_67_GB.pdf.

[139] S. Terui, G. Broggi, Y. Funakoshi, N. Iida, T. Ishibashi, H. Koiso, Q. Liu, A. Morita, Y. Mulee, S. Nakamura, A. Natochii, K. Uno, K. Oide, Y. Ohnishi, and H. Sugimoto. Report on the Results of the First Experiments on a Nonlinear Collimator for SuperKEKB. In *Proc. 21st Annual Meeting of the Particle Accelerator Society of Japan*, pages 104–109, Yamagata, Japan, July 31–August 3 2024. URL https://www.pasj.jp/web_publish/pasj2024/proceedings/PDF/THOA/THOA04.pdf.

[140] M. Tobiyama. Status of SuperKEKB and Experience with Nonlinear Collimation. In *Proc. IPAC'24*, number 15 in IPAC'24 – 15th International Particle Accelerator Conference, pages 1923–1927, Nashville, TN, May 2024. JACoW Publishing, Geneva, Switzerland. doi: 10.18429/JACoW-IPAC2024-WEZD1. URL https://indico.jacow.org/event/63/contributions/3097.

[141] J. Bao, A. Bogomyagkov, Z. Cao, M. Chang, F. Chen, G. Chen, Q. Chen, Q. Chen, Z. Chen, K. Fan, H. Gong, D. Gu, H. Guo, T. Guo, C. He, T. He, K. Hou, H. Hu, T. Hu, X. Hu, D. Huang, P. Huang, R. Huang, Z. Huang, H. Li, R. Li, S. Li, W. Li, X. Li, X. Li, Y. Liang, C. Liu, T. Liu, X. Liu, X. Liu, Y. Liu, H. Lv, Q. Luo, T. Luo, M. Skamarokha, S. Ma, W. Ma, M. Hosaka, X. Miao, Y. Mo, K. Ohmi, J. Pang, G. Pei, Z. Qi, F. Shang, L. Shang, C. Shi, K. Sun, L. Sun, J. Tang, A. Wang, C. Wang, H. Wang, L. Wang, Q. Wang, S. Wang, S. Wang, Z. Wang, S. Wei, Y. Wei, J. Wu, S. Wu, C. Xie, Z. Xiong, X. Xu, J. Yang, P. Yang, T. Yang, L. Yin, C. Yu, Z. Yu, Y. Yuan, Y. Zeng, A. Zhang, H. Zhang, J. Zhang, L. Zhang, N. Zhang, R. Zhang, X. Zhang, Y. Zhang, Y. Zhao, J. Zheng, D. Zhou, H. Zhou, Y. Zhou, Z. Zhou, B. Zhu, X. Zhu, Z. Zhu, and Y. Zou. Conceptual Design Report of Super Tau-Charm Facility: The Accelerator, 2025. URL https://arxiv.org/abs/2509.11522.

[142] S. Marin. Effects of Surface Defects in Primary Collimators in FCC-ee. Presented at the FCC-ee Collimation Meeting, CERN, Meyrin, Switzerland, March 3, 2024, 2024. URL https://indico.cern.ch/event/1504717/contributions/6438352/attachments/3037221/5364016/flatness_marin.pdf.

[143] G. Broggi, A. Abramov, and R. Bruce. Beam Dynamics Studies for the FCC-ee Collimation System Design. In *Proc. IPAC'23*, pages 360–363, Venice, Italy, May 2023. JACoW Publishing, Geneva, Switzerland. doi: 10.18429/JACoW-IPAC2023-MOPA129. URL https://indico.jacow.org/event/41/contributions/1097.

[144] G. Broggi. Tracking Studies for the FCC-ee Collimation System Design. *Il Nuovo Cimento C*, 47, 2024. URL https://cds.cern.ch/record/2918199/files/document.pdf.

[145] A. Abramov et al. Studies of Layout and Cleaning Performance for the FCC-ee Collimation System. In *Proc. IPAC'23*, number 14 in IPAC'23 – 14th International Particle Accelerator Conference, pages 356–359, Venice, Italy, May 2023. JACoW Publishing, Geneva, Switzerland. doi: 10.18429/JACoW-IPAC2023-MOPA128. URL https://indico.jacow.org/event/41/contributions/1314.

[146] R. Kersevan. Private communication, 2023.

[147] R. Kersevan. Vacuum System and Photoelectron Distributions in the Collider. Presented at the FCCIS 2023 WP2 Workshop, Rome, Italy, November 2023. URL https://indico.cern.ch/event/1326738/contributions/5650215/attachments/2750809/4787940/Vacuum%20system%20and%20photoelectron%20distributions%20in%20the%20collider%20-%20FCCIS%20WP2%20-%20Rome%2013-15Nov2023.pdf.

[148] R. Kersevan. Vacuum System in the MDI Region. Presented at the FCC-ee MDI & IR Mockup Workshop, Frascati, Italy, November 2023. URL https://agenda.infn.it/event/37720/contributions/212728/.

[149] M. Boscolo. Overview of MDI Issues Toward the TDR. Presented at FCC Week 2019, Brussels, Belgium, June 2019. URL https://indico.cern.ch/event/727555/contributions/3452794/attachments/1870001/3076685/FCCWEEK19_MDI_Mboscolo_final.pdf.

[150] P. Kicsiny. *Beam-Beam Effects in Future High Energy Circular Lepton Colliders*. Phd thesis, École Polytechnique Fédérale de Lausanne (EPFL), 2024. URL https://infoscience.epfl.ch/entities/publication/9f194f9b-76e8-4ba8-ab62-b19b17597ccc.

[151] P. Kicsiny et al. Benchmark and Performance of Beam-Beam Interaction Models for Xsuite. In *Proc. IPAC'23*, number 14 in IPAC'23 – 14th International Particle Accelerator Conference, pages 686–689, Venice, Italy, May 2023. JACoW Publishing, Geneva, Switzerland. doi: 10.18429/JACoW-IPAC2023-MOPL063. URL https://indico.jacow.org/event/41/contributions/1126.

[152] A. Frasca et al. Radiation Load from Radiative Bhabha Scattering in the FCC-ee Experimental Insertions. In *Proc. IPAC'25*, number 16 in IPAC'25 – 16th International Particle Accelerator Conference, pages 478–481, Taipei, Taiwan, June 2025. JACoW Publishing, Geneva, Switzerland. doi: 10.18429/JACoW-IPAC2025-MOPM067. URL https://indico.jacow.org/event/81/contributions/7309.

[153] H. Ikeda et al. Observations and Efforts to Reduce Sudden Beam Loss at SuperKEKB. In *Proc. IPAC'25*, pages 57–60, Taipei, Taiwan, June 2025. JACoW Publishing, Geneva, Switzerland. doi: 10.18429/JACoW-IPAC2025-MOCD3. URL `https://indico.jacow.org/event/81/contributions/7121`.

[154] S. Marin and A. Lechner. Material Effects on Maximum Beam Loss on Collimators. Presented at the FCC-ee Collimation Meeting, CERN, Meyrin, Switzerland, 25 November 2024, 2024. URL `https://indico.cern.ch/event/1474026/contributions/6247512/attachments/2973619/5233881/beamLoss.pdf`.

[155] A. Lechner. Private communication, 2025.

[156] G. Broggi, A. Abramov, M. Boscolo, R. Bruce, D. Mirarchi, and S. Redaelli. First Studies of Crystal Collimation for the FCC-ee. *Nucl. Instrum. Methods Phys. Res. A*, 1076:170479, 2025. doi: 10.1016/j.nima.2025.170479. URL `https://www.sciencedirect.com/science/article/pii/S0168900225002803`.

[157] A. Sytov, L. Bandiera, K. Cho, G. A. P. Cirrone, S. Guatelli, V. Haurylavets, S. Hwang, V. Ivanchenko, L. Pandola, A. Rosenfeld, and V. Tikhomirov. Geant4 Simulation Model of Electromagnetic Processes in Oriented Crystals for Accelerator Physics. *J. Korean Phys. Soc.*, 83(2):132–139, 2023. doi: 10.1007/s40042-023-00834-6. URL `https://doi.org/10.1007/s40042-023-00834-6`.

[158] E. Bagli. G4_MC_CHANNELING: Simulation of channeling in a straight or bent crystal via Geant4. `https://github.com/ebagli/G4_MC_CHANNELING`, 2025. GitHub repository.

[159] U. Wienands, T. W. Markiewicz, J. Nelson, R. J. Noble, J. L. Turner, U. I. Uggerhøj, T. N. Wistisen, E. Bagli, L. Bandiera, G. Germogli, V. Guidi, A. Mazzolari, R. Holtzapple, and M. Miller. Observation of Deflection of a Beam of Multi-GeV Electrons by a Thin Crystal. *Phys. Rev. Lett.*, 114(7):074801, 2015. doi: 10.1103/PhysRevLett.114.074801. URL `https://link.aps.org/doi/10.1103/PhysRevLett.114.074801`.

[160] V. M. Biryukov. On the Scaling of Electron Dechanneling Length in Bent Crystals, 2022. URL `https://arxiv.org/abs/2201.13113`.

[161] G. Vignola and The DAΦNE Project Team. DAΦNE: The Frascati Φ-Factory. In *Proc. 1991 IEEE Particle Accelerator Conf. (PAC'91)*, pages 68–70, San Francisco, CA, USA, 1991. URL `https://proceedings.jacow.org/p91/PDF/PAC1991_0068.PDF`.

Acknowledgements

I would like to express my deepest gratitude to my supervisor, Roderik Bruce. It has been a true privilege to work under your guidance. Your constant support, insightful feedback, and remarkable organization have been essential throughout this journey. I have learned a great deal from your expertise and have always admired your exceptional professionalism—one of your greatest qualities. This work would not have been possible without your trust and encouragement.

My sincere thanks also go to Manuela Boscolo, my advisor, for her continuous support, availability, and valuable advice over these years. I am particularly grateful for all the opportunities you gave me to present my work and represent our research at conferences and workshops—always supporting and encouraging me to do so. Your trust has been invaluable for my growth as a researcher.

A very special thanks goes to Andrey Abramov, my mentor from my very first day at CERN. From you I learned most of what I know about the simulation tools at the heart of this work. Beyond your technical expertise, your good humour and friendliness made every day more enjoyable. Since you left CERN, the days haven't been quite the same.

I would also like to thank Stefano Redaelli, leader of the CERN BE-ABP-NDC section. I have always appreciated how you make our working environment both pleasant and motivating—light-hearted and humorous, yet serious and focused when needed. I am also grateful for your interest in my work and for the support and attention you have shown throughout these years.

My gratitude extends to all my colleagues in the ABP group, with whom I had the pleasure to collaborate. Working alongside such talented, passionate, and kind people has been an enriching experience, both professionally and personally.

I am grateful to the Future Circular Collider (FCC) project, which funded my Doctoral Studentship and provided an inspiring framework for my research. My sincere thanks go to Frank Zimmermann, FCC Deputy Study Leader, for his unfailing support whenever I needed it.

I would also like to acknowledge the EAJADE programme, which made possible my stay in Japan through its financial support. My heartfelt thanks go to the KEK vacuum group, who warmly welcomed and guided me during my time at KEK. In particular, I would like to thank Takuya Ishibashi and Shinji Terui for their supervision, help, and many valuable discussions. I am especially grateful to Andrii Natochii, from whom I learned a great deal and who provided essential support for the studies on SuperKEKB presented in this thesis. Without his help, this part of the work would not have been possible.

Speaking of SuperKEKB, I would also like to thank Jack Salvesen and Giovanni Iadarola, who played a key role in developing the Xsuite model of SuperKEKB. Their contribution was fundamental to these studies, and I learned a lot from both of them during the model's development.

Finally, I would like to thank my family for their constant support and encouragement throughout these years—nothing would have been possible without them.

To my partner, Mara, for always being there and for her unending support—even though distance has often kept us apart.

To my lifelong friends, for always being present no matter the distance or the years.